VISTA: Long-Duration Balloon Mission to Venus

Group 02

AE3200: Design Synthesis Exercise
2026, Spring Semester, Q4

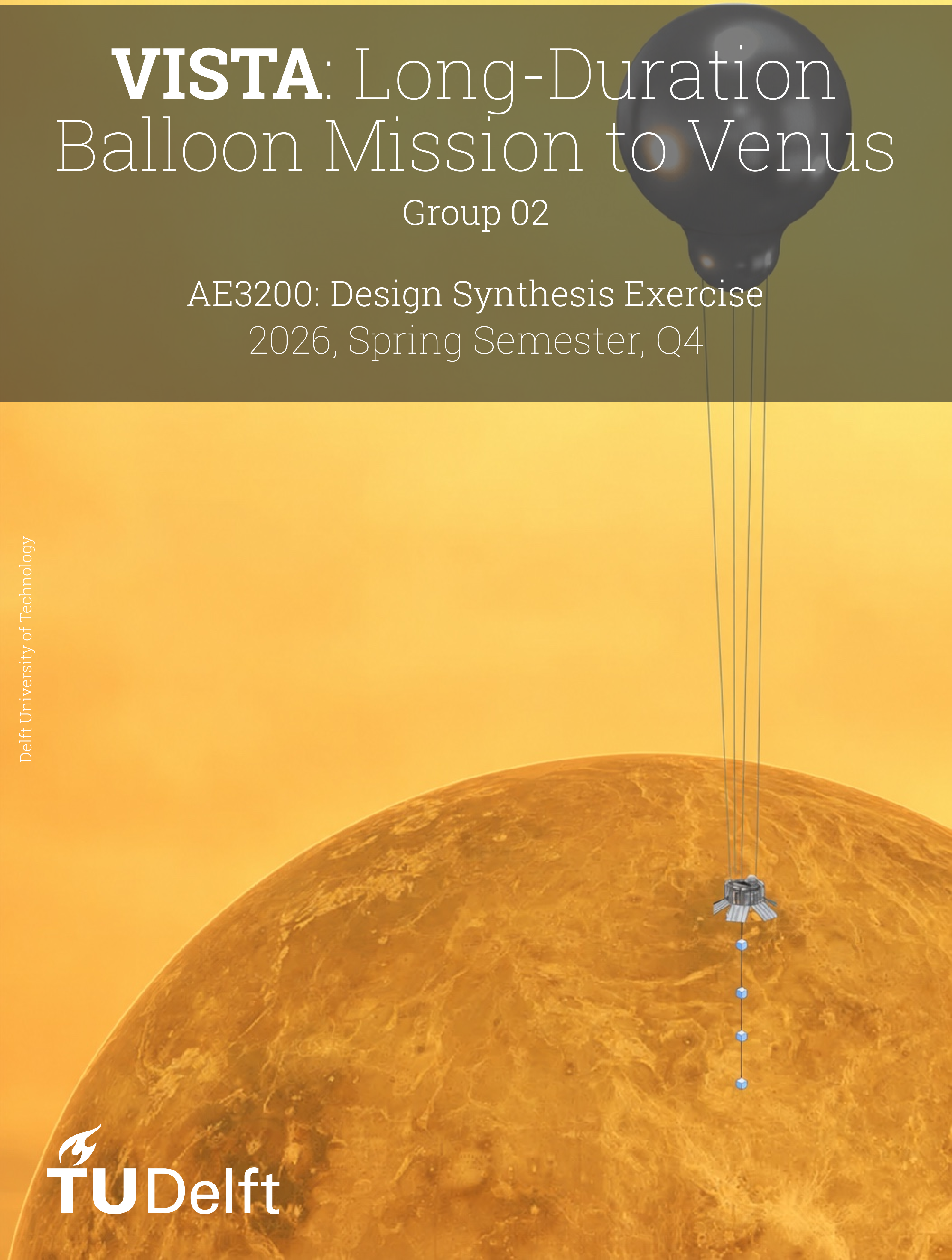

Delft University of Technology

VISTA: Long-Duration Balloon Mission to Venus

by

Group 02

Student Name	Student Number
Juliusz Ameljan-Kowalski	6021670
Filippos Atlasis	5694442
Traian Bistriceanu	5992036
Vadim Bodnarenco	5781027
Twan Burger	5792916
Bartosz Górny	5930952
Taran Kalma	5903831
Emil Wes Lambert	5689767
Nina Mamcarz	5906687
Beatriz Nunes Mascarenhas	5932181

Responsible Instructor:	Ir. J.A. Melkert
Teachers:	Dr.ir. E. Mooij, Dr. J. Guo, Dr. M.D. Pavel, Dr.ir. O.K. Bergsma, Dr.ir. M.F.M. Hoogreef
Principal Tutor:	Dr. E.S. Steenstra
Coaches:	Dr.ir. E.J.O. Schrama, A.F. Luijten, D. Jameux
Project Duration:	April, 2026 - June, 2026
Faculty:	Faculty of Aerospace Engineering, Delft

Cover: A render of the balloon design, with a radar scan map of Venus in the background.

TU Delft

Executive Overview

Venus is Earth's closest planetary neighbour in size, bulk composition, and orbital position, yet its surface environment remains one of the least explored in the inner Solar System, with temperatures above 460° C and pressures above 90 bar. Understanding why Venus evolved so differently from Earth is central to planetary science and to improving models of terrestrial climate evolution. Direct, sustained in situ observations within the Venusian cloud layer address one of the highest-priority measurement gaps identified by the Venus Exploration Analysis Group (VEXAG).

The **Venus In Situ Science and Technical Aerobot (VISTA)** mission concept proposes a balloon-borne aerobot designed to float continuously in the Venusian cloud layer at approximately 56 km altitude, where the ambient conditions are close to those at Earth's surface, with $T \approx 18°\,\mathrm{C}$ and $p \approx 0.46\,\mathrm{bar}$. Previous Venus balloon missions, the Soviet VEGA-1 and VEGA-2 aerobots in 1985, operated for approximately two days[1] before exhausting their lifting-gas reserves. VISTA aims to extend this duration to a **nominal science lifetime of five Earth years** (2036–2041) by addressing the main limiting factor: continuous lifting-gas leakage. This extended lifetime enables long-term observations of large-scale wind patterns, time-dependent atmospheric processes, and Venus' interior through the detection of rare seismic events.

This executive summary covers the mission concept, science objectives, system architecture, subsystem design results, mass and power budgets, reliability, cost, and Phase 0 feasibility assessment. Detailed subsystem analyses, requirement flow-down, and compliance matrices are provided in the main report.

Mission Analysis

The VISTA system comprises an aerobot (the primary in-scope deliverable), a deployment stage, and four external elements outside the design scope: a Launch Vehicle, a Cruise Stage, a Relay Orbiter in a 24-hour elliptical Venus orbit, and the ESTRACK ground network. The aerobot itself consists of:

- **Envelope:** A zero-pressure (ZP) outer balloon with an internal superpressure (SP) bladder, pre-filled with N_2 at deployment.
- **Cables:** Six 30 m suspension cables connecting the envelope to the gondola.
- **Gondola:** A cylindrical shell, housing the Bus and science Instruments.
- **Tether:** A 75 m electromechanical tether suspending five barometers below the gondola.

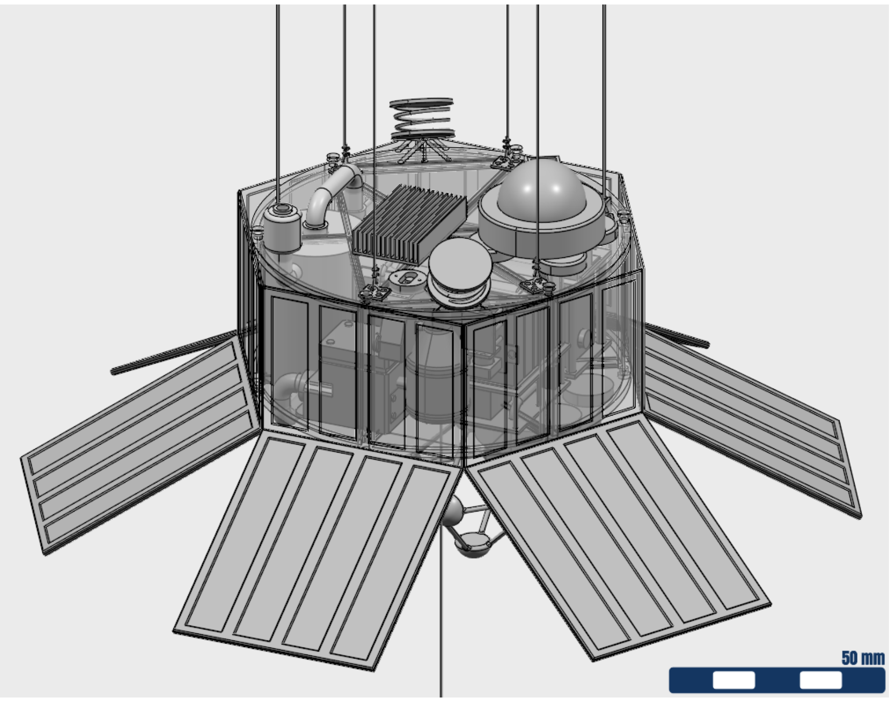

Figure 1: 3D model of the gondola.

---

[1] In this report, by "days" it is always meant Earth days. For Venusian days, this is explicitly mentioned

Following launch in January 2036, a 150-day interplanetary cruise delivers the combined spacecraft stack to Venus. After Venus Orbit Insertion, the Entry Capsule is released onto a direct atmospheric entry trajectory. The autonomous Entry–Descent–Deployment–Inflation (EDDI) sequence lasts approximately 60 min and ends with the aerobot in free float at 56 km altitude. A two-day commissioning phase then activates and checks all subsystems before the aerobot enters its nominal operations cycle.

During nominal operations, the aerobot follows the Venus day–night cycle of approximately six Earth days, with about 3.3 days in sunlight and 2.7 days in darkness. It drifts westward with the super-rotating atmosphere at 60–80 ms^{-1}, completing one circumnavigation of Venus approximately every six days. Relay-orbiter contact is available for about 25% of the mission time, with individual passes lasting between 50 min and 10 h.

Instrumentation

The payload instruments comprise a crucial part of the VISTA mission. The two main science goals for the mission involve seismic detection and atmospheric investigation. Seismology study will be conducted through the detection of infrasound waves that couple to the atmosphere from the epicentre of the venusquakes. Such system will comprise five barometers, one present inside the gondola and four placed uniformly in a 75 m long tether attached beneath the aerobot gondola.

As for the atmospheric measurements, nine instruments are selected to make part of the gondola instrumentation bus. The instrument suite is listed in Table 1, and performs all the remaining required science for the VISTA mission, while also addressing VEXAG roadmap goals.

Table 1: Selected payload instruments and primary function.

Instrument	**Primary Function**
NMS	Measures bulk atmospheric chemical composition, trace gas abundances, and isotopic ratios including D/H.
AFN	Characterises cloud aerosol particle size distribution, number density, and optical properties in situ.
WIS ×3	Temperature sensors that measure atmospheric temperature.
Sonic Anemometer	Measures 3D wind velocity vectors and atmospheric turbulence structure within the cloud layer.
Barometers ×5	Records absolute pressure to detect infrasound signatures associated with seismic activity and vertical wind.
mTLS	High-sensitivity in situ detection of trace gases including SO_2, HCl, and H_2O.
Pyrgeometer ×2	Measures upwelling and downwelling longwave radiative fluxes to characterise the atmospheric energy budget.
TOPS	pH sensor that measures acidity levels at the cloud layer.
OPC	Counts and sizes individual aerosol particles to determine size distribution and concentration.

Aerial Platform

The aerial platform encompasses all hardware that must survive the Venus cloud environment for five years in continuous float. The gondola houses the power, data handling, communications, thermal, ADCS, ISRU gas-management, and previously covered science instrument hardware.

Thermal & Environmental Protection

The Thermal Control Subsystem is based on strong thermal coupling to the Venus atmosphere. The gondola shell is deliberately driven towards ambient temperature through conductive baseplates and a heat sink, preventing excessive internal heat build-up from electronics dissipation. During nominal operations at 56 km nominal altitude, no full-gondola active thermal control is required. The average power usage operational range can be extended to 55.1–60 km and the lower limit could potentially be extended to ≈ 54 km, if the spacecraft reduces power usage. The subsystem is fully passive and has an estimated mass of 1.57 kg.

Environmental protection is implemented through subsystem-level material selection and dedicated filtration systems. Exposed surfaces are protected using application-specific coatings, including PCTFE on the balloon envelope, Parylene on the solar panels, and PTFE (Teflon) on external and internal gondola components. Atmospheric intakes are protected by two main filtering approaches: the ISRU filtration system, which uses a regenerable backflush architecture, and instruments that require direct atmospheric sampling employ heated protected inlets. The subsystems estimated mass is 0.35 kg and power of 2.5 W.

Command & Data Handling

The Command and Data Handling Subsystem (C&DH) acts as the aerobot's central control and data-management hub. It collects science and housekeeping data, stores it between orbiter contact windows, prepares it for downlink, and supports autonomous mission operations. The final design is based on a compact flight-proven on-board computer with an ARM Cortex-M7 processor, 2 MB program Flash, 1.4 MB internal RAM, 32 MB SDRAM, 512 kB MRAM, and 128 MB NAND flash storage. It also includes a watchdog/reset circuit, real-time clock, internal health sensors, and multiple digital and analogue interfaces. The selected storage capacity provides margin for the maximum nominal stored data volume of 54 MB and the worst-case requirement of 80 MB. Including the on-board computer, connectors, and harnessing, the C&DH subsystem has an estimated mass of 0.309 kg and a nominal power demand of 0.293 W during the day and 0.280 W at night.

Communications

The Communication Subsystem provides the aerobot's data and command link through a UHF connection to the relay orbiter, followed by an X-band relay to Earth through ESTRACK. The aerobot–orbiter link is the sizing driver and is designed for 1500 bits^{-1} at a worst-case range of 43,000 km, while satisfying the required link margins for telemetry, science data, and commands.

The final design uses a high-power UHF transceiver with coherent MSK modulation and two outward-inclined helical-ring antennas mounted near the top of the gondola. This configuration improves orbiter visibility, adds redundancy, and reduces dependence on precise attitude control. Including the transceiver, antennas, cable runs, and RF switch, the subsystem has a mass of 258. g and power levels of 0.22 W in receive mode, 6.30 W in transmit mode, and 6.52 W during simultaneous transmit and receive operation.

Electrical Power

Solar power is generated by Spectrolab XTJ Prime triple-junction cells, with an AM0 efficiency of 29.5% and a temperature-corrected effective efficiency of 25.8% at 56 km. The cells are mounted on the gondola body and fixed deployable skirt panels, providing a total active area of 2.17 m^2. At nominal float altitude, the broadband cloud-attenuated solar irradiance at local noon is 860 Wm^{-2}, corresponding to 33% of the exo-atmospheric value. This gives an end-of-life daylight-average power density of 110.8 Wm^{-2}. Including margins, the solar array delivers a peak power of 301.2 W and an orbit-average daytime power of 240.8 W.

Energy storage is provided by two Li-ion battery packs with a total capacity of 2500 Wh. The batteries are sized to sustain the nominal night load of 12.5 W over 96 h at a maximum depth of discharge of 48%. The cell mass is 16.0 kg, increasing to 17.6kg after margins.

Attitude Determination & Control

The ADCS of VISTA is driven by the peculiar configuration of the aerobot: a balloon-suspension cables-gondola-tether flight chain. Since no subsystem requires precise pointing, the ADCS is not designed for active three-axis attitude control. Its role is instead to keep the gondola motion bounded, observable, and compatible with the rest of the system. This is relevant for several subsystem interfaces: the seismic payload requires the tether fundamental mode to remain above the measurement band to filter the dynamic noise out, with $f_1 \geq 0.06$ Hz; the communication antennas require an angular visibility of $\theta \geq 80°$, which drives the suspension-cable length; and the wind sensor requires reliable knowledge of the platform motion for onboard correction. Within these constraints, the design aims to minimise mass, power, cost, and complexity.

The final configuration uses a local inertial sensing approach based on a 6-axis IMU placed close to the gondola centre of gravity and shared with GNS. Roll and pitch are corrected using gravity during dynamically quiet windows, while yaw is reset during orbiter contacts through differential carrier-phase heading determination. The selected suspension geometry uses six 30 m cables, providing an antenna visibility of 81.6°, and a 75 m tether to keep the seismic structural mode above the measurement band. The dynamic response is managed passively through a hybrid damping architecture, targeting a modal damping ratio of approximately $\zeta \approx 0.005$ without operational power. The subsystem has a mass of 3.0 kg and a power demand of about 3.5 W.

Structures

The structures and mechanisms subsystem must comply with several load-carrying requirements and must provide various attachment points for other interfaces. The structure of the gondola is a thin-walled cylinder reinforced with several stiffeners. These included 6 radially spaced stiffeners, 2 rings around the top and bottom lids of the cylinder, and several latitudinal stiffeners.

The structural design first selected the gondola material before sizing the geometry. Al 6061-T6 was chosen because it provides a good balance between specific strength and corrosion resistance. A thin Teflon film covers the gondola shell to provide additional protection against the Venusian cloud environment. With this material selection fixed, the structural sizing was performed. An overview of the gondola structure is shown in Figure 2.

By integrating the ring frames directly into the thin-walled cylindrical skin, the shell's resistance to local buckling failure modes is significantly elevated. This localized reinforcement strategy ensures that high-load attachment interfaces distribute stress smoothly across the primary load paths without adding unnecessary weight to the overall mass budget.

The suspension cable materials were selected consistently with the instrumentation tether system. The load-bearing element is a Vectran rope with a linear density of 0.010 kg m^{-1}. To protect the rope from sulphuric acid exposure in the Venusian cloud deck, it is covered by a fluoropolymer-based sleeve with a linear density of 0.0187 kg m^{-1}. The resulting structural mass contributions are summarised in Table 2.

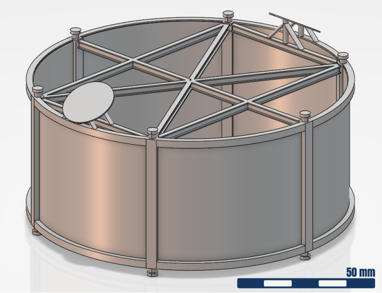

Figure 2: Gondola structural layout with stiffeners and interfaces. Top lid removed.

Table 2: Summary mass budget of the gondola structure and suspension system.

Subsystem	Mass (kg)	Fraction of Total (%)
Shell structure	6.888	31.76
Stiffeners	7.274	33.54
Attachments	0.222	1.02
Total Primary Structure	**14.384**	**66.32**
Cables	5.166	23.80
Tether	2.153	9.93
Total Suspension System	**7.319**	**33.68**
Total System Mass	**21.703**	**100.00**

Guidance & Navigation

The Guidance and Navigation Subsystem (GNS) determines and tracks the aerobot position and defines the altitude-control strategy. For position determination, the subsystem derives altitude from static pressure and estimates latitude and longitude through Doppler communication ranging with the relay orbiter. This method provides a vertical accuracy of up to 50 m and a horizontal accuracy of approximately 5 km. During communication blackout windows, the position is propagated using inertial measurements.

Venus' planetary-scale waves and wind patterns drive atmospheric super-rotation and the formation of polar vortices. Over the mission lifetime, long-term drift may cause the aerobot trajectory to move towards a polar vortex, where the solar flux would be insufficient for continued operation and mission termination would become imminent. This behaviour is strongly altitude-dependent and remains partly uncertain. Monte Carlo trajectory simulations using the Venus Climate Database estimate that, at the selected operational altitude, the probability of vortex entrapment is 3.5% for every Earth year, extending to about 20% over the mission duration.

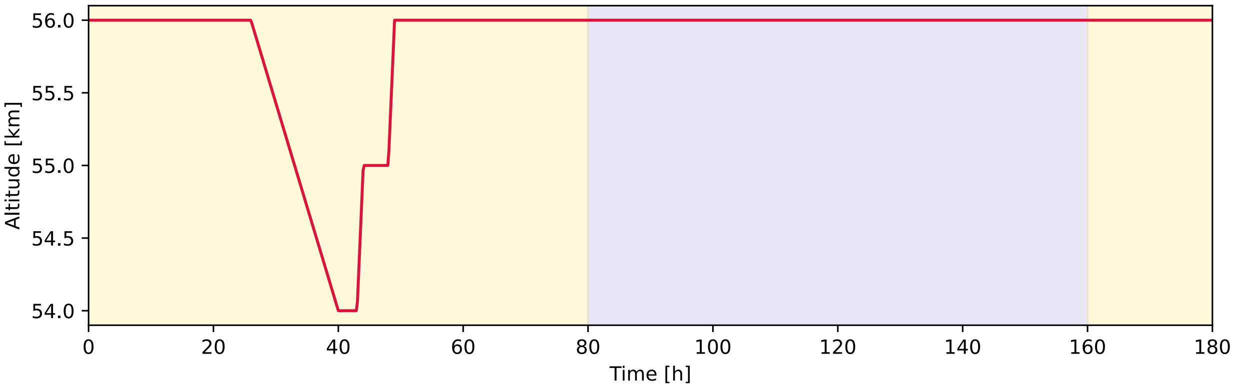

Figure 3: Example altitude profile of the aerobot

The nominal float altitude is set to 56 km. Lower altitudes are constrained by reduced solar flux and increased thermal-control difficulty, while higher altitudes increase the risk of polar-vortex entrapment beyond acceptable levels. An example of a valid altitude profile is shown in Figure 3. During both day and night, the aerobot remains at the nominal altitude of 56 km. Around local solar noon, when the available flux is highest and excess power is available, the aerobot can perform a descent manoeuvre to collect scientific measurements at lower altitude, potentially down to 54 km. After this short science window, the aerobot returns to its nominal float altitude.

Balloon Envelope and Buoyancy Design

The final balloon architecture was chosen to be a large zero-pressure balloon pre-filled with 260kg of N_2, and a fixed-volume superpressure balloon, with an in situ nitrogen top-up.

Balloon Sizing

The zero-pressure envelope uses Aclar for acid resistance, aluminium foil for gas retention, and polyurethane as the sealing layer. The superpressure envelope uses Vectran as the structural layer, since it carries the pressure load, with aluminium foil for gas retention and polyurethane for sealing. The balloon was sized using static force equilibrium, including the drag induced by vertical winds. Envelope leakage was evaluated at each altitude. The design feasibility was then checked over the full sizing range of 53–58 km, assuming a Venus day–night cycle of 84 h in sunlight and 60 h in darkness, for a total cycle duration of 144 h. The final balloon design and its main performance parameters are summarised in the table below.

Table 3: Final balloon configuration parameters.

ZP diameter	SP diameter	N_2 mass	Envelope mass	Leakage rate
11 m	5 m	260 kg	46 kg	1.87 kg/cycle

In Situ Resource Utilization

The In Situ Resource Utilisation (ISRU) system extracts N_2 from the Venusian atmosphere to compensate for envelope leakage and maintain aerobot buoyancy throughout the mission. The system first uses a two-branch filtering architecture with backflush regeneration to remove sulphuric acid aerosols and dust particles before they can enter the main flow path and degrade components over time. After filtration, a pump drives the gas into the separator, where CO_2 and N_2 are separated using a solution–diffusion membrane. The membrane was sized from the required molar flow of CO_2 removal and the corresponding CO_2 flux. The resulting nitrogen-enriched gas is then pumped into the zero-pressure envelope by the altitude-control pump. The same pump also feeds gas into the superpressure balloon when a reduction in altitude is required. The ISRU power consumption was estimated by calculating the pump and compressor power with the adiabatic compressor relation. The remaining component loads, including valves and sensors, were then added with their respective duty cycles. The final ISRU power consumption is estimated at approximately 171 W.

Atmospheric Entry & Deployment

The Entry–Descent–Deployment–Inflation (EDDI) stage is the most mass-intensive element of the VISTA system, with a mass of 373 kg including margin, corresponding to 49% of the total system mass. Since failure at any step would be unrecoverable and would lead to loss of mission, the full sequence is classified as safety-critical and is executed autonomously.

The EDDI sequence proceeds as follows:

1. **Hypersonic entry:** The aeroshell decelerates the capsule from interplanetary velocity and withstands peak axial deceleration loads of approximately $78.6g_0$.
2. **Aeroshell jettison:** The aeroshell is released using pyrotechnic separation devices.
3. **Main parachute deployment:** A subsonic parachute decelerates and stabilises the vehicle through the transonic and subsonic descent phases.
4. **Balloon inflation:** The pre-packed ZP envelope and SP bladder are deployed and inflated during parachute descent, targeting float capture at approximately 56 km altitude.
5. **Parachute release and free float:** The aerobot transitions to free-floating buoyancy-controlled flight. The CDHS confirms the free-float state using the onboard barometric altimeter and initiates the handover to Navigation control.

At the end of EDDI, the inflated aerobot is in free float and Commissioning mode begins. After gondola stabilisation, the tether and barometer array are deployed passively under gravity. Deployment is initiated by a shape-memory-alloy latch release and controlled by a passive eddy-current brake spool. Once deployment is complete, the empty spool is jettisoned using a spring-loaded collet release.

System Verification & Validation

The VISTA V&V programme follows the ESA V-model (ECSS-E-ST-10-02C) and is applied at equipment, subsystem, and system level. Four system-level test campaigns are performed sequentially:

1. **Structural, Mechanical, and Thermal (STM):** qualification of the gondola under launch vibration, acoustic, shock, and thermal-vacuum conditions.
2. **Functional and EMC (EM):** verification of subsystem interfaces, the dual-antenna architecture, the ISRU leakage-control loop, and the end-to-end communication chain with a simulated relay orbiter.
3. **Entry, Descent, and Deployment (PFM):** testing of the complete N_2 inflation chain, balloon-envelope deployment, pyrotechnic separation events, and launch-lock releases.
4. **Earth stratospheric analogue flight:** reduced-scale validation of float stability, tether pendulum dynamics, solar-array performance, and GNS position propagation.

Mass-budget closure is verified probabilistically using a Monte Carlo uncertainty propagation with $N = 100{,}000$ trials over all MEL components. The model includes cross-subsystem cascading effects, from gondola mass growth to EPS resizing, structural mass increase, additional N_2 lift gas, and the corresponding balloon-envelope resizing.

System validation is performed through four complementary strategies of increasing formality. End-to-end information-system validation demonstrates science-data generation, storage, transmission, and reconstruction. Mission-scenario simulation covers five representative cases: deployment, nominal science cycle, altitude control under disturbance, safe-mode recovery, and degraded long-duration operation. Operations-readiness validation is performed through mission rehearsals with a ground-segment simulator. Stress testing is then carried out through Monte Carlo simulation, worst-case analysis, and fault injection under off-nominal atmospheric, thermal, power, communication, and dynamic-disturbance conditions.

The validation approach combines analytical models, component-level sulphuric-acid exposure testing, and integrated mission simulations. The life/endurance test for the balloon envelope and ISRU materials, estimated to require several months of continuous acid-environment exposure, is the long-pole item in the qualification schedule and must begin no later than Phase B.

Conclusion

The technical risk register identifies three main residual risk drivers after mitigation: the ISRU nitrogen leakage and separator degradation chain (TR-ISRU-02 through TR-ISRU-05), post-deployment gondola dynamic instability (TR-D-04), and suspension-cable creep (TR-STR-03).

Closing the reliability gap requires three actions. First, the ISRU compressor and N_2 pump must be redesigned for the mission to extend their characteristic lifetime beyond 44,000 h. Second, the balloon envelope must be further matured to demonstrate a 15.5-year characteristic lifetime, consistent with $> 90\%$ reliability over a five-year mission. Third, nominal operation should remain centred at 56 km altitude to minimise the risk of polar-vortex entrapment.

Contents

Nomenclature

Abbreviations

Abbr.	Definition	Abbr.	Definition
ADC	Analog-to-Digital Converter	HLCL	High-power Latching Current Limiter
AM0	Air Mass Zero (solar reference spectrum)	HRA	Human Reliability Analysis
AWG	American Wire Gauge	I2C	Inter-Integrated Circuit
BPSK	Binary Phase-Shift Keying	JPL	Jet Propulsion Laboratory
CAD	Computer-Aided Design	JTAG	Joint Test Action Group
CAN	Controller Area Network	LCA	Life Cycle Assessment
CBE	Current Best Estimate	LDPC	Low-Density Parity-Check
CFD	Computational Fluid Dynamics	LEO	Low Earth Orbit
CFRP	Carbon-Fibre-Reinforced Polymer	MEMS	Micro-Electro-Mechanical Systems
COCOMO	Constructive Cost Model	MLI	Multi-Layer Insulation
COSPAR	Committee on Space Research	MRAM	Magnetoresistive Random-Access Memory
COTS	Commercial Off-The-Shelf	MSK	Minimum-Shift Keying
CPU	Central Processing Unit	NASA	National Aeronautics and Space Administration
CRC	Cyclic Redundancy Check	NRZ	Non-Return-to-Zero
CTE	Coefficient of Thermal Expansion	OPC	Optical Particle Counter
DAC	Digital-to-Analog Converter	PEEK	Polyether Ether Ketone
DC	Direct Current	PFA	Perfluoroalkoxy Alkane
DGB	Disk-Gap-Band (parachute)	PICA	Phenolic Impregnated Carbon Ablator
DMA	Direct Memory Access	PPS	Pulse Per Second
ECSS	European Cooperation for Space Standardization	PSA	Pressure Swing Adsorption
EEE	Electrical, Electronic, and Electromechanical	QA	Quality Assurance
EIRP	Equivalent Isotropically Radiated Power	QPSK	Quadrature Phase-Shift Keying
EMC	Electromagnetic Compatibility	RAM	Random-Access Memory
EMI	Electromagnetic Interference	RF	Radio Frequency
EPS	Electrical Power System	RH	Relative Humidity
ESA	European Space Agency	RLCL	Retriggerable Latching Current Limiter
EUV	Extreme Ultraviolet	SDRAM	Synchronous Dynamic Random-Access Memory
FEC	Forward Error Correction	SMAD	Space Mission Analysis and Design
FEP	Fluorinated Ethylene Propylene	SPE	Solar Particle Events
FRCI	Fibrous Refractory Composite Insulation	SPI	Serial Peripheral Interface
FSK	Frequency-Shift Keying	SWOT	Strengths, Weaknesses, Opportunities, and Threats
GCR	Galactic Cosmic Rays	TBD	To Be Determined
GFSK	Gaussian Frequency-Shift Keying	TID	Total Ionizing Dose
GMSK	Gaussian Minimum-Shift Keying	UART	Universal Asynchronous Receiver-Transmitter
GNS	Guidance & Navigation Subsystem	UHF	Ultra-High Frequency
GNSS	Global Navigation Satellite System	VCD	Venus Climate Database
GPIO	General-Purpose Input/Output	VHF	Very-High Frequency
GSE	Ground Support Equipment	WBS	Work Breakdown Structure

Symbols

All symbols used in this report are either SI quantities or are defined in-text at their point of first use.

1 Introduction

Venus exploration continues to face significant scientific and engineering challenges, despite the planet's importance for understanding terrestrial planet evolution. Its atmosphere, cloud layer, and interior remain only partially characterized, and existing observations are insufficient to resolve key questions about atmospheric dynamics, aerosol composition, and possible tectonic activity. A long-duration balloon-based aerobot offers a promising approach because it can operate within the Venusian cloud layer, where conditions are less extreme than at the surface, while still enabling meaningful in situ science.

This Design Synthesis Exercise project concerns the pre-phase A study of a long-duration Venus aerobot mission capable of performing sustained atmospheric and seismic investigations. The mission is driven by the need for persistent in-situ measurements over timescales far beyond previous Venus balloon missions. To achieve this, the design must address deployment into the Venusian atmosphere, long-term survival in the cloud layer, lifting gas replenishment, power generation, communication through an orbiter relay, and compliance with mission-level constraints on cost, technology readiness, reliability, and sustainability.

This final report presents the consolidated design of the VISTA Vehicle. The design has been developed from preliminary subsystem trade-offs into an integrated technical architecture centred on the Aerobot, its supporting subsystems, the balloon and buoyancy system, and the deployment sequence. The core design work is presented through the aerial platform subsystems in chapter 6, including thermal control, environmental protection, command and data handling, communications, electrical power, attitude determination and control, structures, and guidance and navigation. The balloon envelope, buoyancy management, and in-situ nitrogen extraction system are developed in chapter 7, while the entry, descent, deployment, and inflation architecture is described in chapter 8. The design is further supported by the future mission design work in chapter 9, where production, assembly, integration, testing, qualification, and cost aspects are considered. The Instrumentation is described in chapter 5.

The remaining chapters provide the mission-level context and supporting analyses required to evaluate the design as a complete system. The market analysis in chapter 2 identifies the scientific gap addressed by a long-duration Venus aerobot and positions VISTA with respect to historical and planned Venus missions. The mission concept of operations in chapter 3 defines the system boundaries, external interfaces, operational timeline, and mission modes that constrain the technical design. Subsystem management and interface control are addressed in chapter 4, ensuring that the individual subsystem designs are integrated consistently. The system-level verification and validation approach is presented in chapter 10, including compliance assessment and numerical-model checks. Finally, chapter 11 discusses technical risk, reliability, maintainability, safety, and sustainability.

2 Market Analysis

The market analysis section places the proposed long-duration aerobot mission within the context of both historical and upcoming missions for Venus exploration. It aims to assess where the concept fits within the current mission landscape, which scientific gaps it is meant to cover, and how it compares to other mission architectures, such as landers, orbiters, and aerial platforms.

2.1. Science-Data Benchmark and Mission Gap

The mission overview above shows that Venus exploration has produced several strong, but architecture-dependent datasets. Orbiters such as Magellan, Venus Express, Akatsuki, VERITAS, EnVision, and the Venus Orbiter Mission provide broad spatial coverage and long-duration remote observations, but they are limited by the need to infer atmospheric or surface conditions indirectly. In contrast, landers and descent probes such as Venera, Pioneer Venus, DAVINCI, and Venus Life Finder provide high-fidelity in situ measurements, but only at a few locations and over short time intervals. The Vega balloons are the closest historical analogue to the proposed aerobot mission, but their operational lifetime was limited to roughly two Earth days.

To identify remaining market and science gaps more clearly, Table 2.1 reorganises mission heritage by scientific data type. This enables comparing what each architecture does well, where its limitations remain, and which gaps a long-duration Venus aerobot could address.

Table 2.1: Venus science-data benchmark by mission architecture.

Scientific data type	Best historical/planned mission	Strength	Limitation / remaining gap
Surface imagery & geology	Venera; Magellan; VERITAS; EnVision; Venus Orbiter Mission [1, 2]	Direct surface imaging and global radar mapping of geology and topography	Lander lifetimes limited by extreme surface conditions; orbiters restricted to remote sensing [3]
Atmospheric vertical profile	DAVINCI; Pioneer Venus probes; Venera descent probes [4]	In situ measurements of temperature, pressure, and composition during descent	Measurements limited to single descent profiles with no temporal coverage [3]
Cloud-layer in situ meteorology	Vega-1/2 balloons [1]	Only in situ measurements of pressure, temperature, and wind in the cloud layer	Balloon operations limited to $\sim 46\,\mathrm{h}$, restricting temporal coverage [3]
Atmospheric circulation & winds	Akatsuki; Venus Express; Vega; Venus Orbiter Mission [1, 2]	Global wind fields inferred from orbital cloud tracking, complemented by in situ balloon drift	Lack of long-duration in situ measurements limits validation of atmospheric dynamics models [3]
Cloud & aerosol chemistry	Venera/Vega descent; Venus Express; DAVINCI; Venus Life Finder; Venus Orbiter Mission [4, 5, 2]	Combined in situ and remote sensing measurements constrain atmospheric composition and aerosols	Vertical and temporal coverage remains limited, especially for sustained cloud-layer sampling [6]
Atmospheric escape & plasma	Venus Express; Pioneer Venus Orbiter; Venus Orbiter Mission [4, 2]	Orbital measurements constrain atmospheric loss processes and plasma environment	Lack of coupled measurements linking upper atmosphere to lower atmospheric processes [6]
Volcanism & thermal anomalies	Venus Express; VERITAS; EnVision; Venus Orbiter Mission [1, 2]	Orbital infrared and radar observations enable the detection of surface changes and thermal anomalies	Absence of in situ measurements limits understanding of surface-atmosphere coupling [6]
Seismic & infrasound	None (proposed multi-platform concepts) [4]	No direct seismic measurements exist to date	Seismic and infrasound detection remains unvalidated and requires new mission architectures [3]

A quick comparison scan of achieved scientific investigations from past, present, and proposed missions from Table 2.1 shows that an aerobot is needed to satiate some of the current unanswered questions about Venus; this is elaborated upon in more detail in the subsequent "Competition Analysis" subsection (section 2.2).

2.2. Competition Analysis

A proposed aerobot mission occupies a distinct position within Venus exploration. Its main added value is that it provides persistent, in situ atmospheric observations over long durations, whereas future missions such as VERITAS, EnVision, and Venus Orbiter Mission focus mainly on orbital remote sensing, while DAVINCI and Venus Life Finder provide short-duration atmospheric probe measurements.

SWOT analysis in Table 2.2 summarises the mission's main strengths and weaknesses, together with external opportunities and threats arising from current and historical Venus exploration landscape.

Table 2.2: SWOT analysis of the proposed Venus aerobot mission

Strengths	Weaknesses
• Provides long-duration, in situ atmospheric observations, which orbiters and descent probes cannot provide. • Directly addresses the project requirement for at least 5 years of operation with continuous atmospheric and seismic investigations and monthly cloud aerosol sampling. • Offers repeated local measurements in the Venus cloud layer, enabling observation of changes over time rather than only snapshots. • Supports future orbital and descent missions by filling the missing niche of long-duration atmospheric presence. • Builds on proven heritage that balloon operations in the Venus atmosphere are feasible. • Orbiters cannot image deep atmosphere accurately, partly due to thick cloud layer of aerosol extending from 62 km down to 47 km. Below the clouds, clear visible imaging is not possible until 10 km from the surface due to scattering.	• Long-duration survival in the Venus atmosphere remains technically challenging. • Balloon leakage control and lifetime extension are central technological risks. • More complex operationally than a one-time descent probe. • Limited spatial coverage compared to orbiters performing global mapping. • Infrasound-based seismology concept has limited heritage. Therefore it must demonstrate that seismic investigations from an atmospheric platform are scientifically credible and feasible.
Opportunities	**Threats**
• Future missions such as VERITAS, EnVision, DAVINCI, Venus Life Finder, and the Venus Orbiter Mission increase interest in Venus and create a broader exploration context in which the aerobot can serve as a complementary mission element. • The aerobot can provide a unique measurement regime that is not covered by orbiters or descent probes. • Long-duration atmospheric monitoring can improve understanding of cloud dynamics, aerosol chemistry, and atmospheric variability. • The mission can position itself as the persistent in situ component of a larger future Venus exploration campaign. • Novelty in long-duration balloon technology can increase scientific attractiveness.	• Future missions may reduce perceived need if reviewers consider orbital or descent data sufficient. • Historical balloon missions such as Vega 1 and Vega 2 may lead to the criticism that the concept is not sufficiently new unless the long-duration aspect is clearly emphasised. • Strong competition from lower-risk orbital and descent architectures may make mission selection more difficult. • Earlier missions (Venus Express, Akatsuki, Venera) already provided valuable data, so VISTA must clearly show that it adds new science rather than repeats past results. • If the mission fails to justify its uniqueness, it may not be seen as a necessary step in Venus exploration. • Venus Life Finder partially addresses cloud-layer aerosol science, so VISTA must clearly emphasise its long-duration, multi-instrument, time-resolved advantage.

Looking at Table 2.2, the Venus Life Finder mission in particular is important for the competitive framing. It targets cloud-layer aerosol science, but only through a short-duration single-instrument probe. This makes it a close scientific comparator, but not a direct replacement for a long-duration aerobot.

Overall, given the user requirements, the product must be highly competitive within a specific niche: long-duration, in situ atmospheric science on Venus. It does not need to compete with orbiters in global mapping or with descent probes in one-time profiling, but it must clearly outperform them in persistent local observations over time. Since the mission requires at least 5 years of operation, continuous investigations, monthly aerosol sampling, nitrogen-based leakage mitigation, and compliance with strict mass, power, data-rate, and cost constraints, the mission's competitiveness depends mainly on uniqueness.

2.3. Increasing Competitiveness within the Market

A minor change that could make the mission more competitive from a cost point of view is to focus primarily on long-duration atmospheric and aerosol measurements, while making seismic investigations secondary. This would reduce payload and operational complexity, likely lowering both cost and technical risk, while preserving the mission's main advantage: continuous in situ observations in the Venus atmosphere. The trade-off is that the mission would cover a narrower range of science objectives, but in return, it would become more feasible and more competitive within the given budget. However, from a scientific investigation point of view, seismic measurements are of high importance in the Venus planetary science community [6], so cutting off seismology from the mission could reduce interest in carrying out the mission in the first place.

Table 2.3: Cost comparison of Venus missions with publicly available budget estimates, normalised to FY2026 euros

Mission	**Type**	**Year**[a]	**Cost [M€, FY2026]**[b]	**Source**
Pioneer Venus Orbiter + Multiprobe	Orbiter + probes	1978	∼940	Planetary Society budget dataset [7]
Magellan	Radar orbiter	1989–94	∼1450	Planetary Society budget dataset [7]
Venus Express	Orbiter	2005–14	∼330[d]	ESA [8]
Akatsuki	Orbiter	2010	∼360	JAXA [9]
DAVINCI	Flyby + probe	2021[c]	∼520	Planetary Society budget dataset [7]
VERITAS	Radar orbiter	2021[c]	∼520	Planetary Society budget dataset [7]
EnVision	Orbiter	2021[c]	∼730	ESA [10]
Venus Orbiter Mission (Shukrayaan-1)	Orbiter	2024[c]	∼135	ISRO [2]
Venus Life Finder	Atmospheric probe	2025	< 9	Rocket Lab / MIT [11]

[a] For flown missions, the year indicates the launch year or operational programme period. For missions in development, it indicates the year of selection, approval, or cost commitment.

[b] Costs are converted to approximate FY2026 euros for order-of-magnitude comparison. NASA mission costs are escalated using the Planetary Society's Planetary Exploration Budget Dataset, which applies NASA's New Start Inflation Index. FY2026 US dollar values are converted to euros using the ECB reference rate of €1 = $1.1702, equivalent to $1 = €0.8546. Non-NASA missions are escalated from their reported source-year values using broad inflation assumptions and should therefore be interpreted as ROM-equivalent values rather than audited programme costs.

[c] Selection or approval cost commitment rather than final flown mission cost.

[d] ESA-stated Venus Express cost of €220 M includes spacecraft development, instruments, launch, and operations.

Again, comparing against Venus Life Finder, competitiveness also depends on demonstrating that proposed aerobot offers more than just cloud-particle detection. The mission should thus emphasise measurement duration, repeated sampling, multi-instrument context, and ability to observe temporal variability. These are the areas where a 5-year aerobot remains clearly differentiated from a short-duration atmospheric probe.

2.4. Stakeholder Analysis

A stakeholder analysis was performed to identify the groups and individuals that may influence, constrain, or benefit from the Venus aerobot mission concept.

2.4.1. Stakeholder Expectations

Firstly, the initial customer expectations are considered, which are taken directly from the project description document [12]. They were broken down into Objectives, Needs, Desires, Capabilities and Other Constraints, and are listed below[1]:

Table 2.4: Stakeholder expectations

Category	**Description**
Need(s)	Answer fundamental gaps in knowledge of Venus' environment.
Goal(s)	Design a long-term, in situ aerobot mission to support Venus exploration.
Objectives	• Record continuous seismic and/or infrasound data over a 5-Earth-year lifetime with duty cycle 100%. • Measure pressure, temperature, wind speed, and cloud dynamics at 5 second intervals. • item Characterise the Venusian cloud-layer environment over the full operational lifetime by combining repeated aerosol sampling, particle-size measurements, trace-gas measurements, acidity measurements, and radiative-flux observations.
Desires	• Include radar mapping for topography investigations • Use optical imaging instruments to take pictures of Venus' landscape and/or balloon deployment procedure

Continued on next page

---

[1] Note that the engineering budgets are not considered in this list, and will be solely accounted for in the list of technical requirements.

Table 2.4 continued from previous page

Category	Description
Capabilities	Balloon-based aerobots can be deployed via an orbiter acting as a data relay.
Constraints	• Total mission cost ≤ 400 million euros (2026 conditions). • All systems must have TRL ≥ 4. • Concept must be novel relative to prior missions. • Must address VEXAG roadmap goals [6]. • Must follow safe manufacturing practices. • Must comply with COSPAR planetary protection. • Operational lifetime ≥ 5 Earth years. • Aerobot survival probability > 90%. • Instrument success probability > 80%.

This list will be expanded to consider inputs from other identified stakeholders.

2.4.2. Identification of More Stakeholders

The stakeholder set for this mission spans academic supervisors, technical advisors, external reviewers, planetary-science institutions, mission-enabling partners, and broader outreach-oriented audiences. They are displayed in the Power-Interest grid (Figure 2.1) - classifying them according to their influence on the project and interest in its outcome. All were classified within four quadrants: high power/high interest, high power/low interest, low power/high interest, and low power/low interest.

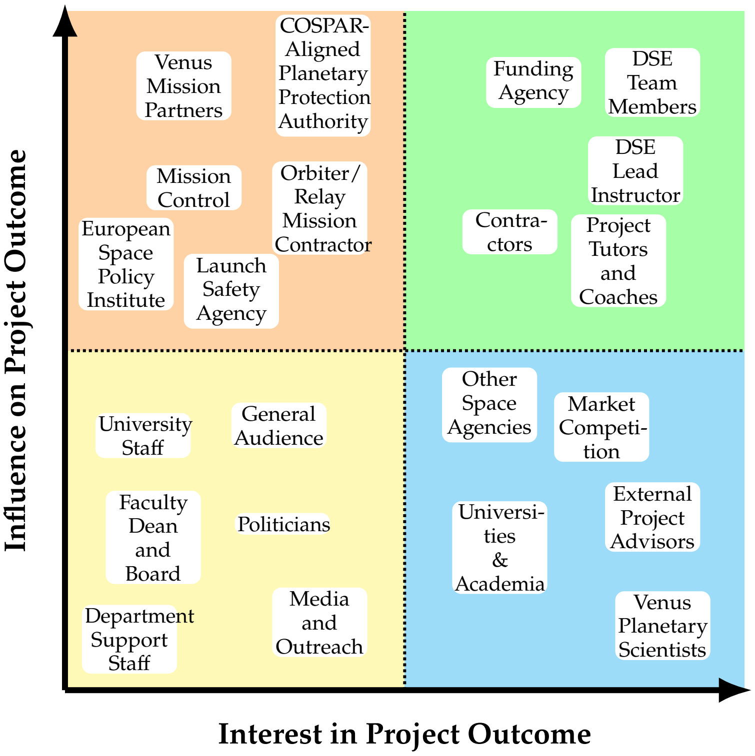

Figure 2.1: Stakeholder influence-interest matrix.

Stakeholders with both high power and high interest must be managed closely, since they can directly affect mission direction and approval while also being highly engaged in the outcome. Those in the green part of the grid are therefore considered the key stakeholders of the mission. For this project, this group includes the project tutor, contractors, the DSE team itself, and key science stakeholders such as ESA- and NASA-related funding representatives. Their involvement is necessary to ensure that the mission concept remains scientifically credible, technically feasible, and aligned with the project requirements.

Stakeholders with high power but lower day-to-day interest are placed in the "keep satisfied" quadrant. Although these actors may not participate in detailed design discussions, their requirements and approvals remain critical to mission viability. They therefore require targeted communication focused on compliance, risk, cost, and feasibility rather than frequent updates.

Stakeholders with high interest but lower formal decision power are classified as "keep informed". Their interest in the mission is substantial because the concept addresses scientifically relevant Venus exploration objectives, but their authority over design decisions is limited.

Finally, stakeholders with both low power and low interest are placed in the "monitor" category. These stakeholders, such as the university staff, faculty dean and board or outreach media, are not central to the design process but remain relevant from an outreach and communication perspective.

Overall, stakeholder analysis helps clarify decision authority and ensure that the mission concept is developed in a way that satisfies both technical and organisational expectations.

2.5. Expanded List of Stakeholder Expectations

Upon finalisation of stakeholder/market analysis, more expectations were identified that arose from stakeholders identified in 2.4.2 Identification of More Stakeholders. The stakeholders considered for this expansion of expectations were those of low-influence / high-interest, since the stakeholders with high-influence / high-interest comprised the expectations in Table 2.4, and stakeholders with low-interest are less relevant.

Table 2.5: Additional stakeholder expectations - low-influence / high-interest quadrant

Category	Stakeholder	Description
Needs	Other Space Agencies	Comparison to their own Venus programs (EnVision, VERITAS/DAVINCI, Shukrayaan-1, Rocket Lab probe) to avoid scientific and technical duplication.
	External Project Advisors	Timely access to design documentation and trade-off rationale so feedback can be substantive within their domains.
	Universities & Academia	Transparent methodology and documented design rationale suitable for peer review, education, and follow-up research.
	Venus Atmosphere Scientists	Mission architecture for long-duration, continuous in situ measurements addressing gaps not covered by concurrent probes.
	Market Competition	Sufficient public-facing information to benchmark competing concepts and detect potential IP conflicts.
Goals	Other Space Agencies	A concept that is scientifically and operationally complementary to their own roadmaps and could inform future cooperative Venus exploration.
	External Project Advisors	A technically credible, well-motivated design reflecting current best practice in atmospheric science, aerosol sampling, materials, and mission concepts.
	Universities & Academia	A publishable study contributing to open literature and engineering pedagogy.
	Venus Atmosphere Scientists	The mission is aligned with the scientific priorities identified in the VEXAG 2019 roadmap [6]. The detailed mapping between these priorities and the selected payload is discussed in chapter 5.
Objectives	External Project Advisors	Schedule review touchpoints at BR, MTR, and FR; Provide access to intermediate drafts; Document trade-offs on which feedback can be provided upon.
	Universities & Academia	Open-access final report; clear methodology documentation; potential conference or journal output.
	Venus Atmosphere Scientists	Carry out aerosol chemical sampling at community-accepted accuracy; Provide a 5-year dataset enabling study of long-timescale processes.
	Other Space Agencies	Provide a technical and scientific baseline that can be cited in own planning and referenced in mission-architecture studies.
Desires	External Advisors	Their input is meaningfully incorporated into the design and acknowledged.
	Universities & Academia	Cross-disciplinary collaboration opportunities; open sharing of novel technical elements (e.g. the in situ N_2 separation approach) so others can build on them.
Capabilities	External Project Advisors	Expertise: Colin Wilson (Venus atmosphere & mission concepts, ESTEC), Iaroslav Iakubivskyi (aerosol chemistry & sampling, MIT), Niels Ligterink (organic chemistry & mission concepts), Yinglu Tang (material science), consuled throughout the project.
	Universities & Academia	Peer review, literature access, prior mission-heritage documentation, and academic benchmarking of the design.
Constraints	Other Space Agencies	Reinforce COSPAR planetary-protection compliance and international treaty obligations; expect adherence to data formats and communication protocols.
	External Project Advisors	Limited availability windows - deliverables must reach them with enough lead time for substantive review.
	Universities & Academia	Academic integrity and originality standards (reinforces existing "no duplicate concept" requirement); attribution of prior work.
	Venus Atmosphere Scientists	Measurement accuracy, calibration, and sampling standards must meet benchmarks to be scientifically usable and comparable with heritage datasets.
	Market Competition	Intellectual Property Considerations - concept must not infringe on patented designs, and originality claim must be defensible.

3 Mission ConOps

The **V**enus ***In** situ* **S**cientific and **T**echnical **A**erobot (**VISTA**) is a long-duration, balloon-borne atmospheric platform designed to perform sustained *in situ* scientific investigations within the Venusian cloud layer for a nominal mission lifetime of 5 Earth years. This section consolidates the full system definition to anchor all subsystem-level design decisions and to satisfy the interface-control obligations identified in the N^2 diagram (section 4.1). Referenced requirements are all listed in Table 10.3 in chapter 10).

3.1. System Definition

The VISTA Aerobot (long-duration Venus atmospheric exploration platform composed of a buoyant balloon system, gondola, and scientific payload) and the Deployment Stage (carrier system responsible for transporting, protecting, and deploying the Aerobot into the Venus atmosphere) is the sole product whose design is within scope of the project.

3.1.1. Internal Boundaries

To aid with understanding and provide a clear responsibility division, a brief outline of definitions of keywords that will be used throughout the report is provided.

- **Ground Systems:** The entire communications and operational architecture on Earth necessary to orchestrate and manage the functioning of all other mission components.
- **Launcher:** The vehicle that delivers the **Cruise Stage** from ground into Earth orbit.
- **Cruise Stage:** Manages the orbital cruise from Earth and towards Venus. Monitors and maintains the **Orbiter** and the **VISTA Vehicle**. Delivers the **Orbiter** to a Venus orbit and the **VISTA Vehicle** to a Venus entry trajectory.
- **Orbiter:** Remains in orbit around Venus for the nominal mission duration and provides a communication link between the **VISTA Vehicle** and the **Ground Systems**. Can also conduct other tasks as determined by its design.
- **VISTA Vehicle:** The vehicle whose design is the concern of this work. It consists of the **Aerobot** and the **Deployment Stage**.
- **Deployment Stage:** Also referred to as the deployment subsystem, it protects and manages the **Aerobot**, starting at separation from the **Cruise Stage**, Venus atmospheric entry, until operational readiness of the **Aerobot**.

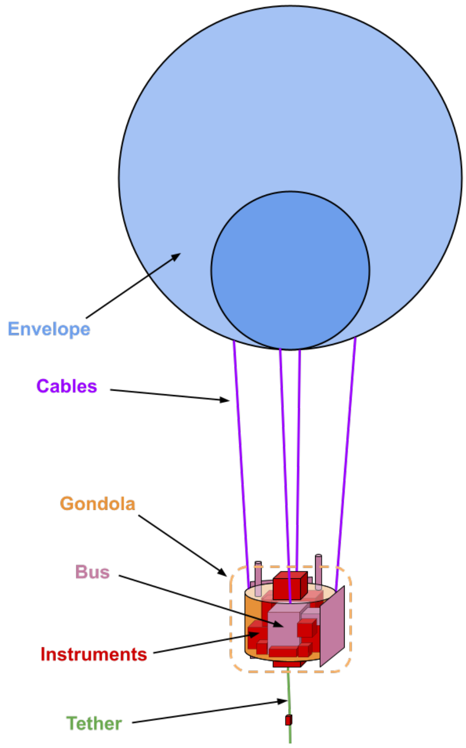

Figure 3.1: Aerobot Segments Diagram

- **Aerobot:** The entire vehicle that floats in Venusian atmosphere for the nominal mission duration. It consists of a **Gondola** suspended from a **Balloon**.
- **Balloon:** The envelope containing lifting gas that provides buoyancy for the **Aerobot**. It interfaces and connects with the **Gondola**.
- **Gondola:** The structure suspended beneath the **Balloon**. It contains the **Bus** and the **Instruments**.
- **Bus:** Also "platform", provides all resources necessary for the **Instruments** to function correctly for the nominal mission duration. Contains the **ISRU Subsystem**, among other subsystems.
- **ISRU Subsystem:** In situ resource utilization subsystem. A key part of the **Aerobot** that is tasked with extracting atmospheric nitrogen to aid with countering lifting gas leakage of the **Balloon**. The design of the **ISRU Subsystem** is of particular interest in this work.
- **Instruments:** Also sometimes referred to as "payload" or "payload instruments". The set of instruments composing the scientific suite of the **Aerobot**, that provides the desired research output over the nominal mission duration.
- **(Attachment) Cables:** The attachment cables that connect the **Gondola** to the **Balloon**.
- **Tether:** The tether used to mount the barometers below the **Gondola** for seismic detection.

3.1.2. External Boundaries

Four external system elements exist at the mission level but are *outside the design scope* of this project:

1. **Launcher** - delivers the Cruise Stage from the Earth surface to the Earth-departure trajectory.
2. **Cruise Stage** - supports interplanetary transfer and delivery to the Venus entry interface.
3. **Relay Orbiter** - remains in a 21-hour elliptical Venus orbit for the full science mission and provides the sole data relay path between the Aerobot and the ESTRACK ground network on Earth. *No orbiter design activity is performed within this project; the orbiter is treated as a mission-provided interface.* The assumptions adopted for the orbiter are stated explicitly in Section 3.1.4.
4. **Ground Systems** - the ESTRACK network and mission-control infrastructure on Earth.

3.1.3. Internal Constraints & Assumptions

This section documents explicit assumptions and constraints internal to the VISTA Aerobot design that drive subsystem-level decisions and performance allocations. These statements are binding on the design throughout Phase 0 unless explicitly revised through change control.

1. **Nominal float altitude:** The Aerobot shall maintain stable float at 57 km (+0, −3 km) above the Venus reference surface (radius 6,051.8 km). This altitude is chosen as a scientific operating point within the cloud layer where ambient temperature and ambient pressure resemble benign Earth-like conditions, and H_2SO_4 aerosol density has a peak concentration of ~0.5–2 mg/m^3 (requires acid-resistant coatings on optical windows and sample inlets).

   Excursions beyond ±100 m of nominal float shall trigger ISRU altitude-correction commands. The float altitude is locked via buoyancy management (N_2 replenishment during the dayside).
2. **Venus atmospheric composition:** Nominal composition at 56 km is assumed as: CO_2 (96.5%), N_2 (3.5%), SO_2 (<200 ppm), CO (<100 ppm), H_2O (vapor, 20–30 ppm), HCl (<10 ppm), HF (<1 ppm), and noble gases (<1% combined). This baseline is derived from Venera 14, Akatsuki (UVI/IR2), and Huygens-analogue spectroscopy. *Assumption:* CO_2 and N_2 combined remain > 99%.
3. **Operational cycles:** At 56 km float altitude in the Venus cloud layer, the Aerobot drifts westward with the retrograde zonal super-rotation at wind speeds of 60-80 m/s, circumnavigating Venus. The effective day-night period experienced by the balloon depends on balloon latitude and altitude - chosen as 50 degrees from the equator and 56 km above the surface, as expected throughout the mission. Based on these values, empirical measurements have been found to set the cycle period experienced by the aerobot as 6 Earth days (3.3 days in sunlight and 2.7 days in darkness) [13].
4. **Mission duration:** The nominal science mission lifetime is 5 Earth years (2036-2041), with launch planned for January 2036. Over the 5-year mission, the Aerobot shall complete $\approx$ 304 full Venus day-night cycles. Duty cycles, data budgets, and power reserves are predicated on this timescale. *Any major orbit maintenance by the relay orbiter (e.g., plane change) that alters the 24-h contact period must trigger immediate re-evaluation of science scheduling and commissioning timelines.*
5. **Ground segment and command authority:** VISTA operations are managed by Mission Operations Center with periodic commanding authority at orbiter passes. All critical sequences (Commissioning, Science transitions, ISRU altitude control) are pre-programmed into CDHS firmware with autonomous fault triggers (FDIR). Ground can modify mode setpoints and science schedules via uplink commands, but only during contact windows. Decisions to enter Safe Mode or End-of-Life are autonomous and not subject to ground override.

3.1.4. Relay Orbiter Interface Assumptions

As stated above, the relay orbiter is outside the design scope of this project. It is treated as a mission-provided asset analogous to the ESA EnVision or NASA VERITAS orbiter class. All link budgets, contact analysis, and navigation calculations depend on the following explicitly stated assumptions. *Any deviation from these assumptions must trigger a re-evaluation of the affected subsystem budgets.*

1. **Orbit definition:** Semi-major axis 37 000 km, eccentricity 0.13, inclination 30° (slight discrepancy with REQ-F-DEP-01 approved by the customer).
2. **Maximum aerobot–orbiter range:** 43 000 km, used as the worst-case UHF link-budget design point.
3. **UHF proximity antenna:** Orbiter UHF antenna gain assumed at 11.8 dBi, representing a moderate-to-high-gain proximity antenna.

4. **Aerobot acquisition concept:** The orbiter is assumed to transmit a UHF acquisition signal; once received, the aerobot starts transmitting.
5. **UHF coverage concept:** Either a low-gain broad-coverage antenna is used for acquisition before switching to 11.8 dBi antenna, or the 11.8 dBi antenna scans the expected region using a pointing mechanism.
6. **X-band Earth link:** High-gain parabolic dish, gain 34.38 dBi transmit / 67.20 dBi receive (ESTRACK 35-m station assumed), UST-Lite transponder.
7. **Doppler navigation:** Orbiter position assumed known to ≤1 km accuracy, anchoring aerobot IMU drift at each contact pass boundary.
8. **Orbiter mass and cost:** Not budgeted within the VISTA €400 M mission cap (REQ-C-COMP-02).
9. **Orbiter design authority:** Orbiter design decisions, including transponder selection, antenna pointing, orbit maintenance, and UHF acquisition strategy, are the responsibility of a separate design team.

3.2. Operational Timeline

The VISTA project timeline is driven by the Venus launch window of late 2035/early 2036 (REQ-C-COMP-03) and the 5-year nominal science mission ending in ~mid-2041 (REQ-C-MIS-01).

As seen in Figure 3.2, the mission is scheduled according to the ECSS mission development phases standard [14]. The corresponding Functional Block Diagram (FBS) and Functional Flow Diagram (FFD) are attached in Appendix A, providing visual interpretation of functions covered before and during operational timeline.

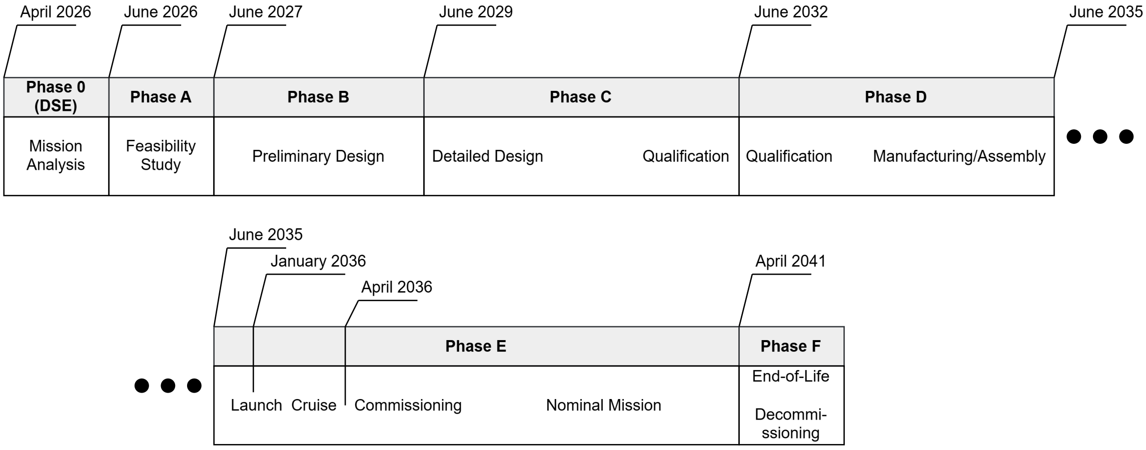

Figure 3.2: Diagram of the Mission Development Phases [15]

3.2.1. Post-Launch to Balloon Float: Macro Timeline

Figure 3.3 presents graphically expected step-by-step post-launch operations leading to atmosphere insertion.

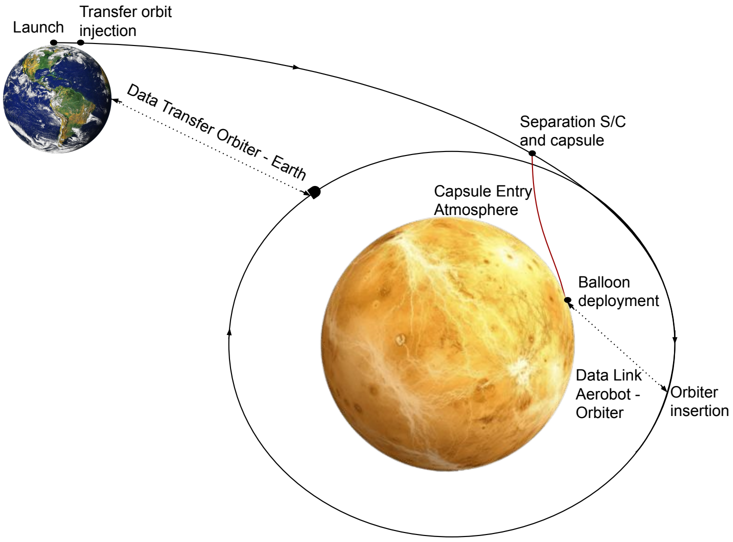

Figure 3.3: Concept of Operations - Cruise and Orbital Transfer

Figure 3.4 presents the planned mission macro timeline, taking place after launch (January 2036). Following the interplanetary cruise phase, the arrival at Venus in mid-2036 initiates entry, descent, deployment, and balloon inflation. The science mission then operates for 5 years (2036 to 2041), consisting of continuous atmospheric measurements supported by daily operational cycles and periodic communications passes via orbiter relay. At EOL, the platform is passivated, balloon is vented and descends passively to surface without active disposal.

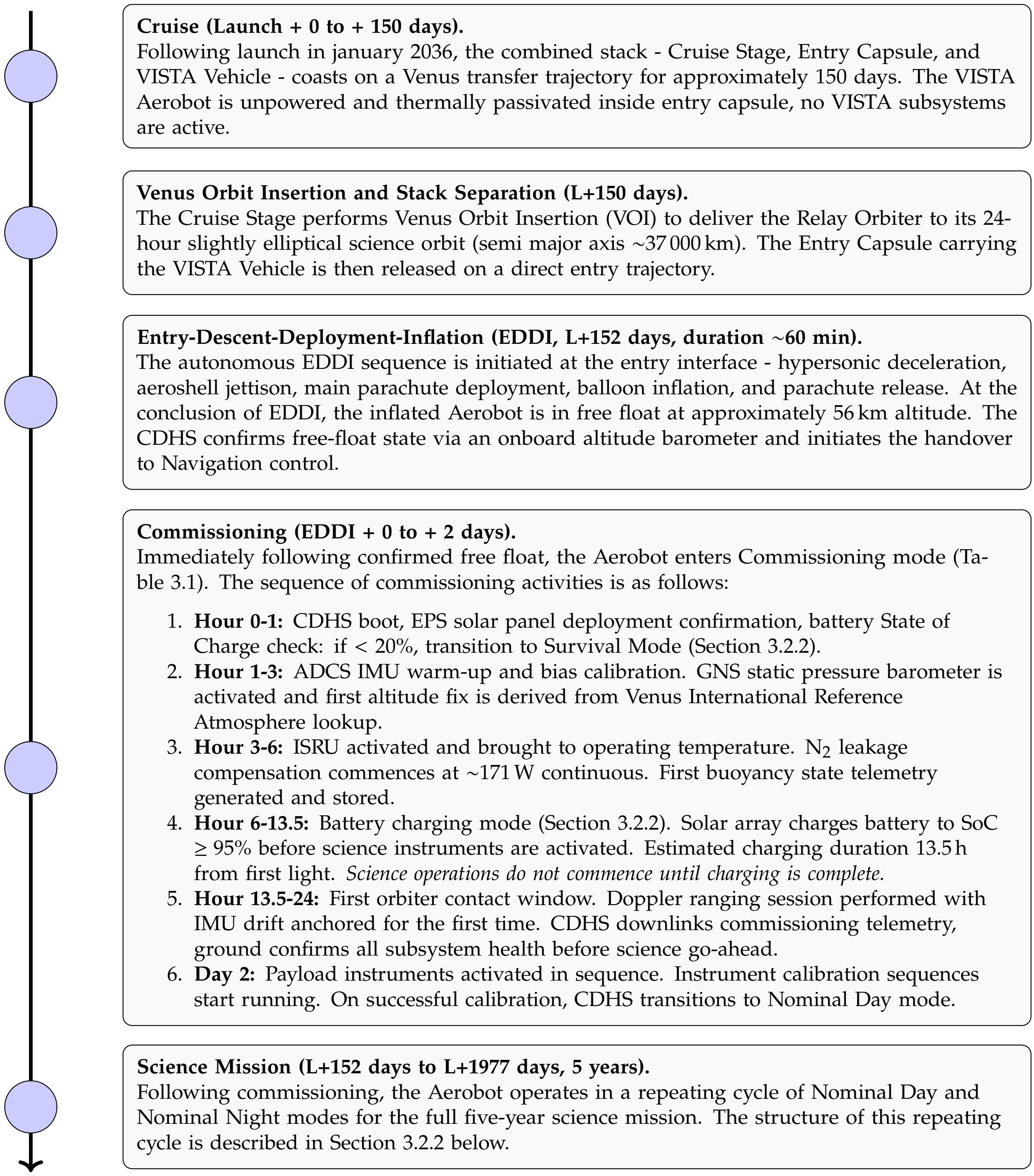

Cruise (Launch + 0 to + 150 days).
Following launch in january 2036, the combined stack - Cruise Stage, Entry Capsule, and VISTA Vehicle - coasts on a Venus transfer trajectory for approximately 150 days. The VISTA Aerobot is unpowered and thermally passivated inside entry capsule, no VISTA subsystems are active.

Venus Orbit Insertion and Stack Separation (L+150 days).
The Cruise Stage performs Venus Orbit Insertion (VOI) to deliver the Relay Orbiter to its 24-hour slightly elliptical science orbit (semi major axis ~37 000 km). The Entry Capsule carrying the VISTA Vehicle is then released on a direct entry trajectory.

Entry-Descent-Deployment-Inflation (EDDI, L+152 days, duration ~60 min).
The autonomous EDDI sequence is initiated at the entry interface - hypersonic deceleration, aeroshell jettison, main parachute deployment, balloon inflation, and parachute release. At the conclusion of EDDI, the inflated Aerobot is in free float at approximately 56 km altitude. The CDHS confirms free-float state via an onboard altitude barometer and initiates the handover to Navigation control.

Commissioning (EDDI + 0 to + 2 days).
Immediately following confirmed free float, the Aerobot enters Commissioning mode (Table 3.1). The sequence of commissioning activities is as follows:

1. **Hour 0-1:** CDHS boot, EPS solar panel deployment confirmation, battery State of Charge check: if < 20%, transition to Survival Mode (Section 3.2.2).
2. **Hour 1-3:** ADCS IMU warm-up and bias calibration. GNS static pressure barometer is activated and first altitude fix is derived from Venus International Reference Atmosphere lookup.
3. **Hour 3-6:** ISRU activated and brought to operating temperature. N_2 leakage compensation commences at ~171 W continuous. First buoyancy state telemetry generated and stored.
4. **Hour 6-13.5:** Battery charging mode (Section 3.2.2). Solar array charges battery to SoC ≥ 95% before science instruments are activated. Estimated charging duration 13.5 h from first light. *Science operations do not commence until charging is complete.*
5. **Hour 13.5-24:** First orbiter contact window. Doppler ranging session performed with IMU drift anchored for the first time. CDHS downlinks commissioning telemetry, ground confirms all subsystem health before science go-ahead.
6. **Day 2:** Payload instruments activated in sequence. Instrument calibration sequences start running. On successful calibration, CDHS transitions to Nominal Day mode.

Science Mission (L+152 days to L+1977 days, 5 years).
Following commissioning, the Aerobot operates in a repeating cycle of Nominal Day and Nominal Night modes for the full five-year science mission. The structure of this repeating cycle is described in Section 3.2.2 below.

Figure 3.4: Mission operational timeline.

3.2.2. Nominal Operations Timeline

This section describes the VISTA Aerobot timeline after deployment and settling on operational altitude.

Superimposing the 6-Earth-day aerobot period (subsection 3.1.3) onto the orbiter period, set at 21 hours as outlined in subsection 3.1.4, the result yields the coupled aerobot-orbiter period of ~21 h. During this period, the orbiter trajectory places the aerobot within line-of-sight of the orbiter approximately 25% of operational mission time. Individual contact passes range from a worst-case duration of ≈ 50 minutes to a best-case of ≈ 10 hours, with an expected mean pass duration of 6 to 8 hours, depending on relative geometric alignment between the orbiter ground track and the drifting aerobot.

Within these windows, the mission uses a two-segment relay communications architecture. The aerobot-to-orbiter link operates in UHF for both uplink and downlink, while orbiter-to-Earth link operates in X-band. Detailed link budgets, antenna pointing, and modulation parameters are defined in section 6.3.

Nominal Aerobot Mode Definitions

Five operational modes post-deployment are defined for the VISTA Aerobot. The identified modes are displayed in Figure 3.5, categorized as primary, contingency, and terminal.

Table 3.1 provides the formal definition of each mode including active subsystems, power consumption, and transition triggers.

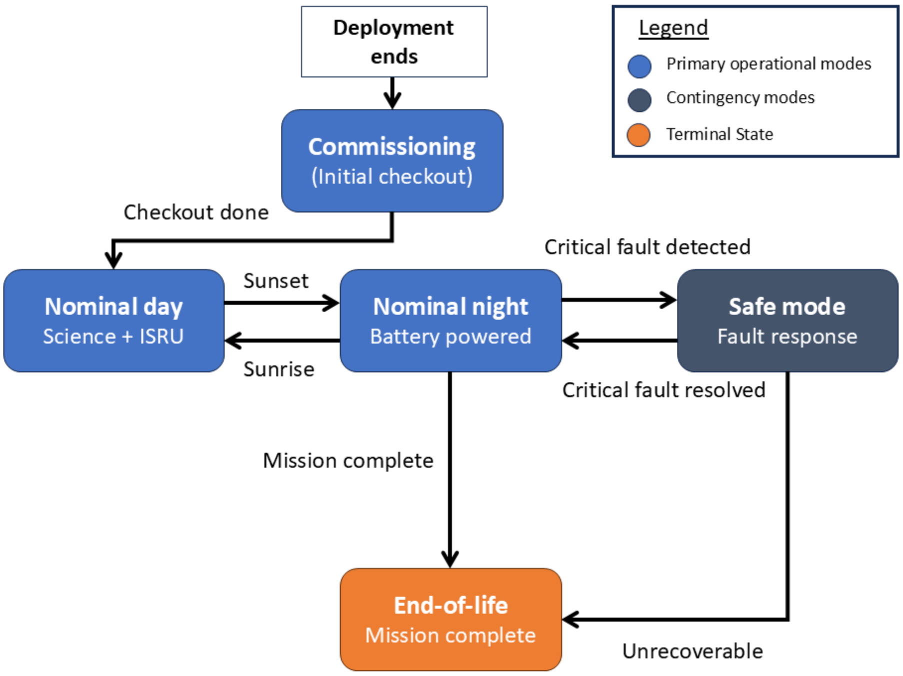

Figure 3.5: Transition state diagram

Table 3.1: VISTA Aerobot operational mode definitions (post-deployment).

Mode	Active Subsystems / Functions	Entry Trigger
Commissioning	All subsystems; initial checkout, sensor cal., ISRU warm-up, first comms. link	Post-EDDI free-float confirmation
Nominal Day	All instruments (duty-cycled), ISRU (leakage compensation), EPS (solar + charging), ADCS, CDHS, TCS (passive + active), GNC	Sunrise (solar panel output > threshold)
Nominal Night	ADCS, CDHS, barometers only; ISRU off; battery discharge	Sunset (solar panel output < 5 W)
Safe Mode	CDHS (minimal), , UHF beacon only, ADCS (IMU only)	fault escalation (over-temp., low SoC < 20%); single battery failure
End-of-Life	CDHS sends final telemetry; all systems shut down sequentially; ISRU vents balloon	Mission complete or battery SoC < 5% irreversible

Nominal Day Mode

During the dayside half-cycle, solar array output is sufficient to power all active subsystems and charge the battery simultaneously. The following activities occur on a repeating basis:

- **Continuous:** ADCS (IMU), CDHS, ISRU leakage compensation, WIS temperature sensor, pyrgeometers (two channels), and all five tethered barometers operate without interruption.
- **Duty-cycled science:** NMS (one session per day, ~58 min, 14 W), mTLS (two surveys per day, 14 W), AFN aerosol sampler (continuous cloud sampling at 40 W, DC = 12.5%), OPC aerosol profiling (30% DC, 15 W), sonic anemometer burst mode (30 min per hour, 2 W), TOPS pH sensor (one sample per orbit, ~10 min). Duty cycles are set to keep daily data generation within the 10 MB/day CDHS storage budget at 1500 bit/s downlink rate.

- **Altitude management:** GNS monitors barometric altitude at slow cadence (several samples per minute). If altitude deviates from the schedule, GNS issues a vent or inflate command to the ISRU superpressure bladder. Altitude manoeuvres are expected to be infrequent.
- **Battery charging:** Surplus solar power after powering loads is directed to battery charging. The battery is maintained at SoC ≥ 95% throughout the dayside to ensure full nightside energy reserve.

Nominal Night Mode

As solar irradiance drops below 100 W (sunset trigger), CDHS transitions to Nominal Night mode. The mode change is designed to be gradual rather than abrupt:

- **Pre-sunset (final 30 min of day):** CDHS halts NMS, AFN, mTLS, OPC, and TOPS sessions. Final data are written to on-board storage.
- **Night entry:** ISRU is shut down to conserve power. The resulting slow buoyancy reduction is accepted as a planned altitude drift of order ~200 m over the nightside, corrected at the following day's ISRU re-activation. The superpressure bladder maintains passive altitude stability within drift range.
- **Night operations:** Only ADCS (IMU), CDHS, barometers (all five), and the UHF beacon run continuously. Average night power consumption is 12.5 W. The battery provides all power. At the nominal night-average load, the battery energy reserve of ~1300 Wh supports approximately 46.7 h (~2 days) of Nominal Night before SoC reaches the 20% Safe Mode threshold, consistent with the ~2.9-day nightside half-cycle.
- **Seismic monitoring:** The barometer array remains active throughout the night. Nightside atmospheric noise is lower than dayside due to reduced convective activity, making night operationally valuable for infrasound seismic event detection.
- **Communications during night:** If an orbiter pass occurs during night (which occurs on average every third night given 21-h orbital period and 2.7-day night), a Communications Overlay session is executed at reduced power. The Doppler navigation fix is performed as normal. Night pass scheduling is prioritised by ground operations to maximise IMU drift correction frequency.
- **Pre-sunrise (first light detection):** Solar panel current is monitored by EPS. When output exceeds 5 W, CDHS triggers the transition back to Battery Charging mode, followed by Nominal Day mode after SoC ≥ 95% is restored. ISRU is reactivated and begins compensating the accumulated nightside N_2 leakage within the first hour of daylight.

Contingency Transition to Safe Mode

The CDHS Fault Detection, Isolation, and Recovery (FDIR) system monitors all subsystem health parameters continuously. The following transitions can interrupt the nominal cycle at any time:

- **Battery SoC < 20%: Automatic transition to Safe Mode. All payload and ISRU shut down; CDHS, ADCS (IMU only), EPS, and UHF beacon retained. Ground is notified at next orbiter pass.**
- **Over-temperature in gondola:** TCS FDIR halts high-power instruments (NMS, AFN) and activates Peltier cooler. If temperature not recovered within 30 min, transition to Safe Mode.
- **Altitude excursion beyond ±75 m:** GNS computes recovery trajectory and issues emergency vent or inflate command overriding the normal altitude management cadence. If altitude trajectory cannot be followed after 1 h, ground is alerted.
- **CDHS watchdog timeout:** Automatic processor reset followed by Safe Mode if nominal boot fails within three attempts.

Additional Functionalities

Moreover, three distinct Functionalities should be defined. As opposed to Modes, Functionalities are not discrete states, and rather are additional processes taking place within capacity of ongoing Modes. The Functionalities include:

1. Battery Charging - Redirects solar energy collected towards battery reserves.
2. Communications Overlay - The CDHS detects the orbiter UHF beacon and initiates a Communications Overlay session, adding 6.52 W (peak) to the current mode's base power. It is compatible with and superimposed on any base mode (Nominal Day, Nominal Night, or Safe Mode) and does not interrupt science instrument operation - science data generation and downlink occur concurrently where power margin permits.
   - Buffered science and housekeeping data are downlinked at 1500 bit/s to the orbiter, which stores and forwards the data to Earth via the X-band deep-space link at 10 kbit/s.

  - Command uplink from ground (via orbiter relay) is received and parsed by CDHS.
  - GNS performs a Doppler ranging session: the exact signal Doppler shift of the UHF telemetry link is measured to derive aerobot range rate and absolute position. The IMU drift accumulated since the previous pass is corrected by anchoring to the Doppler fix at pass entry and exit, halving the effective drift accumulation interval.
  - At pass end, CDHS confirms data volume received by the orbiter and clears the downlinked buffer from on-board storage.
3. High Alert - Increases the measurement capacity via engaging additional instruments, such as all standby barometers, upon detection trigger, i.e. quake-related pressure waves.

Science Mission-Dictated Instrument Duty Cycles

Selection of payload duty cycles is primarily driven by requirement REQ-OP-COM-06, which requires all processed and, where applicable, compressed science data to be downlinked within the available communication budget. The duty cycle of each instrument is therefore selected by balancing three factors: the scientific priority of the measurement, the sampling rate of the instrument, and the processed telemetry rate generated while the instrument is active. In this analysis, the duty cycle is defined as the ratio between the instrument active time and the full day-night operational cycle.

During nominal daytime operations, priority is given to instruments that provide continuous environmental context or high-value atmospheric science. All instruments listed below are on only active during daylight except for the barometers, so 0.56 duty cycle indicates it being on the entire day (3.3 Earth days out of 6-day cycle, as mentioned in subsection 3.1.3). The number of measurements obtained by each instrument is determined by both its sampling frequency $N_{meas} = f_s t_{active}$ and its duty cycle, set according to rationale listed below.

1. The Neutral Mass Spectrometer (NMS) is assigned a high daytime duty cycle because it has both a low processed telemetry rate and a relatively low sampling frequency, producing one full mass spectrum every 64 s. Near continuous daytime operation thus provides a large number of general atmospheric composition measurements without dominating the data budget. Scientifically, this is valuable because repeated NMS measurements allow vertical and temporal variations in bulk composition, trace species, and isotopic ratios to be monitored throughout daylight phase.
2. The Weather Instrument Suite (WIS) is also operated continuously during daylight. The WIS provides atmospheric temperature measurements, which are required as context for almost all other payload data. Temperature affects gas-density estimates, trace-gas retrievals, aerosol behaviour, radiative balance, and the thermal state of the gondola. Since the WIS has a low data rate and low power demand, continuous operation is justified.
3. For pressure measurements, only one barometer is operated continuously in nominal daytime mode. This barometer acts as a low-rate pressure and seismic sentinel. It must be noted that all 5 barometers are active during day and night, but only 1 sends telemetry unless a seismic anomaly is detected. This approach avoids the unnecessary data cost of operating the full barometer array continuously, while still preserving the ability to detect candidate seismic or infrasound events.
4. The two pyrgeometers are operated continuously during daylight because they measure the upward and downward longwave radiative fluxes needed to determine the local radiative balance. These measurements vary more slowly than aerosol or turbulence measurements, but continuous coverage during daylight is scientifically useful for linking the thermal environment to cloud-layer dynamics and atmospheric energy balance. Their low sampling rate and low data volume make continuous daytime operation feasible.
5. TOPs has been assigned a middle-to-low duty cycle. Cloud acidity is expected to change slowly. TOPs should work in parallel with AFN and OPC to provide valuable complementary data but this is not always necessary.
6. Sonic anemometer is given middle-to-high duty cycle as winds/turbulence vary much higher. However, it is not turned on all or nearly all the time as its data needs to be processed with data from the IMU, which increases pressure on the OBC.

Other instruments, such as the AFN, mTLS, and OPC, are more specialised science instruments and generally require higher power and larger telemetry allocations than background environmental sensors. In consideration towards the EPS-governed power budget and CDHS-governed data transmission limits, they are not operated continuously, and their operation is scheduled in dedicated science windows.

1. The AFN is assigned a low duty cycle because its high sampling rate produces a large number of particle measurements in a short period of time; even short operating windows are sufficient to build statistically useful aerosol and fluorescence datasets.

2. The OPC is also assigned a low duty cycle because its particle-size histograms generate a relatively high telemetry load when active. However, the OPC is preferably operated during the same windows as the AFN, since the two instruments provide complementary aerosol information: the OPC gives robust particle size distributions and number concentrations, while the AFN provides optical, fluorescence, and composition-related particle properties.
3. The mTLS is operated with a slightly higher duty cycle, since it provides high-priority trace-gas measurements at a lower processed telemetry rate than the AFN. When it operates, it operates in parellel with the NMS as it can be used to validate its data as well.

OPC and AFN are thus operated simultaneously at low duty cycles, while high duty cycle NMS and MTLs are turned off to reduce pressure on the power subsystem and the OBC. The final duty cycles can be seen in Table 3.2 and Figure 3.6, along with the number of measurements done in the day-night cycle.

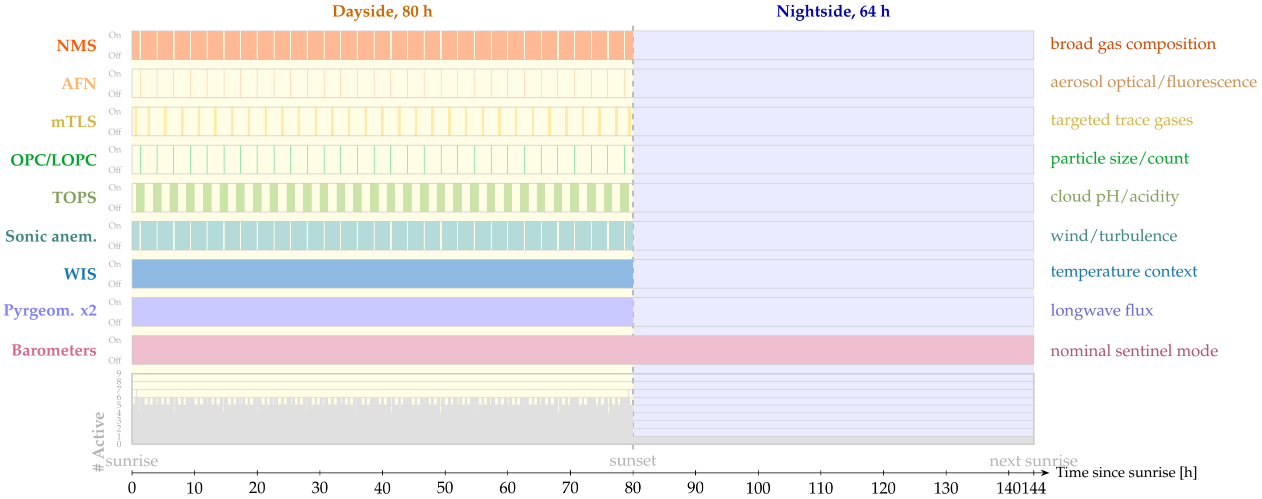

Figure 3.6: Science-payload duty-cycle profile over one nominal Venus day-night cycle. The schedule follows the telemetry model with 30 aerosol-measurement windows: AFN and OPC/LOPC are active simultaneously in short aerosol-measurement windows; NMS and the sonic anemometer are inactive during the corresponding NMS-off blocks; mTLS is scheduled once inside each NMS-active interval; TOPS is divided into 30 longer measurement windows; WIS and the pyrgeometers operate continuously during the dayside; and the barometer telemetry remains active over the full 144 h cycle. The bottom panel shows the instantaneous number of active payload component groups, with the barometer set counted as one group.

Table 3.2: Instrument duty cycle and number of measurements over 8 days

Instrument	Duty over 8 days	Daytime duty cycle	Number of measurements
NMS	0.500	0.900	4,050
AFN	0.030	0.054	155,520
WIS	0.556	1.000	57,605
mTLS	0.070	0.126	18,144
TOPS	0.280	0.504	2,419
Sonic anemometer	0.500	0.900	114,048
Barometers	1.000	1.000	103,680
Pyrgeometers x2	0.556	1.000	57,605
OPC/LOPC	0.030	0.054	7,776

Note: Note that all barometers are sampling but only few measurements from one are sent unless a seismic event is detected.

Expected science instrument duty cycles will be used, among others, for EPS design (section 6.5), thermal modelling (section 6.1), telemetry&storage budget verification (section 6.3), and operational planning.

3.2.3. End-Of-Life and Disposal

Venus hosts no known biosphere, making the practical environmental consequence of depositing battery chemistry, fluoropolymer coatings, or separator membrane materials negligible. COSPAR planetary protection requirements for Venus [16] are correspondingly light and do not drive design constraints. At EOL, the aerobot will be passively deflated, descend through the atmosphere to the Venusian surface, where it will remain indefinitely. Given the extreme surface conditions, with temperatures exceeding 460°C and pressures above 90 bar, most organic materials and polymers will thermally decompose relatively rapidly, and metallic components will oxidise, effectively integrating into the already hostile surface chemistry without introducing biologically meaningful contamination. The hardware can therefore be considered environmentally benign in the Venus context by any practical measure [17].

4 Subsystem Management and Interface Analysis

Before proceeding with subsystem-level design reporting, an overview of their dependencies and emerging expectations should be covered. Such subsystem interface analysis serves two principal purposes. First, it verifies that all required functional dependencies are accounted for and that no subsystem operates without the necessary supporting services. Second, it identifies architectural dependencies that may become critical failure points, design bottlenecks, or sources of increased integration complexity. Understanding these relationships early in the design process enables more effective allocation of redundancy, fault-management strategies, and verification activities. For VISTA, the 9 primary subsystems are:

Table 4.1: VISTA subsystem identifiers and scope.

Subsystem ID	Definition
SYS01	**Structures:** Gondola shell, suspension cables, envelope attachment hardware, payload mounting
SYS02	**CDHS (Command & Data Handling):** Flight computer, telemetry encoder, on-board storage
SYS03	**ADCS (Attitude Determination & Control):** IMU, control algorithms, damping parameters
SYS04	**Navigation (GNS):** Barometric altimeter, Doppler ranging logic, positioning algorithms
SYS05	**Payload:** Nine science instruments + five barometers on 75 m tether
SYS06	**ISRU & Buoyancy:** N_2 separator, lift-gas management, balloon inflation/venting
SYS07	**Power (EPS):** Solar array, battery, DC-DC converters, bus regulation, load-shedding logic
SYS08	**Thermals & Environment:** Insulation, radiative surfaces, heaters, coolers, temperature sensors
SYS09	**Deployment:** Aeroshell, parachute, balloon inflation hardware, pyro separation devices

4.1. Subsystem Interface Architecture

The subsystem architecture is first represented through a Hardware/Software Block Diagram (subsection 4.1.1), providing a high-level overview of physical interfaces, information and power flows throughout the vehicle. This is followed by N^2 interface analysis (subsection 4.1.2), which classifies subsystem interactions and forms the basis for subsequent coupling and criticality computations (subsection 4.1.3-4.1.4).

4.1.1. Hardware/Software Block Diagram

Figure 4.1 presents the resulting HW/SW Block Diagram for the VISTA mission architecture.

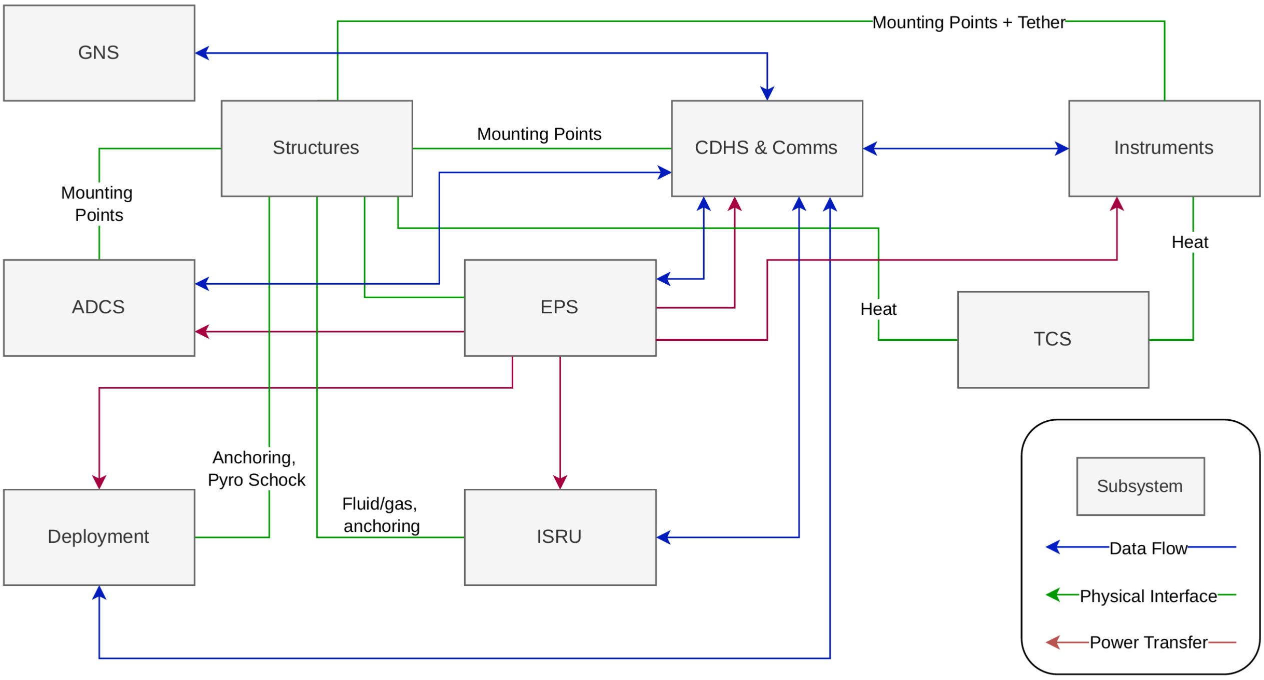

Figure 4.1: Hardware/Software Block Diagram

The Hardware/Software (HW/SW) Block Diagram provides a functional representation of the VISTA Aerobot architecture by illustrating the relationships between physical hardware elements and the software processes responsible for vehicle operation. Unlike the N^2 matrix, which focuses on interface classification and dependency tracking, the HW/SW diagram emphasizes operational information flow and command hierarchy during nominal mission execution.

4.1.2. N^2 Diagram

Full 9×9 N^2 matrix is presented in the Table 4.2. Each off-diagonal cell contains interface-type tag(s) followed by brief description of the interface content. Its importance lies in the possibility to easily determine:

- **Critical hubs** - Subsystems that many others depend on
- **Potential failure cascades** - If subsystem X fails, which others are affected
- **Coupling strength** - Heavy data/power/mechanical coupling implies high design risk

For the purpose of the N^2 diagram, the interfaces between primary subsystems from Table 4.1 have been reclassified into five types:

1. **[M] Mechanical Interface:** Physical load path, mass distribution, mounting provision, structural attachment, vibration/shock transmission, center-of-gravity (CG) contribution.
2. **[D] Data/Command Interface:** Electrical signal exchange (serial, CAN bus, discrete lines), telemetry generation, command reception, state information flow. Includes both real-time control signals and asynchronous telemetry streams.
3. **[E] Electrical/Power Interface:** Power distribution, voltage regulation, load current draw, peak transient power demand, bus protection (fuses, diodes, power switches).
4. **[T] Thermal Interface:** Heat dissipation pathways, radiative coupling, conductive thermal paths, component temperature limits, heater/cooler power demand, temperature telemetry.
5. **[F] Fluid/Gas Interface:** Lift-gas properties (pressure, composition, leakage rate), N_2 supply/demand, balloon inflation sequencing, pressure relief, vent pathways.

Table 4.2: N^2 interface matrix for VISTA subsystem interfaces.

From↓ / To→	**SYS01 Structures**	**SYS02 CDHS**	**SYS03 ADCS**	**SYS04 Navigation**	**SYS05 Payload**	**SYS06 ISRU + Buoyancy**	**SYS07 Power**	**SYS08 Thermals & Env.**	**SYS09 Deployment**
SYS01 Structures	**Structures**	**[M]** CDHS accommodation; harness paths	**[M]** ADCS sensor mounting and alignment	**[M]** Navigation sensor mounting	**[M]** Payload mounting; sample-inlet accommodation	**[M]** Envelope/ gondola support; ISRU mounts	**[M]** Power-system mounts; harness paths	**[M,T]** Structural accommodation; conductive thermal paths	**[M]** Aeroshell interface; parachute/separation hard-points; balloon mass and CG
SYS02 CDHS	**[M]** Antenna size	**CDHS**	**[D]** Attitude-mode commands; setpoints	**[D]** Navigation-mode commands; altitude setpoints	**[D]** Science scheduling; data-storage I/F	**[D]** ISRU and gas-management commands	**[D]** Load-shedding and bus-mode commands	**[D]** Thermal-mode setpoints	**[D]** Deployment-sequence commands
SYS03 ADCS	**[M]** Dynamic loading	**[D]** Attitude telemetry	**ADCS**	**[D]** Attitude state for trajectory computation	–	–	**[E]** Sensor and actuator power demand	–	**[D]** Attitude stability during descent and deployment
SYS04 Navigation	–	**[D]** Altitude, position and trajectory telemetry	**[D]** Drift/ trajectory data for attitude planning	**Navigation**	**[D]** Position/ drift data for science georeferencing	**[D]** Altitude-control commands: vent/inflate requests	**[E]** Navigation sensor power demand	**[D]** Altitude/ position state for thermal-mode selection	**[D]** Trajectory data during descent
SYS05 Payload	**[M]** Payload mass and load distribution	**[D]** Science data stream; instrument health	**[M]** CG configuration	**[D]** Atmospheric data for navigation	**Payload**	–	**[E]** Instrument power demand and duty cycle	**[T]** Heat dissipation; sensor-temperature limits	–
SYS06 ISRU + Buoyancy	**[M]** Envelope tension and suspension loads	**[D]** Lift-gas pressure, leakage and ISRU telemetry	**[D]** Buoyancy feedback affecting attitude	**[D,F]** Lift-gas state for altitude control	–	**ISRU + Buoyancy**	**[E]** Lift-gas and ISRU power demand	**[T]** Gondola temperature for altitude control	**[F,D]** Inflation manifold I/F; gas-charge confirmation
SYS07 Power	**[M]** Power-system mass and vibration loads	**[E]** Regulated bus power. **[D]** Voltage, SoC and fault telemetry	**[E]** Power to ADCS sensors/actuators	**[E]** Power to navigation sensors	**[E]** Power to instruments	**[E]** Power to lift-gas/ISRU systems	**Power**	**[T]** Battery/ regulator waste heat	**[E]** Power for deployment actuation
SYS08 Thermals & Env.	**[M,T]** Thermal-induced structural loads	**[D]** Thermal telemetry; over/under-temp. flags	**[T]** IMU/sensor temperature regulation	**[T]** Navigation sensor temperature regulation	**[T]** Instrument temperature regulation	**[T]** ISRU and envelope thermal regulation	**[T]** Battery thermal regulation	**Thermals & Env.**	–
SYS09 Deployment	**[M]** Pyroshock and separation loads	**[D]** Deployment-event telemetry	**[D]** Initial attitude state at release	**[D]** Initial position/altitude state at release	**[M,T]** Payload-protection state during entry	**[D,M]** Inflation trigger; envelope release	–	**[T]** Thermal gradient/range achieved during descent	**Deployment**

Note: It should be noted that SYS09 (Deployment) is active only during the entry, descent, and deployment. Its row and column entries apply exclusively to that phase - deployment hardware is jettisoned before nominal mission begins.

While the form of the N^2 is important for interface-control documentation and qualitative insights, it does not quantify the coupling strength between subsystem pairs, nor does it expose structural features such as architectural bottlenecks or natural partitioning clusters. These features are of direct interest to systems engineering: a highly coupled subsystem pair imposes co-design obligations, a feedback loop demands iterative resolution in the interface control process, and a bottleneck subsystem whose failure would sever the most communication paths is a priority risk-mitigation target. For that reason, a specialised set of designated algorithms is needed. It has been discussed in the following subsections.

4.1.3. Subsystem Feedback Cycle Detection

A tool has been developed in Python that transforms the raw N^2 interface data into a weighted Design Structure Matrix (DSM) and applies complementary analytical techniques to extract actionable architectural conclusions. First of all, the algorithm detected 577 simple directed cycles of length $\ell \leq 4$ in the interface graph (Figure 4.2).

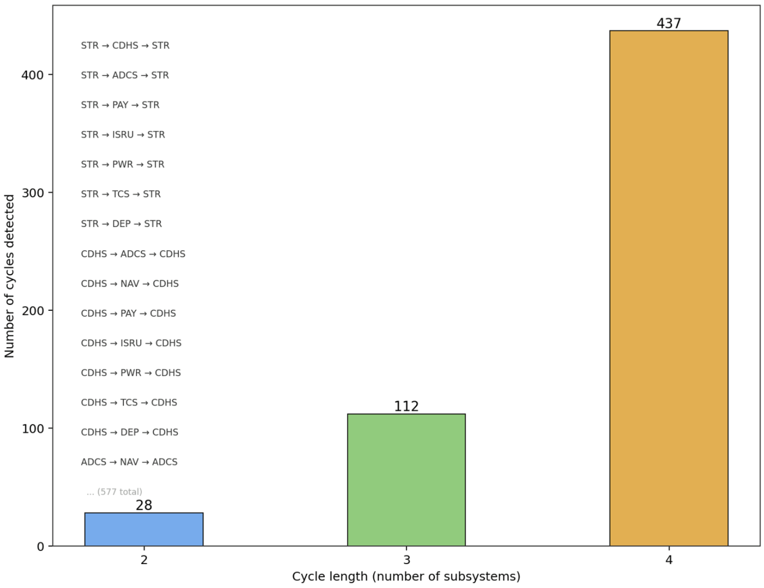

Figure 4.2: Feedback Cycle Detection (Cycles ≤ 4 subsystems)

This large number is driven primarily by the high density of bidirectional pairs: any two mutually interfacing subsystems form a 2-cycle, and any three pairwise-interfacing subsystems form multiple 3-cycles. The high cycle count is not inherently problematic - it reflects the frequent exchange of state information in a tightly integrated system typical of space missions - but it does confirm that the VISTA architecture has no clearly independent subsystem pairs that could be designed in isolation.

4.1.4. Coupling Criticality Ranking

Five interface-type codes from subsection 4.1.2 are assigned weights, based on how hard-constraining they are on the coupling in question:

Table 4.3: Interface type codes and assigned coupling weights.

Code	Type	Weight	Rationale
M	Mechanical/Structural	2	Geometry and load-path constraints propagate broadly but not in real time.
E	Electrical/Power	3	Hard real-time dependency; loss of power disables the consumer immediately.
D	Data/Command	2	Information flow; moderately tight, but asynchronous buffering is possible.
T	Thermal	1	Slow dynamics; thermal time constants are long relative to functional cycles.
F	Fluid/Gas	3	Mass-flow constraint; directly couples lift-gas inventory and ISRU performance.

For any interface carrying more than one type (e.g. the SYS06 → SYS03 link tagged **D+F**), the coupling weight is the *sum* of the individual type weights. The resulting 9×9 weight matrix $\mathbf{W}$ is defined element-wise as:

$$W_{ij} = \sum_{t \in \mathcal{T}_{ij}} w_t \tag{4.1}$$

where $\mathcal{T}_{ij}$ is the set of interface types present on the directed edge from subsystem i to subsystem j, and w_t is the weight of type t from Table 4.3. Diagonal entries ($i = j$) are zero by convention. A total of 63 directed interfaces were encoded from Table 2-3, with a combined type count of 70 (some interfaces carry two types). From W, four scalar metrics are derived for each subsystem i:

$$\text{Fan-out}_i = \sum_{j \neq i} W_{ij} \tag{4.2}$$

$$\text{Fan-in}_i = \sum_{j \neq i} W_{ji} \tag{4.3}$$

$$\text{Total coupling}_i = \text{Fan-out}_i + \text{Fan-in}_i \tag{4.4}$$

$$\text{Autonomy index}_i = \text{Fan-out}_i - \text{Fan-in}_i \tag{4.5}$$

Fan-out measures how strongly subsystem i drives others; fan-in measures how strongly it is driven. A positive autonomy index indicates a net architectural *driver*; a negative value indicates a net *receiver*.

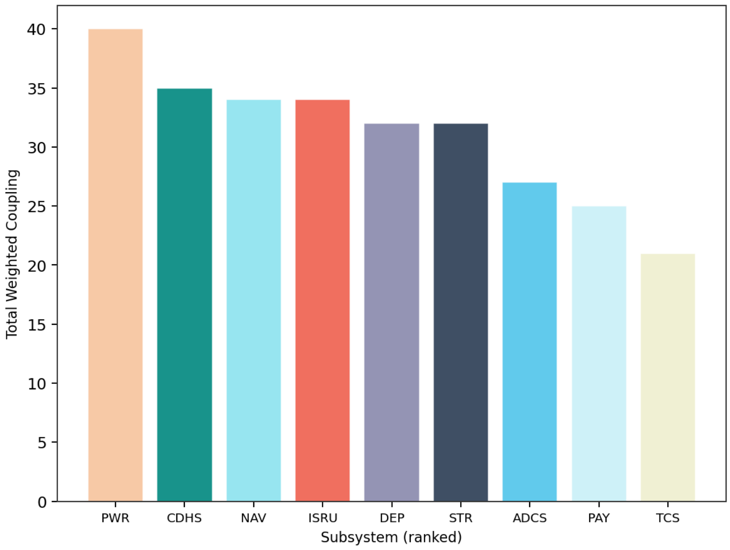

Figure 4.3: Subsystem Coupling Criticality Ranking (Higher = Greater architectural dependency)

Below, design-relevant conclusions drawn from the N^2 matrix and coupling algorithm outputs will be presented.

Power Subsystem (SYS07) as Hub

The EPS is the highest-fan-out subsystem, providing regulated power to all others.

Critical dependency: EPS failure renders the Aerobot inoperable within the battery reserve window. Mitigations include redundant power distribution paths for critical loads, individual fuses on high-current branches, battery cell-bypass diodes to limit capacity loss from a single cell failure, and an end-of-life solar array margin.

CDHS (SYS02) as Command Authority

The CDHS is the central command processor, issuing mode transitions and setpoint commands to all subsystems. It issues load-shedding commands if battery SoC falls below threshold and monitors subsystems via FDIR.

Critical dependency: An unrecoverable CDHS fault escalates to Safe Mode (UHF beacon only). Mitigations include a hardware watchdog timer, flight software partitioned into verified critical and non-critical sections, an external watchdog circuit independent of the main processor, and on-board storage retaining recent telemetry for post-pass ground diagnosis.

Navigation (SYS04) as Altitude Controller

GNS drives ISRU buoyancy management through a closed-loop altitude control algorithm.

Critical dependency: Loss of the altitude control loop causes the Aerobot to drift downward as N_2 leakage goes uncompensated, eventually degrading science operations. Mitigations include a redundant barometer array with a majority-voting algorithm, altitude setpoint persistence in the autonomous controller, and a manual vent/inflate override available via orbiter uplink.

Payload-Thermal-Mechanical Coupling Loop

Payload instruments generate waste heat and mechanical vibration, creating a tightly coupled feedback loop across SYS05, SYS08, and SYS01/SYS03.

- **Heat dissipation (SYS05 → SYS08):** Active science instruments contribute a combined thermal load to the gondola interior during peak science windows, raising internal temperature above ambient. This is managed by passive MLI insulation and active Peltier cooling on thermally sensitive instruments.
- **Vibration coupling (SYS05 → SYS01 → SYS03):** Pump motors and moving-part instruments introduce broadband mechanical excitation into gondola structure, which can couple into the IMU. A 3-tier vibration isolation system (Tier 1: instrument-level elastomer mounts; Tier 2: subsystem air-spring isolators; Tier 3: gondola-to-cable elastomer knots) provides cascaded attenuation sufficient to meet all instrument acceleration tolerances.
- **Temperature feedback (SYS08 → SYS05):** Temperature rise can introduce baseline drift in sensitive sensors. Passive insulation on the affected instruments mitigate this effect.

Design implication: All payload instruments shall be mounted on isolated subframes to thermally and mechanically decouple them from the CDHS, ADCS, and Navigation core subsystems.

4.2. Subsystem Input-Output Grid

Table 4.4 provides a structured summary based on the project status after the Midterm Review, complementing the N^2 matrix. The "Forward Action" column identifies the highest-priority open item.

Table 4.4: Subsystem inputs, outputs, and key forward actions for the Final Report.

Subsystem	Key Inputs	Key Outputs	Highest-Priority Forward Action
ISRU & Buoyancy	Venus atm. composition & T/P profiles; EPS power budget; GNC altitude setpoint	Buoyancy; N_2 leakage/replenishment rate; altitude control commands; ISRU power demand	Iterate balloon sizing with final gondola mass
Payload	Gondola volume/mass allocation; EPS power budget; TCS thermal limits; data budget	Science data streams; instrument heat dissipation; sample inlets (atmosphere)	Detail barometer layout on tether; specify minimum detectable seismic magnitude and range; detail cloud droplet measurement
Comms	CDHS data stream; EPS power; ADCS gondola attitude (pointing loss estimate); orbiter geometry assumptions	Modulated RF signal (UHF, 1500 bit/s useful); link margin (≥3 dB); comms angle cutoff due to balloon diameter.	Calculate comms elevation angle cutoff imposed by balloon shadow; verify Doppler linear velocity between antennas; iterate comms mass budget to confirm feasibility
Thermal & Env.	Gondola geometry; component heat dissipation (EPS, ISRU, payload); Venus T/P/acid environment model; altitude	Component temperatures; gondola heat leak; acid compatibility assessment; altitude adjustment requests to GNC	Identify which subsystems need active cooling at ∼40 °C ambient; quantify heater installed power with SF
Guidance & Nav.	IMU data (continuous); barometer altitude (periodic); Doppler tracking signal from orbiter; EPS power	Altitude state for ISRU; position data for CDHS; trajectory data for ADCS; altitude commands for ISRU	Validate Doppler navigation accuracy with balloon diameter & cable geometry; couple navigation controller to ISRU altitude control
Power (EPS)	Solar insolation (Landis model, altitude, shadowing); battery SoC; all subsystem loads and duty cycles	Regulated 28 V bus; battery SoC telemetry; load-shedding commands; solar array area requirement	Revisit solar cell area with Landis method + shadowing + EOL (action 1); refine all duty cycles to expected values (action 2); explore night-time science configs (action 3)
ADCS	IMU (shared with GNS); gondola geometry & mass; cable layout; disturbance estimates	Gondola attitude; angular rates; dynamic stability flags; damping performance; cable tension	Iterate cable/tether lengths with structures; validate dynamic model against literature pendulum solutions
Structures	ADCS suspension parameters; all subsystem masses; entry loads (Chapter 11); Venus environment	Gondola geometry and mass; cable dimensions; structural margins; mounting provisions for all subsystems	Add overall mass/volume/cost budget to report (addressed here); iterate gondola geometry with final ADCS cable parameters
Deployment	Entry mass (incl. stored N_2); aeroshell sizing; Mach/q trigger parameters; CDHS sequencing commands	Deployment reliability; entry trajectory; EDDI sequence; free-float hand-off state	Add schedule and TRL to next report (addressed here); re-run wet-entry trajectory with stored-N_2 mass; close structure verification

This section provided the architectural foundation for detailed subsystem design. Subsequent chapters elaborate on the implementation of each subsystem within these interface constraints.

5 Instrumentation and Scientific Mission

This chapter presents VISTA's science goals and the corresponding instrumentation to perform such science. First the goals are presented, followed by the documentation of the selected instruments and a deeper dive into the seismology study. Finally, the chosen component data rates are presented at the end.

5.1. Scientific Goals

The VISTA mission is structured around two principal scientific domains, each targeting fundamental gaps in our current understanding of Venus. The first focuses on achieving a comprehensive characterization of the Venusian atmosphere. Through in-situ measurements of chemical composition, pressure, temperature profiles, and wind speed, VISTA aims to provide direct observational insight into the mechanisms driving Venus's extreme environment and atmospheric super-rotation. A central component of this objective is the periodic aerosol sampling and detailed chemical analysis of the upper cloud layer, targeting sulfuric acid haze and other complex chemical species present within it. This is complemented by direct characterization of cloud droplet populations, including their size distribution, number density, and refractive index, which remain poorly constrained by remote sensing alone and are essential for understanding cloud formation processes, radiative feedback, and the microphysical structure of the Venusian cloud deck. By monitoring cloud microphysics and dynamics over time, VISTA will enable the distinction between transient atmospheric phenomena and long-term behavioral trends.

The second scientific domain addresses one of the most significant gaps in planetary science: the near-complete absence of direct seismic data from Venus. Despite being Earth's closest analog in size and bulk composition, Venus's tectonic activity remains poorly constrained. VISTA will conduct continuous investigation of seismic and tectonic activity, enabling the first sustained assessment of the planet's internal dynamics and providing constraints on crustal thickness, lithospheric rigidity, and mantle convection processes. Determining the degree to which Venus remains geologically active carries strong implications for models of planetary thermal evolution and for interpreting the planet's extensive and largely undated volcanic record.

Together, these objectives are directly aligned with the strategic priorities of the Venus Exploration Analysis Group (VEXAG) roadmap (2019) [6]. The specific goals covered by VISTA are presented in Table 5.1.

Table 5.1: VISTA alignment with VEXAG 2019 Goals, Objectives, and Investigations [6]. Coverage: ✓ directly addressed (aerial platform is VEXAG-identified primary modality); ~ partially addressed, complementary data required from other platforms; × not addressed (requires lander, deep-atmosphere probe, or orbiter).

Goal	Objective	Investigation	Cov.	VISTA instruments & rationale
Goal I - Habitability	I.A - Liquid water & temperate past	I.A.1 Hydrous Origins	~	NMS D/H ratio constrains water history; rock identification needs lander.
		I.A.1 Crustal Recycling	~	Barometer seismic array detects tectonic activity; structural mapping requires SAR orbiter.
		I.A.2 Atmospheric Losses	×	Ion escape requires orbital magnetometer/plasma instruments.
		I.A.3 Magnetism	×	No magnetometer on VISTA; requires low-altitude orbiter survey.
	I.B - Venus as planetary evolution template	I.B.1 Isotopes	✓	NMS (noble gases, D/H, ^{12}C/^{13}C); mTLS (SO$_2$, H$_2$O). VEXAG identifies aerial platform as essential modality.
		I.B.1 Lithosphere	~	Seismic array constrains lithospheric activity; elastic-thickness requires orbital gravity.
		I.B.2 Heat Flow	×	Requires orbital gravity + topography; outside VISTA scope.
		I.B.2 Core	~	Large-event surface waves constrain core radius; single-point radial localisation only.
Goal II - Atmosphere	II.A - Global atmospheric dynamics	II.A.1 Deep Dynamics	✓	Sonic anemometer, barometers, WIS, pyrgeometers - continuous 5-yr in-situ record at 54-56 km. VEXAG primary modality.
		II.A.1 Upper Dynamics	×	Above float altitude; requires orbiter UV/visible spectrographs.
		II.A.2 Mesoscale Processes	✓	High-cadence sonic anemometer + barometer array resolves convective cells and gravity waves.
	II.B - Composition & radiative balance	II.B.1 Radiative Balance	✓	Dual pyrgeometers (nadir + zenith) measure net longwave flux continuously; WIS provides T context.
		II.B.1 Chemistry	✓	NMS + mTLS (bulk + trace species); AFN + OPC (aerosol microphysics); TOPS (cloud pH).

(continued on next page)

(Table 5.1 continued)

Goal	Objective	Investigation	Cov.	VISTA instruments & rationale
		II.B.2 Aerosols	✓	AFN (fluorescence, refractive index), OPC (size distribution), TOPS (H_2SO_4 acidity). VEXAG comprehensive modality.
		II.B.2 Unknown UV Absorber	~	NMS spectra + AFN fluorescence may identify candidates; UV spectroscopy from orbiter additionally needed.
		II.B.3 Volcanic Outgassing	~	NMS + mTLS detect SO_2 transients over 5 yr; global spatial coverage needs orbiter.
Goal III - Geology	III.A - Geologic processes & activity	III.A.1 Geologic History	×	Requires high-resolution orbital SAR + altimetry.
		III.A.1 Geochemistry	×	Requires surface lander XRF/LIBS.
		III.A.2 Geologic Activity	✓	Tether barometer array provides sustained infrasound seismic monitoring; detects $M_s \geq 4$ globally over 5 yr. VEXAG identifies aerial infrasound as substantial modality.
		III.A.2 Crustal Structure	~	Surface-wave analysis constrains crustal thickness locally; global mapping requires orbiter.
	III.B - Surface–atmosphere interaction	III.B.1 Local Weathering	×	Requires in-situ surface mineralogy from lander.
		III.B.2 Global Weathering	×	Requires orbital near-IR surface spectroscopy.
		III.B.3 Chemical Coupling	~	NMS + mTLS at cloud-base altitude constrain lower boundary for surface–atmosphere models; deep-probe data additionally required.

5.2. Selected Instruments

The payload instrument suite for VISTA was selected through a systematic trade-off process, balancing scientific return against the strict mass, power, and environmental constraints imposed by the Venusian cloud deck. Each candidate was assessed on its individual merit, compatibility with the sulfuric acid environment, and contribution to the mission's dual scientific objectives. Instruments introducing redundancy without proportional science gain, or incompatible with REQ-F-ENV-03, were eliminated from consideration.

Table 5.2: VISTA Payload Instrument Suite

Instrument	**Mass** (kg)	**Data** (b/s)	**Power** (W)	**Temp.** (°C)	**Vol.** (cm^3)
NMS [18]	10.9	40 [19]	14.0	−20 to 50	10 650
AFN [20]	0.8	1000 [21]	40.0	−10 to 40	100
WIS ×3 [20]	0.1	100	1.0	−40 to 60	98
Sonic Anemometer [22]	0.4	300	2.0	−40 to 50	8000
Barometers ×5 [23]	0.45	60	0.1	−54 to 70	255
mTLS [20]	0.62	500	14.0	−40 to 80	240
Pyrgeometer ×2 [24]	0.65	300	3.0	−40 to 80	3530
TOPS [20]	0.35	800	2.0	−20 to 50	800
OPC [25]	2.0	500	15.0	−50 to 50	4500
Total	18.9	4140	91.1	—	32 725

The chemical analysis suite centres on the NMS as the primary instrument for bulk composition, trace gas detection, and isotopic ratios, complemented by the mTLS for continuous, species-specific monitoring of SO_2, HCl, and H_2O. Aerosol characterisation is jointly achieved by the AFN and OPC, with the former providing bulk scattering properties, fluorescence-based compositional discrimination, and refractive index estimates, and the latter providing particle size distribution and number density. Together, these instruments constitute the primary means of characterising cloud droplet populations. The TOPS pH sensor offers direct acidity measurements at negligible resource cost.

Thermodynamic profiling is handled by the WIS temperature suite and a set of five barometers, the latter serving a dual role as the primary infrasound-based seismic detection instrument. Vertical wind characterisation is performed by the sonic anemometer, while horizontal wind speed is derived from balloon position tracking via the Navigation Subsystem. Radiative flux across the cloud deck is captured by a dual-pyrgeometer configuration, one nadir- and one zenith-facing, providing the net longwave IR balance required by VEXAG atmospheric models.

5.3. Seismic Detection System

Based on previous design trade-offs, an array of barometers suspended from a tether was selected as the baseline architecture for seismic detection. This configuration provides high scientific value at low mass and power cost. Within this architecture, the main mission-level parameters to define are the tether length L_{tether} and the number of barometers $N_{barometers}$. These variables directly affect the minimum detectable quake magnitude and the required localisation resolution. Mounting instruments below the gondola was preferred over placing them above, in order to prevent contamination of atmospheric measurements by heat and outgassing from the gondola body and the balloon, and because routing power and communication lines upward through or around the envelope would add significant engineering complexity. This section presents the working principle, justification, and expected performance of the seismic configuration.

5.3.1. Purpose, Constraints and Objectives

The primary objective of the seismic configuration is the detection of venusquakes, in line with the scientific stakeholder requirements in section 10.4. The current design extends this objective by including a localisation procedure, which increases the scientific return of the measurement system. The performance objectives used to derive the configuration are presented below in order of priority. Subsystem interdependencies, technical resource use (mass, power, and cost), reliability, and sustainability were also considered during the design process.

1. **Detection:** to register a quake above the atmospheric and instrument noise floor. Following [26], a detection is obtained when the signal-to-noise ratio satisfies SNR ≥ 3. It is directly proportional to the quake's magnitude and decreases with the distance between the balloon and the epicentre. If this objective is not achieved, the seismological configuration fails.
2. **Minimum magnitude:** it is desired to detect a large range of quake magnitudes M_s; the lower the magnitudes, the higher the probability of occurrence [27]. A lower detection threshold dramatically increases the number of observable events over the mission lifetime, increasing the scientific value of the mission.
3. **Minimum range:** for a given magnitude M_s, how large is the surface area from which the balloon can detect seismic events? A wider detection range means more of Venus is "covered" at any moment, increasing the probability that a quake somewhere on the planet is detectable. A small seismic field of view requires more frequent seismic activity to expect at least one detection.
4. **Localization:** the ability to assign a detected event to a specific geological region of Venus. The lower the angular localisation error, the better the performance of the design is.

5.3.2. Working Principle & Methodology

The detection concept is a vertical microbarometer array [26]: a set of barometers distributed along a suspended tether below the gondola. By distributing pressure-sensing along the tether, the system forms a vertical aperture. The working principle is illustrated in Figure 5.1. For a plane wave incident at an angle θ from the vertical, the time delay between two barometers with spacing L is $\Delta t = \frac{L\cos\theta}{c}$, where c is the local sound speed. Cross-correlation of the individual pressure measurements recovers θ, which is used to determine the distance between the balloon and the epicentre, providing radial localisation.

The signal travels from the hypocentre (origin of the venusquake) to the pressure sensors in the following way. A quake radiates body and surface waves to the surface above it, the epicentre, where the vertical ground motion acts as a piston on the atmosphere. The dense lower Venusian atmosphere ($\sim 92\,\text{bar}$, $\sim 65\,\text{kg}\,\text{m}^{-3}$ at the surface) couples the ground to the air about sixty times more efficiently than on Earth, so events that are acoustically undetectable on Earth produce a measurable infrasound wave. As it rises into thinner air, energy-flux conservation amplifies the pressure amplitude as $\sqrt{\frac{\rho_0}{\rho(z)}}$ before it reaches the barometers.

The present analysis adjusts the established literature seismic models used for both Earth [28] and Venus [26] to the VISTA mission. First, an empirical solid-to-gas transmission coefficient $\mathcal{T} \approx 0.3$ is applied [28], accounting for the Venusian atmospheric attenuation. While aligned with the literature, this coefficient is still a first level estimate and its value has to be validated on Venus to ensure the value is reliable. Second, as the balloon drifts with the Venusian atmosphere and is not anchored like in [29, 28], the wind noise is modelled as 20% of the absolute wind.

A peculiarity of the design is the complex dynamic behaviour described in detail in section 6.6. The small oscillations of the tether contaminate the seismic measurements of the barometers in two different ways. The change in altitude introduced by the tether dynamics δz shifts the static (hydrostatic) pressure by $\Delta P = \rho g\,\delta z \approx 8.2\,\text{Pa}\,\text{m}^{-1}$ at 56 km, while the corresponding velocity alters the dynamic pressure $q = \frac{1}{2}\rho v^2$. The introduced pressure values are several orders of magnitude larger than the noise level of the microbarometers. Thorough correction is crucial to enable accurate seismic detection. After detailed analysis, the ADCS subsystem decided that the correction through deterministic subtraction is avoided. This is because the uncertainty in the dynamic knowledge of the configuration is too high for the high precision required by the barometers, making the design unreliable. The current approach mitigates this through implementing a low-pass filter: the structure is sized so that all mechanical modes lie above the measurement band of the acoustic waves, which is set at 0.02–0.05 Hz. Hence, the noise introduced by the dynamic disturbances can be filtered out of the pressure signal. If this requirement is not met, the detection ability of the seismic configuration fails, as the seismic pressure waves cannot be distinguished from the disturbances.

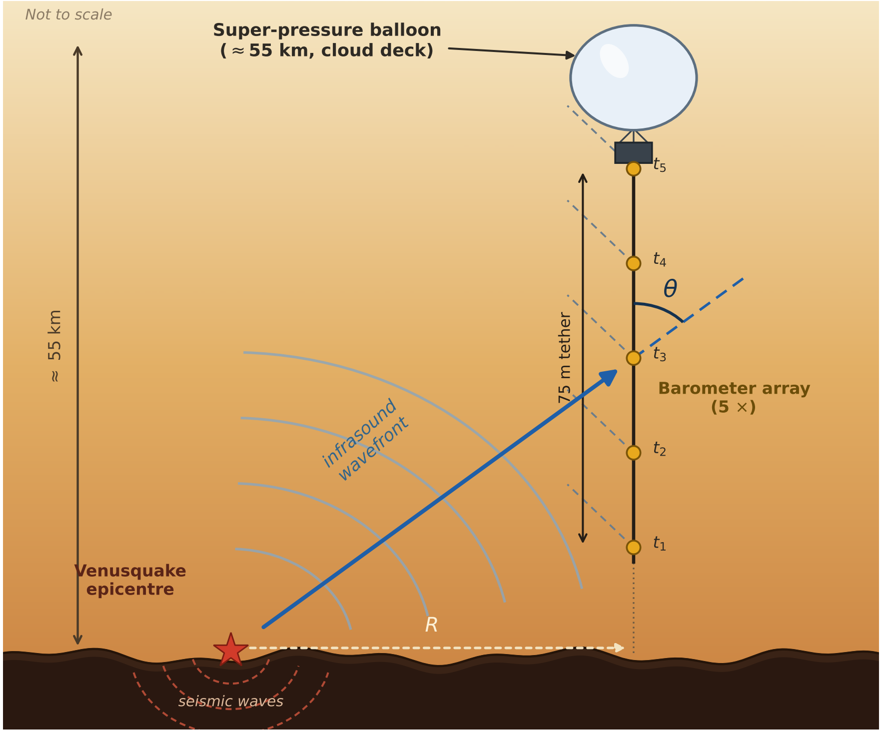

Figure 5.1: Schematic of the working principle, showing the infrasound wavefront traversing the barometer array, for a descend altitude of ≈ 55km.

The low-frequency band (0.02–0.05 Hz) is not detrimental to the performance of the design. A quake radiates over a broad spectrum with a corner frequency that decreases as the magnitude rises. Hence, larger events concentrate their energy at lower frequencies [30]. The 0.02–0.05 Hz band therefore preserves all the seismic information required for the VISTA mission. Its lower bound (0.02 Hz) stays above the atmospheric red-noise and gravity-wave background that rises at longer periods [28, 26], while its upper edge (0.05 Hz) is low enough that the dynamic perturbations of the tether can be filtered out.

The dominant design variable is the tether length Figure 5.2 (b). A longer tether widens the aperture and improves localisation but lowers the dynamic oscillation frequencies, bringing them closer towards the selected acoustic band. The main constraint is therefore frequency filtering: all intrinsic dynamic modes must remain above a frequency of 0.06 Hz (the 0.05 Hz band edge plus a 20% margin). The optimum configuration is thus the longest tether whose fundamental mode still exceeds 0.06 Hz. The changes in the mass budget of the mission are marginal (section 6.7), as long as the tether length stays in the feasible design space.

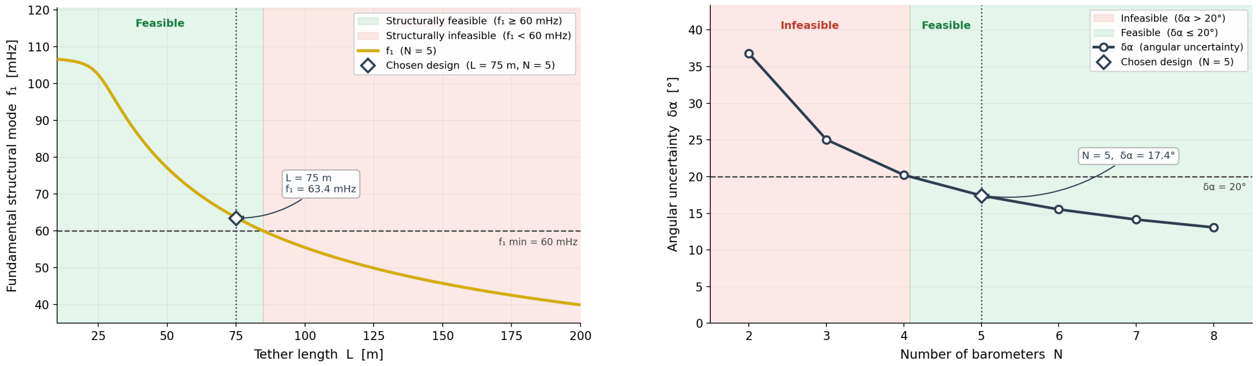

Figure 5.2: Design-space trades for the seismic array configuration: (a) fundamental structural mode f_1 as a function of tether length L (for $N = 5$); (b) angular uncertainty $\delta\alpha$ as a function of the number of barometers N. The selected design ($L = 75\,\text{m}$, $N = 5$) is marked in each panel.

The other design variable is the number of barometers used. While two barometers are enough to fulfil the theoretical functionality of the method, they provide poor localisation performance. The angular uncertainty improves with the number of pairs of barometers, as $\delta\alpha = \arcsin(\sim \frac{1}{\sqrt{N_{pairs}}})$. A maximum angular uncertainty of 20° has been chosen to ensure sufficient accuracy of the design. Figure 5.2 (b) shows the dependency of the angular uncertainty $\delta\alpha$ on the number of barometers along the tether $N_{barometers}$. Furthermore, increasing the number of barometers also improves the detection range of the seismic events (both magnitude M_s and distance), as the $SNR_{array} = \sqrt{N} \cdot SNR_{barometer}$. This is because the signal scales with N while the noise scales with $\sqrt{N}$.

5.3.3. Final Configuration & Performance

Based on the design-space analysis outlined in Figure 5.2, the final seismic configuration is summarised in Table 5.3 and Table 5.4.

Table 5.3: Final seismic configuration.

Quantity	Value
Tether aperture L	75 m
Barometer count N	5
Suspension length L_{susp}	30 m
Measurement band	0.02–0.05 Hz

Table 5.4: Detection performance

M_s	R_{max} [km]	Instantaneous coverage [%]	N_{min} [yr^{-1}]
3		not detectable	
4	571	0.2	89.9
5	2291	3.5	5.6
6	9172	47.3	0.4
7	≥19010	100	0.2
8	≥19010	100	0.2

The vertical aperture is set to the longest tether whose fundamental structural mode (designed by ADCS) can safely be filtered out by implementing a low-pass filter ($f_1 \geq 0.06$ Hz), yielding $L_{tether} = 75$m. The number of barometers is the smallest that meets the self-imposed angular-uncertainty requirement, while also minimising the technical resources (mass, power, data) and ensuring enough redundancy. With $N_{barometers} = 5$ barometers, the signal-to-noise ratio is also improved, extending the detectable magnitude range to smaller, more frequent events. The design gives an angular uncertainty of $\delta\alpha = 17.4°$, comfortably inside the 20° internal requirement and corresponding to a radial distance uncertainty of $\delta R \approx R\,\delta\alpha$.

Table 5.4 presents the detection performance as a function of the venusquake magnitude M_s, where N_{min} is the minimum global event rate required to capture at least one event over the 5-year mission. Events of $M_s = 3$ fall below the detection threshold at all ranges. At the other extreme, the detection radius for $M_s \geq 7$ reaches the antipode, so a single such event anywhere on the planet is detectable. Long-range detection does not rely on infrasound propagating through the atmosphere from the epicentre: distant events are sensed through seismic surface waves travelling through the solid planet, which displace the ground beneath the balloon and re-radiate infrasound locally upward [28]. For $M_s = 4$, $N_{\mathrm{min}} = 89.9\,\mathrm{yr}^{-1}$: detecting such an event requires a global rate of roughly 90 events per year, which can be comfortably met according to current venusquake activity estimates [27].

Implications and limitations. It must be emphasised that the current configuration is axially symmetric about the local vertical: the cross-correlation of the barometer signals recovers only the wave's incidence angle θ, and hence the epicentral distance R (the radial range from the sub-balloon point). The azimuth of the source is not constrained, so the configuration provides **radial localisation only**, placing each detected event on a circle around the balloon rather than at a unique point. A full two-dimensional fix would require a horizontal distribution of the pressure sensors, requiring an estimated horizontal distance of 150m, which was deemed unfeasible for the current design. This is an accepted limitation for VISTA: even radial localisation, combined with the broad detection range, already delivers unprecedented seismic science return, exceeding the performance required by the stakeholders (section 10.4), while keeping the subsystem mass, power, and complexity low. Furthermore, to improve the localisation performance, placing the microbarometers on the suspension cables as well can also be considered. However, this has not been considered in detail, as the suspension cables and the tether are inherently different (e.g. the tether contains the power and signal conductors for the microbarometers). Nonetheless, this option is worth investigating in future, more detailed designs.

5.3.4. Seismic Localisation Recommendations

Simulation results confirmed that a vertical tether array of barometers can constrain epicentral distance, allowing only radial localisation centred on the balloon. With such architecture it is not possible to obtain azimuthal information and therefore source direction can't be determined. Among the complementary mechanisms considered, a fleet of balloons was ruled out due to mass and mission constraints. Other options include modifications of the tether mechanism or making use of the mission orbiter.

Drogue Parachute Tether Deflection

One approach considered for achieving horizontal aperture in the barometer array was the attachment of a drogue parachute at the lower end of the tether. In a sufficiently strong horizontal wind, the drogue would generate drag forces that deflect the tether away from vertical, bowing it into a catenary geometry and introducing a horizontal baseline between sensors. At the float altitude of 56 km, Venus's atmospheric superrotation produces zonal winds of approximately 70–100 m/s at a pressure and density comparable to Earth's surface, generating dynamic pressures of order 3 kPa. This environment is in principle highly favourable for drogue-based tether deflection, and preliminary estimates suggest that deflection angles exceeding 45° from vertical are physically achievable with a modest drogue area, which would yield a useful horizontal baseline of several tens of metres from a 75 m tether.

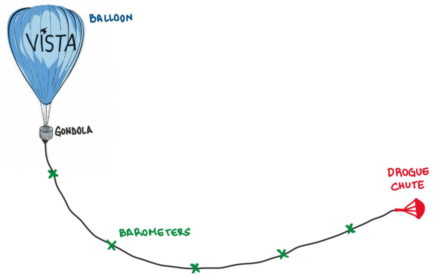

Figure 5.3: Drogue Chute Architecture Sketch

The drogue concept introduces significant feasibility concerns at Venus wind speeds. The continuous horizontal tension imposed on the tether is comparable to or exceeding the vertical gravitational load, complicating the envelope attachment design and increasing structural mass. More critically, the drogue acts as a tip mass on a long flexible structure in high-speed flow, exciting persistent oscillatory modes through vortex-induced vibration and pendulum dynamics that risk masking the mPa-level pressure perturbations the array is designed to detect. Combined with the deployment risk during the entry and float stabilisation phase, these constraints led to the drogue concept being set aside in favour of the orbiter-based directional localisation approach described in the following section.

Directional Localisation via Orbiter Airglow Observations

On Venus, partial ionisation and excitation of CO_2 and O_2 molecules, driven by solar radiation on the dayside and photochemical recombination on the nightside, produce near-infrared airglow emissions at 4.28 μm and 1.27 μm [26]. Seismically generated infrasound and gravity waves propagating upward through the atmospheric column induce measurable fluctuations in these emissions at approximately 95–120 km altitude, observable from orbit as expanding concentric arcs whose curvature and propagation direction encode the azimuthal bearing to the source.

The balloon and orbiter thus provide complementary constraints: the tether array yields epicentral distance, and the orbiter wave-front normal yields source bearing. Their intersection uniquely resolves the epicentre, while the horizontal phase velocity extracted from successive orbiter frames provides an independent estimate of focal depth [26]. The required instrumentation is passive, requiring only a wide-field near-infrared imager sensitive to the 1.27 μm O_2 band (with 4.28 μm as a secondary channel), operating at a frame rate of one to several minutes with spatial resolution of order tens of kilometres. Orbiter design is considered out of scope for this project, however, airglow imaging capability represents a low-mass solution for the localisation issue.

5.3.5. Deployment Mechanism of the Tether

The tether system consists of a 75 m cylindrical tether suspended vertically beneath the gondola, with five barometric sensor nodes distributed along its length. It is pre-spooled onto a passive cylindrical spool mounted to the underside of the gondola, deploying purely under gravity once released. Deployment is triggered by a shape memory alloy (SMA) latch: a spring-loaded pin locks the spool until a brief current pulse contracts the SMA wire and withdraws the pin, freeing the spool to rotate. To prevent excessively rapid deployment, a passive eddy current brake on the spool axle generates a resistive torque proportional to rotational speed, providing self-regulating, contactless speed control without active components or mechanical wear.

Once fully extended, the spool is jettisoned via a spring-loaded collet release actuated by a secondary SMA trigger, eliminating the dead mass while the tether remains independently anchored to the gondola structure. The deployed tether hangs under its own weight and the distributed mass of the sensor nodes, remaining approximately vertical but subject to atmospheric wind loading. A schematic of the deployment mechanism is illustrated in Figure 5.4.

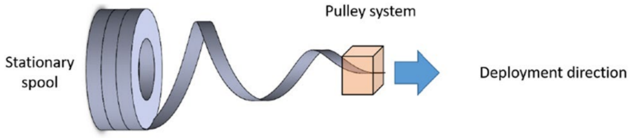

Figure 5.4: Stationary Spool Mechanism [31]

Tether

The tether is an electromechanical umbilical cable that combines a load-bearing structural core with integrated power and signal conductors, based on established designs from oceanographic umbilical cables [32]. The tether cable will be coated with an outer layer of acid resistant polymer in order to prevent degradation. Sensor nodes are attached at set intervals using clamshell collars, which transfer mechanical loads to the tether core while also serving as electrical junctions for power and data. An out of scale sketch of the tether's cross-section is illustrated in Figure 5.5.

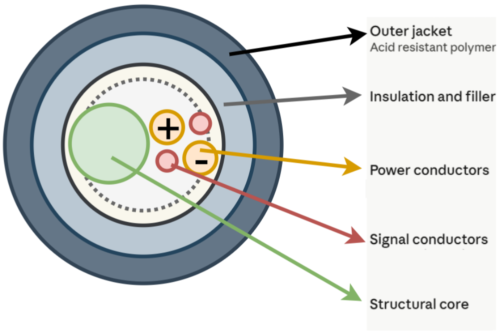

Figure 5.5: Tether Cross-section

5.4. Component data rates

To assess the feasibility of the proposed scientific investigation strategy within the mission's communication constraints, it is necessary to characterize the data output of each payload instrument. Table 5.5 presents, for every component, the sampling rate, the raw data volume per measurement, the resulting raw data rate, and the estimated telemetry rate after onboard processing and compression, together with the corresponding reasoning. These figures are relevant as the telemetry budget directly constrains which instruments can operate continuously and at what resolution, and because the barometer array's seismic event mode, in particular, determines the achievable temporal resolution for infrasound and seismic pressure measurements during the limited downlink windows available to the balloon platform.

Table 5.5: Estimated payload sampling rates, raw data generation, and processed telemetry rates

Component	**Sampling rate**	**Raw data per measurement**	**Raw data rate**	**Telemetry rate**	**Telemetry-rate reasoning**
NMS [19]	$\frac{1}{64} Hz$ given	∼ 1–2 kB per full mass spectrum estimated	∼ 0.1–0.25 kbit/s	40 bit/s	The telemetry value is the compressed transmitted rate, not the raw generated rate. The raw estimate is based on the number of mass scan steps, detector states, mode information, and limited housekeeping. The low telemetry rate is enabled by onboard peak stepping and data compression.
AFN [20, 21]	10 Hz derived	200 bytes/sample, or 120 kB per 60 s block	2000 bytes/s = 16 kbit/s	1000 bit/s	The AFN raw data are reduced using onboard binning, neural-network processing, particle-size distribution summaries, refractive-index statistics, fluorescence summaries, and selected raw-event transmission. Over 60 s, 120 kB raw data are reduced to 7.5 kB, giving an approximate 16:1 reduction.
WIS [20]	0.2 Hz assumed	0.05 kB = 50 bytes = 400 bits	$400 \cdot 0.2 =$ 80 bit/s	20–40 bit/s	The WIS measures slowly varying atmospheric temperature. Packet batching and delta encoding can reduce the generated data by about 2:1 to 4:1, giving a realistic processed telemetry rate of 20–40 bit/s.

Continued on next page

Table 5.5: Estimated payload sampling rates, raw data generation, and processed telemetry rates (continued)

Component	**Sampling rate**	**Raw data per measurement**	**Raw data rate**	**Telemetry rate**	**Telemetry-rate reasoning**
mTLS [20]	0.5 Hz derived	1000 kB per 2 s spectral block	500 kB/s = 4 Mbit/s	500 bit/s	The apparent 8000:1 reduction is not ordinary lossless compression. The raw spectra are processed onboard to retrieve selected gas abundances, uncertainties, fit-quality metrics, timestamps, and housekeeping. Since the mTLS has four narrow pre-selected spectral channels, only relevant absorption features are fitted. Occasional raw spectra are stored or downlinked for calibration and validation.
TOPS [20]	1/60 Hz assumed	1 kB = 8000 bits	8000/60 ≈ 133 bit/s	33–67 bit/s	The TOPS pH measurement is low-cadence and sample-based. Packetisation and moderate compression of about 2:1 to 4:1 are considered realistic, giving a telemetry rate of 33–67 bit/s.
Pyrgeometers ×2 [24]	0.1 Hz assumed	~ 16 bytes per two-sensor sample set	~ 13 bit/s for two sensors	~ 20 bit/s for two sensors	The sensors have a slow response time, so low-rate sampling is sufficient. The downlinked product can be processed upward and downward longwave flux, with small packet and quality overhead.
OPC/LOPC [25]	0.5 Hz given by 2 s accumulation	2048 · 16 bits = 4 kB	4 kB · 8 · 0.5 = 16 kbit/s	~ 400 bit/s	The raw product is a high-resolution pulse-height histogram. The paper states that data are telemetered at reduced resolution, so the downlinked product is assumed to be a reduced particle-size histogram rather than the full 2048-bin raw array.
Sonic anemometer [22]	0.44 Hz given	~ 250–500 kB per 3D wind measurement estimated	~ 0.88–1.76 Mbit/s	80 bit/s	The raw data are high-rate acoustic receive waveforms. Using 3 MSps, 8 ms receive windows, 16-bit samples, and multiple acoustic paths gives hundreds of kB per 3D measurement. These waveforms are processed onboard into three wind-vector components, so only the processed vector and limited overhead are downlinked.
Barometers, nominal [23]	0.2 Hz telemetry cadence assumed	24 bits per pressure sample	24·0.2 = 4.8 bit/s for one active barometer	~ 5 bit/s	In nominal mode, one barometer is operated as a low-rate pressure monitor. Only pressure is included in science telemetry; sensor temperature and status are treated as housekeeping.
Barometers, seismic event [23]	10 Hz assumed event mode	24 bits per pressure sample per barometer	5 · 10 · 24 = 1200 bit/s	~ 1.2 kbit/s before event compression	After a pressure anomaly is detected, all five barometers are activated at higher sampling rate to capture spatially distributed infrasound or seismic pressure variations. This is treated as an event mode, not continuous nominal telemetry.

6 Aerial Platform

This chapter presents the design of the VISTA aerial platform, covering the main gondola subsystems required to support long-duration operation in the Venus cloud layer. It first addresses thermal control and environmental protection, followed by command and data handling, communications, electrical power, attitude determination, structures, and guidance and navigation. Together, these subsystems define how the aerobot maintains safe operation, collects science data, and supports mission autonomy during the five-year float phase.

6.1. Thermal Control Subsystem

The Thermal Control Subsystem (TCS) maintains the gondola components, electronics, and payload instruments within their allowable temperature ranges during the mission. The gondola thermal balance is driven mainly by external convection, absorbed solar flux, internal conduction and convection, and heat dissipation from the electronics. These terms create two design drivers: the Venus atmosphere can overheat the gondola at lower altitudes, while internally dissipated power from electronics can also raise component temperatures and lead to overheat. Cold-case gondola operation is not a design driver due to power and buoyancy limitations. The operating altitude where the aerobot is able to keep internal temperature within allowable ranges with keeping average power usage is 55.1–60 km, and the nominal altitude is set to 56 km. The temperature vs altitude graph shown below comes from [33]. It can be seen that at the operating altitudes the temperature variation is ≈ 10°C per kilometer.

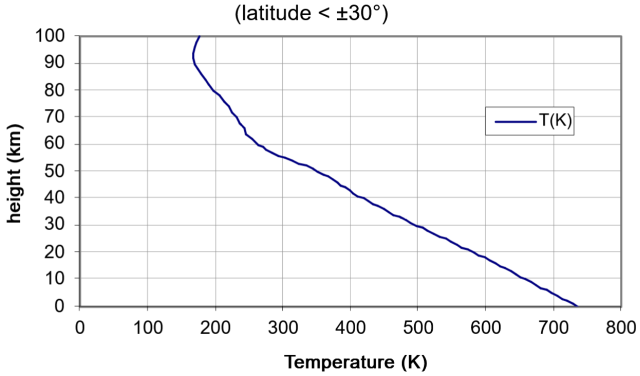

Figure 6.1: Venus atmospheric temperature variation [33].

6.1.1. Thermal Requirements

The component allowable temperature limits are shown in Figure 6.2 with dark grey indicating operating limits and light grey bars adding survival limits. The main hot-case drivers are the battery cells and AFN, currently limited to 40 °C. Most other avionics and payload components tolerate higher temperatures of 50 °C or more.

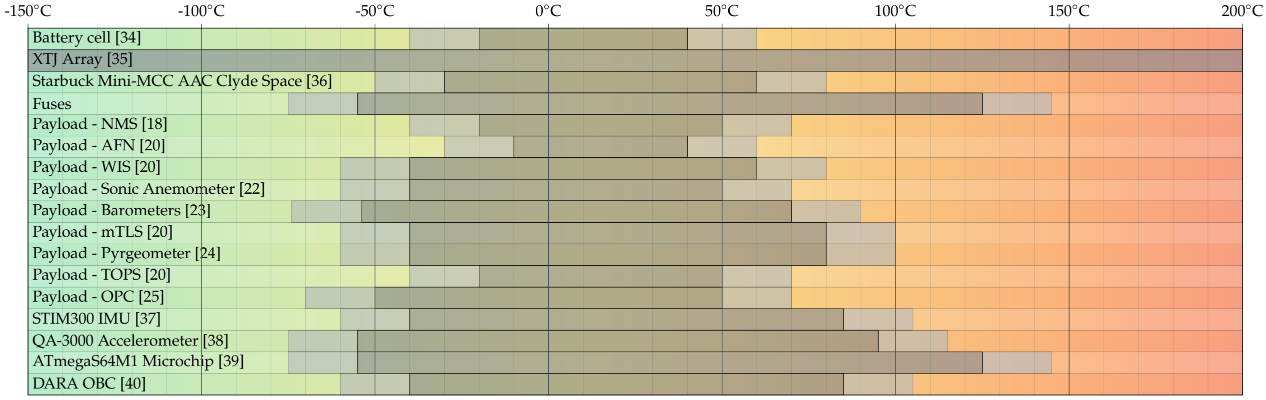

Figure 6.2: Operating temperature ranges of selected components.

It should be noted that operating temperature ranges were taken from components' datasheets, however since data available in manufacturers' public documents does not provide the survival temperatures, it has been assumed that a margin of +20 °C on the hot boundary and −20 °C on cold boundary can be added. Passing the operational limit but staying within survival limits means a particular instrument will not break if turned off, but if on, will lead to measurement errors, erratic behavior, and severe performance drops.

6.1.2. Thermal-Control Architecture

Early thermal-control concepts assumed a highly insulated gondola enclosure, supported by active heating and cooling for temperature-critical components. As the trajectory design matured, active heating was removed from the nominal architecture. The cases in which the gondola becomes too cold occur only at altitudes of approximately 60–61 km, which lie outside the allowed buoyancy and navigational operating envelope (subsection 6.8.3). These conditions are therefore not considered as drivers for thermal design. Fully insulated gondola concept was also rejected after simulation results showed that internal heat dissipation becomes the limiting case: excessive insulation traps waste heat generated during daytime operations and can drive the internal components above their allowable temperatures. Active cooling was also removed from the TCS architecture. Although it could provide additional margin for temperature-critical components, its high power demand and inherently poor performance were judged unsuitable for the optimal design. For these reasons, active cooling is not used as a baseline thermal-control method. Instead, the design relies on passive heat rejection through conductive coupling to the gondola structure and external atmosphere, supported by altitude control to keep the vehicle within a favourable ambient-temperature range.
The selected architecture therefore favours strong thermal coupling between the gondola and the Venus atmosphere, so that the gondola temperature remains as close as possible to the ambient temperature. When thermal adjustment is required, altitude control is used as the primary mechanism. Internally, the components are divided into two thermal groups: *cold-critical components*, with an upper temperature limit of 40 °C, and *warm components*, with an upper temperature limit of 50 °C. This separation allows the most temperature-sensitive components to be connected to a dedicated heat sink sized to maintain acceptable temperatures for both groups. Waste heat from the warm-component group is distributed through the gondola structure, while the cold-critical components are coupled more directly to the external atmosphere by a conductive thermal path to a heat sink.

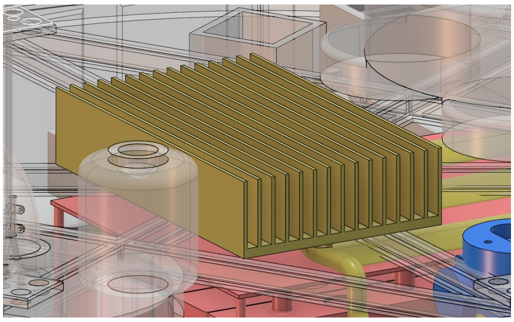

Figure 6.3: Modelled heat sink

6.1.3. Simulation

A lumped-parameter thermal model of the gondola was developed in Simulink to evaluate the thermal behaviour of the gondola over the operational altitude range. The model contains thermal nodes representing the outer shell, internal gas volume, and two component groups. It also incorporates a conductive path and a heat sink used for battery cells and the nephelometer. Heat exchange mechanisms included in the model are: external convection with the Venus atmosphere, absorbed solar heat, conduction through the gondola walls, internal convection and conduction, and dissipated heat from the onboard electronics.

Altitude-dependent atmospheric conditions were applied using Venus temperature profile (same as in Figure 6.1). The simulations were used to assess whether the selected thermal architecture can keep the component groups, particularly the battery cells and AFN, within their allowable operating limits.

The model assumes:

- Material properties are constant over the analysed temperature range
- Radiation exchange inside the gondola is neglected
- The external convection coefficient is constant for each simulation case
- Electronics heat dissipation is proportional to electrical power consumption and duty cycle
- The Venus atmosphere temperature depends only on altitude and does not change for day and night
- The solar flux diffuses within the Venus cloud layer, therefore, the incident solar flux is modelled as isotropic heat load on the exposed gondola surfaces, rather than as direct beam radiation on a single sun-facing side
- Degradation of coatings, insulation, and contact conductance over mission lifetime is not included

External convection coefficient.

The external convection coefficient is estimated from the Churchill–Chu natural convection correlation and the Hilpert forced-convection correlation for a cylindrical body, using CO_2-dominated atmospheric properties at 56 km altitude [41]. The calculated combined value is $h_{\text{in}} = 3\,\mathrm{W\,m^{-2}\,K^{-1}}$ for the gas inside and $h_{\text{atm}} = 4.3\,\mathrm{W\,m^{-2}\,K^{-1}}$ for the atmospheric convection.

Table 6.1: Main assumptions and parameters used in the preliminary Simscape thermal model.

Parameter	Description	Value	Unit
h_{atm}	External convection coefficient between Venus atmosphere and gondola shell	4.3	$\mathrm{W\,m^{-2}\,K^{-1}}$
h_{in}	Internal convection coefficient	3	$\mathrm{W\,m^{-2}\,K^{-1}}$
A_{shell}	Effective external gondola area exposed to convection	1.18	$\mathrm{m^2}$
$q_{\text{solar,day}}$	Incident solar heat flux during day-side operation	1200	$\mathrm{W\,m^{-2}}$
α_{shell}	Solar absorptivity of gondola outer surface [42]	0.13	–
ϵ_{shell}	Solar emissivity of gondola outer surface [42]	0.8	–
$q_{\text{solar,night}}$	Effective solar flux heat input during night-side operation	0	$\mathrm{W\,m^{-2}}$
m_{shell}	Thermal mass of gondola outer shell	6.7	kg
$c_{p,\text{shell}}$	Specific heat capacity of aluminium	896	$\mathrm{J\,kg^{-1}\,K^{-1}}$
m_{gas}	Equivalent thermal mass of internal gas volume	0.1	kg
$c_{p,\text{gas}}$	Specific heat capacity of internal gas	657	$\mathrm{J\,kg^{-1}\,K^{-1}}$
P_{warm}	Electrical power consumed by warm components group	144.5	W
P_{cold}	Electrical power dissipated by cold components group	4.44	W
f_{heat}	Fraction of electrical power dissipated as heat	100	%

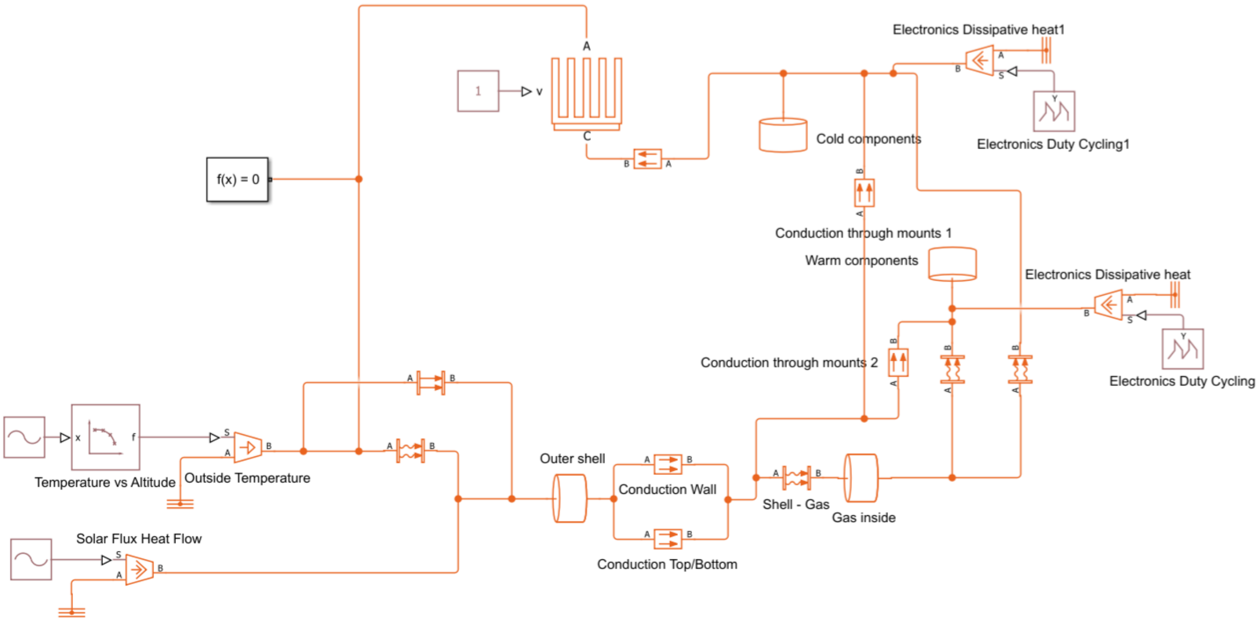

Figure 6.4: Simscape Simulink model

Cases

The analysis was performed on multiple different cases, the most important four are shown below:

1. **Nominal optimal-altitude case at** 56 km**:** with slight variations of 0.1 km in altitude, used to assess steady-state operation.
2. **Safe hot case:** a low-internal-power case in which only the altitude-control system is operating at a low power of 50 W, combined with the warmest external conditions at the lower boundary of the operating altitude.

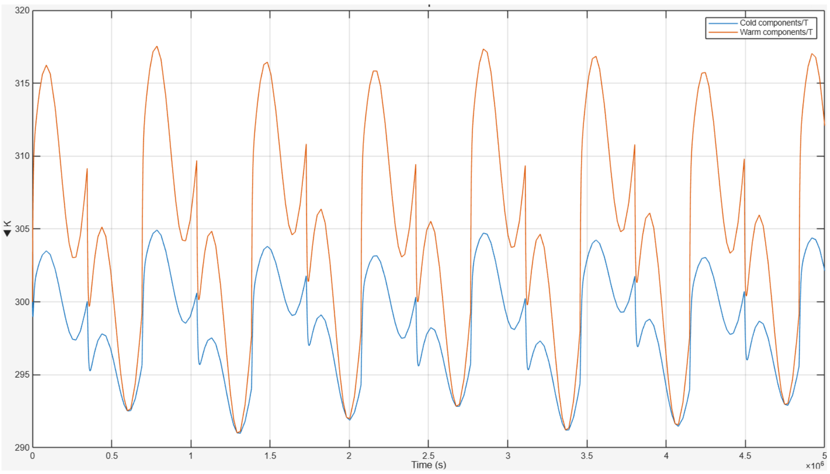

(a) Nominal operation 56 km, average power use

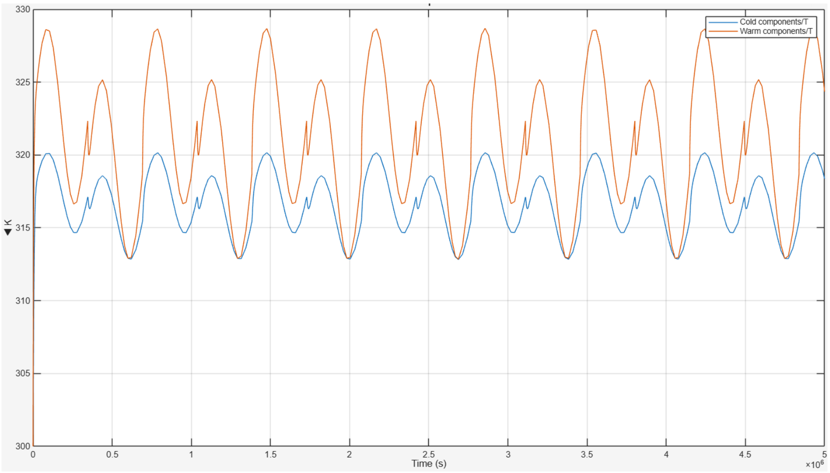

(b) Reduced-power case: 54 km, 50 W power use

Figure 6.5: Temperature evolution at selected nodes in the thermal-control model.

6.1.4. Results

The preliminary simulations support controlled heat rejection to the Venus atmosphere as the baseline TCS approach. Within the nominal operating altitude of 56 km, the passive architecture is expected to maintain all components within their allowable temperature limits, provided that internal heat is conducted efficiently to the external shell and rejected by convection to the surrounding atmosphere. The hot-case driver remains the battery cells and the AFN, both currently limited to approximately 40 °C. The lower-altitude and critical hot-case simulations are therefore the main cases to consider for the TCS. If these component limits cannot be increased by component selection or qualification, lower duty cycling may be required during off-nominal conditions. All of the cold-case simulations (not shown in the report) showed no need for local heater power. Overall, the model indicates that full-gondola active temperature control is unnecessary. Instead, a passive gondola was deemed to be the most suitable architecture.

6.1.5. Verification

The TCS shall be verified by running the thermal model for the main operational cases. For each case, the predicted temperatures of the batteries, avionics, payload, sampling hardware, shell, and internal gondola gas are checked against their operational and survival limits. The design passes if all components remain within limits with margin. The measured temperatures shall be compared with the model results, and the model updated if needed.

6.1.6. Recommendations

In the future design iterations, active cooling could be revisited and considered locally as a contingency option for particularly temperature-sensitive components.

6.2. Environmental Protection

The VISTA aerobot operates inside the Venusian cloud layer for a nominal lifetime of five Earth years. In this environment, the major environmental hazard is prolonged contact with sulfuric-acid cloud droplets and the associated chemical corrosion. The environmental-control strategy therefore has two main goals: first, to prevent sulfuric-acid aerosols from degrading structural, electrical, and balloon-envelope surfaces; and second, to ensure that the atmospheric inlets used by the science payload and ISRU system remain functional without compromising the quality of the sampled gas data.

The Venus cloud deck between approximately 48 and 70 km altitude contains aerosol droplets predominantly composed of 75–92% H_2SO_4 by weight, partitioned into three particle size modes first characterised by the Pioneer Venus Large Probe Cloud Particle Size Spectrometer: mode 1 particles with mean radius $r_1 \approx 0.30\,\mu$m, mode 2 particles with $r_2 \approx 1.0\,\mu$m, and the larger and more spatially confined mode 3 particles with $r_3 \approx 3.0$–$4.0\,\mu$m, which are concentrated in the middle and lower cloud layers, with concentration generally decreasing with altitude [43, 44, 43]. Previous Venus atmospheric instruments have identified clogging due to acid droplets. For VISTA, this risk is amplified by the five-year mission lifetime, making passive protection alone insufficient for all inlet paths.

6.2.1. External Coatings and Materials

The selected protection material across all gondola applications is polytetrafluoroethylene (PTFE), also known as Teflon. PTFE offers essentially complete chemical resistance to sulfuric acid across the full concentration range encountered in the cloud layer and withstands continuous service at the temperatures expected at float altitude [45, 46]. PTFE coating for the external surfaces will be applied at a target film thickness of $t_{\text{coat,ext}} = 25\ \mu$m. The balloon envelope is protected against sulfuric-acid exposure by its outer PCTFE layer, which acts as the primary acid barrier. The solar panels are similarly protected using a thin, transparent Parylene coating. Since the detailed design of these protective layers is covered in chapter 7 and section 6.5, respectively, they will not be discussed here.

Although the internal volume is not expected to be continuously exposed to sulfuric-acid droplets during nominal operation, full internal coating is selected as a conservative protection measure for a five-year mission. This avoids relying on perfect long-term sealing of every inlet, valve, tube, and feedthrough. The internal coating is applied at a target film thickness of $t_{\text{coat,int}} = 50\ \mu$m. This is thicker than the external coating because internal surfaces include less accessible corners, brackets, local supports, and inlet-adjacent regions where coating uniformity is harder to guarantee. The larger internal thickness is therefore treated as a robustness margin rather than as a strictly optimised value.

Special attention is required at discontinuities. Inlet housings, fasteners, antenna mounts, sensor apertures, optical windows, and cable feedthroughs are more vulnerable than uninterrupted shell panels because sulfuric-acid droplets can accumulate at edges, gaps, and seals. These regions are going to be protected with overlap coatings, seals, and flow-path geometries that avoid stagnant liquid traps. Exposed metallic edges are covered by coated fairings.

Coating mass sizing

The gondola is approximated as a cylinder with diameter $D_g = 0.58$ m and height $h_g = 0.25$ m. For the external coating, a 20% area allowance is added for fittings, seams, brackets, and overlaps, with a 25 μm PTFE coating, $\rho_{\text{PTFE}} = 2150$ kg/m^3, and a 30% margin this gives an external coating mass of 0.082 kg.

For the internal coating, the same shell area is used as the baseline, with a 100% area allowance to account for complex internal geometries. This gives $A_{g,\text{int}} = 1.96$ m^2. With a 50 μm PTFE coating, the internal coating mass is 0.274 kg after the same 30% margin.

Table 6.2: Preliminary environmental-control coating sizing summary.

Item	Area [m^2]	Thickness [μm]	Booked mass [kg]
External gondola PTFE coating	1.18	25	0.082
Internal gondola PTFE coating	1.96	50	0.274

6.2.2. Atmospheric Interface Classification

The VISTA gondola contains several atmospheric interfaces rather than a single common inlet. These interfaces are divided into three categories according to their function and contamination sensitivity:

1. **Filtered gas-sampling paths:** used by gas-composition instruments such as the NMS and mTLS, and by the ISRU feed system. These paths must admit atmospheric gases while rejecting liquid droplets, aerosols and large particles.
2. **Aerosol-preserving sampling paths:** used by aerosol instruments such as the AFN, OPC, and TOPS. These paths must preserve the particle composition and therefore cannot use droplet-excluding filtration approach as the gas instruments.
3. **Exposed sensing interfaces:** used by barometers, WIS temperature sensors, the sonic anemometer, pyrgeometers, antennas, and optical or radiative windows. These interfaces do not necessarily ingest bulk atmosphere, but their exposed surfaces must resist acid deposition and avoid measurement bias.

A filter that protects the NMS from sulfuric-acid droplets would remove the same aerosol particles that the AFN is intended to characterise. Gas sampling, aerosol sampling, and exposed environmental sensing are therefore treated as separate interface classes with distinct protection strategies.

6.2.3. Aerosol-Sampling Path Protection

Aerosol instruments require a fundamentally different strategy. The AFN, OPC, and TOPS must sample cloud particles rather than exclude them, and therefore these inlets use short, direct, acid-compatible flow paths with minimal bends and minimal dead volume. The internal walls of the aerosol path are coated with PTFE surfaces to avoid chemical interaction between the sulfuric-acid droplets and the material of the flow path.

6.2.4. Gas-Sampling Path Protection

Inlet clogging by sulfuric acid cloud particles has been a persistent failure mode in previous Venus in situ mission. On Venera-9, micro-pore mass-spectrometer intakes were blocked by cloud particles that only evaporated at lower altitudes. The Pioneer Venus Large Probe Neutral Mass Spectrometer likewise suffered a clog from a sulfuric acid droplet, which subsequently contaminated the instrument's measurements [47]. Given that the gondola operates continuously within the cloud layer at altitude, where the sulfuric acid aerosol concentration is highest, a reliable aerosol exclusion system is a critical requirement for the scientific goals of the mission.

The gas-analysis instruments require atmospheric gas access while being protected from sulfuric-acid droplets and cloud particles. Two separate protected gas inlets are therefore used: one for the Neutral Mass Spectrometer (NMS) and one for the mid-infrared Tunable Laser Spectrometer (mTLS). The design follows the philosophy employed on the DAVINCI Venus Mass Spectrometer, which couples heated inlet tubes with filters of passivated, sintered metal spheres to prevent clogging of capillary flow restrictors [47, 48].

The ISRU intake is treated separately from the scientific gas inlets because it has a much larger required throughput. Its dedicated two-branch filtering architecture with backflush capability is described in chapter 7.

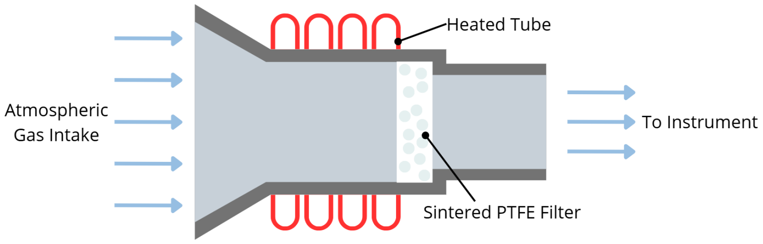

Figure 6.6: Heated inlet sketch

Sintered PTFE Filter Element.

The filter material is selected as sintered PTFE rather than passivated sintered metal as in [47]. It is selected for long-duration exposure to concentrated sulfuric acid. PTFE has essentially complete chemical resistance to sulfuric acid across the full concentration range encountered in the cloud layer (75–92% H_2SO_4) and withstands continuous service well above the temperature at the gondola float altitude.

Heated Inlet Tube

As an additional safeguard for instrument inlets, a resistively heated copper wire upstream of each critical inlet is employed. Heating the tube wall to approximately 150 °C, roughly 60–90 °C above the local saturation temperature of H_2SO_4 droplets at float altitude, ensures vaporisation of any droplets surviving. This approach is directly inherited from the DAVINCI VMS design [47].

Instrument Gas-Inlet Filter Sizing

For the protected NMS and mTLS gas inlets, the objective of this sizing is not to determine the final filter pore size or detailed pressure drop, but to obtain a preliminary mass and power budget for the environmental-protection hardware. Detailed filter permeability, pressure drop, and clogging behaviour shall be verified in later design phases using sulfuric-acid aerosol exposure tests.

The sizing was performed in CAD assuming inlet diameters of 10 mm for NMS and 2 mm for mTLS [20]. The sintered PTFE filter disks of sub-centimeter thickness each are in order of 1 gram mass. For the mass budget, the full inlet assemblies are booked, including the inlet alumnium housing and heating unit made of copper, summing up to:

Table 6.3: Preliminary mass estimate for the NMS and mTLS protected gas inlets.

Item	NMS inlet [kg]	mTLS inlet [kg]
Sintered PTFE filter disk	0.001	0.001
PTFE-lined housing	0.060	0.030
Heated inlet tube	0.023	0.018
Total	0.084	0.049

The power demand was derived from the convective heat loss from each heated tube, when heated to 150 degrees Celsius, the inlet heaters are assumed to be active only during the corresponding instrument operation windows. Using the current operational duty-cycle assumptions of $DC_{\text{NMS}} = 0.9$ and $DC_{\text{mTLS}} = 0.126$, the average heater power becomes: The protected gas-inlet budget is summarised in Table 6.4.

Table 6.4: Preliminary mass and power budget for the protected gas-analysis inlets.

Item	Mass [kg]	Peak power [W]	Average power [W]
NMS protected gas inlet, $D = 10$ mm	0.084	5.4	4.86
mTLS protected gas inlet, $D = 2$ mm	0.049	1.5	0.189
Total, 20% margin included	0.16	6.9	2.5

6.2.5. Verification and Risk Mitigation

The environmental-control design shall be verified through combined material-exposure, clogging, and functional tests. Coating coupons, balloon-laminate samples, inlet filters, valves, seals, and representative electrical connectors shall be exposed to sulfuric-acid aerosol under representative Venus-cloud temperature and pressure conditions. The test programme shall include both static soak tests and flowing-aerosol tests in order to capture long-term material degradation, deposition, and clogging behaviour. For gas-sampling paths, the verification criterion is that the pressure drop across the inlet remains below the operational limit and that the NMS and mTLS composition measurements remain within calibration uncertainty after repeated exposure. For aerosol-sampling paths, the verification criterion is that particle-size and acidity measurements are not biased by the inlet geometry beyond the instrument-level accuracy requirement. The main residual risks are long-term PTFE coating delamination, filter clogging beyond the design service interval, acid accumulation in dead volumes, and measurement bias caused by inlet protection hardware. These risks are mitigated by separating gas and aerosol sampling paths, using fluoropolymer wetted surfaces throughout the sampling system, applying acid-resistant external and internal coatings, avoiding stagnant liquid traps, and qualifying all inlet and coating materials against representative Venus cloud aerosols prior to flight.

6.2.6. Sustainability note

Although PTFE is selected because of its excellent compatibility with concentrated sulphuric acid, its sustainability impact must be acknowledged. PTFE belongs to the fluoropolymer group of PFAS materials, and the main environmental concern is associated with production rather than its in-flight use. Therefore, PTFE use in VISTA is treated as a mission-critical material choice rather than a default coating solution. Procurement should prioritise suppliers with closed-loop emission control, documented PFAS management, and avoidance of legacy high-concern processing aids. In Phase B, alternative acid-resistant coatings or surface treatments should be reassessed, but only if they can provide equivalent five-year resistance to high sulphuric-acid aerosols without increasing mission risk.

6.3. Command & Data Handling Subsystem

The Command and Data Handling Subsystem forms the central control and data-management unit. The subsystem requirements used to guide this design are listed in section 10.4.

6.3.1. Storage Characteristics

To obtain a value for the required storage, the telemetry data rates from section 5.4 along with the operational schedule for the payload from subsection 3.2.2 are used. For the expected nominal operation based on contact window requirements on which the preliminary design was based, the accumulation of scientific and housekeeping data along with the transmission of this data is summarized in Figure 6.7.

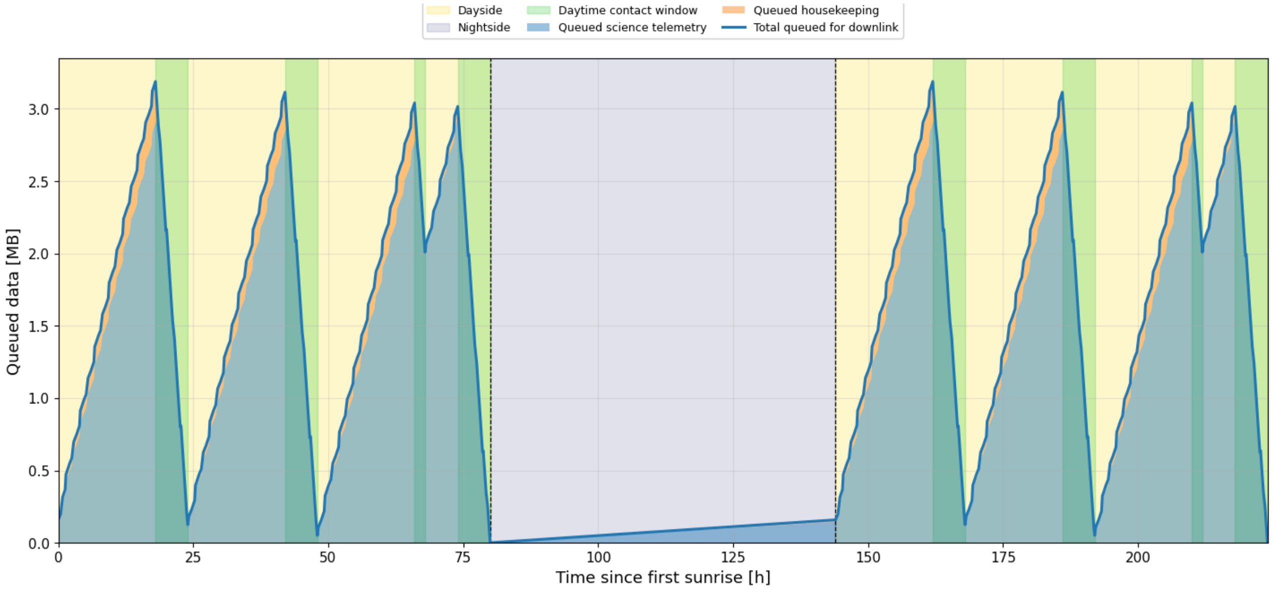

Figure 6.7: The stored scientific and housekeeping data over time over one and a half daynight cycle

For the detailed data-generation analysis, additional data sources were included beyond the nominal science and housekeeping telemetry along a real balloon-orbiter link connection simulation. This resulted in the stored-data profile shown in Figure 6.8.

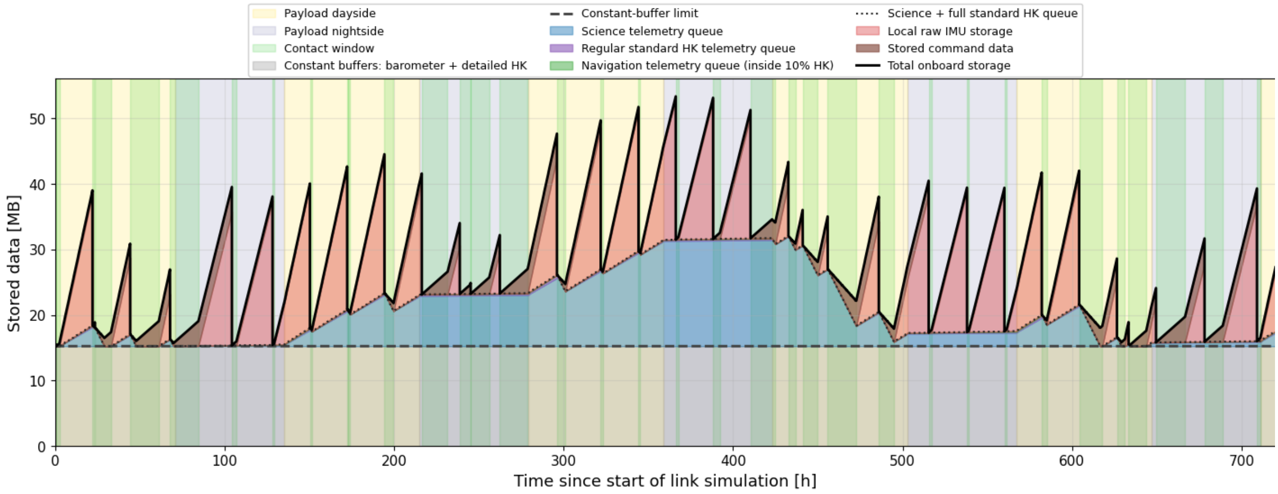

Figure 6.8: Simulation of the amount of data stored vs. time

For this figure, a bad scenario was chosen in which large communication windows fall at night and short ones during the day over the course of a few days. The average contact time fraction with the orbiter over a long period is indeed higher than 25% as required, allowing all data to be transmitted over long periods. It also includes the constant command rate received during contact times at day and night, which is saved until the end of the next contact period. This is assumed because the balloon must retain the latest validated command sequence during autonomous operation between communication windows. During a new contact, the previous command package is kept until the new one has been fully received and validated, after which the older package can be safely deleted. This is an approximation of command-data retention logic. Also, If the balloon enters seismic mode it must also save the pre-seismic event data of the barometers adding around 3.24MB of buffer data that must be constantly saved. Unlike the nominal housekeeping stream, which is downlinked at low rate within the regular telemetry budget, a detailed diagnostic housekeeping data buffer stores higher-resolution local health data for the previous 6 hours. To avoid excessive storage, a tiered sampling approach is used: slow thermal and state variables are stored at 0.2 Hz, medium-rate electrical and payload diagnostics at 1 Hz, and only selected event-sensitive channels at 10 Hz. Assuming 80 slow channels, 40 medium-rate channels, 16 fast channels, and 128 packed status bits, the 6-hour buffer requires approximately 11.6 MB. This data is only sent and prioritized over science data in case of minor or major fault detection or upon a request from command. In addition to housekeeping data, 5 raw data measurements are stored during each day for processing verification diagnostics, increasing diagnostic data to 12MB. From Figure 6.8, it can be concluded that the maximum stored data is 54MB. To account for a worst case scenario, it was assumed that one contact window would be missed. It represents a realistic off-nominal event while still remaining within the expected operational design space. Contact opportunities may be missed due to pointing errors, temporary link outages, orbiter scheduling conflicts, atmospheric attenuation, or spacecraft safe-mode events. In these simulations the science data could still be transmitted in this case, as the orbiter has a slightly higher contact fraction time with balloon than the minimum requirement for which was designed. After iterating over what would happen if 1 contact window would be missed for each contact window, the worst case storage requirement would be **80MB**. Other operational modes would clearly change data stored vs time graph in Figure 6.8. The modes are chosen such that all required data can be sent away and these modes will not generate more data than the nominal science mode and are thus not analyzed.

6.3.2. Flight software Characteristics

To determine the required flight software characteristics, the functions that the data handling must perform have to be identified. C is selected for the software-size estimate instead of C++ because the C&DH software is expected to be low-level embedded flight software running on a resource-constrained OBC. C provides direct hardware access, predictable execution behaviour, low memory overhead, and strong compatibility with microcontroller drivers and real-time operating systems.

The software-size estimate follows a bottom-up COCOMO-II-informed function-point approach [49, 50]. The OBC flight application is first decomposed into mission-specific onboard functions. For each function, the required external inputs, external outputs, external inquiries, internal logical files, and external interface files are identified and classified as low, average, or high complexity according to the COCOMO II unadjusted-function-point procedure. The resulting unadjusted function points are then converted to C source lines of code using the COCOMO II default conversion factor of 128 SLOC/UFP for C. This provides a preliminary estimate of delivered mission-specific C source code.

An additional 25% is added on top of this estimation as this bottom up approach usually tends to underestimates the number of SLOC [51] giving 84800 SLOC. Using Hatton's C conversion factor of 17 ± 3.5 object-code bytes per C source line [52] gives an estimate of the mission-specific code size range of approximately **1.1-1.8MB** for the OBC.

6.3.3. Processing characteristics

The RAM budget is instead estimated from the sum of RTOS and task stacks, interface receive/transmit buffers, packetisation buffers, storage-cache memory, current housekeeping and fault-state tables, short IMU/barometer history windows needed for processing, and temporary science-processing workspaces. The large temporary science buffers are assigned to SDRAM, while the internal RAM is reserved for deterministic real-time software state such as stacks, interrupt buffers, command handling, queue metadata, and FDIR state. This gives an estimated internal RAM requirement of approximately **1.2-1.3MB**. The SDRAM requirement is driven mainly by the mTLS spectral buffer, sonic-anemometer processing buffer, AFN/OPC binning workspace, barometer filtering workspace, compression workspace, and NAND/file-system cache. Including a 50% preliminary margin, the required SDRAM is estimated as approximately **8.5MB**. Processor sizing is performed from the estimated onboard workload rather than from an assumed candidate OBC clock frequency. For each dominant C&DH and payload-processing function, an equivalent operation count N_i and execution period or deadline T_i are assigned. The required minimum clock frequency is then estimated as

$$f_{clk,min} = \frac{\gamma}{U_{max} IPC_{eff}} \sum_{i=1}^{N} \frac{N_i}{T_i} \tag{6.1}$$

where γ is the timing-growth and implementation allowance, U_{max} is the maximum allowed processor utilisation, and IPC_{eff} is the effective instructions per clock for the mixed embedded workload. An effective value of $IPC_{eff} = 0.7$ is used as a conservative preliminary estimate, since the flight software contains a mixture of numerical processing, packet handling, branching, interrupts and interface management rather than ideal single-cycle instruction execution [53, 54, 55]. Based on the functions identified in the C&DH software sizing, the dominant workload including driver, interrupt and scheduling overhead is estimated at approximately 58.8 Mops/s. With $\gamma = 1.5$, $U_{max} = 0.70$, and $IPC_{eff} = 0.7$, the minimum required clock frequency is approximately 180 MHz. In addition to clock speed, the processor should provide a 32-bit embedded real-time architecture, a hardware floating-point unit, DSP or multiply-accumulate support, low-latency interrupt handling, DMA, hardware timers, and CRC/checksum support to reduce execution time for instrument processing, packet handling, data validation and FDIR.

6.3.4. Electrical Interface Characteristics

The data-handling architecture requires a combination of robust subsystem-level interfaces and simple local peripheral interfaces. The payload instruments generate the main science data, so robust serial data links are required between the payload block and the central data-handling system. RS-422 is suitable for these payload links [56], especially for instruments such as the NMS, mTLS, AFN, OPC, sonic anemometer and barometer acquisition electronics, because its differential signalling provides better noise immunity than single-ended serial links and is appropriate for point-to-point data transfer across internal harnesses. For lower-rate housekeeping-type sensors, such as temperature sensors, simple environmental sensors or local monitoring electronics, I^2C is useful because several addressed devices can share the same two-wire bus, reducing harness complexity [57]. CAN is desirable for subsystem-level command and status communication, for example to the EPS, thermal-control electronics, ISRU controller module and other smart subsystem interfaces, because it supports multi-node communication, message arbitration and error detection [58]. UART is useful for simple point-to-point links, debug access, and radio/transceiver interfaces where a straightforward asynchronous serial data stream is sufficient [59]. GPIO, ADC and PWM capability are still required for discrete enable lines, reset lines, analogue housekeeping measurements and simple control signals. However, interface-heavy subsystems should not connect every sensor and actuator directly to the central computer. In particular, the ISRU subsystem contains valves, pumps, compressor/separator hardware and pressure/status sensors, so a local microcontroller is useful as an ISRU controller module. This local controller can drive the low-level actuators, read local sensors, perform simple limit checks and return one aggregated command/status interface to the central data-handling system. This reduces the number of required OBC ports.

6.3.5. Additional characteristics

The data-handling system also requires several fault-recovery and autonomy features in addition to its nominal processing and interface functions. A hardware watchdog and reset circuit is needed to recover the OBC if the onboard software hangs, enters an invalid state, or stops executing its periodic health checks. In such a case, the watchdog can force a processor reset or short power-cycle, allowing the system to restart without ground intervention. This is important for a Venus balloon mission because communication windows are intermittent and the aerobot must remain autonomous between contacts. After a reset, non-volatile MRAM is required to preserve the reset cause, critical housekeeping data, last valid mission mode, fault counters, and queue checkpoints. Unlike volatile RAM, MRAM retains this information through resets or temporary power interruptions, allowing the restarted software to determine whether nominal operations can safely resume or whether the aerobot should remain in, or enter, safe mode. An independent real-time clock is also useful because it maintains timing across resets or temporary power interruptions, allowing science schedules, packet time tags, and contact-window logic to remain consistent. Finally, internal voltage, current, and temperature monitoring supports anomaly detection and can trigger protective actions before the fault propagates to payloads, storage, or subsystem interfaces.

6.3.6. C&DH subsystem design

An OBC that adheres to all requirements stated in this section is the DARA OBC. The characteristics of the DARA OBC are shown in Table 6.5.

Table 6.5: Main properties of the selected DARA OBC [40].

Property	Value / description
Processor	ARM Cortex-M7, 32-bit CPU with FPU, up to 280 MHz
Power and supply	280 mW typical, 3.3 V nominal supply

Property	**Value / description**
Program and working memory	2 MB program Flash, 1.4 MB internal RAM, and 32 MB SDRAM
Persistent storage	512 kB MRAM for critical status and 128 MB NAND Flash for science and housekeeping data
Optional storage	2× microSD card slots, up to 64 GB each
Integrated sensors	IMU with 3-axis magnetometer, gyroscope, and accelerometer; board voltage, current, and temperature sensors
Interfaces	3× RS422, 2× CAN, UART, 2× I^2C, SPI, GPIO, ADC, PWM, PPS, and JTAG
Fault recovery and timekeeping	Hardware watchdog/reset circuit and RTC with independent power supply option
Environment, mass, and size	−40 °C to 85 °C, 115 g, 93.3 mm, 89.3 mm and 12.6 mm
TRL	9

Figure 6.9 gives the centralized data-handling architecture, with Table 6.6. The high-data-rate payload instruments, with specific raw data rates shown in Figure 6.9, are distributed over the available science-data links; according to the science schedule in subsection 3.2.2, only a limited subset of the NMS, AFN, mTLS, OPC and TOPS operate at the same time, so the simultaneous raw data rate remains within the available interface capacity. UART is therefore kept as an auxiliary data path rather than as a duplicated continuous science-data stream; it can be used when the primary science-data links are occupied. The pyrgeometers do not require a separate command-data interface, since they can be enabled or disabled through the EPS by switching their protected load channel. GPIO connections are not all drawn explicitly in the figure, but are assumed to be available to most subsystem interfaces for simple enable, reset, fault and status signals; these lines are not used for high-rate data transfer. The UHF transceiver is connected through a UART KISS interface because KISS provides a simple packet-framing layer over a standard asynchronous serial link, making it well suited for transferring packetised telecommands and telemetry between the radio and the OBC. The ATmegaS64M1 is used as a local controller for the ISRU subsystem because it can handle the many low-level signals needed for valves, pumps, pressure sensors, temperature sensors and safety interlocks. Instead of connecting every ISRU sensor and actuator directly to the central OBC, the microcontroller aggregates them into one command/status interface, reducing the number of required OBC I/O lines. Its CAN, UART, SPI, ADC, DAC, PWM/timer and watchdog capabilities make it suitable for local actuator control, sensor monitoring and simple fault handling. This also allows the ISRU subsystem to enter a local safe state if communication with the OBC is lost [39].

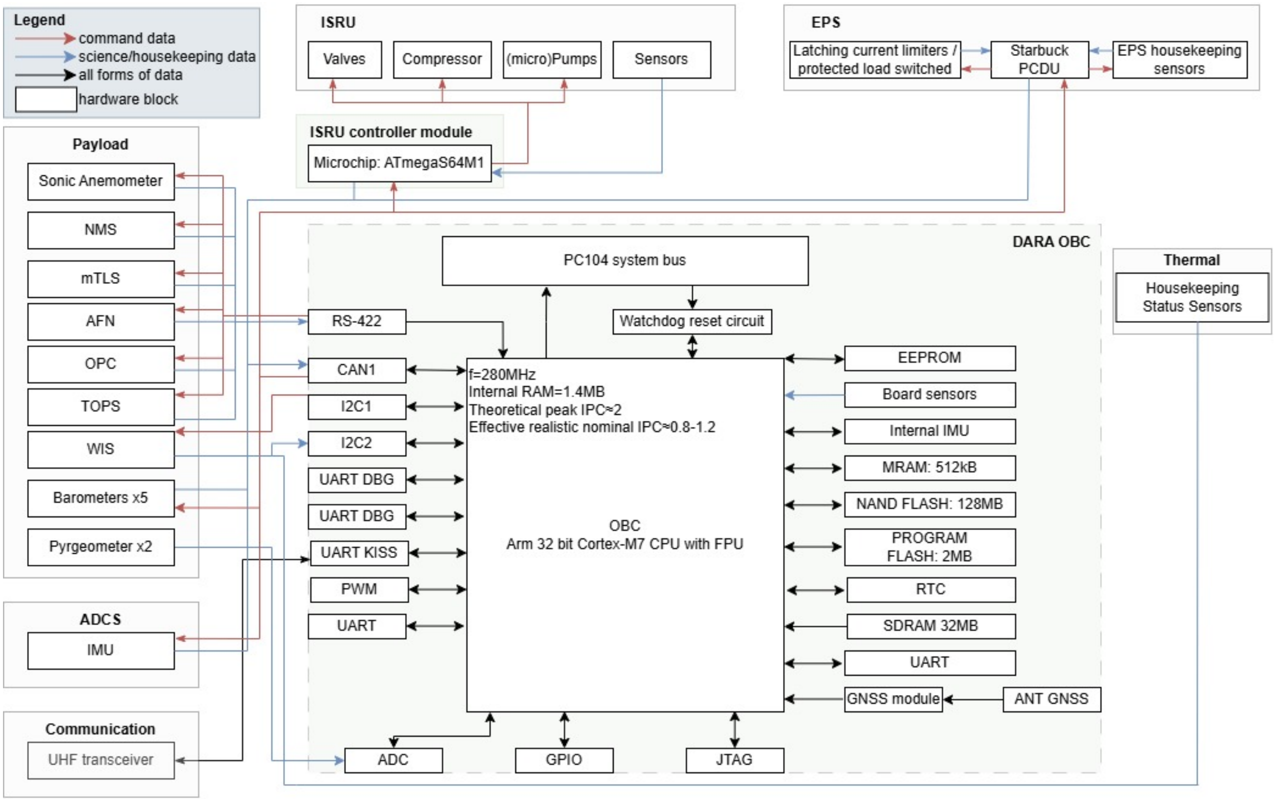

Figure 6.9: Data handling subsystem hardware block diagram

Table 6.6: Active raw data rates to and from the OBC, excluding duty-cycle effects.

Component	To OBC [kbit/s]	From OBC [kbit/s]	Component	To OBC [kbit/s]	From OBC [kbit/s]
NMS	0.10–0.25	0.10	AFN	16	0.20
WIS ×3	0.080	0.05	Sonic anemometer	880–1760	0.20
Barometers, nominal	0.0048	0.05	Barometers, event mode	1.2	0.10
mTLS	4000	0.30	TOPS	0.133	0.05
Pyrgeometers ×2	0.013	0.05	OPC / LOPC	16	0.20
Internal IMU	2.3	0.05	DARA board sensors	~ 0.5	~ 0.05
EPS / PCDU / batteries	~ 1.0	~ 0.5	Thermal housekeeping sensors	~ 0.3	~ 0.2
ISRU controller module	~ 2–5	~ 1.0	UHF transceiver	~ 0.6	~ 1.6

The mass & power breakdown of the C&DH subsystem in Figure 6.9 is shown in Table 6.7. The connector and harness mass was estimated using a bottom-up interconnection approach based on the data-handling architecture and the approximate gondola layout. Each required OBC-to-subsystem link was assigned an estimated routed cable length, cable mass per metre based on type of cable required for link, and connector-pair allowance. The resulting link masses were summed, after which an allowance was added for shielding, strain relief, routing slack, clips, and small auxiliary wires. A larger margin was applied to this item because the final harness routing and connector selection are still uncertain at this design stage.

Figure 6.9.

Table 6.7: CDHS mass and nominal day/night power budget including component-level mass margins

Component	Base mass [kg]	Mass margin	Mass with margin [kg]	Day power [W]	Night power [W]
DARA on-board computer	0.115	5%	0.121	0.280	0.280
ATmegaS64M1 ISRU controller chip	0.00847	5%	0.00889	0.013	0.000
Connector and harness system	0.149	20%	0.179	0	0
Total CDHS	**0.260**	–	**0.309**	**0.293**	**0.280**

6.3.7. C&DH verification and validation

The C&DH subsystem is verified against the requirements listed in section 10.4. REQ-F-CDH-01 and REQ-F-CDH-03 are verified by data-flow and buffer-management analysis, supported by engineering-model tests with representative payload and subsystem data streams to confirm data acquisition, time-tagging, validation, buffering, routing, and event-buffer retention. REQ-F-CDH-02 is verified by storage sizing, comparing the nominal data budget and one missed-contact case with the available NAND flash and MRAM storage, including the required 25% margin. REQ-F-CDH-04 is verified by command-storage tests, confirming that the previously validated command set is retained until a new command set has been fully received, checked, and accepted. REQ-C-CDH-05 and REQ-C-CDH-06 are verified by software-size, memory-allocation, processor-load, and timing analyses, checking the required 25% memory margin and 30% processor-utilisation margin. REQ-F-CDH-07 is verified by interface review and engineering-model interface tests with the payload, communication, EPS, GNS/ADCS, thermal, and ISRU-controller interfaces. REQ-F-CDH-08 and REQ-F-CDH-09 are verified by reset, power-interruption, watchdog, and fault-injection tests, confirming preservation of critical mission state and autonomous recovery.

Validation is performed on the selected OBC running representative flight software and connected to payload, subsystem, communication, and ground-segment simulators. The validation scenarios include nominal day/night operation, an orbiter contact pass, event-buffering, one missed communication window, safe-mode entry, and recovery from reset or power interruption. The C&DH design is considered valid if the computer correctly acquires, protects, stores, prioritises, and routes science and housekeeping data, preserves command and mission-state information, and resumes safe autonomous operation without immediate ground intervention. At C&DH level, the communication interface is validated by checking that the OBC correctly handles the data-flow consequences of the assumed link budget, including limited contact duration, delayed downlink, missed passes, command reception, and telemetry prioritisation.

6.4. Communication Subsystem

The Communication Subsystem provides the aerobot's command and telemetry link by connecting the gondola to the relay orbiter through a UHF proximity link, after which data are forwarded to Earth through the orbiter's X-band link. The subsystem requirements used to guide and verify this design are listed in section 10.4.

6.4.1. Frequency band

The frequency band selection is a key design driver because it affects achievable data rate, antenna gain, transmitter power, link margin, propagation losses, ground-station compatibility, and frequency-allocation constraints. For the orbiter–Earth link, the main ESTRACK-compatible deep-space options are S-band, X-band, and Ka-band, as summarised in Table 6.8. X-band is selected as the baseline because it provides the best compromise between reliability, data-rate capability, antenna size, and ESTRACK compatibility. Compared with S-band, it offers higher bandwidth and higher antenna gain for a given antenna size; compared with Ka-band, it is less sensitive to atmospheric attenuation, rain losses, and pointing errors, making it more robust for a relatively low-data-rate Venus mission.

Table 6.8: Candidate ESTRACK-compatible frequency bands for the orbiter–Earth link.

Band	Uplink: Earth to orbiter	Downlink: orbiter to Earth
S-band	2110–2120 MHz	2290–2300 MHz
X-band	7145–7190 MHz	8400–8450 MHz
Ka-band	34.2–34.7 GHz	31.8–32.3 GHz

For the aerobot–orbiter relay link, direct use of X-, S-, or Ka-band is less attractive because the balloon gondola has limited pointing capability and power. The candidate proximity-link bands are therefore VHF, UHF, and S-band, as shown in Table 6.9. VHF has low path loss and is robust, but requires larger antennas and has less modern planetary relay heritage. S-band is possible, but has higher path loss and generally requires better antenna gain or pointing. UHF is selected as the baseline because it is well-suited to short-range planetary relay, low data rates, low spacecraft complexity, broad antenna coverage, and weak pointing requirements.

Table 6.9: Candidate frequency bands for the aerobot–orbiter communication link.

Band	Frequency range
VHF	30–300 MHz
UHF	300 MHz–3 GHz
S-band	2–4 GHz

6.4.2. Antenna Design and Configuration

The aerobot operates at UHF and has nearly no control over its attitude, making omnidirectional antennas with broad angular coverage over the upper hemisphere the most suitable option.

No single antenna provides perfectly uniform hemispherical coverage. Therefore, pointing losses at low elevation angles are always present. To reduce this sensitivity, a two-antenna configuration is selected. The antennas are placed near opposite top edges of the gondola and inclined (30°) outward towards the horizon. This improves low-elevation visibility, reduces blockage during gondola tilt, and provides redundancy with only a small mass penalty. The two-antenna arrangement also relaxes the attitude-control requirement, because at least one antenna is more likely to maintain a favourable radiation direction during an orbiter pass.

The selected aerobot antenna is the helical-ring antenna proposed by Morlaas et al. [60]. This antenna behaves approximately as a circularly polarized Huygens source, producing a radiation pattern mainly directed into one half-space without requiring a large reflector. The radiation pattern and approximate geometry are shown in Figure 6.10. For the modified four-turn design with two metallic disks, Morlaas et al. report a simulated maximum directivity of approximately 5.4, dBi at 0.59GHz [60]. The half-power beamwidth is approximately 120°. Based on the selected inclined two-antenna configuration, the pointing loss near the horizon is reduced from approximately 8, dB to approximately 3, dB.

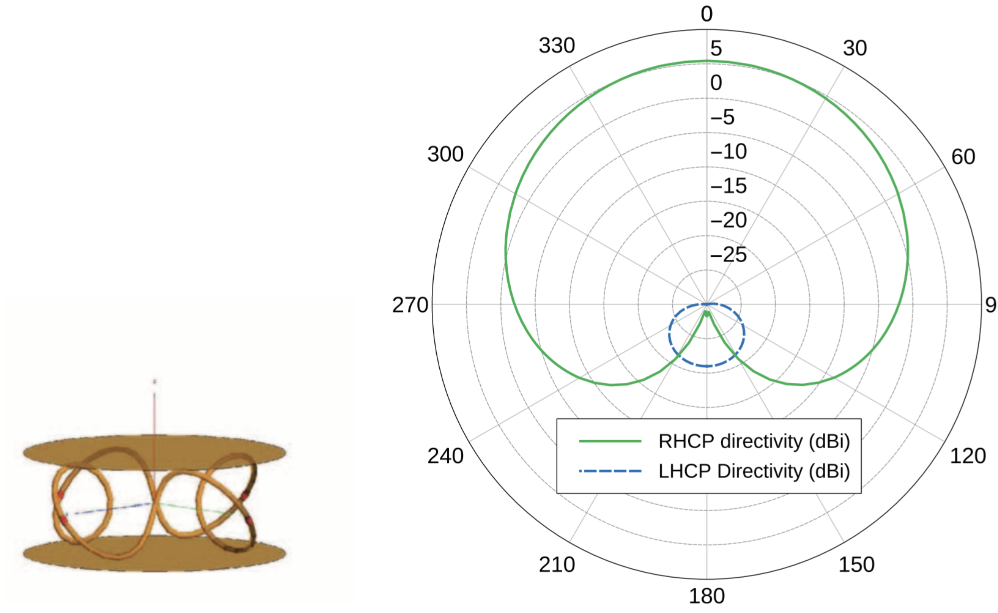

Figure 6.10: Helical-ring antenna two-dimensional radiation pattern in dBi at 0.59 GHz [60].

Experimental validation of the helical-ring concept was performed by Morlaas et al. using a four-turn prototype. The measured intrinsic antenna efficiency was 93.4%, after removing the effect of the feeding circuit. The measured axial ratio remained below 3, dB over more than 180° in the upper half-space, indicating very good right-hand circular polarization over the useful angular coverage region as seen in Figure 6.11. The TRL of the helical-ring antenna is estimated at 5.

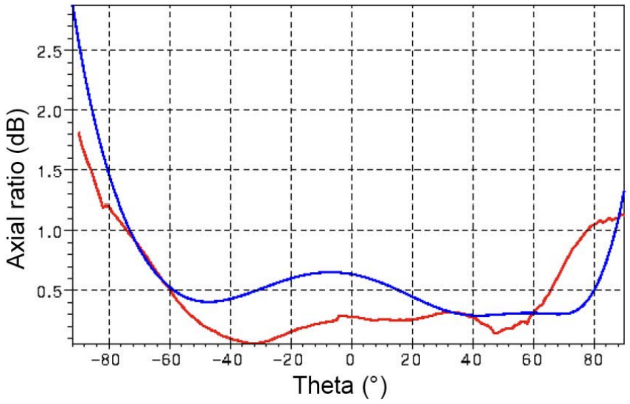

Figure 6.11: Axial ratio (dB) in the xOz plane: measurement (red) and simulation (blue).

6.4.3. Propagation losses

The simplest source of propagation loss is the free-space path loss, which represents the spreading loss of an electromagnetic wave as it propagates through space. It is given by Equation 6.2

$$L_{fs} = 20 \log_{10} \left(\frac{4\pi d}{\lambda} \right) \tag{6.2}$$

where L_{fs} is the free-space path loss in dB, d is the distance between the transmitter and receiver, and λ is the signal wavelength. The maximum link distance is obtained from navigation simulations.

The second source of signal loss is absorption by atmospheric gases. The atmosphere of Venus consists of approximately 96.5% CO_2 and 3.5% N_2. Figure 6.12 shows the absorption rates, expressed in dB/km, of several gases in the Venusian atmosphere for X-band and S-band frequencies. The figure also shows that below altitudes of approximately 50 km, the abundance of H_2SO_4 becomes significant, extending down to about 30 km. At lower frequencies, such as those in the UHF range, these absorption rates are expected to be even lower.

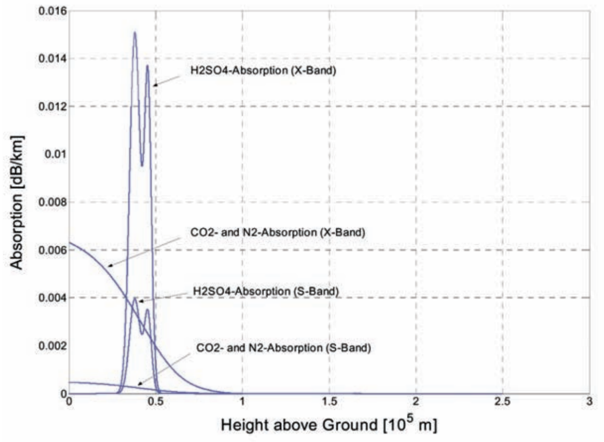

Figure 6.12: Average absorption profile as a function of altitude for $H_2SO_4(g)$, CO_2, and N_2 in the atmosphere of Venus [61].

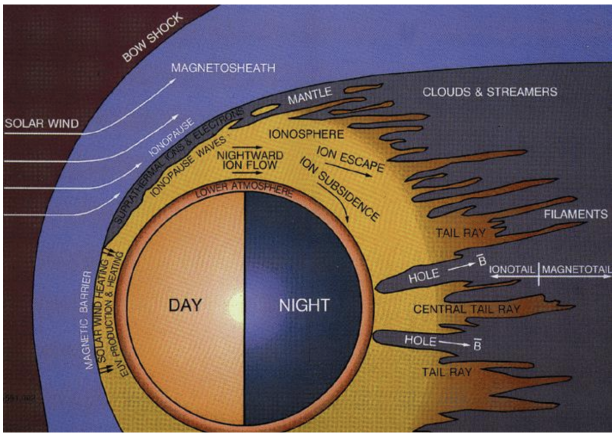

Figure 6.13: A sketch of the most important plasma boundaries and interaction regions in the environment of Venus [62].

The Venus ionosphere is dynamic because electron density varies with altitude, solar illumination, solar activity, and solar-wind conditions. Since Venus lacks a strong intrinsic magnetic field, its plasma environment is mainly shaped by interaction with the solar wind, forming an induced magnetosphere as illustrated in Figure 6.13. These variations can affect UHF propagation between the aerobot and orbiter and are therefore included in the link-budget loss model.

For the link budget, a conservative case is used by taking the maximum electron-density envelope and the highest ionopause condition. The ionospheric absorption loss is calculated as in Equation 6.3[63].

$$L_{\text{ion,abs}} = \frac{1.17 \times 10^{-6}\, \nu\, \text{TEC}}{n_{\text{re}} f^2} \tag{6.3}$$

where $L_{\text{ion,abs}}$ is the absorption loss in dB, ν is the effective electron collision frequency, f is the signal frequency, and n_{re} is the real part of the plasma refractive index. For UHF, $n_{\text{re}} \approx 1$, since the signal frequency is much larger than the local plasma frequency.

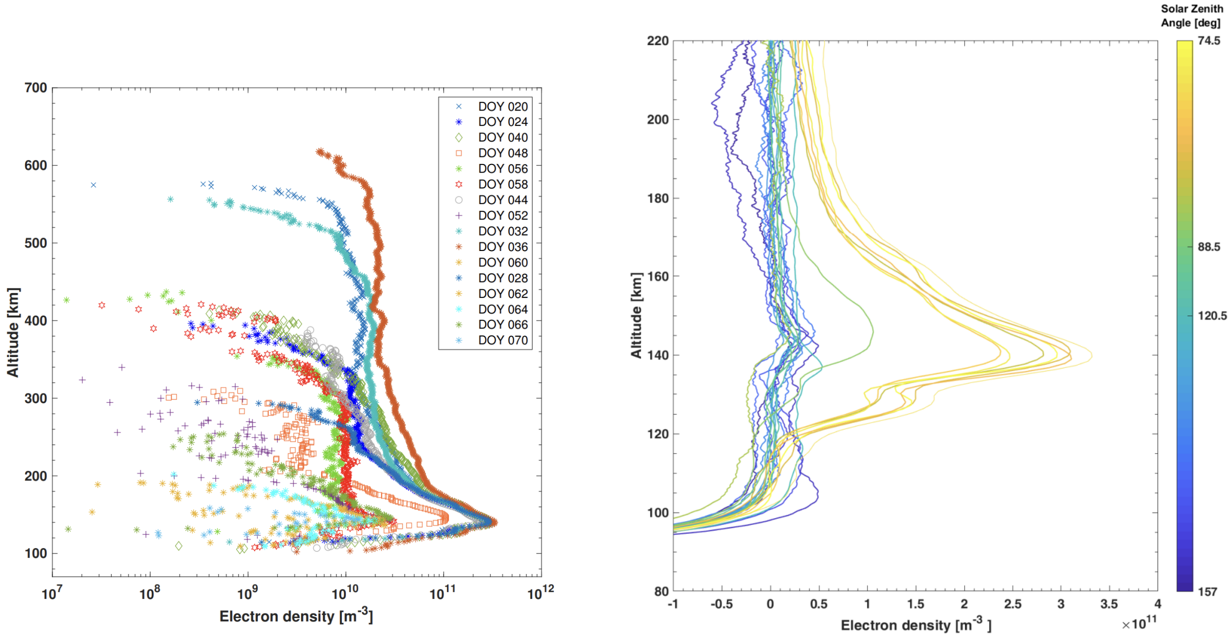

(a) Electron density measured at different time instances

(b) Electron density measured for different solar zenith angles

Figure 6.14: Electron density vs. altitude: (a) at different time instances and (b) for different solar zenith angles [64].

The total electron content along the path is given by Equation 6.4

$$: \text{TEC} = \int_{\text{path}} N_e(s)\, \mathrm{d}s, \tag{6.4}$$

where $N_e(s)$ is the electron density along the signal path. A numerical tool was used to evaluate atmospheric and ionospheric losses for different elevation angles and altitudes, including the lowest altitude of 52 km. Combining the conservative ionospheric model with atmospheric gas and cloud losses gives a maximum total propagation loss of $L_{\text{gases,ionosphere}} = 2.5$ dB, which is used in the UHF link budget.

Since the aerobot-orbiter link operates at UHF, ionospheric scintillation may cause short-term amplitude and phase fluctuations, especially at low elevation angles. Therefore a 2 dB fading margin is incorporated in accordance with SMAD [65]. The total atmospheric attenuation due to the Earth is given to be $0.3dB$ for operational conditions, and $0.5dB$ in case of moderate rain [66].

6.4.4. Link Budget Iterative Process

For the link budget, the end-to-end BER is approximated as the sum of the BER contributions of the individual communication links. Therefore, the BER allocation for the aerobot–orbiter link is chosen to be less strict than that of the orbiter–Earth link, such that the total system requirement of BER $\leq 10^{-6}$ is satisfied. The aerobot–orbiter link is the most design-driving part of the communication system, since the aerobot is more constrained in mass, volume, and available transmitter power than the orbiter. The required aerobot uncoded data rate is taken as $R_b = 1500\ bits/s$.

The aerobot UHF transmit antenna gain, orbiter UHF receive antenna gain, and receiver system noise temperature are taken from the previous subsystem estimates. For each candidate modulation, the number of bits per symbol, m, is defined. Together with the FEC code rate, ρ, and the roll-off factor, α, this determines the spectral efficiency as shown in Equation 6.5 [65]:

$$\eta = \frac{m\rho}{1+\alpha} \tag{6.5}$$

where η is the spectral efficiency in $bits/s/Hz$. The required bandwidth can then be estimated from the selected bit rate and spectral efficiency.

For different required BER values, the required uncoded value of $\frac{E_b}{N_0}$ is first determined from the modulation performance. A coding gain is then applied based on the selected FEC code rate and coding scheme. The resulting required E_b/N_0 is converted to the required carrier-to-noise ratio using Equation 6.6:

$$\frac{C}{N} = \frac{E_b}{N_0}\frac{R_b}{B} \tag{6.6}$$

where B is the occupied bandwidth. This required $\frac{C}{N}$ is then used in the link budget to determine the required aerobot transmitter power, P_t using the link budget. For the aerobot–orbiter UHF link, the orbiter receiver is assumed to point toward Venus during communication. The antenna noise temperature is therefore dominated by Venus hot-body radiation, which is taken as approximately 600 K following Morabito et al. [67]. Adding a representative low-noise receiver front-end contribution of approximately 100 K gives $T_{sys} + T_{rx} \approx 700K$.

Channel coding is included in the link budget as a coding gain, while the code rate determines the increase in transmitted bit rate and occupied bandwidth. Candidate schemes include convolutional coding with Viterbi decoding, Turbo coding, and LDPC coding, with approximate coding gains derived from Figure 6.15. From the iterative link-budget process, a code rate of $\rho = 0.5$ was selected as the best compromise between coding gain and bandwidth increase. Turbo coding is selected for the science and telemetry links, namely the aerobot–orbiter uplink and the orbiter–Earth downlink. These links are the most link-margin-critical, so the high coding gain is more important than the additional decoding complexity and block latency. A coding gain of 9.6 dB is used for these links. Convolutional coding is selected for the command links, namely the orbiter–aerobot downlink and the Earth–orbiter uplink. These links have larger link margins, so the lower coding gain is acceptable. The main advantages are lower decoding complexity and lower latency, which are especially beneficial for command reception on the aerobot. A coding gain of 5.8 dB is used for these links. Pulse shaping is applied using a raised-cosine roll-off factor. This reduces intersymbol interference, but increases the occupied bandwidth. A roll off factor of $\alpha = 0.35$ is used. Next, the modulation schemes considered during the iteration were BPSK, MSK, GMSK, 2-FSK, and QPSK [68]. These schemes were selected for comparison because the communication link must remain robust at low transmit power, making good E_b/N_0 performance important.

They also allow relatively simple and reliable hardware implementations, which is beneficial for the mission. Since the required data rates are low, bandwidth is not the primary sizing driver; instead, robustness and amplifier efficiency are more important. Based on these considerations, MSK is selected for the UHF proximity link. Specifically, MSK provides a constant-envelope signal, allowing efficient operation of the power amplifier, while still offering good noise performance and a compact spectrum. It was also chosen as the best configuration in combination with earlier parameters and due to compatibility with existing hardware. Specifically, coherent MSK with a modulation factor of h=0.5. The coded and randomized bitstream is represented using simple NRZ line coding before being applied to the coherent MSK modulator. Manchester coding is not selected, since the additional transitions would increase the occupied bandwidth without providing a major benefit for this receiver architecture.

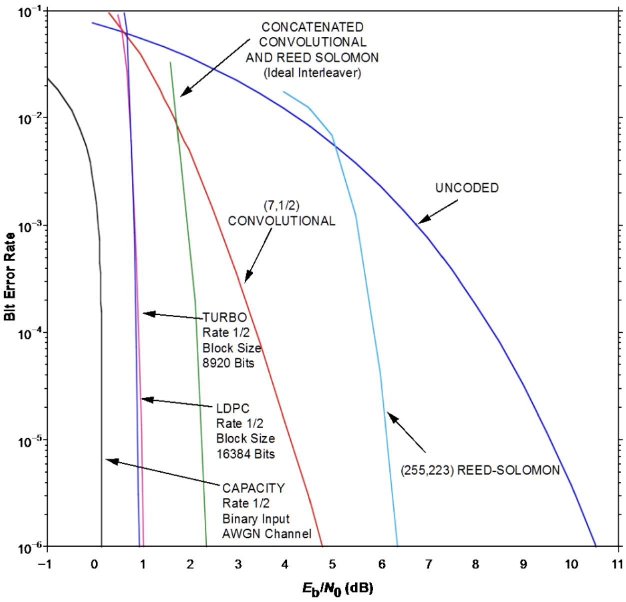

Figure 6.15: Performance comparison of selected convolutional, Reed–Solomon, concatenated, LDPC, and Turbo codes [69].

6.4.5. Communication System Design

Based on subsection 6.4.4, the optimal configurations was compared with available space-grade transceivers. The GAUSS high-power UHF transceiver is selected for the aerobot because it covers the required UHF relay band, supports the selected MSK/GMSK-type modulation and FEC options, and provides sufficient data-rate and RF-power margin for the 1500 bit/s aerobot–orbiter link.

Table 6.10: Main GAUSS high-power UHF radio specifications.

Parameter	Value
Frequency range	RX: 390–500 MHz; TX: 400–450 MHz
RF output power	Software-configurable, 30–40 dBm; maximum specified value of 40.1 dBm at 400 MHz
Data rate	0.3–250 kbps; current maximum stated as 100 kbps
Sensitivity	−122 dBm at 1.2 kbps; −119 dBm at 9.6 kbps; −109 dBm at 50 kbps
RF efficiency	Typically 40–55%, up to 59%, depending on RF output power
Supported modulation / coding	FSK, MSK, GFSK, GMSK; Viterbi, Reed–Solomon FEC, and turbo coding supported
Supply voltage	3.3 V digital supply and 7–12 V power-amplifier supply
Electrical power usage	≈ 0.22 W in standby/reception; 17.2–19.6 W at maximum RF output with 12 V PA supply
Mass and size	37 g; 75 × 31.5 × 12.5 mm
Temperature range	−40°C to +85°C
TRL	9 (successful mission in Earth orbit)

As a reference for the link budget, the orbiter communication subsystem is assumed to have performance comparable to a UST-Lite-class transceiver. The relay architecture uses an acquisition-and-tracking approach. The orbiter first detects or pings the aerobot using either a broad-coverage UHF antenna or a moderate-gain antenna operated in a scanning mode. After receiving the ping, the aerobot returns a low-data-rate tracking signal, allowing the orbiter to estimate its approximate position. The orbiter can then use, or switch to, a moderate-gain directional UHF antenna for the main communication link.

A receiver antenna gain of 11.8dBi is assumed for the orbiter. This is still a moderate-gain antenna at UHF, with an approximate half-power beamwidth of 55° to 65°. Therefore, once the aerobot position is approximately known, the antenna can provide useful gain while still maintaining relatively broad coverage. The link budget of the final design can be seen in Table 6.11. Note that the aerobot-orbiter link drives the design and that worst case conditions are assumed across all links. The link budget satisfies the minimum link-margin requirements of 3 dB for telemetry and science data and 6 dB for command links [70].

Table 6.11: Communication subsystem link budget summary.

Parameter	**Unit**	**Aerobot–Orbiter Uplink**	**Orbiter–Aerobot Downlink**	**Earth–Orbiter Uplink**	**Orbiter–Earth Downlink**
Frequency and transmitter					
Frequency	MHz / GHz	390 MHz	401 MHz	7.175 GHz	8.425 GHz
Transmitter type	–	Aerobot UHF transceiver	UST-Lite UHF module	ESTRACK ground station	UST-Lite X-band module + PA
Transmitter antenna type	–	Helical-ring antenna	Moderate-gain UHF antenna	ESTRACK dish	High-gain parabolic dish
Transmitter antenna gain	dBi	5.09	11.80	65.81	34.38
Transmitter RF power, P_t	dBW	4.71	8.45	43.01	11.85
Transmitter line loss	dB	0.50	0.50	1.00	1.00
Backoff / implementation loss at transmitter	dB	0.00	0.00	0.00	0.00
EIRP	dBW	9.30	19.75	107.82	45.23
Propagation path					
Propagation range	km	43 000	43 000	261 000 000	261 000 000
Free-space path loss	dB	176.93	177.17	277.89	279.28
Atmospheric / ionospheric losses	dB	2.50	2.50	0.50	0.50
Scintillation / fade margin	dB	2.00	2.00	0.00	0.00
Pointing / pattern loss	dB	2.50	1.50	0.70	0.70
Polarization loss	dB	0.00	0.00	0.20	0.20
Combined path loss, L_{comb}	dB	183.93	183.17	279.29	280.68
Receiver					
Receiver type	–	UST-Lite UHF module	Aerobot UHF transceiver	UST-Lite X-band module	ESTRACK ground station
Receiver antenna type	–	Moderate-gain UHF antenna	Helical-ring antenna	High-gain parabolic dish	ESTRACK dish
Receiver antenna gain	dBi	11.80	5.09	32.99	67.20
Receiver line loss	dB	0.50	0.50	1.00	0.30
Received carrier power, C	dBW	-163.33	-158.83	-139.48	-168.55
System noise temperature, T_s	K	700.00	300.00	150.00	25.00
System noise temperature, $10\log_{10}(T_s)$	dB-K	28.45	24.77	21.76	13.98
Receiver G/T	dB/K	-17.15	-20.18	10.23	52.92
Receiver C/N_0	dB-Hz	36.82	45.00	67.36	46.07
Data and link performance					
Data rate, R_b	bit/s	1500	500	1500	10000
Data rate, $10\log_{10}(R_b)$	dB-Hz	31.76	26.99	31.76	40.00
Modulation	–	MSK	MSK	BPSK	BPSK
Code type	–	Turbo	Convolutional	Convolutional	Turbo
Code rate, ρ	–	0.50	0.50	0.50	0.50
Target BER	–	7×10^{-7}	7×10^{-7}	3×10^{-7}	3×10^{-7}
Roll-off factor, α	–	0.35	0.35	0.35	0.35
Occupied bandwidth	Hz	4050	1350	4050	27000
Available E_b/N_0	dB	5.06	18.01	35.60	6.07
Uncoded required E_b/N_0	dB	10.66	10.66	10.95	10.95
Coding gain	dB	9.60	5.80	5.80	9.60
Modem implementation loss	dB	1.00	1.00	1.00	1.00
Required E_b/N_0	dB	2.06	5.86	6.15	2.35
Link margin	dB	3.00	12.15	29.44	3.72

Furthermore, the final mass and power budget and the communication block diagram are shown in Table 6.12 and Figure 6.16, respectively. The coaxial cable mass is estimated from space-grade microwave coaxial cable mass per metre and the expected harness length [71], while the coaxial switch mass is based on a space-qualified latching RF switch [72].

Table 6.12: Aerobot UHF communication subsystem mass and power budget

Mass item	**Dimensions / description**	**Mass [g]**	**Margin [%]**	**Mass after margin [g]**
GAUSS High Power UHF Radio	$75\times31.5\times12.5$ mm	37.0	5	38.9
Two two-plate HRA antennas	$2\times(\varnothing 88\times22$ mm)	120.0	10	132.0
Coaxial cables	Short UHF RF cable runs and connectors	35.0	10	38.5
CTS switch	RF switching hardware for antenna selection	45.0	10	49.5
Total mass	–	**237.0**	–	**258.9**

Mass item	Dimensions / description	Mass [g]	Margin [%]	Mass after margin [g]
Power mode / item	**Description**	**Power [W]**		
Required RF output power	Worst-case link-budget value	2.96		
Receive mode	Transceiver receiving only	0.22		
Transmit mode	Estimated maximum operational transmit mode	6.30		
Transmit + receive mode	Simultaneous transmit and receive	6.52		

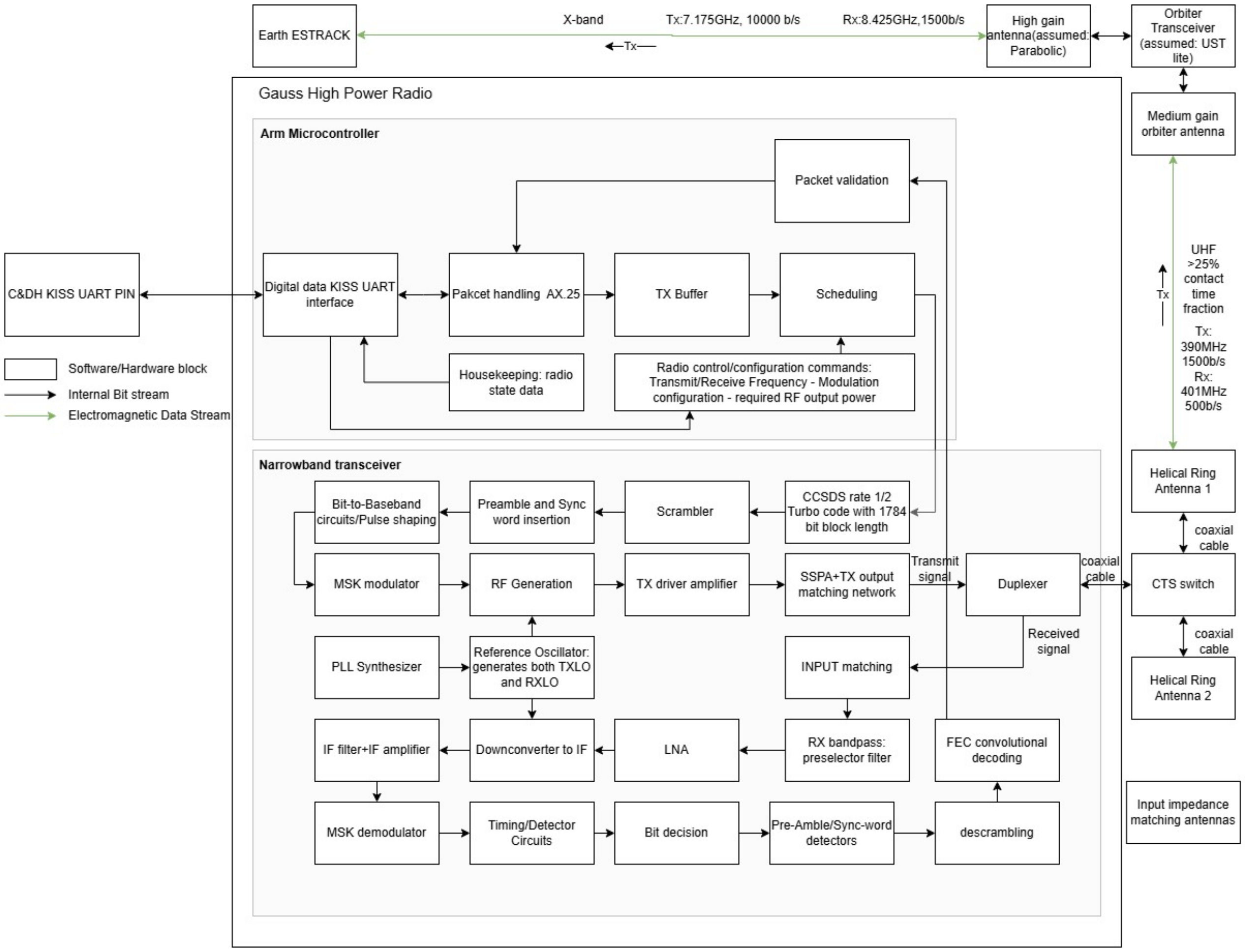

Figure 6.16: Communication flow diagram

6.4.6. Communications Verification and Validation

The communication link-budget tool is verified by comparing its outputs against independent hand calculations for free-space path loss, received power, noise level, and link margin, with additional sensitivity checks on transmitter power, antenna gain, propagation losses, and data rate to support REQ-COM-04. REQ-COM-01 and REQ-COM-02 are verified through representative transceiver tests under worst-case attenuation, where the achieved data rate, packet success rate, and bit error rate are measured against the required communication performance. REQ-COM-03 is verified by inspection of the selected frequency bands, modulation, coding scheme, data interface, and ESTRACK-compatible relay architecture. REQ-COM-05 is verified through antenna radiation-pattern measurements, RF-chain loss measurements, orbiter-pass coverage simulations, and environmental tests of the exposed antenna and cable interfaces. Validation is performed using mission-level relay scenarios with a representative aerobot–orbiter–Earth communication chain. The link-budget model itself is partially validated by comparison with independent references and can be planned for full experimental validation using representative UHF/X-band radios, attenuators or a channel emulator, ground-segment simulators, and antenna radiation-pattern measurements once representative RF hardware is available.

6.5. Electrical Power Subsystem

The Electrical Power Subsystem (EPS) generates, stores, conditions, and distributes electrical power to all aerobot subsystems throughout the five-year mission at the nominal 56 km float altitude. The Venus cloud-layer environment drives the design in four ways: the super-rotating aerobot experiences a worst case (equator) day–night cycle of roughly eight Earth days, requiring about 96 h of autonomous night-time operation on stored energy; the cloud deck attenuates and reshapes the available sunlight; the ambient temperature of approximately 59 °C at 56 km degrades photovoltaic conversion; and the sulfuric acid aerosol requires chemically inert protection of all exposed surfaces. This chapter presents the subsystem requirements (Section 6.5.1), the power budget (Section 6.5.2), the solar array design and sizing (Section 6.5.3), the energy storage design (Section 6.5.4), power management and distribution (Section 6.5.5), the subsystem mass budget (Section 6.5.6), verification and validation (Section 6.5.7), and a sensitivity analysis (Section 6.5.8).

6.5.1. Functional Analysis and Requirements

The EPS performs four functions: power generation by photovoltaic conversion during the day arc, energy storage for the night arc and contingencies, power conditioning and regulation, and protected distribution. From the mission requirements and the environmental analysis, the driving requirements of Table 6.13 are derived.

Table 6.13: Driving EPS requirements.

Identifier	Requirement
VISTA-EPS-01	The EPS shall deliver a peak power of at least 301.2 W (incl. margin) in Nominal Day mode.
VISTA-EPS-02	The EPS shall deliver an orbit-average power of at least 240.8 W over the 96 h day arc (226.9 W average day load plus 13.9 W battery recharge).
VISTA-EPS-03	The EPS shall store at least 1 200.5 Wh of usable energy to sustain Nominal Night mode (12.5 W average, incl. margin) for 96 h.
VISTA-EPS-04	The battery depth of discharge shall not exceed 40 % during a nominal night arc.
VISTA-EPS-05	The EPS shall sustain Survival mode (0.5 W) from stored energy, independent of solar availability.
VISTA-EPS-06	The EPS shall meet all power requirements at end of life, after five years at the 56 km float altitude.
VISTA-EPS-07	All externally exposed EPS surfaces shall withstand sulfuric acid aerosol exposure within the budgeted coating loss.
VISTA-EPS-08	EPS components shall operate within their allowable temperature ranges (battery −20 to +40 °C, PCDU −30 to +60 °C, fuses −55 to +125 °C; array −150 to +100 °C).
VISTA-EPS-09	The EPS shall protect the distribution network against overcurrent faults by fusing on all primary lines.

6.5.2. Power Budget

The power budget is maintained in the Power Equipment List (PEL), which assigns to every component a power draw, a maturity-based design margin, and a duty cycle in each of the five operational modes. Margins follow the maturity classification of the master equipment list, from 5 % for flight-qualified (class A) components up to 20 % for early estimates. Table 6.14 summarises the peak and expected-average power per mode; Table 6.15 gives the subsystem breakdown of the sizing case, Nominal Day. For the full/complete PEL, please refer to [73].

Table 6.14: Power summary by operational mode (from the PEL).

Mode	Peak [W]	Peak w/ margin [W]	Avg. [W]	Avg. w/ margin [W]
Commissioning	219.0	238.9	218.3	238.2
Nominal Day	277.3	301.2	209.8	226.9
Nominal Night	16.6	17.5	11.9	12.5
Safe mode	0.5	0.5	0.5	0.5

The ISRU gas-processing unit dominates the day-time demand: its pump/compressor alone draws 142.4 W with margin, 47 % of the mode peak. The night load is deliberately minimal, retaining only the on-board

Table 6.15: Nominal Day power breakdown per subsystem (incl. margins).

Subsystem	**Power [W]**	**Share [%]**
ISRU (gas processing and altitude control)	171.3	56.9
Payload	99.9	33.2
Battery recharge	13.9	4.6
Communications	6.6	2.2
Environmental protection	5.0	1.7
ADCS	3.7	1.2
Structures (tether instrumentation)	0.5	0.2
CDHS	0.3	0.1
Total	**301.2**	**100**

computer, the IMU, duty-cycled communications, and the low-power atmospheric instruments (temperature sensors, anemometer, barometers, pyrgeometer), so that the stored-energy requirement stays compatible with a battery of reasonable mass; ISRU and the high-power spectrometers are suspended at night.

display the power demand and power available over a 96 hour Venus day and a 96 hour Venus night. Components are turned ON/OFF every hour based on a random draw with a probability equivalent to their duty cycle. Components that need to function simultaneously are switched ON/OFF at the same time.

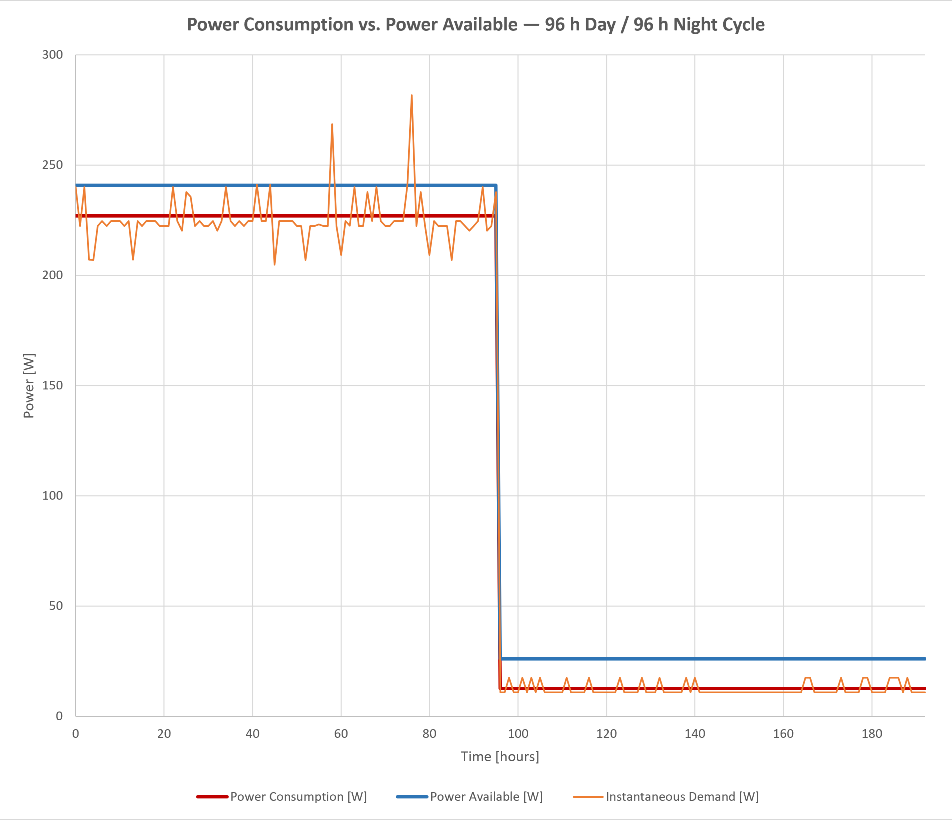

Figure 6.17: Power timeline

6.5.3. Solar Power Generation

Solar Environment at Float Altitude

The available flux is obtained by scaling the ASTM E-490 AM0 reference spectrum to the Venus orbit, where the exo-atmospheric solar constant is 2 600 W/m^2, a factor 1.90 above the terrestrial value, and attenuating it through the upper cloud deck [33]. Wavelength-dependent transmission ratios I/I_0 for 45–65 km, taken from in situ Venus flux measurements, are applied to the scaled spectrum in 25 nm bands from 300 to 1 100 nm

[74]. The attenuation is strongly wavelength-dependent, with the near-infrared suppressed more than the visible. At the nominal 56 km altitude the broadband net irradiance at local noon is $860\,\mathrm{W/m^2}$, about 33 % of the exo-atmospheric value; the cloud deck both absorbs and back-scatters the remainder, with the strongest attenuation in the near-infrared [74].

Cell Technology Selection

Triple-junction $GaInP_2/GaAs/Ge$, dual-junction, and single-junction GaAs cells were compared. Because the cloud deck reshapes the spectrum, the comparison cannot use AM0 efficiencies alone: in a series-connected multi-junction stack the subcell currents must remain matched, and preferential attenuation penalises the limiting junction [74]. A bandgap-cutoff quantum-efficiency model integrates the photon-weighted irradiance over each junction band ($GaInP_2$: 300–680 nm, GaAs: 680–880 nm, Ge: 880–1 100 nm) and identifies the current-limiting junction [74]. The middle GaAs junction limits the stack throughout the float band. The triple-junction cell retains the highest effective efficiency at and above the float altitude and has the strongest flight heritage. Thus, a triple-junction solar cell with spaceflight heritage is selected, such as the Spectrolab XTJ Prime cell (29.5 % at 28 °C, AM0) [35].

Effective Efficiency

Cell efficiency is corrected from the 28 °C datasheet condition to the float-altitude temperature using the maximum-power-point temperature coefficients, which give a normalised power sensitivity of −0.24 %/°C. At the 56 km ambient temperature of 19 °C,

$$\eta(T) = \eta_{28}\left[1 + \frac{1}{P_0}\frac{\mathrm{d}P}{\mathrm{d}T}(T - 28)\right] = 0.295\,[1 + (-0.0024)(59 - 28)] = 27.3\,\%. \tag{6.7}$$

The multi-junction current-matching penalty is captured separately by a spectral-mismatch factor M, defined as the limiting-junction current under the Venus spectrum relative to the exo-atmospheric spectrum. At 56 km, $M = 0.943$, so the reconciled effective efficiency is

$$\eta_{\mathrm{eff}} = \eta(T) \cdot M = 0.273 \times 0.943 = 25.8\,\%. \tag{6.8}$$

This separation is important and is revisited in Section 6.5.7: the atmospheric attenuation is carried by the net-flux term, the temperature loss by $\eta(T)$, and the spectral mismatch by M, so that each effect is applied exactly once.

Environmental Coating and Lifetime

The sulfuric acid aerosol requires a protective coating; Teflon FEP, Parylene, and coverglass were down-selected as chemically compatible candidates, and Parylene is baselined on the strength of a demonstration (TRL 5) in which a coated panel survived 96 hours of 96 % H_2SO_4 aerosol with no corrosion, at a measured 5 % transmission penalty [75].

The 96-hour immersion test in 96% H_2SO_4 [75] establishes survivability but not the five-year lifetime, so the gap is treated as a qualification activity rather than an assumption. The residual risk is bounded on two grounds. First, the demonstration over-stresses the chemical environment, using full-strength liquid immersion against the dilute sulfuric-acid aerosol and vapour actually present at 56 km. Second, the attack mechanism is benign: Parylene F is chemically inert to non-oxidising sulfuric acid, exhibiting only minor, largely reversible swelling rather than corrosion [76], so no fast pathway to failure exists. The remaining uncertainty—the combined long-duration action of acid, ultraviolet, and the 59 °C float temperature—is addressed by an accelerated combined-environment life test, in which coated coupons and a witness cell are exposed to elevated-temperature sulfuric-acid aerosol under representative ultraviolet, with periodic transmission and I–V measurement, run to beyond five mission-years of Arrhenius-equivalent dose with margin in order to extract a degradation rate. Flight witness coupons read against a reference cell then validate that ground model in situ, so the 5 %/yr coating-loss budget can be confirmed or revised during operations.

For lifetime degradation, the generic 5 %/yr inherent-degradation envelope of [65] is conservative for this case: the selected XTJ Prime cell retains 94 % of its maximum power after a 1×10^{14} 1 MeV e^-/cm^2 fluence (Spectrolab's 10-year LEO benchmark) [35], i.e. below 1 %/yr from radiation, and single-junction GaAs cells retain over 90 % at LEO-typical fluences. The 56 km float environment, shielded by ~50 km of dense CO_2 and free of trapped-particle belts, is markedly more benign than LEO for fluence degradation. A 3 %/yr annual degradation is therefore adopted as a conservative lumped factor covering radiation together with ultraviolet and acid aging of the coating, giving an end-of-life retention over the five-year mission of

$$L_d = (1 - 0.03)^5 = 0.86. \tag{6.9}$$

Daylight-Average Power and Array Sizing

Because the aerobot circumnavigates Venus with the super-rotating cloud layer and Venus has a negligible obliquity of 2.6°, the solar zenith angle (SZA) sweeps from 0° to 90° approximately linearly in time over the 96 h day arc. The daylight-average power therefore follows from a time-weighted (trapezoidal) integration of the SZA-dependent net flux. Applying the temperature-corrected efficiency of Equation (6.7) gives a noon power density of $234.8\,\mathrm{W/m^2}$ and, with a shape factor of 0.578, a daylight-average of

$$\bar{P}_{\mathrm{BOL}} = 135.8\ \mathrm{W/m^2}. \tag{6.10}$$

Including the coating transmission ($\eta_{\mathrm{coat}} = 0.95$) and the end-of-life factor of Equation (6.9), the deliverable end-of-life density is $\bar{P}_{\mathrm{EOL}} = 135.8 \times 0.95 \times 0.86 = 110.8\,\mathrm{W/m^2}$. With the day-arc requirement of $P_{\mathrm{req}} = 240.8\,\mathrm{W}$ (Section 6.5.2), the required active cell area is

$$A_{\mathrm{req}} = \frac{P_{\mathrm{req}}}{\bar{P}_{\mathrm{EOL}}} = \frac{240.8}{110.8} = 2.17\ \mathrm{m^2}. \tag{6.11}$$

The circumferential part of the cylindrical gondola body provides $0.4555\,\mathrm{m^2}$ of mounting area (at 80 % placement efficiency); the remaining $\sim 1.8\,\mathrm{m^2}$ is provided by fixed deployable "skirt" panels, for a total available area of $2.2\,\mathrm{m^2}$. The $2.17\,\mathrm{m^2}$ requirement is therefore met within the available area. Applying the spectral-mismatch factor of Equation (6.8) as well (the fully reconciled basis) raises the requirement to $2.30\,\mathrm{m^2}$; this is retained as the conservative bound, and concentrating ISRU and high-power science operations near local noon, where the available density approaches its $234.8\,\mathrm{W/m^2}$ peak, is identified as a contingency that recovers the difference without enlarging the array.

6.5.4. Energy Storage

Energy storage was traded between high-specific-energy lithium-ion cells, a proton-exchange-membrane regenerative fuel cell (RFC), and a unitised regenerative fuel cell (URFC). At the multi-kilowatt-hour scale required here the mass advantage of regenerative fuel cells does not materialise at acceptable technology readiness, while lithium-ion offers flight heritage, simple thermal integration inside the gondola, and high round-trip efficiency; lithium-ion is baselined [17].

The battery is sized by the night-arc energy balance of Table 6.16. The Nominal Night average load with margin is 12.5 W over 96 h, requiring 1 200.5 Wh. With an installed capacity of 2 500 Wh the depth of discharge is 48.0 %, appropriate for the roughly 230 charge–discharge cycles accumulated over five years of eight-day diurnal cycling, and the configuration sustains night loads up to 26 W before full discharge. Recharging the night-arc energy through a 90 % round-trip efficiency requires 1 333.9 Wh over the following day arc, i.e. an average charge power of 13.9 W, carried in the Nominal Day budget. The battery, which is referenced from [34], comprises two units of five cells (1.6 kg per cell, 16.0 kg total, 187.5 Wh/kg at pack level), mounted inside the gondola within the −20 to +40 °C allowable range; the two-unit split provides graceful degradation, with all possible modes being sustainable even if one of the two batteries fails.

Table 6.16: Night-arc energy balance and battery sizing.

Parameter	Value
Night duration	96 h
Average night power (incl. margin)	12.5 W
Energy required over night	1 200.5 Wh
Installed capacity	2 500 Wh
Depth of discharge	48.0 %
Maximum sustainable night load	26 W
Round-trip charge efficiency	90 %
Recharge energy from array	1 333.9 Wh
Average recharge power over day arc	13.9 W
Battery mass (2 units × 5 cells, incl. margin)	17.6 kg

6.5.5. Power Management and Distribution

Power conditioning and distribution is performed by a Starbuck Mini-MCC unit (AAC Clyde Space), which provides maximum-power-point tracking of the array, battery charge regulation, and switched, current-limited distribution on a 28 V bus, and is qualified for 5–7-year missions. All primary lines are additionally protected by fuses (two units) per requirement VISTA-EPS-09. The harness (3.24 kg) connects the gondola-internal loads and the distributed sensors along the suspension cables and the 75 m tether, using 28 AWG aluminium power runs and 30 AWG data runs helically wrapped along the tether with a 7.3 % length overhead. The dominant remote loads are the four tether-mounted barometers; the ohmic analysis yields 0.07 W of line loss against 0.40 W of delivered instrument power, accounted for in the structures line of the budget.

6.5.6. Mass Budget

Table 6.17 summarises the EPS mass with margins, as carried in the master equipment list. The solar array mass is consistent with the 2.17 m^2 sizing of Equation (6.11).

Table 6.17: EPS mass budget, including margins (from the MEL).

Element	**Mass [kg]**
Solar array (XTJ Prime CIC assembly)	1.90
Parylene coating	0.284
PCDU (Starbuck Mini-MCC)	0.44
Harness	3.24
Battery (2 units × 5 cells)	17.60
Fuses (2×)	0.34
Total EPS	**23.813**

6.5.7. Verification and Validation

The models were verified and validated at three levels. First, the spectral attenuation model was checked against the published in situ flux profiles from which the I/I_0 curves were digitised, reproducing the source broadband irradiance within the digitisation accuracy. Second, the photovoltaic performance model was reconciled. An earlier formulation evaluated the array two ways that disagreed: an SZA method that applied the temperature-corrected efficiency to the measured net flux, and a spectral method that applied a combined current factor to the full solar constant. The discrepancy was traced to a double-counting of atmospheric attenuation, which appears both in the measured net flux and in the spectral current factor. The reconciled model of Equations (6.7)–(6.8) resolves this by applying attenuation once (in the net flux), temperature once (in $\eta(T)$), and the spectral-shape mismatch once (in $M = 0.943$). At 55 km the reconciled noon density of 175 W/m^2 falls between the SZA estimate (186 W/m^2) and the erroneous double-counted spectral value (108 W/m^2), confirming the correction. Third, the energy budget was verified by an automated balance check: the night-arc discharge of 1 200.5 Wh stays within the 48 % depth-of-discharge limit, the maximum sustainable night load (26 W) exceeds the budgeted load by a factor 1.87, and the day-arc recharge is feasible within the array average power, confirming closure of the diurnal cycle. Mode totals were independently re-summed, reproducing the 301.2 W Nominal Day peak.

6.5.8. Sensitivity Analysis

The available solar power is by far most sensitive to float altitude, so this dependence was quantified across the full 50–60 km band rather than at the nominal point alone. Figure 6.18 shows the resulting daylight-average power density, which rises from 42 W/m^2 at 50 km to 261 W/m^2 at 60 km — a factor of six over the band, and 136 W/m^2 at the nominal 56 km.

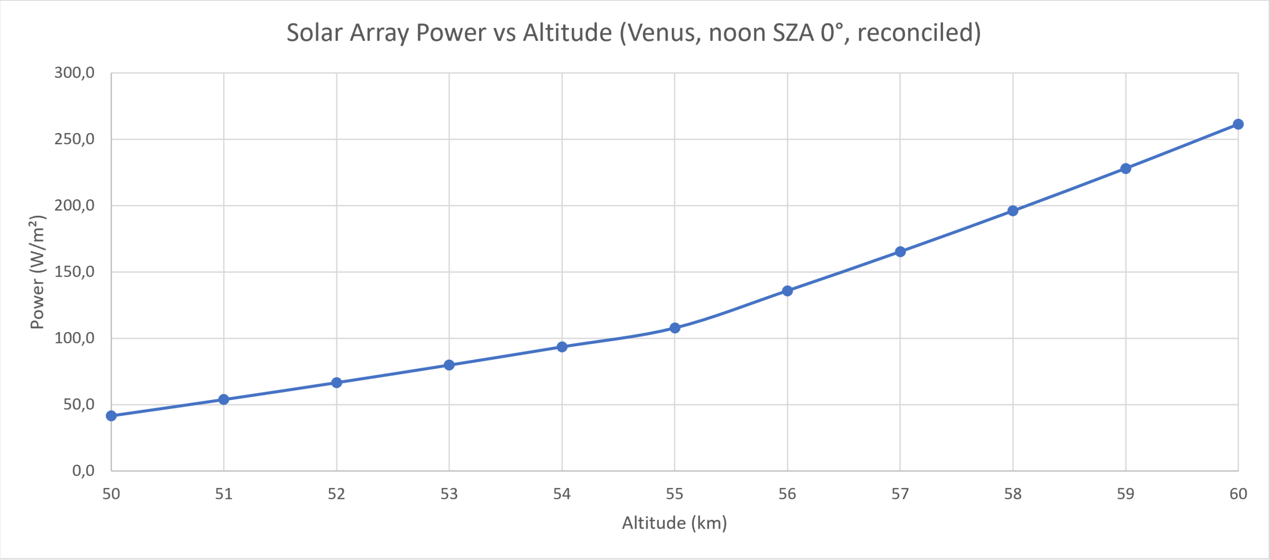

Figure 6.18: Daylight-average solar power density versus float altitude for the triple-junction XTJ Prime cell (before coating and end-of-life losses, which scale every point by the same factor 0.95 × 0.86). Each point is the product of the altitude-dependent net flux, the temperature-corrected efficiency at that altitude, and the 0.578 daylight shape factor.

The steep, slightly convex rise has a clear physical origin: altitude acts on the power through two effects that reinforce one another. Climbing reduces the depth of cloud above the aerobot, so less sunlight is attenuated and the net flux increases; and the ambient temperature falls, so the cell efficiency $\eta(T)$ improves. Because both move in the same direction, their product grows faster than either alone, which is why the curve accelerates toward higher altitudes.

The quantification follows directly from the sizing model of Section 6.5.3: at each altitude the daylight-average power density is the noon net flux multiplied by the temperature-corrected efficiency $\eta(T)$ and by the daylight shape factor of 0.578. Table 6.18 shows the decomposition at representative altitudes, making the two compounding inputs explicit.

Table 6.18: Decomposition of the daylight-average power density by altitude.

Altitude [km]	Noon net flux [W/m^2]	Temp. [°C]	$\eta(T)$ [%]	Daylight-avg. [W/m^2]
50	300	107	24.0	42
55	700	69	26.6	108
56	860	59	27.3	136
57	1020	49	28.0	165
60	1500	19	30.1	261

Near the nominal altitude the local sensitivity is roughly +22 % per kilometre climbed and −21 % per kilometre lost. Because the array is sized to meet the full day-arc requirement at 56 km, sustained operation below this forces a proportional reduction of the discretionary loads — chiefly ISRU and the high-power science instruments — while the low-power night and survival load set remains supportable across the whole band; above nominal, the surplus is available for faster recharge or expanded operations. Altitude control is therefore as much a power-system function as an aerodynamic one.

Three further sensitivities are second-order by comparison. The temperature coefficient of −0.24 %/°C implies only a ∓4.8 % power change for a ±20 °C excursion about the nominal 59 °C. The end-of-life assumption shifts the required area from 2.17 m^2 at 3 %/yr to 2.41 m^2 at 5 %/yr. The spectral-mismatch factor moves the requirement from 2.17 m^2 (temperature only) to 2.30 m^2 (fully reconciled), a 6 % effect that cell-level testing under a Venus-representative spectrum would resolve.

6.5.9. Electrical Block Diagram

The electrical block diagram that visualized the power subsystem is presented in Figure 6.19. The abbreviations in the diagram represent the following:

- **MPPT**: Maximum Power Point Tracking
- **BCDR**: Battery Charge and Discharge Regulator
- **LCL**: Latching Current Limiter
- **HLCL**: Heater Latching Current Limiter
- **RLCL**: Re-triggerable Latching Current Limiter

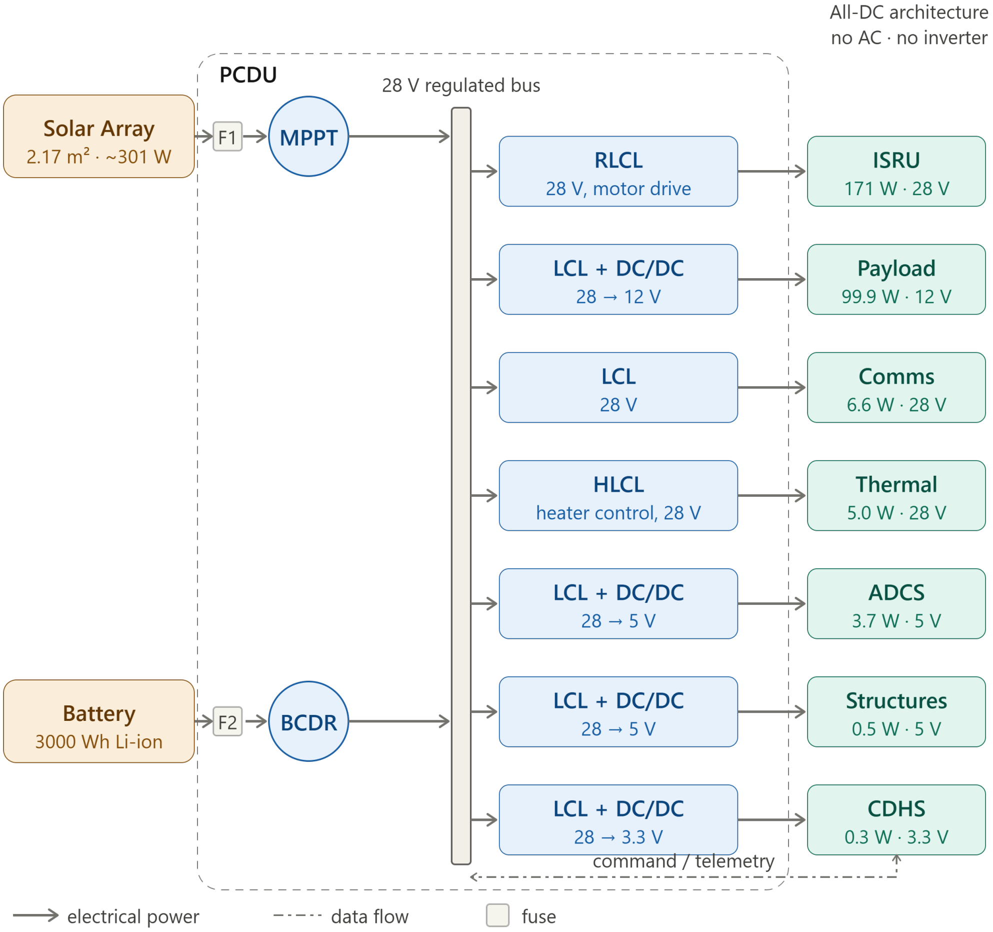

Figure 6.19: Electrical Block Diagram.

Note, before the electrical load reaches each respective subsystem, the current limiters: LCL, RLCL, and HLCL, regulate that the current of the electrical flow is safe and optimal for the users.

6.5.10. Conclusions and Recommendations

The EPS closes the diurnal energy cycle of the VISTA aerobot at 56 km with a 23.813 kg subsystem built around triple-junction XTJ Prime cells with a Parylene acid-protection coating, a 2 500 Wh lithium-ion battery at 48 % depth of discharge over the 96 h night arc, and a flight-heritage PCDU with fused distribution. The 2.17 m^2 array is met within the 2.2 m^2 of body-mounted and deployable area. Three activities are recommended for the next phase: cell-level testing under a Venus-representative filtered spectrum to confirm the spectral-mismatch factor and collapse the 2.17–2.30 m^2 spread; characterisation of Parylene transmission degradation under combined ultraviolet and sulfuric-acid exposure beyond the 96 h demonstration to substantiate the five-year lifetime; and confirmation of the deployable-panel configuration and its acid protection, with noon-centred load scheduling retained as a power-margin contingency.

6.6. Attitude Determination and Control System

The VISTA aerobot is a suspended balloon–gondola system, not a rigid spacecraft. Its ADCS is therefore not designed as a standard three-axis pointing system, but as a subsystem for determining, managing, and monitoring the dynamic state of the configuration. Since no subsystem requires precise pointing, the main objective is to keep the gondola motion bounded, observable, and compatible with the rest of the system. This applies to the scientific payload (chapter 5), the communication link, which uses omnidirectional antennas (section 6.4), and the power subsystem (section 6.5), since the diffuse flux in the Venusian cloud layer removes the need for solar-panel pointing. A three-axis active control system is therefore not selected, as it would add mass, power demand, and complexity without providing a clear mission benefit. The ADCS scope is limited to three functions: determining the gondola attitude, shaping the passive dynamic behaviour of the flight configuration, and monitoring this behaviour during the mission. Global navigation, altitude control, and trajectory reconstruction remain outside the ADCS scope and are covered by GNS section 6.8.

Three aspects have changed since the midterm design, following further analysis and expert consultation, including input from Colin Wilson. First, the former suspension-cable constraint, $L_{\text{cable}} \geq 10\text{m}$, introduced to avoid solar-panel shadowing, has been removed, as the shadowing is not significant due to the Venusian cloud scattering. Second, the communications subsystem now imposes a visibility constraint for each antenna, $\theta \geq 80^\circ$, which drives the cable length L_{cable}. Third, the coupling between ADCS and the instrument design has been refined through the detailed seismology configuration described in section 5.3.

6.6.1. Constraints and Interdependencies

The ADCS configuration is defined by the subsystem interfaces that depend on the dynamic behaviour of the aerobot. This section sets the resulting design-space boundaries. Within these constraints, the design objectives are to minimise mass, power, cost, and also complexity, in line with the reliability requirement in section 10.4.

The seismic payload imposes the most demanding dynamic constraint. The fundamental structural mode of the tether must remain above the measurement band, with $f_1 \geq 0.06\text{Hz}$, so that structural contamination can be removed by low-pass filtering (section 5.3). The wind sensor also requires knowledge of the platform motion. Since the IMU is placed at the gondola, this motion is measured directly and can be subtracted from the wind signal. The limitation is that IMU noise and drift propagate into the corrected wind estimate, so the gondola dynamic knowledge must remain reliable. Therefore, it is crucial to minimise the uncertainties of the dynamic configuration.

The communications subsystem drives the suspension geometry. Each antenna must maintain an angular visibility of $\theta \geq 80^\circ$, to prevent obstruction of the radio signal by the balloon, as one of its components is aluminium (chapter 7). The only obstruction is the balloon envelope, so an antenna placed at gondola radius R_g must see past the balloon. The grazing-line construction in figure 6.20 gives the minimum cable length as:

$$\tan\phi = \frac{\sin\theta}{R_b/R_g - \cos\theta}, \qquad L_{\min} = \frac{R_g}{\sin\phi} - R_b, \tag{6.12}$$

where θ is the angle at the balloon centre between the local vertical and the antenna, R_b is the balloon radius, and the cable length is measured from the bottom of the envelope to the gondola. For the current envelope, with $R_b = 5.5\text{m}$ and $R_g = 0.29\text{m}$, this gives $L_{\min} \approx 24.5\text{m}$. The minimum cable length selected $L_{cable} \geq 30\text{m}$ provides visibility up to 81.6°, accommodating tolerances for the visibility constraint.

Three additional couplings are relevant. The navigation subsystem uses the same inertial measurements to propagate the trajectory between orbiter contacts (section 6.8). The coupling with Structures (section 6.7) is bidirectional: the flight chain transfers oscillatory loads to the cables and attachment points, while the structural configuration sets the dynamic response through the gondola mass, moments of inertia, and attachment geometry. The dynamic behaviour also affects payload processing (section 6.3), as the corrections required by the wind sensor will be processed on board, to lower the load on the communication subsystem (section 6.4).

6.6.2. Attitude Determination Configuration

The sensor selection is unchanged from the midterm design and is summarised here. In the Venus float environment, classical attitude references are limited: star trackers, sun sensors, horizon sensors, and surface sensing are unreliable due to cloud scattering, while magnetic heading cannot be used because Venus has no reliable global magnetic field. The retained baseline is therefore a local inertial sensing approach based on a 6-axis IMU placed close to the gondola centre of gravity, avoiding the need for additional lever-arm corrections ($\omega \cdot r$) between the IMU and the gondola motion. The gyroscopes measure the angular rates associated with swing, yaw, spin, and torsional motion, while the accelerometers provide the three-axis accelerations used for

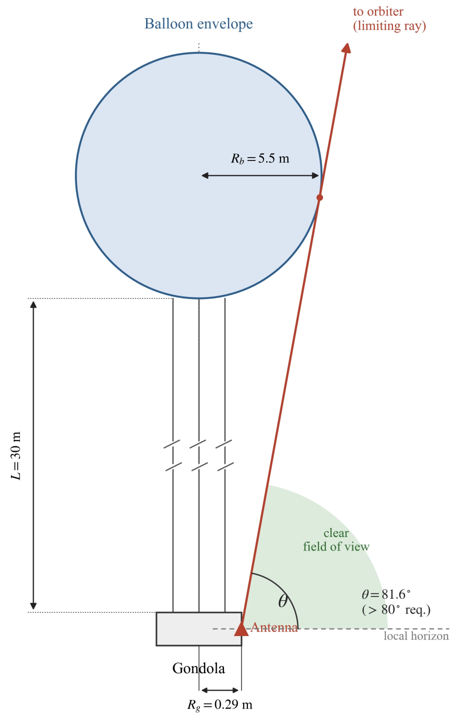

Figure 6.20: Antenna visibility geometry defining the minimum suspension-cable length. Schematic not to scale.

roll and pitch estimation relative to local gravity and for shock detection. Since the gyroscopes only propagate relative attitude and are subject to drift, periodic absolute references are required. Roll and pitch can be corrected using gravity during dynamically quiet windows, whereas yaw is corrected through the orbiter link, as described in subsubsection 6.6.2. The same IMU is shared with GNS, since both subsystems require continuous inertial-state information.

Absolute Yaw through Differential Carrier Phase

A MEMS-class gyroscope typically drifts by 1–10°/h [13]. Between orbiter contacts (section 6.8), the accumulated yaw error can reach several tens of degrees. Without an absolute reference, heading knowledge is therefore effectively lost between passes. The orbiter link is the only available absolute reference and is used for this purpose.

The method has flight heritage. Recovering heading from the carrier-phase difference between two antennas is the working principle of the GNSS compass [77, 78] and of classical phase-comparison direction finding. In the Venus context, the VEGA balloons were tracked through differential radio techniques [79], although only their position was recovered. The new element here is the onboard use of the technique for heading determination.

The position of the orbiter is available from the ephemeris, and during a pass, its carrier reaches the two gondola-mounted antennas with a small path difference that depends on the orientation of the antenna baseline. The measured phase difference is

$$\Delta\varphi = \frac{2\pi b}{\lambda} \sin\gamma \cos\alpha, \tag{6.13}$$

where b is the distance between the two antennas, λ is the carrier wavelength, γ is the angle between the line of sight and the local vertical, and α is the azimuth of the orbiter in the gondola body frame. This gives the orbiter azimuth relative to the gondola. Comparing this body-frame azimuth with the known sky azimuth gives the absolute yaw. The IMU prior resolves the $\pm\alpha$ ambiguity by choosing the value closer to the current IMU estimate, and the yaw is reset once per pass. Figure 6.21 visually shows these steps.

A feasibility analysis has been performed after consultations with expert Colin Wilson. Feasibility is governed by the ratio between antenna baseline and carrier wavelength. With antennas mounted on opposite sides of the gondola shell, $b \approx 0.58$m, and a UHF carrier wavelength of $\lambda \approx 0.75$m, the system operates at $b/\lambda \approx 0.75$. For realistic phase noise, a value of ±3° was chosen, while averaging over a contact pass reduces the per-pass estimate below one degree. In figure 6.22, three different geometries are assessed. For an antenna spacing $b = 0.08$m, the phase difference detected by the differential carrier phase is buried in noise and cannot be used

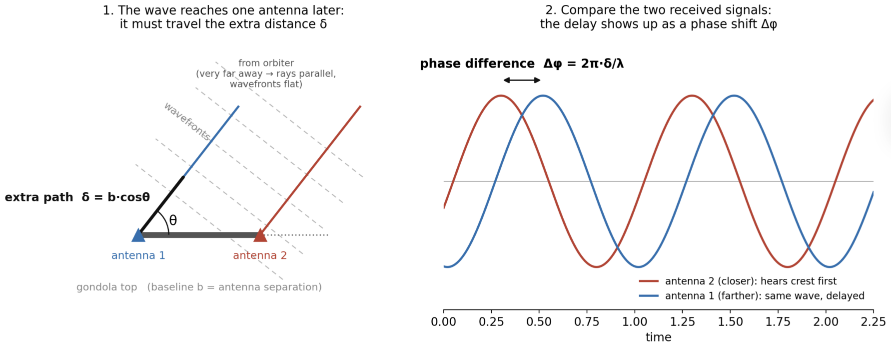

Figure 6.21: Working principle of the differential carrier-phase heading determination: path-difference geometry on the left and the resulting signals measured by the two antennas on the right.

to correct the yaw measurement. On the other hand, if the antenna spacing is too high (e.g. $b \geq 3$m), there is no unique solution for the yaw correction that can be used as the IMU absolute reference. The current VISTA configuration $b = 0.58$m (in the middle panel) is perfectly compatible with the differential yaw correction employed; hence, this method is feasible.

6.6.3. Dynamic Behaviour Methodology

The VISTA aerobot configuration has a complex dynamic behaviour, given by the connected flight chain between the balloon, suspension cables, gondola and the 75m scientific tether. In this analysis, it is modelled as a multi-body pendulum with a bifilar torsional mode: twisting the gondola relative to the balloon raises the suspended mass against gravity, so the cable bundle provides the restoring yaw torque, while the suspended masses set the pendulum modes. For this, a simplified numerical model, presented in [80], has been created, aligned with the methods of Kassarian et al. [81]. This models the balloon-cable-gondola structure as an N-pendulum system. This system has been analysed by dividing the cable and tether elements into multiple nodes, each with its own degrees of freedom: pendulum angle and torsional angle. An instantaneous snapshot of the dynamic configuration is illustrated in Figure 6.23.

The design space is defined by the cable length L_{cables} and count N_{cables}, the attachment radius $r_{attachment}$, the tether length L_{tether}, and the mass distribution. The constraints from section 6.6.1 bound this space from two sides: the seismic requirement $f_1 \geq 0.06,\text{Hz}$ sets a frequency constraint, while the antenna-visibility requirement sets a minimum length of $L \geq 30,\text{m}$. Within these bounds, the final configuration is selected using secondary criteria: mass, complexity, subsystem interfaces, and sensitivity of the modal frequencies to parameter uncertainty.

If left undamped, the flight chain dissipates little energy. Balloon-flight heritage reports modal damping ratios of order 10^{-3}, with documented swing–yaw coupling [81]. The EBEX mission also observed persistent torsional oscillation throughout flight after omitting a damper [82]. The baseline design therefore introduces passive damping, targeting a modal damping ratio of $\zeta \approx 0.005$, with an expected range of 0.003–0.01. This is approximately one order of magnitude above the natural damping level, decreasing the settling time and minimising the cumulative errors introduced by the disturbances.

The damping architecture is retained from the midterm design: passive, hybrid, and fluid-free. Pendulum damping is placed at the upper cable terminations, close to the effective pivot. Wire-rope inserts dissipate swing motion through strand friction, with component damping of 5–15% and TRL 9 [83, 84]. Torsional damping is placed at the gondola-side suspension interface, where a compact eddy-current rotary damper dissipates relative yaw motion without contact or wear, at TRL 8–9 [85]. The concept requires no operational power, is suitable for the long mission duration, and adds a ROM mass of 0.7kg with a single moving part.

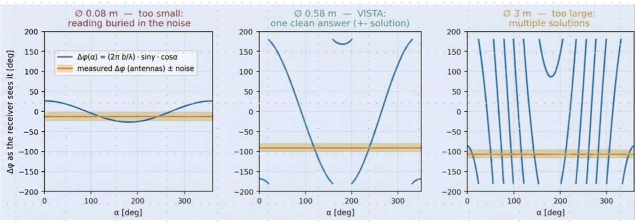

Figure 6.22: Phase difference $\Delta\phi(\alpha)$ (blue) vs. measured $\Delta\phi\pm$ noise (orange) for three gondola diameters. Too small ($b = 0.08m$): swing buried in noise. VISTA ($b = 0.58m, b/\lambda \approx 0.75$): one clean fix (± mirror). Too large ($b \geq 3m$): many ambiguous solutions.

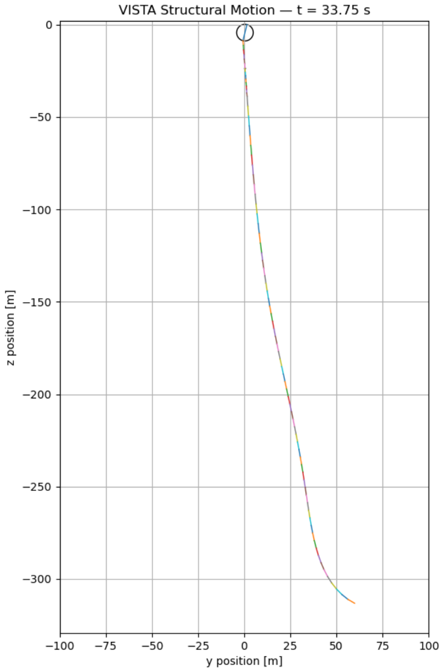

Figure 6.23: Dynamic simulation of the VISTA aerobot.

Both dampers are located at existing structural interfaces. The integration feasibility of the torsional damper was only assessed conceptually; therefore, it is crucial that further analysis is performed in the next phases.

The sensitivity analysis of the model shows that the lengths mainly control the time scale of the suspended system. Increasing L_{cable} and L_{tether} increases the dominant pendulum and torsional periods and reduces the yaw-rate response, but it also increases settling time, angular amplitudes, and the physical balloon–gondola separation. The number of cables N_{cables} has little effect on the global pendulum and torsional response, so its relevance is mainly structural: load sharing, redundancy, and deployment complexity. The attachment radius is the dominant torsional design variable. Increasing $r_{attachment}$ stiffens the torsional mode and reduces twist amplitude, but it also increases yaw-rate response and torsional interface demand. Moreover, the layout of the gondola has also been analysed. It was found that, for the same mass, a geometry with a greater mass moment of inertia (MMOI) is desirable, as it makes the design more resistant to disturbances. The values chosen for these design parameters follow the same reasoning as for the midterm design.

6.6.4. Final Configuration

The final ADCS configuration is summarised in table 6.19. The configuration satisfies the constraints from section 6.6.1, and was obtained by following the outlined design objectives. The 30m cables meet the antenna-visibility requirement with tolerance applied; the tether fundamental mode remains above the seismic measurement band with L_{tether} = 75m. The IMU supports both navigation propagation and payload motion compensation, and the interface loads are carried through the existing structure.

Table 6.19: ADCS baseline configuration.

Category	Item	Qty/Value	Mass	Power
Geometry	Cable length L_{cable}	30 m	see section 6.7	—
	Cable length L_{tether}	75 m	see section 6.7	—
	Number of cables N_{cables}	6	see section 6.7	—
	Attachment radius $r_{\text{attachment}}$	0.29 m	—	—
Sensing	Honeywell QA-3000 accel. [37]	3	~0.21 kg	~2 W
	Safran STIM300 gyro [38]	1	~0.06 kg	~1.5 W
Damping	Enidine WR/CR isolator [84]	6	~0.2 x 6 = 1.2 kg	0 W
	Oerlikon ECD-100 ECD [85]	1	~1.5 kg	0 W
	Mounting + margin	—	~0.7 kg	—
Total			**~2.97 kg**	**~3.5 W**

6.7. Structures and Mechanisms Subsystem

In this section, first the structural layout is given, in which various stiffeners are added to the original cylindrical shell design, After this, the structural stresses are given for the peak loads during entry, and the load type for the cables and tethers are explained. Consequently, the sizing methodology and results are given. Finally the overall mass budget is provided.

6.7.1. Structural Configuration

For the midterm design, the main shape of the gondola was concluded to be cylindrical. The main reason for this was radial symmetry, which allowed simplifications for the ADCS system. For this design phase a more detailed analysis was performed. This revealed that the cylindrical shell alone was insufficient. To avoid thin skin buckling, and meet maximum deformation requirements, additional stiffeners had to be introduced.

Structural Layout

As illustrated in the layout, the primary load path goes uniformly through the axial stiffeners to distribute compression loads. The circular ring frames are introduced to prevent cross-sectional ovalization from lateral entry loads. This optimization allows the thin-walled primary cylindrical wall to remain stable under peak deceleration conditions without buckling.

As mentioned, the main shell consists of a thin cylinder with two end caps. Additionally, several stiffeners were introduced, to withstand the highest load case. These consist of 6 axial stiffeners, spaced equally along the cylindrical shell wall, and 2 circular stiffeners, placed along the top and bottom lid. Furthermore, to diffuse the induced stresses along this primary structure, and prevent local deformation of the lids, several smaller lateral stiffeners were introduced along the top and bottom lids. An overview of this setup, excluding the top lid, is given in Figure 6.24.

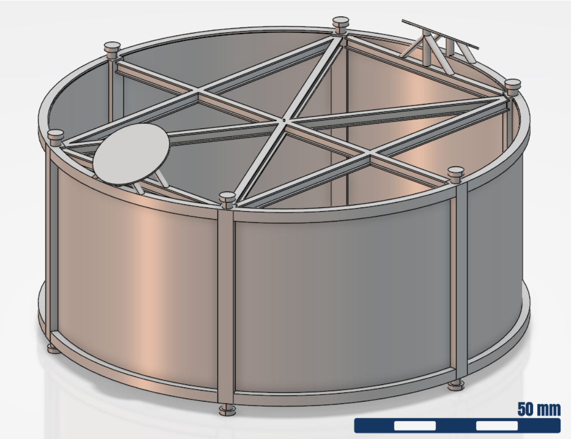

Figure 6.24: Overview of the final gondola structural layout, introducing various stiffeners and attachment points. The top lid has been removed for clarity.

Stiffeners

Since the highest load case has been assumed to be during entry of Venus, these peak loads will be axial. In order to achieve the most streamlined load path, it has been chosen that the deployment attachment points were placed on the top and bottom of each axial stiffener.

The most dominant stress modes for these axial stiffeners will be the axial compressive loads and lateral bending moments, introduced at the deployment attachment points. Since the bending moments will be applied across various angles, a simple rectangular cross-section beam design was chosen. For the circular stiffeners, its main function is to both distribute loads along the mentioned axial stiffeners, and to resist any torsional induced loads. For this reason, these stiffeners are also chosen to have a rectangular cross-section. Lastly, the lateral diffusion beams. Since the primary objective of these beams is to prevent local deformation of the end lids, these will be objected mostly to bending moments, and have been designed as I-beams.

Structural Interfaces

There are several attachment points connected to the gondola. The ones considered are those for the cables, the tether, and the deployment attachment points.

For both the cables and tether attachment points, a simple plate base was considered with a cable loop. For the cables, these base plates will be directly attached to the lateral stiffeners right under the top lid of the gondola. For the tether, this attachment point will be placed in the centre of the lower lid of the gondola, mounted to the bottom lateral beams. A model of these is given in Figure 6.25.

Aside from these, the structure was required to provide mounting points for the antenna's. These points needed to be spaced 180° apart, and point the antenna's outwards by 30° w.r.t. the horizontal axis. These also had to be placed 10 cm upwards, to avoid disturbance of the gondola structure in the signal.

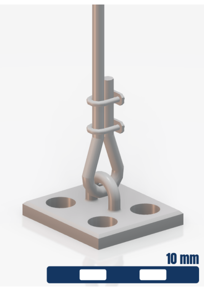

Figure 6.25: Cable and tether attachment point.

The attachment of the balloon structure to the cables was considered very briefly. It is suspected to be a circular structure, connected to the super pressure balloon by identical attachment points as for the gondola. The additional mass of this interface is included in the mass margin of the balloon envelope.

6.7.2. Structural Loads

The structural loads are considered in two separate phases. For the gondola shell and internal components, it is assumed that the peak stresses will be induced during Venus atmospheric entry, introduced at the deployment attachment points. For the cable and tether attachment points, the highest stresses will be induced by atmospheric gusts, while the structure is fully deployed.

Deployment Loads

For the structural loads of the gondola structure, during entry, the loads have been estimated to be 78.62 g in the axial direction. Considering a maximum entry misalignment of 6°, a 10% margin of 7.87 g was taken for the lateral loads.

Axial Loads

As mentioned, the primary load path of this phase will go uniformly through the axial stiffeners. For pure axial loads, these stiffeners will endure axial stresses (σ_{ax}) throughout the entire lengths, as well as shear stresses (τ_{max}) at the surfaces where the shell wall panels and lateral beams are attached.

Lateral Loads

When considering the lateral load cases, additional stresses occur. The 7.87 g lateral load induced cross-axis coupling. This introduces both out-of-plane and in-plane bending of the axial stiffeners. Furthermore, both end lids are subjected to out-of-plane bending stresses as well ($\sigma_{\text{lid,bending}}$). These are driven by their own weight plus the weight of attached instrumentation/system components.

Multi-axial Loads

Since the axial and circular stiffeners are subjected to multi-axial loading, the worst-case combination of stresses needs to be taken into account. For the axial stiffeners, this consists of peak axial compression and localized bending ($\sigma_{\text{stringer,comb}}$), alongside local shear stresses (τ_{max}). To predict this multi-axial yielding, Von Mises distortion energy criterion ($\sigma_{\text{von\_mises}}$) was implemented. For the circular stiffeners, Roark's formulas for circular rings were implemented to determine the peak combination of stresses ($\sigma_{\text{ring,total}}$) [86].

Buckling Stability

Furthermore, to ensure the stability of the thin cylindrical wall, four distinct geometric buckling modes were evaluated in accordance with NASA SP-8007 guidelines [87]. Local skin wrinkling ($\sigma_{\text{cr,skin}}$) was checked against the localized thin-plate threshold under peak deceleration compression (σ_{ax}), while global shell collapse ($\sigma_{\text{cr,global}}$) was monitored via the critical stiffened-shell threshold. Cross-sectional distortion from radial entry loads was assessed using the critical ring frame ovalization hoop buckling limit to safely resist the applied load. Finally, individual stringer column buckling was tracked using the localized critical Euler column buckling stress ($\sigma_{\text{cr,euler}}$) to ensure overall structural stability.

Cable and Tether Loads

For the cable and tether, the peak loads are assumed to occur while fully deployed. Since these are both flexible elements, only axial tension was considered. This tension consists of both the weight of the connected components, as well as their induced centrifugal forces from pendulum oscillations.

The entire balloon-cable-gondola-tether system can be evaluated as a multi-body pendulum. The cables experience tension driven by the static buoyancy of the balloon, counteracted by the suspended gondola mass. The tether will experience the tension dictated by the attached barometer weights. Aside from these static axial stresses, dynamic load spikes can be induced by wind gusts. Due to these gusts, the attached components will experience pendulum-like behaviour, as analysed in section 6.6. These induced dynamic loads were deemed outside the scope of this report, instead an extra safety margin was implemented.

6.7.3. Sizing Methodology

Sizing Approach

For the sizing of the gondola shell and stiffener thicknesses, a Python script was implemented [80]. The inputs of this script were ranges for each of these dimensions, as given in Table 6.20. Using these ranges, all possible combinations were considered by the code and structural analysis was done for each combination. Their stresses were compared to the maximum allowed stresses, and out of all viable options, the lightest one was selected.

Unlike for the wall and lid thicknesses of the cylinder, a minimum of 5 mm was chosen for the stiffener dimensions. This lower bound was chosen to avoid unrealistically slender stiffener geometries. Stiffeners with dimensions below this 5 mm, would be sensitive to local buckling, which was not considered in the analysis.

Table 6.20: Input parameters for the Python script, used for the gondola primary structure sizing.

Design Parameter	Symbol	Min	Max	Step	Unit
Cylinder Wall Thickness	t_{skin}	1.0	10.0	0.2	mm
Cylinder Lid Thickness	t_{lid}	1.0	10.0	0.2	mm
Axial Stiffener Width	w	5.0	25.0	0.5	mm
Ring Frame Depth	d	5.0	25.0	0.5	mm
Ring Frame Width	b	5.0	20.0	0.5	mm
Stiffener Count	N	6	10	1	-

Material Selection

For the gondola, a material trade-off was conducted using 2 material indices: the specific strength $M_1 = \sigma_y/\rho$, and the specific stiffness $M_2 = E/\rho$. Here σ_y is the yield strength, E is the Young's modulus and ρ is the material mass density. This first index is commonly used for lightweight aerospace structures, as it selects materials which have a relative high yield strength, compared to their mass density. The second index is mostly applicable for thin-walled designs which are prone to buckling failure. For the analysis, 3 commonly applied materials were considered [88]. These are given in Table 6.21 [89].

Table 6.21: Considered materials with their relevant material indices.

Material	**Density** [kg/m^3]	**Yield Strength** [MPa]	**Young's Modulus** [GPa]	M_1	M_2
Al 6061-T6	2700	276	69	0.102	0.0256
Al 7075-T6	2810	503	72	0.179	0.0256
Ti-6Al-4V	4430	880	114	0.199	0.0257

From these options, it can be seen that Ti-6Al-4V (grade 5 titanium) outperformed both aluminium alloys in terms of specific strength (M_1). For specific stiffness (M_2) however, the three considered materials give very similar results. However, material selection is not solely governed by these indices. Although titanium offers superior structural performance, it is both more expensive and difficult to manufacture compared to aluminium alloys. Consequently, the selection was narrowed down to the 2 aluminium alloys. While Al 7075-T6 gives a more favourable result for M_1, since these materials have comparable specific stiffness, implying similar buckling performance, and Al 6061-T6 has better corrosion resistance, the latter was chosen as final gondola material [90, 88]. Additionally, the entire gondola will also be covered by a thin Teflon film layer, to ensure corrosion resistance [91]. This thin layer will only add 0.0543 kg/m^2 to the overall structural mass.

Regarding the cables and tether, it was decided upon to choose a strong internal structural rope, with a corrosion-protective outer sleeve. For the structural part, a lightweight Vectran rope has been chosen (0.010 kg/m). Vectran exhibits a service temperature of up to 200 °C, low elongation under load, and very low creep, making it suitable for long-duration structural applications [92]. For the protective outer sleeve, a cross-linked fluoropolymer-based material was chosen. Similarly to the internal material, this polymer can be subjected to 200° C, it provides excellent corrosion resistance. However, this added protection comes at the cost of increased mass compared to the internal load-bearing fibre (0.0187 kg/m).

6.7.4. Sizing Results

Using the above methodology and chosen materials, the final dimensions were determined. An overview of these are given in Table 6.22.

These parameters resulted in a total structural mass of 14.4 kg. An overview of all mass contributions are given in Table 6.24. An overview of all stress states for these parameters is given in Table 6.23.

Fom this is can be concluded that the given geometry passes all stress requirements.

This design results in a stiffener count of $N = 6$. This given that the gondola will be attached to the balloon with 6 cables as well. Using this number of cables, the tilt angle in case of single-cable-failure can be found using:

$$\phi = \arctan\left(\frac{D}{H} \cdot \frac{1}{(N-1)}\right) = 22^\circ. \tag{6.14}$$

This value satisfies the requirement given, of maximum 25°.

Table 6.22: Final parameters for the gondola primary structure.

Design Parameter	**Symbol**	**Value**	**Unit**
Cylinder Diameter	D	0.58	m
Cylinder Height	H	0.25	m
Cylinder Wall Thickness	t_{skin}	3.0	mm
Cylinder Lid Thickness	t_{lid}	2.5	mm
Axial Stiffener Width	w	24.0	mm
Ring Frame Depth	d	24.0	mm
Ring Frame Width	b	19.0	mm
Stiffener Count	N	6	-

Table 6.23: Overview of the stress and geometric stability analysis of the gondola primary structure under peak entry load conditions.

Structural Failure Mode	**Symbol**	**Calculated Stress**	**SF**	**Allowable Limit**
Material Yielding Evaluations *(Requirement: Calculated Stress < Allowable Limit)*				
Peak Deceleration Compression	σ_{ax}	39.54 MPa	1.25	324.00 MPa
Radial Joint Interface Shear	τ_{max}	11.01 MPa	1.25	186.95 MPa
Stringer Edge Normal Interaction	$\sigma_{\text{stringer,comb}}$	248.56 MPa	1.25	324.00 MPa
Stringer Von Mises Distortion Energy	$\sigma_{\text{von\_mises}}$	249.29 MPa	1.25	324.00 MPa
Ring Frame Hoop & In-Plane Bending	$\sigma_{\text{ring,total}}$	116.48 MPa	1.25	324.00 MPa
Clamped Flat End Lid Bending	$\sigma_{\text{lid,bending}}$	114.78 MPa	1.25	324.00 MPa
Structural Failure Mode	**Symbol**	**Critical Capability**	**SF**	**Applied Load**
Geometric Instability / Buckling *(Requirement: Critical Capability > Applied Load)*				
Thin-Skin Local Wrinkling	$\sigma_{\text{cr,skin}}$	185.34 MPa	1.50	39.54 MPa
Stiffened-Shell Global Buckling	$\sigma_{\text{cr,global}}$	511.20 MPa	1.50	39.54 MPa
Stringer Weakest-Axis Column Buckling	$\sigma_{\text{cr,euler}}$	60.21 MPa	1.50	39.54 MPa

Table 6.24: Mass budget for the gondola primary structure and suspension system.

Design Element	**Mass (kg)**	**Mass Fraction (%)**
Primary Structure		
Cylinder Wall	3.463	24.08
Top and Bottom Lids	3.225	22.42
Longitudinal Stiffeners	2.303	16.01
Ring Stiffeners	4.290	29.82
Lateral Stiffeners	0.609	4.23
Antenna Booms	0.031	0.22
Cable Attachment Points	0.191	1.33
Total Primary Structure	**14.112**	**100.00**
Suspension System		
Cables – load-bearing core	1.800	24.59
Cables – protective sleeve	3.366	46.01
Tether – load-bearing core	0.750	10.25
Tether – protective sleeve	1.403	19.13
Total Suspension System	**7.32**	**100.00**
Total System Mass	**21.70**	–

6.7.5. Mass Budget

The mass budget or mass equipment list (MEL) of VISTA is presented in Table 6.25. The MEL follows the hierarchical structure like the one below:

- **Segment** (Level X) - A grouping of elements that are closely related and which often physically interface.
- **Element** (Level X.X) - A complete, integrated set of subsystems capable of accomplishing an operational role or function.
- **Subsystem** (Level X.X.X) - A functional grouping of components that combine to perform a major function within an element.
- **Component** (Level X.X.X.X) - A functional subdivision of a subsystem and generally a self-contained combination of items performing a function neccessary for subsystem operation.
- **Part** (Level X.X.X.X.X) - A hardware element that is not normally subject to further subdivision or disassembly without destruction or designated use.

The margin philosophy follows the rules outlined in the ESA Philosophy Margin document [93]. For the full breakdown of the MEL (including components, parts, labelled margin e.t.c.) please refer to [94].

Table 6.25: VISTA Master Equipment List

PBS	Name	Mass with margin [kg]
1	VISTA	757.278
1.1	Gondola	74.188
1.1.1	ADCS	4.184
1.1.2	CDHS	344
1.1.3	COM	259
1.1.4	ISRU	10.443
1.1.5	PAY	19.120
1.1.6	PWR	23.813
1.1.7	STR	14.112
1.1.8	TCS	1.913
1.2	Buoyancy	310.094
1.2.1	Buoyancy System	310.094
1.3	EDDI	372.996
1.3.1	Entry & thermal-protection	157.924
1.3.2	Descent & deceleration	24.789
1.3.3	Inflation & float-capture	183.093
1.3.4	Separation & release	2.530
1.3.5	Sequencing / sensing & control	4.660

6.8. Guidance & Navigation Subsystem

Classically, the Guidance & Navigation subsystem handles locating the spacecraft in 3D space, tracks the position history, predicts and plans trajectory, and computes commands for the propulsion subsystem required to maintain the trajectory. Since the VISTA mission is a free-floating balloon, the operational tasks of the GNS are more limited.

6.8.1. Operationl Tasks

For the nominal VISTA mission, the task fundamentally boils down just to position tracking. Active control of horizontal position would require countering the winds. Since the balloon follows with winds that reach up to 60 [m/s] (at 56 [km] altitude), active position control in the horizontal direction is unfeasible. Altitude control through the buoyancy/weight balance is possible, and necessary to allow for conducting scientific investigation at different altitudes, support thermal management or to counter disturbance from vertical winds (up to a few meters per second).

During nominal operation, the Guidance and Navigation subsystem has two primary operational tasks: acquiring and storing tracking data from on-board sensors (Figure 6.26), and using the Doppler effects of the radio connection with the orbiter to estimate absolute location and attitude (Figure 6.27). The GNS also cooperates with the buoyancy and nitrogen extraction subsystem to monitor and control the aerobot altitude (Figure 6.28).

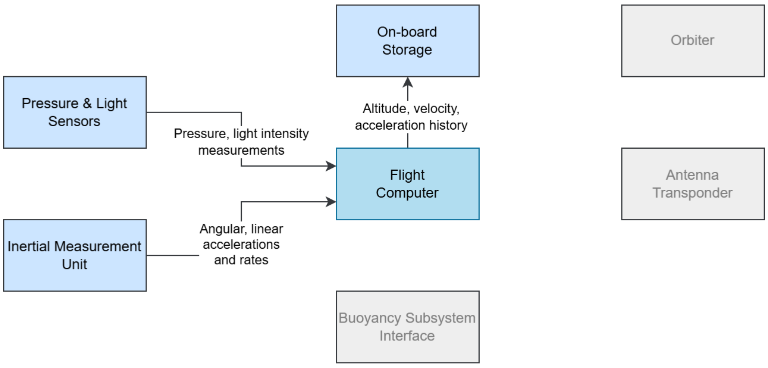

Figure 6.26: GNS data flow of measurement acquisition

During measurement acquisition, which keeps occurring throughout the nominal mission, the flight computer periodically samples the static pressure sensor (and the ambient light intensity sensor, if available). The inertial measurement unit runs continuously. The information about position and accelerations is logged and stored for later use.

Active Doppler ranging is an operation mode that can only be active when the communication window to the orbiter is open and there is sufficient power available (it might be unfeasible to run this mode at night). During the transmission of standard telemetry or scientific data, the exact signal signature is studied to determine the distance between the aerobot and the orbiter (range), as well as the velocity and attitude change of the aerobot (range rate). If necessary for the procedure, a dedicated tracking signal will be transmitted instead. Using the tracking data, the absolute reference for the IMU can be updated.

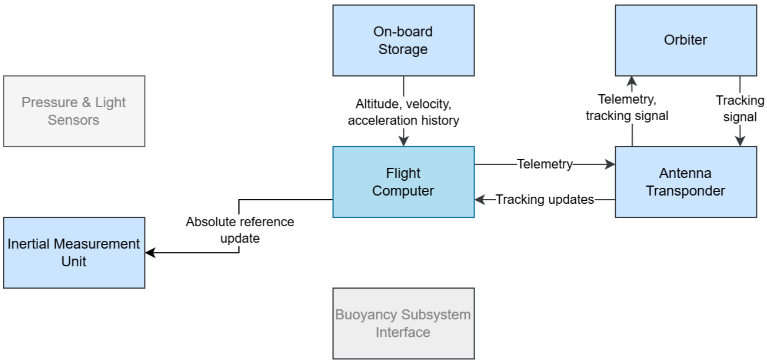

Figure 6.27: GNS data flow during active Doppler ranging

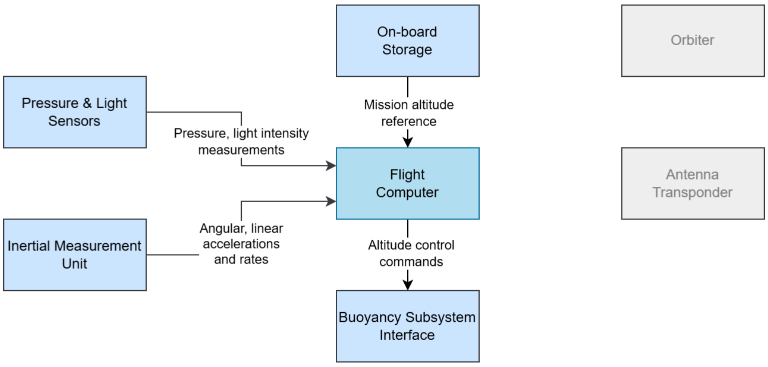

Figure 6.28: GNS data flow during altitude control

The GNS monitors and controls altitude continuously. The measured state is compared to a reference derived based on scientific targets and mission planning. The altitude control command is computed and sent to the buoyancy subsystem. The exact abstraction level of the navigation controller interface with the buoyancy subsystem code is undecided at this stage. A promising design for a model predictive altitude controller is given in [95], and is based on sequential convex programming for repeatedly approximating non-linear aerobot dynamics. It is not implemented in this work due to time constraints.

The nominal cruise altitude is 56 kilometres, with potential excursions designed down to 54. An example of a plausible altitude profile is presented in Figure 6.29 below. The altitude is desired to be as high as possible, as guided by thermal control stability and solar flux availability. However, altitudes above 56 [km] have prohibitively large risk of polar vortex entrapment (as covered later in this section). Occasional descent to lower altitudes greatly improves the range of scientific measurements obtained. These excursions can only take place around the time of solar noon, when the solar flux is large enough to allow for sufficient power deeper in the cloud layers. They should also last no longer than a few hours each, as battery use might be necessary and the load on the thermal subsystem increases greatly.

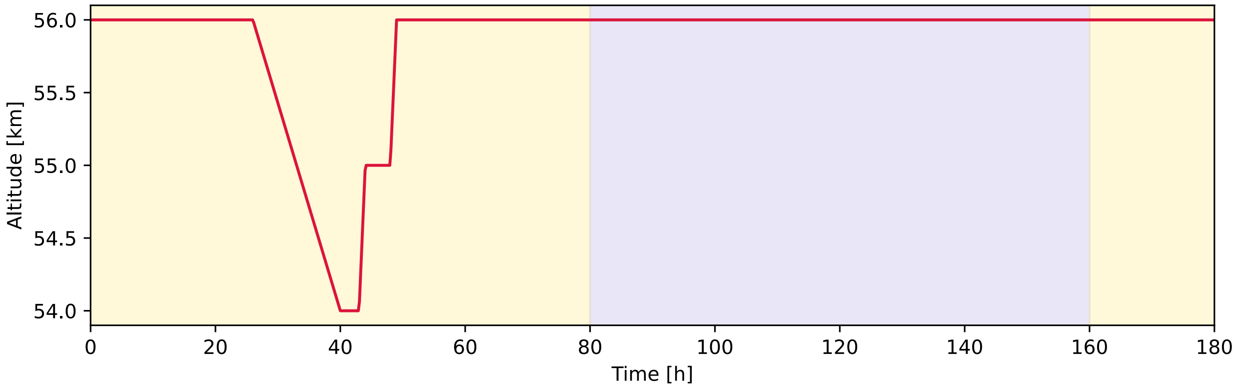

Figure 6.29: Example altitude profile of the aerobot

Note that altitude raising manoeuvres are significantly faster than altitude lowering manoeuvres. This is a direct result of using super-pressure altitude control. To increase buoyancy, lifting gas is moved from the fixed-volume super-pressure balloon to the surrounding zero-pressure envelope. This follows the pressure gradients and requires simply opening a release vent. To lower the altitude, lifting gas must be moved from the zero-pressure back into the super-pressure balloon. This action is rate-limited by the gas compressor to 0.8 [kg/h], thus putting an upper bound on the descent rate of around 180 [m/h]. If emergency altitude lowering is necessary, lifting gas can be vented out and lost into the environment. This is covered in detail in chapter 7.

6.8.2. Navigation Accuracy

Antenna Doppler ranging is a pretty standard technique of calculating position and velocity data, and has already been investigated for the Venusian use case [13]. The method relies on the orbiter knowing its own position with high accuracy, such that it can be used to anchor the position estimates for the aerobot. Absolute attitude reference is attained through differential techniques using the two on-board antennas. By timing and measuring Doppler shift of the signal, range and range rate can be measured. The specifics of these implementations are outside the scope of the project. As a reference, [13] found that Doppler ranging on Venus can achieve around 5 [km] position accuracy and 0.5 [m/s] velocity accuracy. Absolute altitude can be estimated to within tens of meters through measuring static pressure.

These absolute measurements are used as a starting point for inertial propagations using accelerometers and gyroscopes, collectively referred to as the inertial measurement unit. The drift error of the IMU is roughly quadratic over time (due to double integration of constant acceleration error). Consequently, shortening the time over which IMU propagation is necessary has a great effect in improving position estimation accuracy. For this, inertial back-propagation will be utilised. IMU outputs at high frequency are stored throughout the entire blackout period. After a new contact window opens, the IMU data can be used to propagate the position forward from the previous contact window and backward from the new contact window. This halves the effective propagation time and thus reduces drift magnitude by a factor of four. A visual comparison of the drift errors can be seen in Figure 6.30.

Since the exact timing of the next communication window cannot be known ahead of time (though can be approximated), it is impossible to determine whether at a certain time forward or backward propagation should be used. As such, it is necessary to store the high-frequency raw IMU data throughout the entire communication blackout period, in order to be integrated once the next communication link is established.

The on-board storage requirement is up to 25 MB per communication blackout. Another consequence of this strategy is that the aerobot has relatively poor awareness of its own position in real time, especially in the hours right before the next contact window. Luckily, this is not a significant issue, as detailed positional information is only really relevant to localise the scientific measurements, and those are all studied post-facto on Earth.

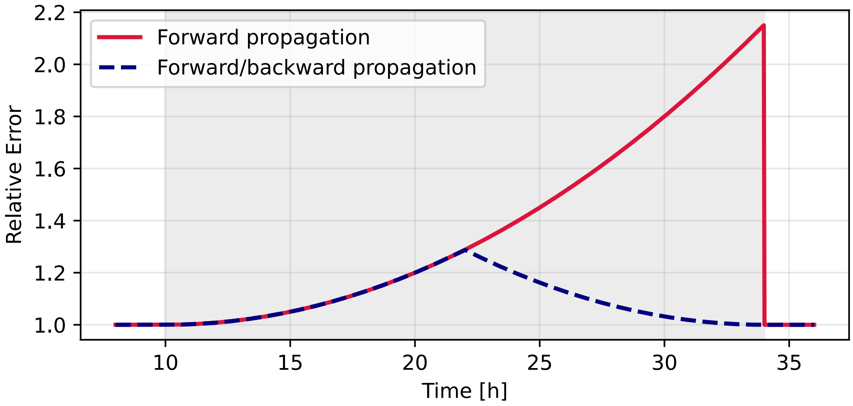

Figure 6.30: Representative comparison of IMU drift errors. The first contact window ends at hour 10, while the second window starts at hour 34.

6.8.3. Aerobot Trajectory Simulation

In order to investigate the aerobot trajectory over the mission span, Monte Carlo trajectory simulations are conducted with the help of the Venus Climate Database [96, 97, 98]. The VCD enables sampling properties like wind, temperature, solar flux, etc. at any point in Venus' atmosphere and any time of Venusian day. It also supports generating atmospheric perturbations using empirical orthogonal functions (EOF). Each EOF sample can be thought of as a single coherent instantiation of what potential Venusian weather might look like. For more details, the reader is referred to the VCD documentation [99].

General Trajectory Behaviour

For this Monte Carlo run, 300 individual balloon simulations are propagated in time for a period of 300 Earth days. The balloons are set to follow the horizontal winds exactly, and to track an altitude of constant density, around 55.5-56.0 [km]. The starting positions of the balloons are at 0° longitude, and at latitudes uniformly distributed from -50° to 50° in 10° increments. The key VCD configuration parameters are shown in Table 6.26 below:

Table 6.26: Configuration parameters for sampling the VCD

Config parameter	Value	Explanation
`hires_key`	`0`	low resolution retrieval improves execution time
`EUV_scena`	1	standard illumination conditions
`albedo_scena`	1	standard albedo conditions
`perturb_key`	2	use large scale perturbations from EOFs

The ground tracks of the 300 samples are presented in Figure 6.31, and the overall visit density is shown in Figure 6.32. As is apparent, significant majority of the balloons converge to regions around 40°-50° latitude and remain there. This is expected, and can be explained by the separation between two different kinds of planetary-scale atmospheric waves (see the works by [100, 101]). Interestingly, while some balloons end up diverging to the southern polar vortex, none end up in the northern vortex. This kind of asymmetry is a recognised feature of the VCD, and its exact cause is unclear. In an email exchange, Sébastien Lebonnois indicated that this is dependent on the numerical model used, and likely relates to surface topography.

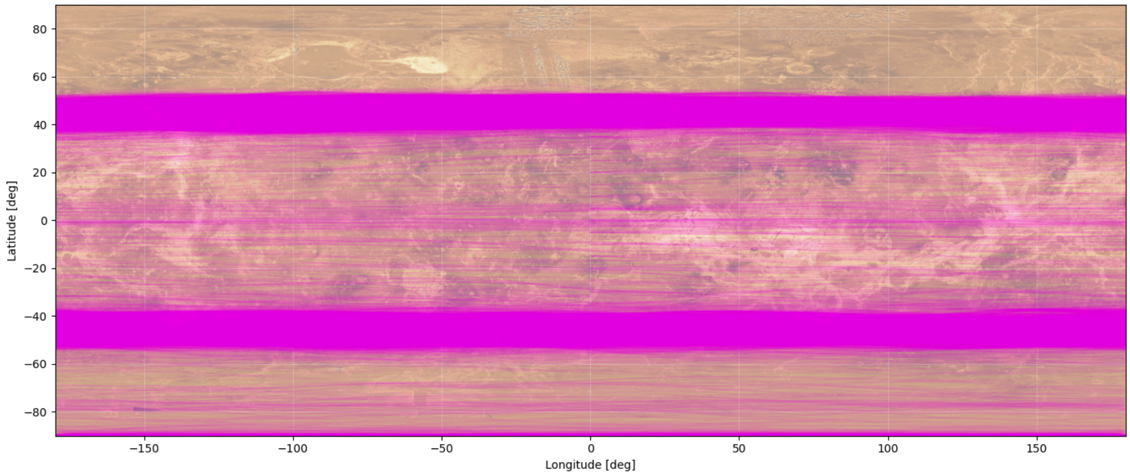

Figure 6.31: MC ground track paths.

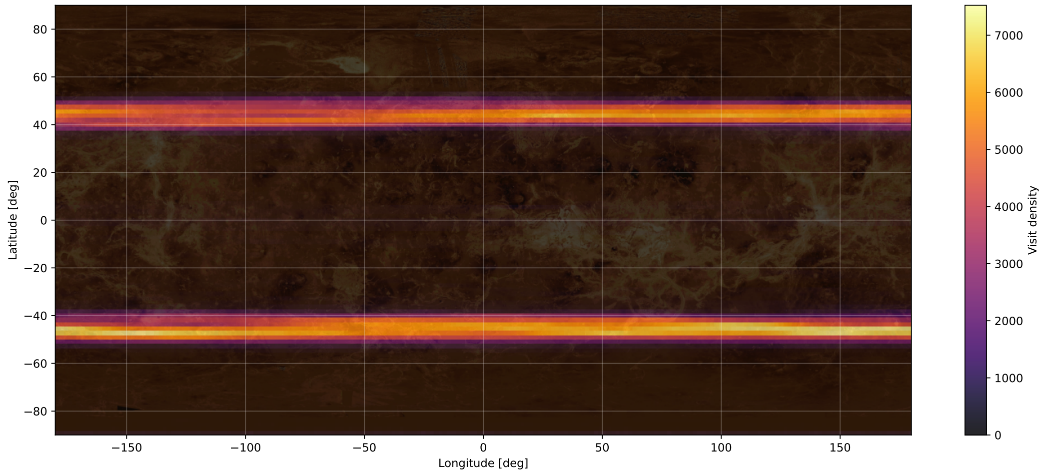

Figure 6.32: Visit density distribution over latitude and longitude for the MC samples.

Polar Vortex Entrapment

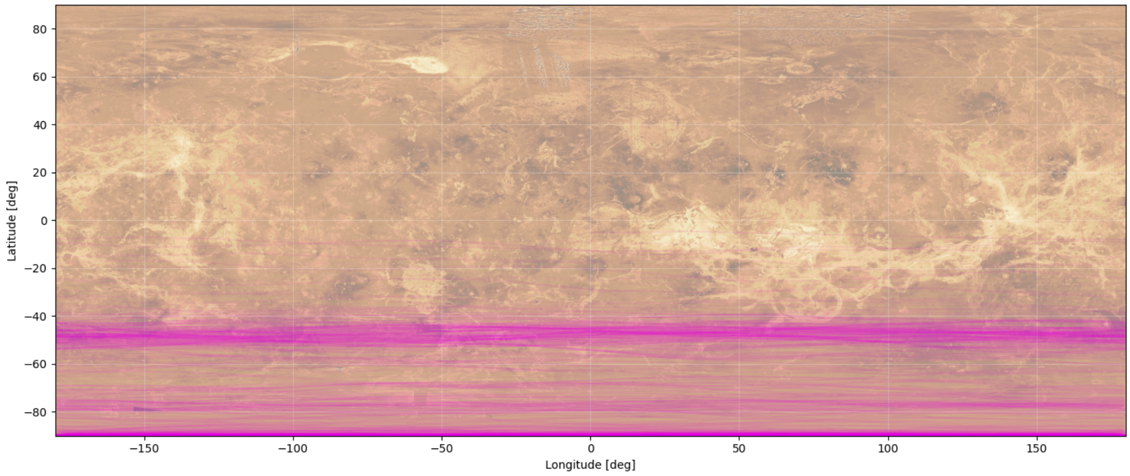

Figure 6.33: MC ground track paths for balloons trapped in the polar vortex (subset of Figure 6.31).

The primary threat to the mission from the navigation point of view is the risk of the aerobot being trapped in one of the polar vortices. At such high latitudes, the solar flux is simply insufficient to properly power the aerobot, enforcing mission termination. As in Figure 6.33, the vortex-trapped samples start circumnavigating around the standard 40°-50°. At some point, however, they start slowly diverging towards around 80°, and eventually coast towards the very pole. This state is irrecoverable.

Over the 300 Earth days of simulation time, 11 out of the 300 samples diverged towards a polar vortex, which is about 3.7%. Treating this value as a Bernoulli trial and extending to the nominal mission duration of 5 Earth years yields polar entrapment chance of 20%. Since this interaction is unavoidable and weather cannot be affected, this gives an upper bound of mission reliability of 80%.

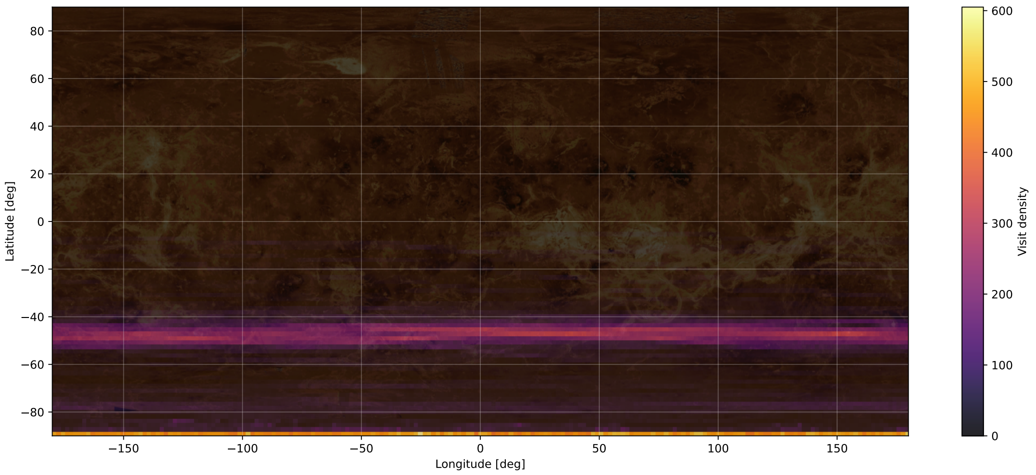

Figure 6.34: Visit density distribution over latitude and longitude for the MC samples trapped in the polar vortex (subset of Figure 6.32).

Altitude Variations

To investigate the influence of operating altitude on trajectory evolution, four smaller trials of 50 balloons each were ran at 54, 55, 56, and 57 kilometres altitude (Figure 6.35). At 56 [km], the trajectories are mostly stable around 50° latitude. At 55 and 54, the stability point moves closer to the equator, to around 45° and 40° latitude. This trend in fact continues, until around 52 [km], where the trajectories become stable around the equator itself. Lower trajectories were not investigated, as they are far outside the feasible thermal and power envelope. Notice that not far above the operating altitude, at 57 [km] already, the trajectories diverge towards the polar vortices completely. That region is not feasible for nominal operation.

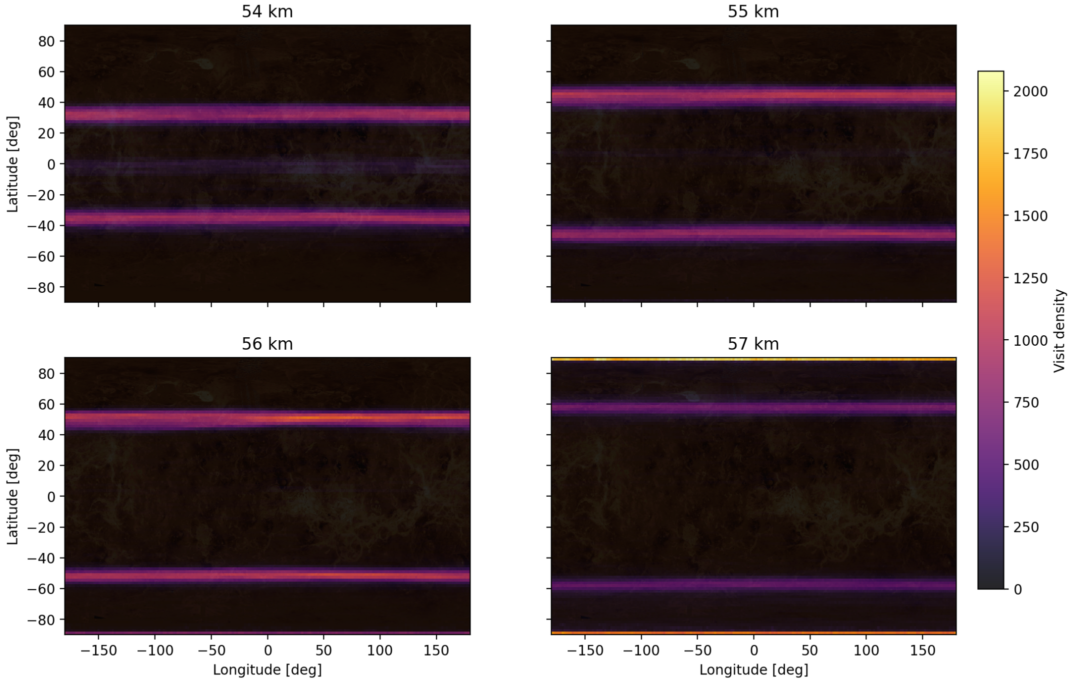

Figure 6.35: MC trajectory comparison between altitudes.

7 Balloon Envelope and Buoyancy Design

This chapter focuses on the design, sizing and reliability estimation of the balloon and the in situ nitrogen replenishment system (ISRU). It also presents the estimated ISRU power consumption.

7.1. Design Choices

This section briefly introduces the design choices which led to the selection of the balloon architecture, nitrogen separation system and the envelope material.

7.1.1. Balloon architecture

Initially, three potential balloon architectures were identified and considered:

- **Option 1:** A large balloon initially partially filled with helium, then gradually filled with in situ obtained nitrogen, using atmospheric CO_2 as ballast for altitude control.
- **Option 2:** A pre-filled nitrogen balloon, using in situ nitrogen only for leakage top-up, with altitude control provided by an internal superpressure bladder.
- **Option 3:** An initially empty nitrogen balloon with an internal superpressure bladder, supported during early operation by a temporary disposable helium balloon while the ISRU system fills the main balloon.

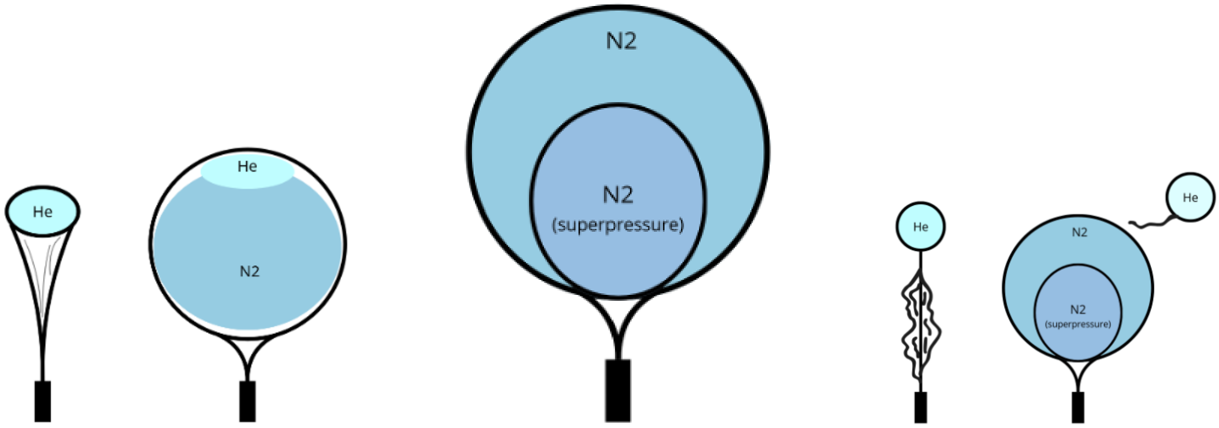

(a) He start with gradual N_2 filling. **(b)** Pre-filled N_2 balloon with SP bladder. **(c)** Empty N_2 balloon with temporary He support.

Figure 7.1: Simplified visualisation of the three balloon architecture options considered.

The main design drivers were the ability to use in situ obtained nitrogen for leakage compensation, the total aerobot mass, and the power consumption requirements.

Option 1 is advantageous because it uses helium initially to keep the balloon afloat, meaning that it does not need to be filled with N_2 by the ISRU system immediately after deployment. Nevertheless, it is unfeasible, since filling it with 260 kg of nitrogen to stay afloat at an altitude of 55 km would require the ISRU system to extract around 5 kg of N_2 per Earth day for almost two months. This would consume approximately 900 W of continuous power, which does not comply with the power requirement.

Option 2 was the most promising choice, as it is the simplest of the three, is operational directly after deployment because it is already filled with N_2, and does not rely on the in-situ resource utilisation system for early operation. It does require all 260 kg of N_2 to be brought from Earth, but this is countered by its operational simplicity, lower early-mission risk, and lower initial power demand.

Option 3 is a valid concept and is essentially a combination of Options 1 and 2. However, it is extremely power consuming at the beginning of the mission and also introduces additional mass, complexity, and an extra point of failure by adding a disposable helium balloon.

Based on this, Option 2 was selected as the most suitable architecture for the mission due to its simplicity and fewer potential points of failure than the other options.

7.1.2. Gas Separation System

Three potential N_2 separation systems were considered:

- **Membrane Separation:** Uses a CO_2-selective polymer membrane through which CO_2 permeates by solution-diffusion, retaining the N_2-rich stream.
- **Cryotrapping:** Cools the atmospheric feed so that $\mathrm{CO_2}$ is frozen out, leaving a more $\mathrm{N_2}$-enriched gas stream.
- **Chemical Getters:** Uses reactive material to chemically bind or remove $\mathrm{CO_2}$, leaving $\mathrm{N_2}$ behind.

Membrane Separation has been chosen as the best gas separation method. Its advantages include the fact that the membrane itself doesn't consume any power, can be relatively compact as described in Section 7.2.4, and doesn't need regeneration as it continuously separates CO_2 from N_2 by permeation. Its potential points of failure include clogging or degradation due to corrosion, which can be overcome by a proper filtering system which will be described later in the chapter. Cryotrapping wasn't chosen as its main disadvantages are power consumption and mass. Since it needs to constantly cool a large amount of gas, it would require a cryocooler, heat exchangers, insulation and thermal rejection hardware, making it highly demanding in both power and mass, as well as increasing system complexity. Finally, chemical getters are only good as long as they are treated as consumable. However, since $\mathrm{N_2}$ is only 3.5% of the atmosphere, the $\mathrm{CO_2}$ mass that must be removed is roughly:

$$\frac{m_{\mathrm{CO_2}}}{m_{\mathrm{N_2}}} = \frac{0.965 \cdot 44}{0.035 \cdot 28} \approx 43 \tag{7.1}$$

Therefore, for 100 grams of $\mathrm{N_2}$, about 4.3 kg of $\mathrm{CO_2}$ must be removed, which corresponds to over 8 tonnes of $\mathrm{CO_2}$ over a 5-year mission duration. This makes the technology infeasible from a mass point of view. On the other hand, if the getter were made regenerable, it would lose much of its simplicity and would require extra power and regeneration hardware.

7.1.3. Envelope Material Selection

The three material architectures were considered as a potential balloon envelope material:

- **Architecture A – JPL[102] Gen-1 laminate:** this architecture consists of an FEP outer acid-barrier and solar-reflective layer, an aluminised Mylar gas-barrier layer, a Vectran structural fabric layer, and a polyurethane adhesive/sealing layer
- **Architecture B – JPL Gen-2 laminate with aluminium foil:** this architecture consists of an Aclar/PCTFE outer acid-barrier layer, an aluminium foil gas-barrier layer, a Vectran structural fabric layer, and a polyurethane adhesive/sealing layer
- **Architecture C – high-barrier thin-ply laminate:** this architecture consists of a PFA outer acid-barrier layer, a PCTFE gas-barrier layer, a Vectran structural fabric layer, a second PCTFE gas-barrier layer, and a polyurethane adhesive/sealing layer

Architecture A, based on the JPL Gen-1 laminate, has strong heritage and good structural performance, but aluminised Mylar gas barrier is vulnerable to pinhole formation, reducing long-term gas retention. Architecture B replaces this with a Gen-2-style laminate using an Aclar/PCTFE outer acid barrier, aluminium foil gas barrier, Vectran structural fabric, and polyurethane sealing layer, giving better nitrogen retention and acid resistance while keeping acceptable flexibility and heritage. Architecture C uses a higher-barrier thin-ply polymer laminate with PFA and PCTFE layers, but has lower demonstrated Venus balloon heritage and greater uncertainty.

Architecture B was considered to provide the best balance between gas retention and heritage-based reliability, while also maintaining acceptable deployment flexibility, thermal/UV stability and TRL. The Aclar (PCTFE) outer layer was selected because Hall et al. (2011) [103] report no degradation in sulfuric acid exposure tests, it is tougher than FEP, and no Al surface is exposed to acid contact [102]. The continuous Al foil, with a thickness of 8-12μm, has no intrinsic polymer permeability channel, while its pinhole density is suppressed by lamination quality control, making the $\mathrm{N_2}$ barrier dramatically superior to metallised film [102]. The Vectran fabric is identical to Gen-1, while the areal density is reduced, as the Aclar and Al foil are lighter than the FEP and Al-Mylar stack. Aclar, with an elongation of 100–250%, is substantially more flexible than FEP. Although the Al foil is brittle at fold lines, the Vectran fabric constrains the fold geometry within the laminate, and the Gen-2 prototype was handled without observed delamination [102, 104]. Aclar is inherently UV-stable, while the Al foil provides an additional UV block to Vectran. However, the CTE mismatch between Al and the polymer over 1825 cycles is a long-term concern that has not been fully tested [102]. Aclar/Al-foil/Vectran/PU laminate samples were tested in acid and optical tests, while aerial deployment was also tested [102]. However, no full-duration 5-year test has been performed. The selection is reinforced by the highest available TRL. The Aclar/Al-foil/Vectran/PU laminate has been manufactured, acid-tested and deployed by the JPL team [102], making it the most mature Venus-specific balloon laminate in the open literature. Some of the important material properties are summarised in Table 7.1. The sustainability implications of the selected fluoropolymer-containing envelope materials, including PFAS-related production and disposal concerns, are discussed in section 11.3.

Table 7.1: Selected VISTA balloon envelope laminate specification (Architecture B).

Ply	Material	Function	Thick.	Areal mass	Key references
1 (out.)	Aclar PCTFE film	Acid barrier, abrasion resistance	25 µm	$\approx 38\,\mathrm{g/m^2}$	[102, 105]
2	Aluminium foil (hard-rolled)	Gas barrier (N_2/He)	10 µm	$\approx 27\,\mathrm{g/m^2}$	[102]
3	Vectran HS fabric, 2×2 twill	Superpressure structural layer	$\approx$180 µm	$\approx 75\,\mathrm{g/m^2}$	[106, 107]
4 (inn.)	Polyurethane adhesive/seal coat	Bonding, seaming, inner seal	15 µm	$\approx 15\,\mathrm{g/m^2}$	[106]
Total laminate				SP: $117\,\mathrm{g/m^2}$ ZP: $80\,\mathrm{g/m^2}$	Within nominal ROM σ case.

7.2. Balloon and ISRU Sizing

This section focuses on describing the balloon sizing process, including all the necessary assumptions, constants, procedure itself and final results. The aim is to size a balloon envelope in such a way that would be feasible for all the altitudes it needs to operate at, as well as to minimise the leakage rate.

7.2.1. ISRU and Balloon Architecture

The selected ISRU and balloon architecture is shown in Figure 7.2, while the material properties used for the balloon sizing are summarised in Table 7.2.

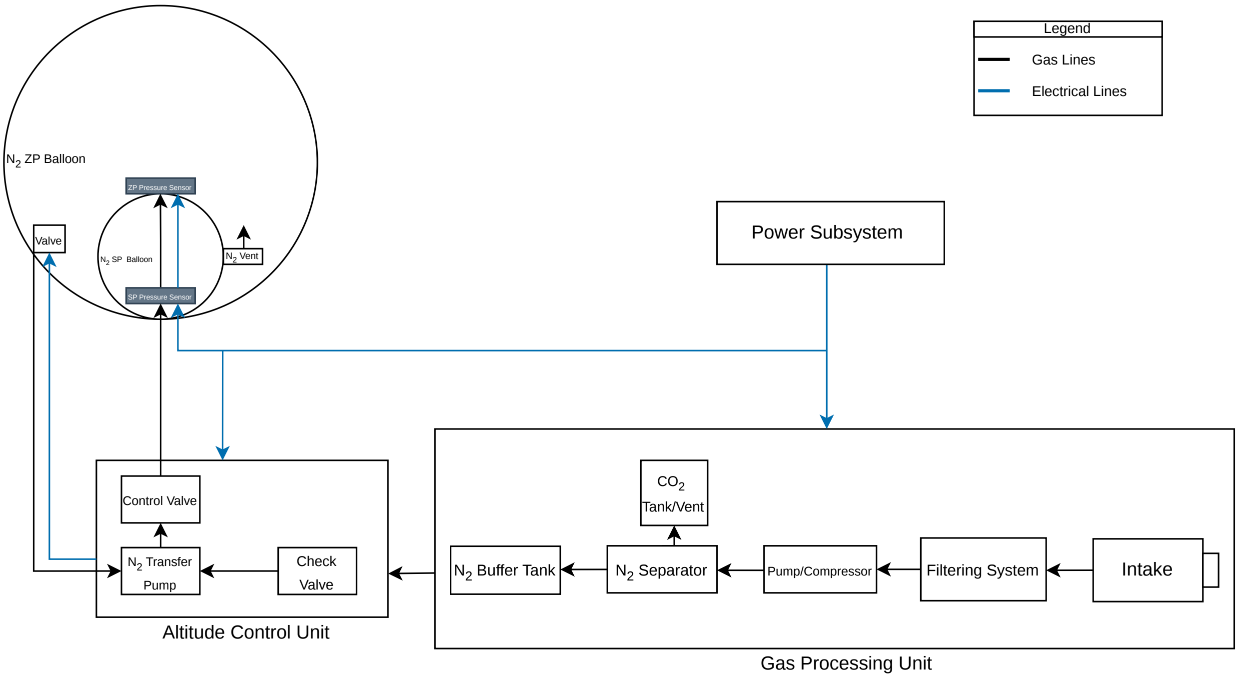

Figure 7.2: ISRU and Balloon System

Table 7.2: Material properties used for the balloon envelope sizing.

Material layer	**Main role**	**Thickness [μm]**	**Areal density [g/m^2]**	**N_2 permeability [Barrer]**
Aclar PCTFE	Acid / gas barrier	25	38	0.188 [108]
Aluminium foil	Gas barrier	10	27	0.1
Vectran HS	Structural layer	180	75	1.0×10^6
Polyurethane (PU)	Seal / gas barrier layer	15	15	3.25 [109]
Outer ZP envelope	Aclar + Al + PU	50	80	0.21
Inner SP envelope	Vectran HS + PU + Al	205	117	1.96

* Effective permeability calculated using the series-resistance approximation [110]:

$$P_{\text{eff}} = \frac{t_{\text{tot}}}{\sum_i \frac{t_i}{P_i}}$$

where t_i and P_i are the thickness and nitrogen permeability of each layer. The Vectran permeability is set to a very large value in the model, meaning that it is treated as a structural layer rather than a gas-barrier layer. The permeability value for Aluminum foil is assumed to be 0.1 [111], in order to account for pinholes, connections and potential defects. It is a conservative, defect-adjusted effective permeability for the aluminum foil layer.

The constants used for balloon sizing are also listed in the following table:

Table 7.3: Constants used in the balloon sizing model

Symbol / variable	**Definition**	**Value**
$x_{N_2,\text{Venus}}$	Venus atmospheric nitrogen mole fraction	0.035
M_{N_2}	Molar mass of nitrogen	0.0280134 kg/mol
g_{Venus}	Venus gravitational acceleration	8.87 m/s^2
C_D	Balloon drag coefficient	0.5
M_{carry}	Gondola, payload, and support mass	75.2 kg
B_{SI}	Barrer-to-SI conversion factor	3.348×10^{-16} mol m/(m^2 s Pa)
margin$_{\text{env}}$	Envelope mass margin	0.15
FS_{SP}	Superpressure balloon factor of safety	2.0
$\sigma_{\text{Vectran,ult}}$	Vectran ultimate tensile strength	3×10^9 Pa
k_{crimp}	Crimp knockdown factor	0.80 [103]
k_{biaxial}	Biaxial loading knockdown factor	0.77
k_{seam}	Seam knockdown factor	0.80
k_{thermal}	Thermal knockdown factor	0.75
t_{cycle}	Day–night cycle duration (84 h light + 60 h dark)	144 h

7.2.2. Main Sizing Model Assumptions

This sizing model is preliminary, hence several assumptions are made to simplify the sizing approach:

1. The balloon is assumed to be spherical. In reality, the balloon will have changes in curvature, seams, local wrinkling, and non-spherical deformation.
2. The gas is assumed to behave ideally, so the gas density is calculated using:

$$\rho = \frac{pM}{RT} \tag{7.2}$$

   where ρ is the gas density, p is the pressure, M is the molar mass, R is the universal gas constant, and T is the temperature.

3. The superpressure-to-zero-pressure diameter ratio **at deployment only** is fixed at:

$$\frac{D_{\text{SP}}}{D_{\text{ZP}}} = 0.5 \tag{7.3}$$

   based on Hall et al. [103]. Since volume scales with diameter cubed:

$$\frac{V_{\text{SP}}}{V_{\text{ZP}}} = \left(\frac{D_{\text{SP}}}{D_{\text{ZP}}}\right)^3 = 0.125 \tag{7.4}$$

4. The superpressure differential is fixed at:

$$\Delta p_{\mathrm{SP}} = 25{,}000\ \mathrm{Pa} \tag{7.5}$$

as a representative preliminary superpressure value based on Hall et al. [103]. **Valid only at deployment**.

5. The difference between the calculated leakage rate at the beginning of life and the end of life differs by a factor of 3
6. The wear-out factor for a Weibull reliability model is assumed to be $\beta = 2$, as the number of failures is assumed to be increasing linearly with time
7. The day-night cycle of Vista is assumed to be 144 hours, where 84 hours are spent in the light, and 60 hours in the dark

7.2.3. Balloon Sizing Approach

It has been decided that the balloon will operate between 54 km and 57 km altitude. Therefore, the sizing procedure is conducted from 53 km to 58 km in order to include a safety margin. The balloon sizing procedure consists of two parts. First, the balloon is sized at the deployment condition, where the main assumptions are applied and the envelope mass is estimated. Then, the final configuration is defined by fixing the SP diameter, selecting the maximum ZP diameter, and splitting the required N_2 mass between the ZP and SP envelopes.

The sizing is based on the equilibrium procedure by Hall et al. [103], originally developed for helium and adapted here for nitrogen. The model considers the Venus cloud-zone altitude range from 50 km to 62 km, with temperature, pressure, and density specified at each altitude, listed in Table 7.4.

Table 7.4: Venus atmospheric properties used in the sizing model

Altitude [km]	Temperature [K]	Pressure [Pa]	Density [kg/m^3]
50	350.5	106600	1.5940
51	342.0	93470	1.4320
52	333.3	81774	1.2840
53	323.0	71162	1.1530
54	312.8	61682	1.0320
55	302.3	53183	0.9207
56	291.8	45626	0.8183
57	282.5	38930	0.7212
58	275.2	33071	0.6289
59	268.7	27972	0.5448
60	262.8	23571	0.4694
61	258.7	20080	0.4053
62	254.5	16588	0.3411

Following Hall et al. [103], a worst-case sustained vertical wind speed of 3 m/s is considered. The corresponding drag force is converted into an equivalent mass penalty:

$$m_{\mathrm{drag}} = \frac{F_{\mathrm{drag}}}{g_{\mathrm{Venus}}} = \frac{\rho_{\mathrm{atm}} S_{\mathrm{ref}} v_{\mathrm{wind}}^2 C_D}{2 g_{\mathrm{Venus}}}, \tag{7.6}$$

where ρ_{atm}, S_{ref}, v_{wind} and C_D are the atmospheric density, projected balloon area, vertical wind speed and drag coefficient, respectively.

A static force balance is used to find the required outer balloon volume. The displaced atmospheric mass must balance the carried mass, envelope mass, nitrogen mass and drag penalty:

$$\rho_{\mathrm{atm}} V_{\mathrm{outer}} = M_{\mathrm{carry}} + m_{\mathrm{env,total}} + \rho_{N_2} V_{\mathrm{ZP}} + \rho_{N_2,\mathrm{SP}} V_{\mathrm{SP}} + m_{\mathrm{drag}}. \tag{7.7}$$

Here, M_{carry} is the gondola, payload and support mass, taken as 75.2 kg. Since the envelope and drag areas depend on the balloon volume, the equation is solved numerically for V_{outer} using bisection.

The SP volume follows from the assumed deployment diameter ratio $D_{\mathrm{SP}}/D_{\mathrm{ZP}} = 0.5$:

$$V_{\mathrm{SP}} = \left(\frac{D_{\mathrm{SP}}}{D_{\mathrm{ZP}}}\right)^3 V_{\mathrm{outer}}, \qquad V_{\mathrm{ZP}} = V_{\mathrm{outer}} - V_{\mathrm{SP}}. \tag{7.8}$$

Assuming spherical envelopes, the surface areas follow from the corresponding diameters. Using the areal densities from Table 7.2, the total envelope mass is

$$m_{\mathrm{env,total}} = w_{\mathrm{outer}} A_{\mathrm{outer}} + w_{\mathrm{SP}} A_{\mathrm{SP}}. \tag{7.9}$$

The nitrogen densities follow from the ideal gas law. The ZP balloon is at ambient pressure, while the SP balloon carries an imposed superpressure of $\Delta p_{\mathrm{SP}} = 25$ kPa at deployment:

$$\rho_{N_2} = \frac{p M_{N_2}}{RT}, \qquad \rho_{N_2,\mathrm{SP}} = \frac{(p + \Delta p_{\mathrm{SP}}) M_{N_2}}{RT}. \tag{7.10}$$

The nitrogen mass is then split between the two volumes:

$$m_{N_2,\mathrm{total}} = \rho_{N_2} V_{\mathrm{ZP}} + \rho_{N_2,\mathrm{SP}} V_{\mathrm{SP}}. \tag{7.11}$$

The envelope equivalent thicknesses are obtained from the areal density and equivalent material density, $t = w/\rho_{\mathrm{mat}}$. Since the SP balloon is pressurised, its envelope experiences membrane stress, which for a thin spherical pressure vessel is

$$\sigma_{\mathrm{SP}} = \frac{\Delta p_{\mathrm{SP}} \cdot r_{\mathrm{SP}}}{2 t_{\mathrm{SP}}}. \tag{7.12}$$

The leakage rate is estimated with a steady-state permeation model:

$$\dot{n}_{N_2} = \frac{\Pi_{\mathrm{eff}} A \Delta p_{N_2}}{t}, \qquad \Delta p_{N_2,\mathrm{outer}} = p\left(1 - x_{N_2,\mathrm{Venus}}\right), \tag{7.13}$$

where Π_{eff}, A, Δp_{N_2} and t are the effective permeability, envelope area, nitrogen partial-pressure difference and envelope thickness, respectively. The nitrogen replenishment rate is assumed equal to the external leakage through the outer envelope, accumulated over the full day–night cycle, which is roughly 84 hours in the light plus 60 hours in the dark, hence 144 hours combined, converted to a per-cycle (kg/cycle) basis via

$$\dot{m}N_2, \mathrm{cycle} = \dot{n}N_2 \cdot M_{N_2} \cdot 144 \cdot 3600. \tag{7.14}$$

This calculation is repeated for each altitude and wind case.

A worst-case SP structural check is performed over all altitude and wind cases. Since membrane stress increases with radius, the largest SP radius defines the stress-required thickness:

$$t_{\mathrm{SP,stress}} = \frac{\Delta p_{\mathrm{SP}} r_{\mathrm{SP,max}}}{2\sigma_{\mathrm{allow,SP}}}, \qquad \sigma_{\mathrm{allow,SP}} = \frac{\sigma_{\mathrm{Vectran,ult}}\, k_{\mathrm{crimp}} k_{\mathrm{biaxial}} k_{\mathrm{seam}} k_{\mathrm{thermal}}}{FS_{\mathrm{SP}}}. \tag{7.15}$$

The final SP design thickness is $t_{\mathrm{SP,design}} = \max\left(t_{\mathrm{SP,material}}, t_{\mathrm{SP,stress}}\right)$. If the stress-required thickness exceeds the selected material thickness, the SP areal density is updated and the altitude–wind sweep repeated, since the increased envelope mass affects the required volume and all dependent outputs.

Based on the preliminary deployment sizing, a maximum ZP diameter of 11 m and a fixed SP diameter of 5 m were selected as the final architecture. The 11 m ZP envelope provides sufficient buoyant volume near the upper operating altitude, while the 5 m SP envelope reduces mass and nitrogen storage compared with retaining the deployment diameter ratio. The fixed parameters are summarised in Table 7.5.

Table 7.5: Final balloon configuration parameters.

Gondola mass	ZP diameter	SP diameter	N_2 mass	Envelope mass
75.2 kg	11 m	5 m	260 kg	46 kg

The selected configuration is then checked across the required cloud-altitude range. Unlike the first part of the procedure, this step does not resize the envelopes. The SP volume is fixed and the ZP envelope may expand up to its 11 m limit. For each altitude–wind case, the force balance is solved in residual form,

$$F(V_{\mathrm{outer}}) = \rho_{\mathrm{atm}} V_{\mathrm{outer}} - m_{\mathrm{total}} - m_{\mathrm{drag}}, \tag{7.16}$$

where m_{total} is the dry mass plus the fixed nitrogen inventory and m_{drag} follows from the drag-penalty equation above. Equilibrium is found by bisection, with the SP volume as the lower bound, as the ZP envelope cannot contract past the SP bladder, and the maximum outer volume as the upper bound. If the residual is negative at maximum volume, the system is too heavy even fully inflated, while if it is positive at the lower bound, the system is too buoyant. An altitude case is therefore feasible only if

$$F(V_{\text{SP}}) \leq 0, \qquad F(V_{\text{outer,max}}) \geq 0. \tag{7.17}$$

With $V_{\text{ZP}} = V_{\text{outer}} - V_{\text{SP}}$, the ZP nitrogen mass follows from the ideal gas law at ambient pressure, the remainder is stored in the SP bladder, and the required SP pressure and overpressure are

$$m_{N_2,\text{ZP}} = \frac{pM_{N_2}V_{\text{ZP}}}{RT}, \qquad m_{N_2,\text{SP}} = m_{N_2,\text{total}} - m_{N_2,\text{ZP}}, \tag{7.18}$$

$$p_{\text{SP}} = \frac{m_{N_2,\text{SP}}RT}{M_{N_2}V_{\text{SP}}}, \qquad \Delta p_{\text{SP}} = p_{\text{SP}} - p. \tag{7.19}$$

Two further physical checks are performed: the SP nitrogen mass must be positive, otherwise the chosen total inventory is too small for the required ZP volume, and the SP pressure must remain above ambient, otherwise the bladder no longer behaves as a superpressure balloon:

$$m_{N_2,\text{SP}} > 0, \qquad \Delta p_{\text{SP}} > 0. \tag{7.20}$$

The effective permeabilities defined earlier are then used in the same permeation model at each altitude, with $\Delta p_{N_2,\text{outer}} = p\,(1 - x_{N_2,\text{Venus}})$ for the outer envelope and $\Delta p_{N_2,\text{SP}} = \Delta p_{\text{SP}}$ for SP-to-ZP leakage. The SP-to-ZP leakage is accounted for in the altitude-control subsection of the ISRU power consumption estimation.

This procedure is repeated over the full altitude–wind sweep, storing the inflated ZP diameter, SP overpressure, and leakage values. The leakage is evaluated inside the loop because the ZP envelope area changes with altitude. A safety factor of 2.0 is applied to account for pinholes, tubes, interfaces, and other leakage paths not captured by the ideal membrane model. Since nitrogen permeates continuously, the leaked mass is accumulated over the full 144-hour cycle and converted to a per-cycle basis via:

$$\dot{m}_{N_2,\text{BOL}} = \text{SF}_{\text{leak}} \cdot \dot{n}_{N_2} \cdot M_{N_2} \cdot 144 \cdot 3600. \tag{7.21}$$

The EOL leakage is assumed to be three times the BOL value,

$$\dot{m}_{N_2,\text{EOL}} = 3 \cdot \dot{m}_{N_2,\text{BOL}}, \tag{7.22}$$

and the maximum values are used for ISRU sizing to cover the worst case.

The results are summarised below. Figure 7.3 shows the inflated ZP diameter across the altitude-wind sweep, as well as the BOL and EOL leakage rates, respectively. Once again, the cycle is 144 hours, where 84 hours are spent in the light and 60 hours in the dark. The variation in leakage rate between beginning of life and end of life over the five-year mission was not modelled, as this would require material ageing tests and further analysis. The increase is not expected to be linear, since material degradation is likely to accelerate over time, resulting in a relatively small increase during the early mission phase and a steeper rise towards the end of life.

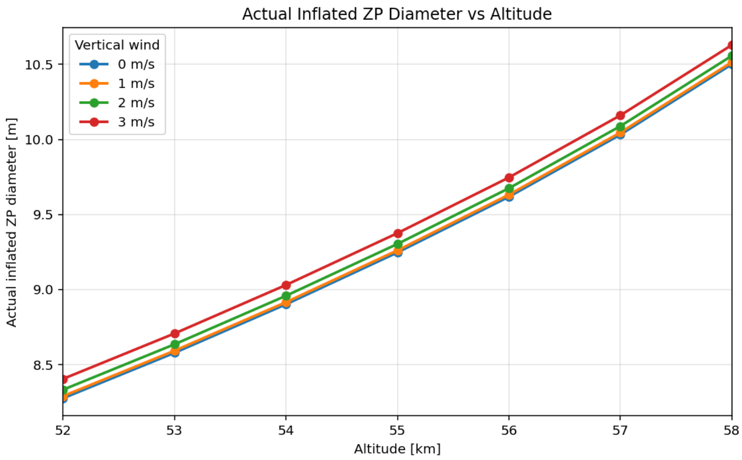

(a) Actual inflated ZP diameter

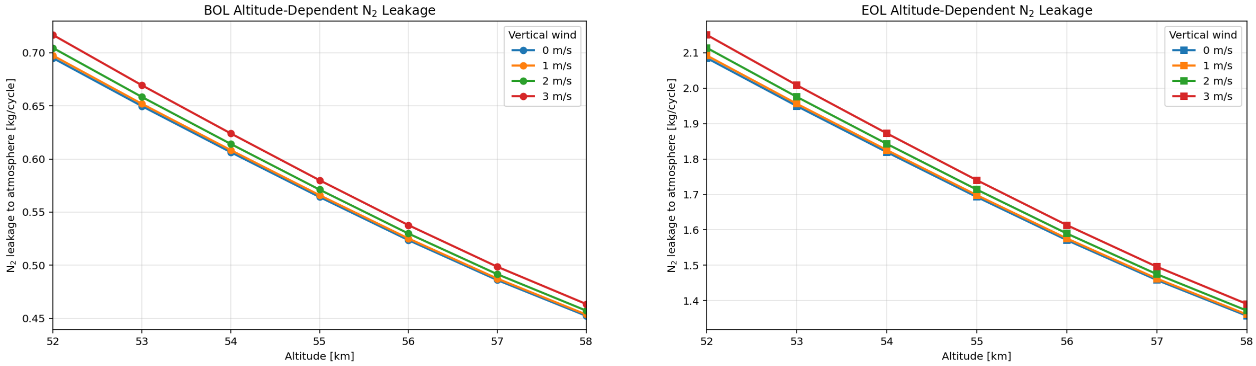

(b) BOL N_2 leakage

(c) EOL N_2 leakage

Figure 7.3: Altitude-wind sweep results for the selected balloon configuration.

Finally, the dry envelope mass of the selected configuration is calculated from the design surface areas and corresponding areal densities. A 15% mass margin is then applied:

$$m_{\mathrm{env,total,margin}} = \left(w_{\mathrm{outer}} A_{\mathrm{outer,design}} + w_{\mathrm{SP}} A_{\mathrm{SP,design}}\right) \cdot (1 + \mathrm{margin}). \tag{7.23}$$

The final results are summarised in the tables below:

Table 7.6: Balloon N_2 leakage rates at 54km, 3m/s vertical wind

Case	Leakage rate [kg/cycle]
Beginning of life (BOL)	0.624
End of life (EOL)	1.8725

Table 7.7: Envelope mass with and without margin.

Case	Envelope mass [kg]
Without margin	39.6
With 15% margin	45.6

7.2.4. In Situ Resource Utilization System (ISRU) Sizing

Next, the system that extracts N_2 from the Venusian atmosphere needs to be sized. This system can be seen in Figure 7.2, and consists of a gas processing unit and an altitude control unit. The atmosphere is forced in through the intake. Since the aerosols in the cloud layer consist primarily of concentrated sulphuric acid solution with concentrations of approximately 80–95%, a filtering system is needed, which will be discussed in more detail later. After the filtering system, the filtered gas flow is forced into a separator, where CO_2 is separated from N_2, with the enriched nitrogen stream continuing on to the altitude control unit, while the CO_2 is disposed of through a special vent. In the altitude control unit, the enriched N_2 stream is forced into the ZP balloon, compensating for leakage. When needed, the N_2 pump relocates nitrogen from the ZP to the SP balloon to lower the altitude. The final ISRU CAD model can be seen in Figure 7.4, starting with the filtering system on the left and ending with the N_2 pump on the right.

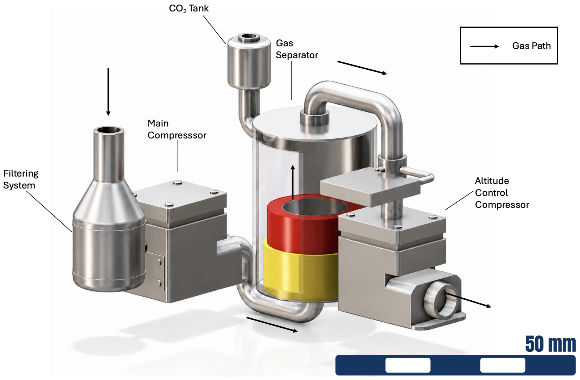

Figure 7.4: In Situ Resource Utilization System CAD

Filtering system

This subsection focuses on the design of the filtering system. The main issue encountered was clogging. Since the aerobot needs to be fully operational for at least 5 Earth years, clogging becomes a limiting risk. Therefore, a system that regenerates the filter has been developed.

As can be seen in Figure 7.5, atmospheric gas enters through the intake and is split into two branches through the inlet manifold, with a differential pressure sensor between them. The intake flow is forced through the system by the main pump/compressor, placed downstream of the filters. The two-branch layout is needed for two reasons, namely redundancy and continuous operation. First, if a component in one branch fails, the filtering system remains operational through the other. Second, while one branch is being regenerated, the other one can operate as intended.

The filter itself consists of two layers. The first layer is a backflushable pre-filter, protecting the system from large aerosols and dust particles. Reverse gas flow can be used to remove the accumulated particle layer and reduce the pressure drop, allowing the repeated regeneration of the pre-filter [112]. The second layer is the hydrophobic aerosol barrier, which captures the finer aerosols. On both branches, there is a micro pump needed for pre-filter regeneration. During normal operation, the main pump/compressor forces the atmospheric gas through both branches towards the gas separation system. During regeneration, one of the branches can be isolated using the valves, while the micro pump drives a reverse CO_2 flow through the pre-filter. A pressure difference of 10 kPa has been selected as a preliminary clogging-detection threshold, triggering backflush before the pressure drop becomes large enough to compromise ISRU operation.

Backflush regeneration is not assumed to restore the filter completely, as some fine aerosols still remain within it. The initial efficiency is assumed to be 80% [113]. A conservative end-of-life backflush efficiency of 70% is adopted, corresponding to the lower end of the experimentally measured range [113]. The efficiency is modelled as

$$\eta_{\mathrm{bf}}(t_{\mathrm{op}}) = 0.80 - 0.10 \cdot \frac{t_{\mathrm{op}}}{440},$$

where t_{op} is the cumulative ISRU operating time in hours. The ISRU system operates for approximately 440 h over the total mission duration of approximately 44,000 h. The backflush efficiency therefore decreases from 80% at the beginning of life to 70% after 440 h of operation. This preliminary degradation model needs to be verified through testing and exposure to representative sulphuric acid aerosols.

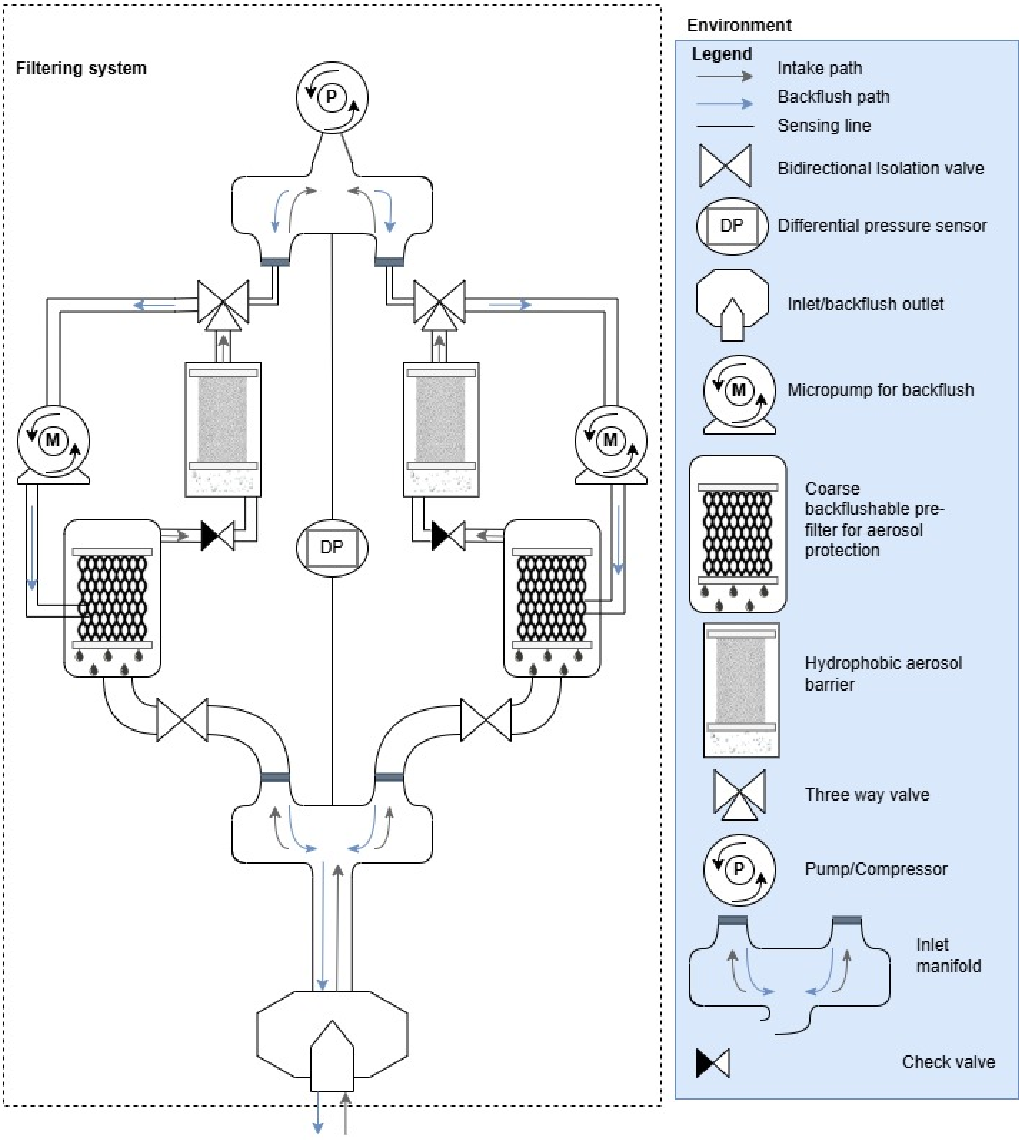

Figure 7.5: ISRU Filtering System

Nitrogen Separator Membrane Sizing

This section describes the nitrogen separator membrane sizing procedure. As mentioned in section 7.1, a polymeric membrane separator is used to separate the N_2 from the CO_2. The separator is a pressurised vessel containing a CO_2-selective layer. Following the solution-diffusion mechanism, CO_2 permeates through the dense polymer, while N_2 is retained on the feed side. A porous support layer is needed for the membrane to retain structural integrity. For the selective layer, Pebax is used [114], as it provides good CO_2 permeability, while for the porous support, polysulphone has been chosen, which provides good structural integrity. PEEK has been chosen as the main casing material, as it is light and provides the necessary protection for the membrane.

Although CO_2 is larger and heavier than nitrogen, it permeates more easily through Pebax due to its high solubility in the polar polyether segments and its linear molecular shape. The permeated CO_2 is collected for the filtering system backflush and later vented, while the retained N_2 is sent further into the balloon. In order to find the membrane area, a membrane thickness of 5 μm is first assumed [115], together with a typically used separator operating pressure of 2 bar [116] and a Pebax CO_2 permeability of 100 Barrer [114]. Next, the CO_2 flux through the membrane is calculated using [117]:

$$J_{CO_2} = \frac{\Pi_{CO_2}}{t_{\text{mem}}} \cdot \Delta p_{CO_2} \tag{7.24}$$

with the CO_2 partial-pressure difference defined as:

$$\Delta p_{CO_2} = x_{CO_2} \left(p_{\text{sep}} - p_{\text{amb}} \right) \tag{7.25}$$

This pressure difference is needed to generate flux, as without it the membrane would not function. This is the reason the feed gas must first be compressed above ambient pressure.

Next, the CO_2 fraction that must be rejected is calculated from the feed flow already computed, multiplied by the fraction of CO_2 in the atmosphere:

$$\dot{n}_{CO_2} = x_{CO_2} \cdot \dot{n}_{\text{feed}} \tag{7.26}$$

The membrane area is then computed by dividing the required CO_2 rejection rate by the flux:

$$A_{\text{mem}} = \frac{\dot{n}_{CO_2}}{J_{CO_2}} \tag{7.27}$$

This gives a membrane area of roughly 11.2 m^2. Table 7.8 summarises all the material and membrane properties:

Table 7.8: Membrane module material properties

Component	**Material**	**Thickness [μm]**	**Density [kg/m^3]**
Selective layer	Pebax	5	1140
Porous support layer	Polysulfone	100	1250 [118]
Casing	PEEK	–	1310 [119]
Overall membrane area		**11.2 m^2**	

Now the casing that will hold the membrane needs to be sized. First, the membrane mass is calculated as:

$$m_{\text{membrane}} = A_{\text{mem}} \left(\rho_{\text{selective}} t_{\text{selective}} + \rho_{\text{porous}} t_{\text{porous}}\right) \tag{7.28}$$

In order to account for the membrane, spacers, support etc., the packaging thickness of the membrane is assumed to be around $t_{\text{pack}} = 0.5$ mm. The packaging volume is then calculated as:

$$V_{\text{pack}} = A_{\text{mem}} \cdot t_{\text{pack}} \tag{7.29}$$

and a safety margin of 1.5 is applied, hence:

$$V_{\text{module}} = 1.5 \cdot V_{\text{pack}} \tag{7.30}$$

The casing is then estimated to be cylindrical, and its length is assumed to be 0.25 m. Solving the volume equation for the diameter:

$$V_{\text{cylinder}} = \frac{\pi d^2 L}{4} \tag{7.31}$$

This results in a cylinder diameter of 0.17 m.

In order to estimate the thickness of the casing, the thin-walled pressure vessel formula is used. The pressure inside the cylinder is the separator operating pressure of $2 \cdot 10^5$ Pa, while the lowest ambient pressure over the operating range, according to Table 7.4, is 33071 Pa, hence the worst-case pressure differential is 166929 Pa. The ultimate tensile strength of PEEK is $\sigma_{\text{ult}} = 116$MPa [119], and a safety factor of 3.0 is assumed, meaning $\sigma_{\text{allowed}} = 38.7$ MPa:

$$t_{\text{req}} = \frac{\Delta p \cdot r}{\sigma_{\text{allowed}}} \tag{7.32}$$

which gives a value of 0.316 mm. The actual wall thickness, however, is taken as $t_{\text{case}} = 1$ mm to provide an additional margin of safety. With this in mind, the mass of the cylinder shell and the two end caps can be calculated as:

$$m_{\text{shell}} = 2\pi \cdot r \cdot L \cdot \rho_{\text{PEEK}} \cdot t_{\text{case}} \qquad m_{\text{endc}} = 2 \cdot \pi r^2 \cdot \rho_{\text{PEEK}} \cdot t_{\text{case}} \tag{7.33}$$

Applying a 20% margin:

$$m_{\text{case}} = 1.2 \cdot (m_{\text{endc}} + m_{\text{shell}}) \tag{7.34}$$

Finally, the total mass of the separator can be computed as:

$$m_{\text{tot}} = m_{\text{case}} + m_{\text{membrane}} \tag{7.35}$$

Which gives a total separator mass of 1.832 kg.

The final separator model CAD drawing is shown in Figure 7.6. The gas from the filtering system is pumped into the separator through the tube on the left. The layer highlighted in red represents the porous support layer, while the layer shown in yellow represents the selective layer, which performs the actual gas separation. The tank located at the top-right of the separator corresponds to the CO_2 storage and vent system, where part of the separated CO_2 is stored and later used for backflushing the filtering system when required, while the rest is vented into the atmosphere. The tube on the right is then used to direct the N_2-enriched gas into the altitude control system.

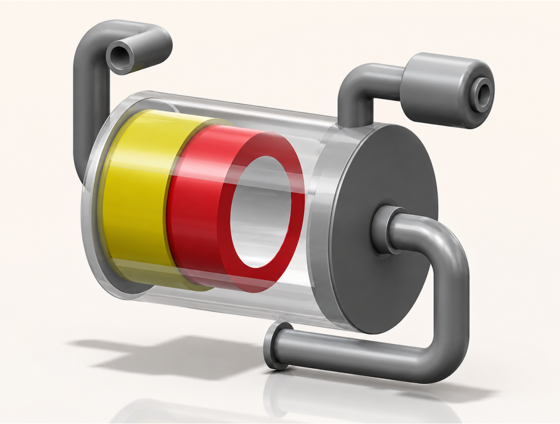

Figure 7.6: N_2 Separator Model

7.3. Balloon Envelope and ISRU Power Consumption Estimation

This section aims to quantify the reliability of both the balloon envelope and the ISRU system. Since the system is still at its planning stage and cannot be tested yet, the reliability cannot be quantified with high accuracy, but only approximately, which is appropriate at this stage of development.

7.3.1. Envelope Reliability Estimation

In order to quantify the reliability of the balloon envelope, Weibull survival model will be used, where reliability is defined as [120]:

$$R(t) = P(T > t) = \exp\left[-\left(\frac{t}{\eta}\right)^{\beta}\right] \tag{7.36}$$

where

- $R(t)$ is the reliability function, defined as the probability that the component survives beyond time t.
- T is the random variable representing time to failure.
- t is the operating time or mission duration.
- η is the characteristic life parameter.
- β is the Weibull shape parameter. For wear-out failures, $\beta > 1$ [121].

In the case of a balloon envelope, β value of 2.0 has been chosen, as the number of potential failures is expected to increase toward the end of the mission, due to material degradation.
For the characteristic life η, on the other hand, there is no reliable known value. It is defined as the period by which approximately 63.2% of the envelopes would have failed, which is roughly equivalent to $\frac{2}{3}$. No representative heritage missions exist, apart from Vega-1 and Vega-2, which both lasted approximately two Earth days. If this value were used as the characteristic life, the reliability would essentially be 0. Therefore, a different approach has been used. Reliability was not computed directly. Instead, the value of η was adjusted such that the reliability is able to comply with the requirement (> 0.9). This could be useful for testing in the future stages of the mission. With the mission lifetime $t = 5$ years, wear-out factor $\beta = 2$, and reliability $R(t) > 0.9$, the characteristic life needed is approximately 5650 Earth days, or approximately 15.5 years. This means that in order for the balloon envelope designed for a 5-year mission to have a reliability greater than 0.9, out of 100 identical balloons placed in the same operating environment, approximately 63 would only be expected to have failed by 15.5 years.

7.3.2. ISRU Components Reliability

The component reliability has also been quantified using the Weibull survival model. Some existing components have been identified, and their expected operational lifetime in hours has been chosen as a slightly conservative characteristic value. The same β of 2.0 as for the envelope has been chosen. The same formula (7.36) has then been applied to each component, and summarised in the table below:

Table 7.9: ISRU component reliability inputs.

Component	Number of components	η	Mission Exposure	Component reliability
Valves	11	10m cycles [122]	10000 cycles	0.999
Pre-filter	2	30000h [112]	22000h	0.584
Filter	2	30000h [112]	22000h	0.584
Differential pressure sensor	1	1.7m hours [123]	22000h (5y)	0.999
Backflush micro-pump	2	10000h [124]	200h	0.999
Main pump/compressor	1	20000h [125]	22000h	0.298
N_2 separator	1	40000h [126]	22000h	0.739
N_2 pump	1	20000h [125]	22000h	0.298
Pressure sensor	2	1.7m hours [123]	22000h	0.999
Tubes/connections	1 set	–	22000h	0.95

The filtering system, however, has two branches, hence the reliability of each branch was calculated in parallel using:

$$R_s = 1 - \prod_{i=1}^{n} (1 - R_i) \tag{7.37}$$

Which resulted in:

$$R_s = 1 - \left(1 - 0.999^6 \times 0.584 \times 0.584\right)^2 = 0.566 \tag{7.38}$$

For the remaining components, the subsystem reliability was calculated by raising the single-component reliability value to the power of the number of identical components. The results can be seen in Table 7.10.

Table 7.10: Total ISRU system reliability.

Parameter	Value
Total ISRU reliability	3.53%

The 3.5% reliability is far below the 90% set by the requirements. This is due to the ISRU system still being at its planning stage, meaning that it cannot yet be manufactured or tested. Therefore, the reliability can only be roughly estimated, and will also be much lower due to the large number of components, the lack of representative heritage data, and the uncertainty in long-term operation within the Venus atmospheric environment. As a result, this value should not be interpreted as a final reliability prediction, but rather as an indication that the ISRU system would require significant testing, redundancy, and design optimisation in later development stages.

7.3.3. ISRU Power Consumption Estimation

As can be seen in Figure 7.2, some components consume power from the battery. This power needs to be estimated, in order to determine whether the aerobot will be able to comply with the requirement regarding power consumption 10.4.

Some of the constants used in the power consumption estimation process, as well as some power values from known components are listed in Table 7.11:

Table 7.11: Fixed input values used in the ISRU power estimation

Variable	Description	Value
x_{N_2}	Nitrogen mole fraction in Venus atmosphere	0.035
x_{CO_2}	Carbon dioxide mole fraction in Venus atmosphere	0.965
T_{ref}	Reference compressor inlet temperature	302.3 K [103]
p_{ref}	Reference atmospheric pressure at 55 km	53183 Pa [103]
p_{sep}	Separator operating pressure	2×10^5 Pa
γ	Feed gas specific heat ratio (CO_2-rich)	1.3
γ_{N_2}	Nitrogen specific heat ratio	1.4
η_{comp}	Compressor efficiency	0.50
η_{N_2}	N_2 recovery efficiency	0.70
f_{active}	Active operating fraction	0.5
$SF_{p,\text{gas}}$	Gas processing pressure margin	1.2
$SF_{P,\text{gas}}$	Gas processing power margin	1.3
$SF_{p,\text{alt}}$	Altitude control pressure margin	1.2
$SF_{P,\text{alt}}$	Altitude control power margin	1.3
Δp_{line}	Altitude control line pressure loss	2000 Pa
$\dot{m}_{N_2,\text{transfer}}$	N_2 transfer between ZP and SP balloons in one Cycle	45 kg/cycle
P_{valve}	Rated valve power (×11)	0.4 W
DC_{valve}	Valve duty cycle	0.5
P_{sensor}	Pressure sensor power (×3)	0.5 W
$P_{\text{pump,micro}}$	Filter backflush micro-pump power	0.7 W
$DC_{\text{pump,micro}}$	Filter backflush micro-pump duty cycle	0.01

Power estimation starts with the maximum amount of nitrogen that needs to be replenished per cycle. Since the balloon is set to operate at an altitude of 54–57 km, the highest leakage value is chosen from graph 7.3c at a wind speed of 3 m/s, leading to $\dot{m}_{N_2} = 1.872$ kg/cycle.Since the ISRU only operates during the dayside, the required production rate must be increased. For simplicity, the ISRU is assumed to be operational for 50% of the full cycle. Therefore, an active fraction of $f_{\text{active}} = 0.5$ is imposed, leading to a molar production rate of:

$$\dot{n}_{N_2} = \frac{\dot{m}_{N_2}}{M_{N_2}\, t_{\text{cycle}}\, f_{\text{active}}} \tag{7.39}$$

Since Venus's atmosphere is only 3.5% N_2, and the separator recovery efficiency is assumed to be only 70% ($\eta_{N_2} = 0.7$), the total atmospheric feed that must be passed through the ISRU, and the corresponding feed mass flow, are:

$$\dot{n}_{\text{feed}} = \frac{\dot{n}_{N_2}}{x_{N_2}\, \eta_{N_2}}, \qquad \dot{m}_{\text{feed}} = \dot{n}_{\text{feed}}\, M_{\text{feed}} \tag{7.40}$$

where $M_{\text{feed}} = x_{N_2} M_{N_2} + x_{CO_2} M_{CO_2}$ is the mean molar mass of the feed gas.

The feed gas is compressed from the ambient pressure $p_{\text{amb}} = 53{,}183$ Pa to the separator pressure of 2×10^5 Pa, providing the partial pressure difference necessary to keep the separator working. To account for pressure losses in the intake, tubing, and separator module, the target pressure is increased by a pressure margin $SF_{p,\text{gas}}$ of 1.2:

$$p_{\text{sep,eff}} = SF_p\, p_{\text{sep}}, \qquad PR = \frac{p_{\text{sep,eff}}}{p_{\text{amb}}} \tag{7.41}$$

The compressor power is then calculated using the standard adiabatic compressor equation:

$$P_{\text{gas}} = \dot{n}_{\text{feed}}\, R\, T\, \frac{\gamma}{\gamma - 1} \left[PR^{\frac{\gamma-1}{\gamma}} - 1 \right] \frac{SF_P}{\eta_{\text{comp}}} \tag{7.42}$$

with $\gamma = 1.3$ for the CO_2-rich feed, compressor efficiency $\eta_{\text{comp}} = 0.50$, and a power safety factor $SF_P = 1.3$ covering heat losses and modelling uncertainty. This term dominates the total ISRU power budget.

Next, the altitude control system is responsible for pumping the gas into the ZP balloon and between the ZP and SP envelopes in order to control the buoyancy and hence the altitude. The pump must overcome the overpressure of the balloon, which is the difference between the ambient pressure and the pressure inside the SP balloon. For safety, a Δp of 25 kPa was chosen, plus an assumed line pressure loss of 2,000 Pa, with an additional pressure margin $SF_{p,\text{alt}}$ of 1.2 applied to the sum:

$$\Delta p_{\text{eff}} = SF_p\left(\Delta p + \Delta p_{\text{line}}\right), \qquad PR_{\text{alt}} = \frac{p_{\text{ref}} + \Delta p_{\text{eff}}}{p_{\text{ref}}} \tag{7.43}$$

This is sized to account for the losses with a generous margin. In reality, at that altitude range this overpressure will never be reached with the envelope parameters used. The specific compression work per kilogram of N_2 uses the same adiabatic relation, with $\gamma_{N_2} = 1.4$ and c_p from the specific gas constant of nitrogen:

$$w = c_p\, T_{\text{ref}}\left[PR_{\text{alt}}^{\frac{\gamma_{N_2}-1}{\gamma_{N_2}}} - 1\right]\frac{1}{\eta_{\text{comp}}}, \qquad c_p = \frac{\gamma_{N_2}}{\gamma_{N_2}-1}\frac{R}{M_{N_2}} \tag{7.44}$$

The N_2 transfer mass is then assumed to be 45 kg/cycle between the ZP and SP envelopes, which is also a very conservative value, as an N_2 mass difference of roughly 4.5–5.5 kg is needed to alter the altitude by 1 km in that altitude range. The power of the altitude control pump then follows from the per-cycle N_2 transfer mass of 45 kg/cycle, spread over the dayside operating hours, with a power safety factor $SF_{P,\text{alt}}$ of 1.3:

$$P_{\text{alt}} = \frac{\dot{m}_{N_2,\text{transfer}}\, w}{t_{\text{cycle}}\, f_{\text{active}}}\, SF_P \tag{7.45}$$

Next, smaller electrical components such as valves, pressure sensors and micro-pumps for backflush are accounted for, with their respective duty cycles. They sum up to:

$$P_{\text{aux}} = N_{\text{valve}} P_{\text{valve}} DC_{\text{valve}} + N_{\text{sens}} P_{\text{sens}} + P_{\text{pump,micro}} DC_{\text{pump,micro}} \tag{7.46}$$

The power consumption estimation is considered for the worst-case leakage scenario at end of life. The table summarising the power consumption summary can be seen in Table 6.15.

7.4. Verification and Validation

Verification and preliminary validation were carried out for both the balloon sizing and ISRU power consumption estimation. Verification was based mainly on analytical checks of the equations used in the models and comparisons with the code outputs.

The balloon sizing model was checked against the altitude range, envelope mass, structural sizing and leakage requirements. The model shows that the aerobot can operate within the required atmospheric pressure and temperature range, therefore supporting REQ-C-ENV-01 and REQ-C-ENV-02 from section 10.4. In a sensitivity case with a maximum altitude of 62 km, the required envelope mass is 67.22 kg. When the maximum altitude is decreased to 58 km, the envelope mass drops to 45.54 kg, corresponding to a mass saving of roughly 32%.

The superpressure balloon design was verified by comparing the required thickness from the pressurised sphere formula with the selected material architecture thickness. The leakage rate was verified by checking the permeability conversion and confirming that leakage scales correctly with zero-pressure envelope area, pressure difference and thickness. The resulting N_2 replenishment rate was then used as an input to the ISRU power estimation model.

The ISRU power estimation model was verified by recomputing the compressor power by hand for a unit N_2 requirement and comparing it with the code output, confirming that the power scales linearly with the required replenishment rate. The energy conversion from compression work per kilogram to average power was also checked, and the main power components were separated into auxiliary power, gas processing power and altitude-control power. The required intake volumetric flow was additionally checked against the rated flow of the selected COTS pump.

Both models are still preliminary. Analytical verification has been completed, while validation remains limited to comparison of the main assumptions with existing aerobot studies, including static force equilibrium, SP/ZP volume behaviour, ideal gas assumptions and pressure-based altitude-control logic [103]. Long-term material degradation, seam leakage, corrosion damage, manufacturing damage and clogging are not modelled directly. Their effects are represented through conservative degradation and leakage factors or considered qualitatively in the design. These effects are particularly important for REQ-F-ENV-03 in section 10.4. Further validation should include Venus cloud material exposure testing, permeability testing of the final laminate including seams, manufacturing defect inspection, and clogging tests for the ISRU intake and separator.

8 Entry, Descent, Deployment, & Inflation

This chapter covers the Entry, Descent, and Deployment & Inflation (EDDI) phase: from the entry interface at ∼140 km (inertial entry velocity) down to free-float capture at ≈56 km, spanning ≈879 s in total (parachute deploy at 81.6 s plus ≈800 s of subsonic descent and inflation). Within this envelope, Deployment owns the aeroshell aerodynamics and TPS, the parachute system, trigger logic, the separation and jettison sequence, and inflation flow control. It interfaces with, the ISRU/inflation gas inventory, the structural integration of the COPV-as-structure and ring loads (STRUC), transient power delivery (EPS, Table 8.6), and the deployment sequencer and telemetry (CDHS).

8.1. System Architecture Overview

The selected EDDI architecture is a DGB pilot and reefed-to-full ringsail main, packed inside a 45° sphere-cone aeroshell with an all-composite CFRP sandwich structure and carbon-phenolic TPS. The entry is spin-stabilised, the parachute sequence is initiated by a single mortar, and the mass is optimised by integrating the lifting gas storage into the load path.

The architecture is retained because it is heritage-anchored, and reliability optimised, closes at 321.1 kg without margin and 373.0 kg with margin. The Mach 1.44 deployment point also avoids relying on a late transonic deployment. The full trade is not repeated here and is given in the Midterm Review [17].

Configuration and Layout

The entry stack fits inside a 1.86 m diameter aeroshell with $S_{ref} = 2.72\,\mathrm{m}^2$, $R_n = R_{base} = 0.93\,\mathrm{m}$, a forebody depth of about 0.93 m, and a total stack height of about 1.5 m. The COPV is placed on the base of the stack, the gondola sits above, followed by the balloon envelope and parachute. The deployed ringsail has a diameter of 8.0 m, giving a 4.3× increase in linear size and roughly an 18× increase in area compared to the stowed aeroshell diameter.

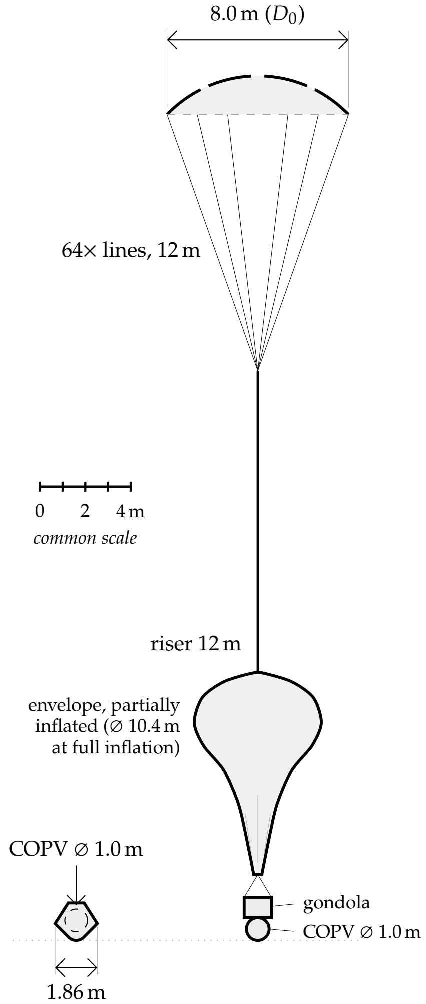

(a) Stowed entry aeroshell **(b) Deployed aerial inflation under main**

Figure 8.1: Stowed-versus-deployed scale figure showing the 1.86 m aeroshell and the 8.0 m ringsail during aerial inflation of the balloon envelope.

Table 8.1: EDDI component ledger from the live bottom-up MEL: ECSS-maturity-margined mass.

Component group	**CBE [kg]**	**+marg. [kg]**
1.3.1 Entry & thermal protection		
Aeroshell structure	99.9	112.1
Thermal protection (ablator)	38.0	44.9
HS release	0.8	1.0
1.3.2 Descent & deceleration		
Pilot DGB	4.3	4.8
Main ringsail stack	18.0	20.0
1.3.3 Inflation & float capture		
COPV storage (shell, saddles)	146.1	174.1
Inflation flow path	5.7	6.8
Apex	1.9	2.2
1.3.4 / 1.3.5 Separation, sequencing		
Aeroshell separation	2.0	2.3
Chute cut-away	0.2	0.2
Trigger	0.2	0.2
Controller	3.5	3.9
Telemetry & safing	0.4	0.5
Total	**321.1**	**373.0**

The packed component volume is approximately $0.96\,\mathrm{m}^3$ inside an available internal volume of about $1.4\,\mathrm{m}^3$, giving $\eta_{\text{pack}} \approx 69\%$. A 10% installation allowance is reserved for harnessing, fittings, and local structural clearances, leaving ≈ 21% net volume headroom. The stack CG is on-axis at $z \approx 0.82$ m, about 70 mm ahead of the volumetric centroid. The forward COPV placement keeps the CG favourable for entry stability. Table 8.1 gives the frozen component ledger.

EDDI Operations Sequence

The EDDI sequence runs from entry interface to free float in about 879 s. The final event order is shown in the updated sequence figure.

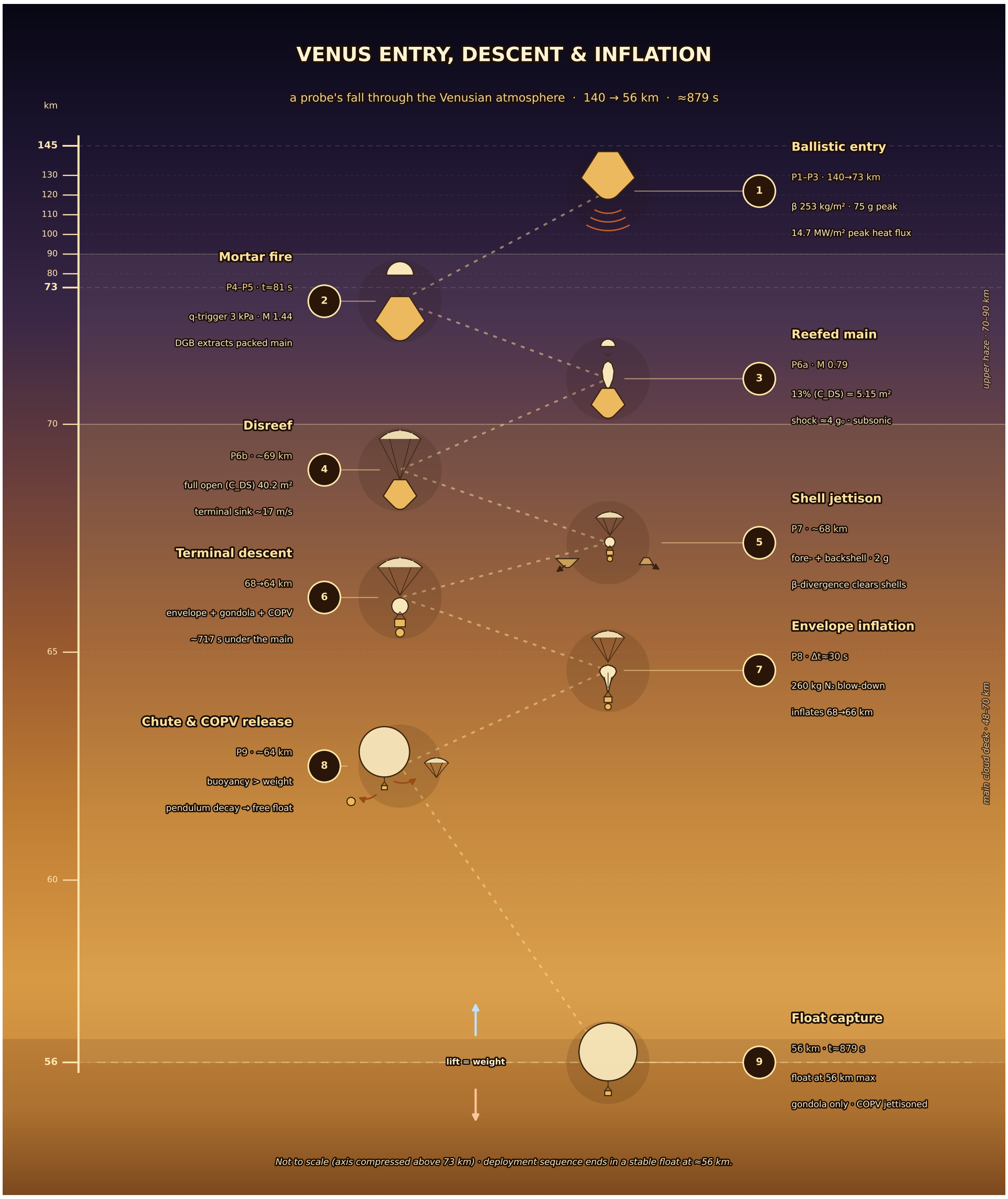

Figure 8.2: Venus atmospheric entry and EDDI deployment sequence from entry interface to float capture, ≈879 s end-to-end: ballistic entry, dynamic-pressure-triggered mortar fire, DGB extraction of the reefed ringsail, disreef, aeroshell jettison, terminal descent, 260 kg N_2 blow-down inflation, parachute release, and float capture at 56 km.

During P1–P3 the vehicle flies a ballistic entry on the aeroshell at $\beta = 253\,\text{kg/m}^2$, decelerating from the entry interface to the deployment gate at 73 km. The p97.5 load case sets the structural envelope: 78.6 g_0 peak deceleration at $t \approx 39$ s and a peak forebody heat flux of $14.7\,\text{MW/m}^2$.

Parachute deployment is triggered on dynamic pressure, $q = 3000\,\mathrm{Pa}$, reached at 72.7 km and Mach 1.44 ($t \approx 82\,\mathrm{s}$). A verticle position accuracy of tens of meters is expected from the barometer as seen in Subsection 6.8.2. A single mortar fires the DGB pilot, which extracts the main ringsail in its reefed state. Reefing to 13% of the full $C_D S$ ($5.15\,\mathrm{m}^2$) caps the opening shock at 24.7 kN, approximately $3.65\,g_0$, and carries the stack subsonic to Mach 0.79.

Disreef to $C_D S = 40.2\,\mathrm{m}^2$ follows at approximately 69 km, settling the stack to a terminal sink rate of approximately 17 m/s. Once subsonic, the forebody and backshell are jettisoned at approximately 68 km under a $2.0\,g_0$ separation load. Re-contact is not expected, as the discarded shells rapidly separate from the decelerating stack due to differences in ballistic coefficient.

Balloon inflation runs during terminal descent, between approximately 68 km and 64 km: 252.5 kg of N_2 is blown down from the COPV in approximately 30 s, with a further 7.5 kg retained as make-up gas. At approximately 64 km the ringsail and inflation flow path are released, and the gondola transitions through pendulum decay to free float, capturing the float band with a 56 km ceiling. Active interfaces over the sequence are CDHS sequencing and telemetry throughout, pyro channels across P5–P9, inflation flow control during P8, and the STRUC load path through P1–P7. The thermal effect of rapid N_2 blow-down is not closed at Phase 0: adiabatic/Joule–Thomson temperature drops in the COPV, regulator, valves, and inflation lines must be checked in the next thermal-flow model.

8.2. Entry Trajectory and Deployment Performance

The vehicle arrives at the entry interface datum of 140 km at a planet-relative entry interface velocity of $V_{\mathrm{entry}} = 11.0\,\mathrm{km/s}$ on a nominal flight-path angle of $\gamma_E = -8.0°$, with the ±0.5° dispersion band carried through to the sensitivity analysis (Section 8.6). The corresponding Venus-centred inertial velocity is $V_{\mathrm{inertial}} = V_{\mathrm{entry}} + V_{\mathrm{atm}}$, where the atmospheric superrotation at 140 km is approximately 60 m/s prograde [127], giving $V_{\mathrm{inertial}} \approx 11.06\,\mathrm{km/s}$. The dispersed run is anchored to the wet entry mass of 689.1 kg, with maturity margins ($\beta = 253.4\,\mathrm{kg/m^2}$), and the dispersed run is to be repeated at this mass. The centre of gravity sits on the stack axis at $z \approx 0.82\,\mathrm{m}$, forward of the centroid for static stability, and the stack is treated as a spin-stabilised symmetric body. Spin-axis and transverse moments of inertia are estimated through Heritage-bounded ROM values, benchmarked against Pioneer Venus Large Probe heritage ($m = 316.5\,\mathrm{kg}$, $D \approx 1.5\,\mathrm{m}$ for the flight probe; an earlier Atlas/Centaur design gives $D = 1.397\,\mathrm{m}$ and a 45° sphere-cone forebody; [128, 129]) and bounded using the VISTA component-ledger mass distribution, give:

$$I_{zz} \approx 100\,\mathrm{kg\,m^2} \text{ to } 130\,\mathrm{kg\,m^2}, \qquad I_{xx} = I_{yy} \approx 140\,\mathrm{kg\,m^2} \text{ to } 160\,\mathrm{kg\,m^2}, \qquad \frac{I_{zz}}{I_{xx}} \approx 0.65 \text{ to } 0.73. \tag{8.1}$$

The inertia ratio indicates a slightly oblate configuration about the spin axis. During atmospheric entry, aerodynamic restoring moments remain larger than gyroscopic stiffness effects, ensuring that the vehicle naturally aligns heatshield-first. This behaviour is consistent with heritage 45° sphere-cone entry probes.

Trajectory Simulation Method

The atmosphere follows VIRA [127], represented by an exponential density fit anchored at both ends of the EDDI altitude range,

$$\rho(h) \;=\; \rho_{56}\, e^{-(h-56)/H}, \qquad \rho_{56} = 0.93\,\mathrm{kg/m^3}, \quad H = 6.05\,\mathrm{km}, \tag{8.2}$$

which reproduces $\rho(72.69\,\mathrm{km}) = 0.051\,\mathrm{kg/m^3}$ at the deployment gate and $\rho(56\,\mathrm{km}) = 0.93\,\mathrm{kg/m^3}$ at the float ceiling. Density-model uncertainty is not a free parameter here; it enters as a sensitivity input in Section 8.6. Entry to parachute deploy is integrated as a planar ballistic trajectory. The vehicle is modelled as a point mass at zero lift, so the equations of motion reduce to:

$$\dot{V} = -\frac{\rho(h)\,V^2}{2\beta} - g\sin\gamma, \qquad V\dot{\gamma} = \left(\frac{V^2}{R_V + h} - g\right)\cos\gamma, \qquad \dot{h} = V\sin\gamma, \tag{8.3}$$

with γ measured positive above the local horizon, ballistic coefficient $\beta = m/(C_d S)$, regime-dependent drag coefficient $C_d(M)$ (Table 8.3), Venus radius $R_V = 6051.8\,\mathrm{km}$, and gravity held at the value $g = 8.87\,\mathrm{m/s^2}$. The integration is Monte-Carlo dispersed, with p50 and p97.5 percentiles reported.

Aeroshell drag terminates at parachute deployment, below which, the descent reduces to a quasi-terminal one-dimensional balance: weight equals drag within a few seconds of each canopy stage opening, so the stack settles to:

$$v_t(h) = \sqrt{\frac{2mg}{\rho(h)\,C_D S}}, \qquad T_{sub} = \int_{h_f}^{h_0} \frac{\mathrm{d}h}{v_t(h)}, \tag{8.4}$$

evaluated from deploy to the 56 km hand-off with the stage-appropriate $C_D S$ and the post-jettison mass in each phase.

Entry Performance Results

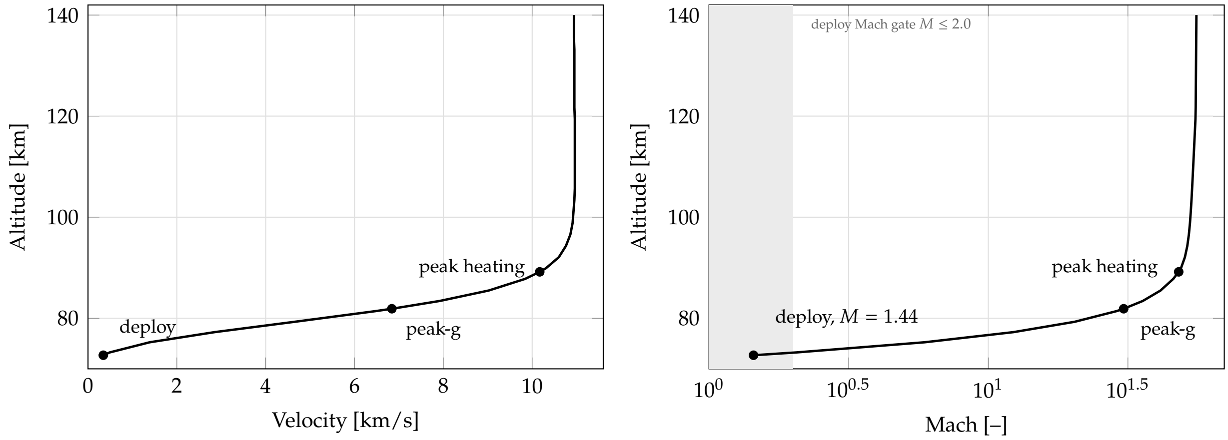

Figure 8.3: Altitude versus velocity (left) and Mach number (right) for the locked $\gamma_E = -8.0°$ nominal entry from the 140 km interface. Markers: peak heating ($t \approx 33.5$ s, 89.2 km), peak deceleration ($t \approx 39.5$ s, 81.9 km), and parachute deploy ($t \approx 81.6$ s, 72.7 km, $q = 3000$ Pa, $M = 1.44$). Shaded band: deploy Mach gate $M \leq 2.0$.

Peak deceleration is 75.4 g_0 (p50) and 78.6 g_0 (p97.5) at $t \approx 39.3$ s, a factor of ≈2.5 below the 200 g_0 structural cap. Peak dynamic pressure coincides with peak-g; by the deployment gate, q has decayed to the 3000 Pa cap.

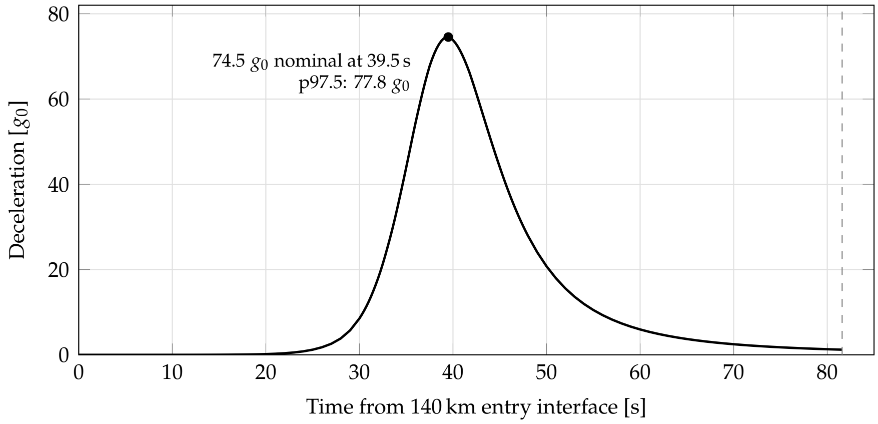

Figure 8.4: Sensed deceleration versus time for the nominal −8.0° entry from the 140 km interface. The peak of 74.5 g_0 nominal (77.8 g_0 at p97.5) occurs at $t \approx 39.5$ s and remains a factor ≈2.7 below the 200 g_0 structural cap. Mortar fire occurs at $t \approx 81.6$ s when $q = 3000$ Pa and $M = 1.44$.

Peak heat flux is 13.7 MW/m^2 for the synced baseline and 14.7 MW/m^2 at p97.5. This is below the 20 MW/m^2 peak heat flux reported for the ESA Venus Entry Probe 45° sphere-cone concept at a 40° entry angle; the same source reports carbon–phenolic capability of approximately 300 MW/m^2, so the 20 MW/m^2 value is used here only as a mission-reference case, not as a material limit [130]. Relative to that reference case, the p97.5 heat-flux margin is $(20/14.7) - 1 \approx 34\%$. The integrated heat load is 17 540 J/cm^2, comparable to the ~ 20 kJ/cm^2 range cited for Venus and sample-return-class entries [131].

Deployment Trigger Definition

Deployment fires when q enters the 200–3000 Pa window with $M \leq 2.0$; the nominal firing point is $M = 1.44$ at $q = 3000$ Pa, 72.69 km, and $t = 81.6$ s. The window guarantees the DGB brings the stack subsonic ($M \leq 0.8$; terminal $M = 0.79$) before ringsail disreef.

The deployment trigger is issued when the forebody pressure transducer measures $q \leq 3000\,\mathrm{Pa}$ and $M \leq 2.0$. For the current 140 km interface state, nominal deployment occurs at $t = 81.6\,\mathrm{s}$, altitude 72.69 km, $M = 1.44$, and $q \approx 3000\,\mathrm{Pa}$. To guarantee deployment within the qualified 200 Pa to 3000 Pa corridor, the pressure transducer requires an absolute accuracy of at least ±300 Pa (±10% of the trigger threshold). Near deployment, dynamic pressure decreases at approximately 157 Pa/s, so this uncertainty corresponds to a trigger-time uncertainty of approximately ±1.9 s. The current p95 deployment interval is 77.9 s to 85.4 s from the 140 km interface, equivalent to 117.1 s to 124.6 s on the old 200 km clock. A redundant accelerometer provides a backup trigger, arming the timer sequence once deceleration falls below ~5 g_0 following the entry peak-g event, in the event of pressure-sensor failure.

EDDI Timeline and Phase Summary

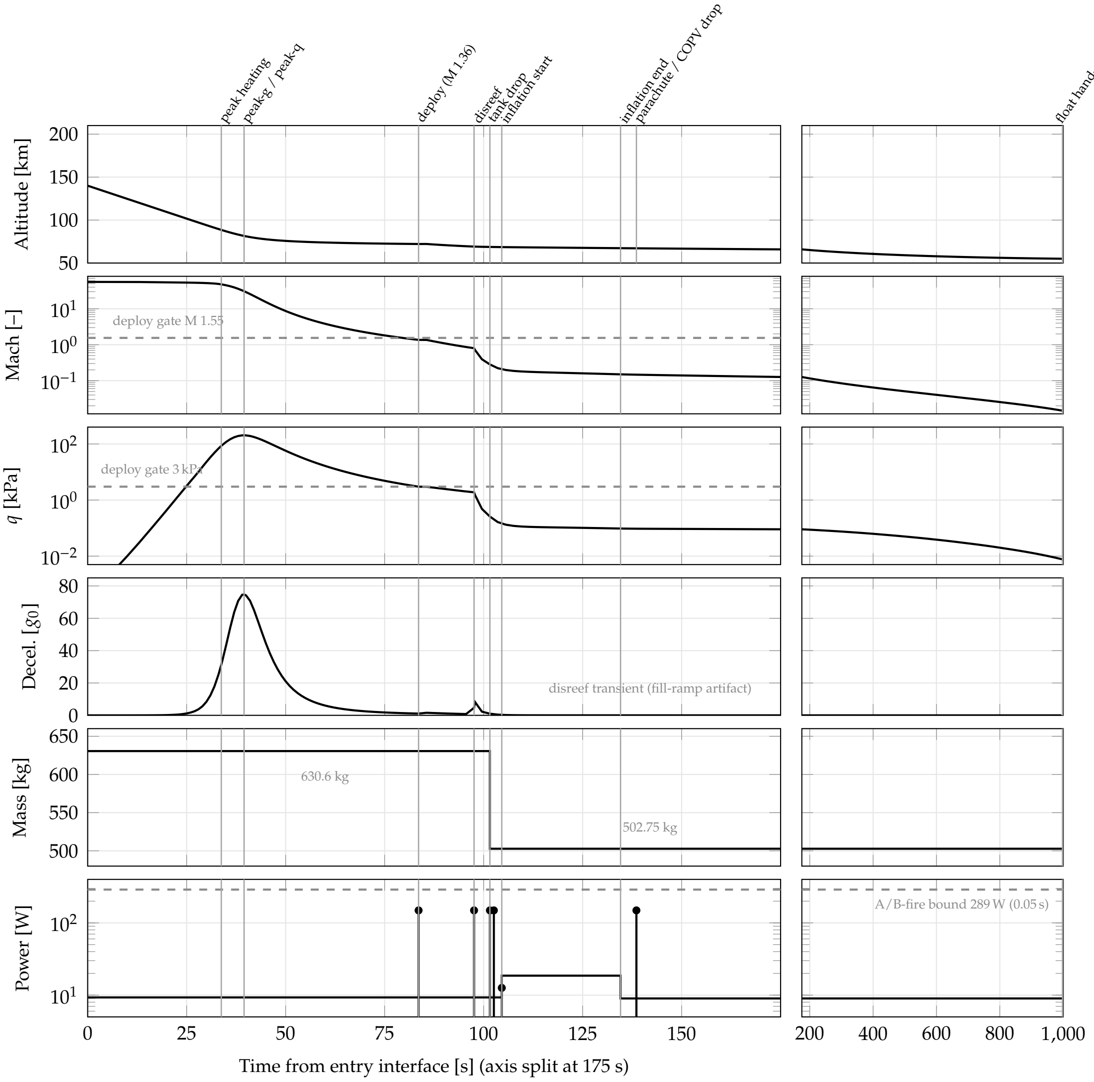

Figure 8.5: EDDI composite timeline from the 140 km entry-interface initial condition to float hand-off: altitude, Mach, dynamic pressure, sensed deceleration, stack mass, and EDDI bus power on a shared time axis, split at 175 s (expanded left of the break, compressed right). Entry channels are the locked $\gamma_E = -8.0°$ nominal Monte-Carlo run; descent channels are the 1D post-deploy model (deploy $t = 83.6\,\mathrm{s}$, disreef $t = 97.6\,\mathrm{s}$, tank drop $t = 101.6\,\mathrm{s}$, inflation 104.6 s to 134.6 s, parachute/COPV drop $t = 138.6\,\mathrm{s}$, float hand-off at 55 km, $t = 997.8\,\mathrm{s}$). Mass steps follow the model basis (630.6 kg entry stack, 502.75 kg post-jettison); power per Table 8.6 with 0.05 s pyro transients drawn as stems; the disreef deceleration spike is a model fill-ramp artifact, not a booked load.

Events are marked at entry ($t = 0$), peak heating (33.5 s), peak-g and peak-q (39.3 s), deploy (81.6 s, Mach 1.44), disreef (~69 km), separation (~68 km), inflation (P8), and float hand-off (≈56 km, $t \approx 879\,\mathrm{s}$). Table 8.2 summarises each phase by altitude band, key event, and success criterion.

Table 8.2: EDDI phase-by-phase summary.

Phase	Alt. band	Key event	Success criterion
P1–P3 Entry	140→72.7 km	peak-g 75.4 g_0, peak flux 13.7 MW/m^2	survive g & flux caps
P4–P5 Trigger	72.7 km	mortar fire, M 1.44, q 3000 Pa	deploy inside q window
P6a Reefed inflate	72.7→68.8 km	opening shock 24.7 kN (~3.65 g_0)	stack reaches disreef gate (M 0.80)
P6b Disreef	68.8 km	full ($C_D S$) 40.2 m^2	full-ringsail drag state established
P7 Separation	68.4 km	forebody + backshell jettison, M 0.31	clean β-divergence
Descent	67.0→56.0 km	quasi-terminal descent to t = 879.6 s	altitude for float capture
P8 Inflation	68→64 km	260 kg N$_2$, 30 s	envelope full, buoyant
P9 Chute release	64 km	ringsail + flow-path release	buoyancy takeover
Float capture	56.0 km	56-km crossing, residual descent ~6.8 m/s	transition to float-control/capture

8.3. Aerodynamic, Structural and Stability Characteristics

Aerodynamic Characteristics

The aeroshell is a 45° sphere-cone with reference area $S_{ref} = 2.72\,\mathrm{m}^2$. Its drag coefficient is constructed by modified-Newtonian theory and anchored to flown / proposed sphere-cone databases (Pioneer Venus, Galileo, DAVINCI); Table 8.3 carries the regime-by-regime justification. The ballistic coefficient follows directly,

$$\beta = \frac{m}{C_d\, S_{ref}} = \frac{689.1}{1.00 \times 2.72} = 253.4\,\mathrm{kg/m^2}. \tag{8.5}$$

The DGB pilot has $C_{d0} = 0.52$ on $D_0 = 4.2\,\mathrm{m}$ ($S_0 = 13.85\,\mathrm{m}^2$), giving $C_D S = 7.20\,\mathrm{m}^2$; it delivers a supersonic deceleration of ≈21.6 kN (≈3.5 g_0) and brings the stack to a terminal Mach of ≈0.79 at ~72 km. The main ringsail deploys reefed to ~13% of full $C_D S$, i.e. $C_D S \approx 5.15\,\mathrm{m}^2$, which caps the opening shock at ≈3.65 g_0 (24.7 kN). Fully open, the ringsail provides $C_{d0} = 0.80$ on $D_0 = 8.0\,\mathrm{m}$ ($S_0 = 50.3\,\mathrm{m}^2$), giving $C_D S = 40.2\,\mathrm{m}^2$ and a terminal sink of ≈17 m/s after disreef.

Table 8.3: Working $C_d(M)$ database for the EDDI trajectory model (aeroshell on S_{ref}; parachutes on S_0).

Body	Mach	C_d	Basis
Sphere-cone	25 / 10 / 5	1.05 / 1.04 / 1.02	45° sphere-cone anchor; smooth hypersonic model taper [132]
Sphere-cone	1.44 (deploy)	1.01	Model deploy-point interpolation from sphere-cone curve [132]
Sphere-cone	0.8 / 0.5	0.92 / 0.88	Low-Mach interpolation from sphere-cone curve [132]
DGB pilot	2.0 / 1.0 / 0.2	0.48 / 0.55 / 0.62	Model points within DGB C_{D0} ~ 0.4–0.7 range; MSL subsonic bound [133, 134]
Ringsail	0.6 / 0.2	0.78 / 0.80	Representative subsonic ringsail value, C_{D0} ~ 0.8 [133]

Structural Characteristics

Three load events size the deployment structure (Table 8.4). The governing inertial case is entry peak-g: 78.6 g_0 (p97.5) on the 689.1 kg entry mass, producing an ultimate ring reaction of 743.6 kN (limit ×1.4). The parachute opening shock peaks at $F_{max} \approx 24.7$ kN (≈3.65 g_0), or 34.6 kN ultimate, an order of magnitude below the ring reaction, so the riser path does not drive the primary structure. The P7 separation impulse of ≈2.0 g_0 is ≈2.5% of the entry load and is non-binding.

Table 8.4: Deployment load cases at key interfaces.

Event	Load	Interface	Status
Entry peak-g (Event 1)	78.6 g_0	aeroshell ring (127 kN/m)	governing
Reefed opening (Event 2)	24.7 kN (≈4 g_0)	riser / confluence	closed
Separation (Event 3)	2.0 g_0	pusher / backshell IF	non-binding

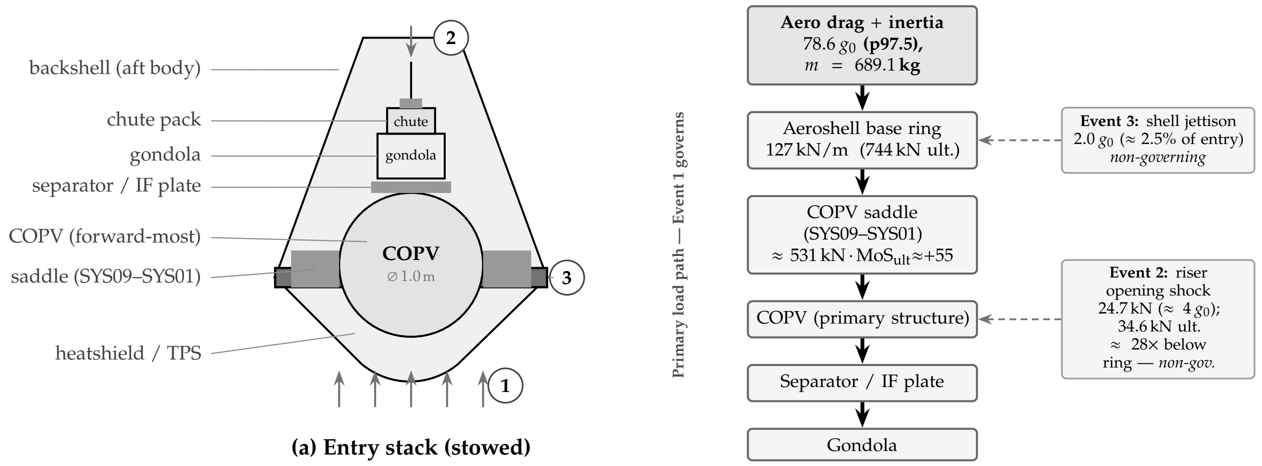

(a) Entry stack (stowed)

not to scale

(b) Load path

Figure 8.6: Deployment structural load path for the stowed entry stack. Panel (a) identifies the structural elements and the three sizing load events; panel (b) traces the governing inertial load. Event 1 (entry peak-g, 78.6 g_0 at p97.5 on $m = 689.1$ kg) reacts at the aeroshell base ring (127 kN/m, 744 kN ultimate) and passes through the COPV saddle (SYS09–SYS01 mechanical interface; ≈531 kN; $\mathrm{MoS}_{\mathrm{ult}} \approx +55$) into the COPV-as-primary-structure, then the separator plate to the gondola. The COPV sits as far forward as possible (lower half inside the forebody cavity) to keep the CG at $z \approx 0.82$ m ahead of the volumetric centroid for static stability. Events 2 and 3 are an order of magnitude smaller and non-governing; saddle joint margins are deferred to FEM at PDR.

The saddle local stresses and joint margins are deferred to more detailed design phases. The deployment-to-structures mechanical interface is captured by the SYS09–SYS01 N^2 interface and by REQ-F-STR-09, which requires the structure to provide the deployment attachment point to the gondola. The saddle reaction set is established at approximately 531 kN at entry peak-g, based on the current 689.130 kg entry mass and 78.6 g peak deceleration. The bondline shear closes with $\mathrm{MoS}_{ult} \approx +55$: the peak shear is $\tau_{peak} \approx 0.089$ MPa against an allowable of ~5 MPa.

Stability Characteristics

The stack enters spin-stabilised at an assumed 10–60 rpm, a range consistent with spin-stabilised planetary entry-probe heritage. The blunt 45° sphere-cone places the centre of pressure aft of the CG at hypersonic incidence, giving positive static pitch stability during the hypersonic entry phase. The main dynamic-stability concern is the known reduction in blunt-body pitch damping near the transonic regime; this is mitigated by deploying the DGB at Mach 1.44, after which riser tension provides additional damping.

The wake-vented DGB carries direct supersonic deployment heritage, and the riser length of $L \approx 12$ m lies within the tested 5–10× forebody-diameter wake-distance range [135, 136]. The reefed ringsail is subsonic-stable by design: disreef occurs only once the stack is subsonic (terminal Mach 0.79 against the 0.8 bound), so supersonic squidding is excluded by the trigger logic rather than by canopy design. At separation, β-divergence drives the jettisoned shells away from the decelerated stack without re-contact.

At parachute release, the gondola swings as a pendulum on the suspension length,

$$T = 2\pi\sqrt{\frac{L}{g_{eff}}} = 2\pi\sqrt{\frac{12}{8.87}} \approx 7.3\,\mathrm{s} \qquad (0.137\,\mathrm{Hz}), \tag{8.6}$$

With $g_{\mathrm{eff}} = 8.87\,\mathrm{m/s^2}$ and $L \approx 12$ m, the parachute–payload system has a natural period of approximately 7.3 s. The first quarter-cycle therefore gives a 1.8 s initial attitude-capture interval, while one full swing period defines a conservative 7.3 s disturbance window. For a 10° release swing, $\dot{\theta}_{\mathrm{max}} \approx 0.15$ rad/s, and the no-slack peak suspension tension is only ≈ 1.2 kN for $m_{\mathrm{float}} = 130.5$ kg. The P8/P9 hand-off is therefore non-sizing relative to the 24.7 kN reefed-opening load.

8.4. Materials and Thermal Design

Aeroshell and TPS Materials

The aeroshell is constructed from an all-composite CFRP sandwich structure with an areal density of approximately 0.75 kg/m^2. By integrating the bond directly into the structure, the design saves 8 kg relative to an aluminium-honeycomb setup. Thermal protection is provided by a carbon-phenolic TPS, drawing on Pioneer Venus and Galileo heritage, while PICA remains a qualified backup material. The TPS is benchmarked against the 20 MW/m^2 peak heat flux reported for the ESA Venus Entry Probe 45° sphere-cone concept at a 40° entry angle; this value is a mission-reference case, not a carbon–phenolic material limit [130]. At the design point, the dual-layer layup has an areal density of 16–20 kg/m^2 and an expected recession of 6.3 mm, leaving a 10.2% margin to this reference flux.

COPV Materials

The inflation system uses a lined composite overwrapped pressure vessel (COPV) sized for a 700 bar MEOP. The tank stores 260 kg of N_2 for initial inflation including a 7.5 kg make-up reserve, requiring an internal volume of 0.43 m^3. The resulting tank mass is 121.50 kg. The COPV remains with the vehicle until P9, where it is discarded momentarily after the parachute.

Parachute Materials

The parachute system follows planetary-entry pilot/main heritage and the ringsail design methods compiled by Knacke [137]. The DGB pilot is released after main-canopy deployment, while the ringsail is jettisoned at approximately 64 km during Phase P9. The remaining soft-goods consist of suspension lines, risers, reefing cutters, and canopy reinforcement. Structural sizing is governed by the 24.7 kN reefed-opening load, closing REQ-F-DEP-07 on opening shock.

TRL and Heritage Assessment

Table 8.5 summarises the material TRLs and heritage basis assessed against the Venus qualification matrix (materials × stressors: $T(z)$, $\rho(z)$, sCO_2, H_2SO_4, γ-dose, and mechanical loading). Overall, the deployment architecture is built around materials with strong flight heritage and TRLs of 7–9. The main remaining qualification item is associated with the aeroshell structure, where the face sheets, core, and TPS bondline have relevant entry-system heritage but have not yet been qualified against the Venus entry heat pulse. This is carried as Risk 2 and will require Venus-representative coupon and thermal-environment testing. For the COPV, the primary challenge is demonstrating the final high-pressure spherical vessel configuration and closing the remaining qualification delta at article level.

Table 8.5: Revised material TRL and Venus qualification status for EDDI. ✓ = qualified or demonstrated heritage, △ = partial or analogous heritage, × = open qualification gap, – = not design-driving.

Material	Subsystem	TRL	Heritage basis	$T(z)$	$\rho(z)$	sCO_2	H_2SO_4	γ	Mech.
CF/Al-HC face sheets	Aeroshell	8	Composite entry-structure heritage; Venus heat-pulse qualification remains.	×	✓	–	–	–	✓
Al-HC core	Aeroshell	8	Honeycomb-core entry-structure heritage; Venus heat-pulse qualification remains.	×	✓	–	–	–	✓
PICA ablator	TPS forebody	9	Stardust SRC/MSL heat-shield heritage; backup TPS.	✓	✓	–	–	–	✓
FRCI-12 tile	TPS backshell	7	Shuttle/MER backshell-tile heritage; less direct than forebody TPS.	△	✓	–	–	–	✓
RTV-560 bondline	TPS bondline	8	MSL/Genesis bondline heritage; coupon testing still required.	△	✓	–	–	–	✓
CF T1000 overwrap	COPV	8	Spaceflight/commercial COPV heritage; exact spherical article remains to qualify.	△	–	△	△	△	✓
Al-2219 liner	COPV	9	Spaceflight tank-liner heritage; short-duration EDDI duty only.	✓	–	–	–	✓	✓
Ringsail broadcloth	Main chute	9	Parachute fabric heritage plus Mars/Earth ringsail heritage.	✓	✓	–	–	△	✓
DGB broadcloth	Pilot chute	9	Strong DGB planetary-entry heritage.	✓	✓	–	–	△	✓

Thermal and Envelope Hand-Off

Post-entry soak-back penetrates $\delta \approx 10.7$ mm into the TPS at the −8.0° profile; the bondline temperature stays below the adhesive allowable, so no active mitigation is required between peak heating and separation. The folded envelope sees a peak of ~370 K during descent, against a 430 K qualification limit. Acid exposure is bounded by design: the envelope transits the H_2SO_4 cloud deck stowed, and the deployed transit is sub-minute and single-use, so both the thermal and chemical cases close without dedicated protection.

Mechanically, the folded envelope fit is supported only at packed-volume level: Section 7.1 gives a packed component volume of approximately 0.96 m^3 inside an available internal volume of about 1.4 m^3, with a 10% installation allowance and ~21% net volumetric headroom. This supports Phase 0 packaging feasibility but does not close local wall-clearance verification. At P7, the jettisoned deployment hardware is released at approximately 68.4 km and $M \approx 0.31$; the separation concept relies on ballistic-coefficient divergence to maintain clearance, while final envelope-to-TPS clearance remains a future phase CAD and separation-tolerance check.

8.5. Mass, Power and RAMS

Mass Budget

The deployment ledger (Table 8.1) supersedes the midterm review Table 11-8 [17] following the change to a bottom-up approach: the entry mass closes at 689.1 kg and 755.7 kg with ECSS maturity margins. The entire EDDI total (321.1 kg) is jettisoned during the sequence, the aeroshell at ≈138.7 kg, the parachutes at ≈22.3 kg, and the COPV/flow path at ≈151.8 kg released with the ringsail at P9, leaving ≈390.5 kg at float hand-off (gondola, envelope, lift gas).

Against the 700 kg entry cap, the ledger leaves 10.9 kg (≈1.6%) of headroom. Including the ECSS-E-ST-10-02C margin, the ledger goes 55.7 kg over budget (≈8.0%); mass closure at full system margin is therefore not yet achieved. The principal recovery lever in the deployment system is to reduce the hand-off altitude to reduce the required N_2 wet mass at the cost of additional strain on the ISRU subsystem.

Interface Power Profile

Table 8.6 updates MTR Table 11-11 with the EPS-agreed values on a 28 V regulated bus with ESI-class initiators. EPS sizing is driven by peak firing power rather than average energy: the bounding pyro cases are ≈ 149 W for a single fire and ≈ 289 W for the worst-credible A/B fire at the 0.05 s pulse width. The continuous EDDI loads (trigger logic, sequencer, and deployment telemetry) use the table allocation, while the inflation flow-control electronics draw only during the ~30 s P8 window. Heater loads are not included in this table and remain an open DEP/EPS/TCS interface item; ISRU pump/separator loads are outside this EDDI transient-power interface.

Table 8.6: EDDI transient-power interface to EPS (sourced estimates).

Load / function	Power [W]	Dur. [s]	Basis
Trigger logic, inhibits & arming	3	879	low-power control reserve; EDDI window [138]
Firing-unit arming / cap charge	0.3	60	trickle-charge reserve, < 10 mA
Deployment & jettison sequencer	3	879	actuator-command and release-interface logic [139]
Aeroshell separation firing	140	0.05	EED pulse reserve: 28 V×5 A [139, 138]
Restraint / cover release firing	140	0.05	ESI-class mortar/cutter/release pulse; 1W/1A no-fire basis [140]
Valve & regulator actuation	12.6	2	Marotta MV602 opening power at 28 V [141]
Inflation flow-control electronics	3	30	P8 pressure/valve-state logic window
Deployment telemetry & sensors	3	879	separation switches, pressure sensors, event flags
Post-deployment safing	3	300	inhibit reset and state confirmation
Bounding peak — single fire	**≈149**	0.05	1 fire + active control overhead
Bounding peak — A/B fire	**≈289**	0.05	2 fires + active control overhead

Reliability and RAMS

Reliability Model

EDDI reliability is assessed using a Phase 0 reliability-ranking model for the selected architecture. The deployment sequence is represented as nine non-recoverable phase gates, P1–P9: if any gate fails without recovery, the vehicle does not reach confirmed float. The resulting ranking metric is therefore the product of the phase reliabilities, $R_{\text{rank}} = \prod_i R_i$. Each R_i combines heritage judgement, subsystem maturity, and the dominant unresolved evidence gap for that phase, such as release validation, Mach/q trigger robustness, parachute extraction, shell separation, inflation flow-path behaviour, or float hand-off. The model is used to identify reliability drivers and compare architecture risk at Phase 0; it is not a qualified flight-reliability prediction until the release, trigger, parachute, inflation, and separation chains are tested.

Table 8.7: EDDI reliability-ranking inputs for the selected architecture.

Phase	Event / dominant open driver	R_i
P1	Entry-stage decouple; release/separation evidence gap	0.950
P2	Coast / entry acquisition; sparse passive-phase heritage	0.990
P3	Atmospheric interface; entry-state uncertainty and model gap	0.990
P4	Mach/q trigger; sensor, sequencer, or trigger-box error	0.971
P5	Main mortar and DGB extraction; mortar, line, or canopy-deployment fault	0.965
P6	Reefed-ringsail descent; reefing and descent-chain uncertainty	0.979
P7	Forebody/backshell jettison; recontact or separation-chain fault	0.984
P8	Envelope inflation / flow path; regulator, manifold, or string-level fault	0.999
P9	Parachute release and float capture; release or pendular hand-off fault	0.999
	$R_{\text{rank}} = \prod_i R_i$	≈ 0.839

The selected case applies a common-cause factor $\beta_{\text{cc}} = 0.005$ to the redundant pyro/inflation paths, with a conservative workbook case of $\beta_{\text{cc}} = 0.020$. Across this range, the ranking metric changes only from $R_{\text{rank}} \approx 0.839$ to ≈ 0.838, so the current reliability ranking is driven mainly by the series phase gates P1–P7 rather than by the assumed common-cause coupling. The A/B firing paths retain separate arm/inhibit logic and galvanic isolation, but the residual shared exposure is carried through β_{cc} rather than treated as fully independent.

Availability and Maintainability

The mission is one-shot: no repair is possible after launch, so availability is delegated to reliability, $A = R$, and no separate availability analysis is carried out. Maintainability is likewise not applicable post-launch. It is addressed only in the ground phase, pyrotechnic and COPV handling procedures during integration and test, and is covered by the safety assessment below.

Safety Assessment

Pyrotechnic safety follows European ESI-class low-voltage initiator practice, using the ECSS 1W/1A no-fire basis [140]. The selected initiator class is therefore treated as no-fire at 1 A or 1 W for 5 min, while the firing architecture uses independent pre-arm/select/arm/fire functions and electrically isolated A/B firing circuits in line with ECSS explosive-system practice. The COPV is the dominant stored-energy hazard: the 260 kg N_2 inventory, including the 7.5 kg make-up allocation, is stored at 700 bar MEOP in 0.43 m^3, giving a pV energy scale of ≈30 MJ. The 1.5× burst-factor basis, staged pressurisation, and late electro-explosive device installation define the ground-handling controls; both pyro and COPV hazards remain carried in the risk register (section 8.7).

8.6. Sensitivity Analysis

Trajectory Sensitivities

Entry Mass Sensitivity

The ballistic coefficient scales linearly with entry mass ($\beta \propto m$ at fixed $C_d S_{ref}$), so a ±10% mass perturbation moves β from 245.2 kg/m^2 by ±24.5 kg/m^2. A heavier vehicle penetrates deeper before decelerating: peak-g falls slightly while peak heat flux and the deployment altitude shift downward. The mass effect on the trajectory is second-order; its first-order consequence is on the budget; at 689.1 kg CBE, +10% (≈69 kg) exceeds the 10.9 kg headroom to the 700 kg cap outright.

Flight-Path Angle Sensitivity

The flight-path angle is swept ±2° about the locked $\gamma_E = -8.0^\circ$. Steeper entries raise peak deceleration and peak heat flux, eroding the g- and flux-cap margins; shallower entries lower both but introduce skip risk and depress the deployment altitude toward the bottom of the trigger window. γ_E is the strongest single driver of the entry environment, which is why the nominal is locked and the dispersion band is carried explicitly.

Atmospheric Density Sensitivity

VIRA density-model uncertainty acts twice: on the deployment altitude (the $q = 3000$ Pa trigger surface moves with $\rho(h)$) and on the subsonic descent time, which scales as $T_{sub} \propto \sqrt{m}/\sqrt{C_D S}$ through the quasi-terminal balance of Equation 8.4. Neither effect threatens the sequence directly, the trigger fires on measured q, not on altitude, but the descent-time shift propagates into the P8 inflation window and the battery-energy budget.

Inflation Sensitivities

Nitrogen Inventory Sensitivity

The N_2 inventory is perturbed by ±15% about the 260 kg nominal value, corresponding to ±39.0 kg. At the 56 km target altitude, however, the downward margin is much smaller than the perturbation range: using the chapter 7 fixed ZP/SP geometry, the worst-case 3 m/s vertical-wind balance gives $\Delta p_{SP} \approx 6.1$ kPa at 260 kg, while the SP overpressure vanishes at approximately 246.4 kg. The usable loss margin is therefore only about 13.6 kg unless a lower SP-pressure reserve is accepted. Additional inventory is geometrically feasible at 56 km and can be vented after inflation, but it is paid directly in stored gas and COPV tankage mass.

Reliability Sensitivities

Common-Cause Failure Sensitivity

The common-cause factor β_{cc} is swept over its 5–15% band to bound its effect on R_{rank}. Because the A/B pyro channels and flow path are the only redundancy in an otherwise series chain, R_{rank} is near-linearly sensitive to β_{cc} at the high end of the band; the sweep establishes how much of the redundancy benefit survives a pessimistic common-cause assumption.

Key Design Drivers

Table 8.8 condenses the sensitivity sweeps into a driver matrix: perturbation against entry loads, float hand-off, and mass margin. The protected parameters are entry mass, γ_E, N_2 inventory at the 56 km target, reefing fraction, and TPS allocation. Entry mass controls cap closure, γ_E controls the entry environment, N_2 inventory controls float hand-off, reefing sets the parachute opening load, and TPS allocation remains the largest EDDI mass-recovery lever.

Table 8.8: Key design drivers — perturbation versus response.

Perturbation	**Peak-g / loads**	**Float / hand-off effect**	**Mass-margin effect**
Entry mass ±10%	~∓ through β; second-order trajectory effect	minor trajectory shift	CBE mass is 689.1 kg; margined mass is 755.7 kg. The 700 kg cap leaves 10.9 kg CBE headroom, while the margined case is 55.7 kg over the cap. Applying a further +10% to the margined case gives 831.3 kg, or 131.3 kg over the cap.
$\gamma_E \pm 2°$	strongest entry-environment driver	shifts deploy altitude and descent timeline	indirect only; may force TPS / structure growth if steep case drives sizing
Density-model uncertainty	minor to moderate through q and $\rho(h)$	shifts q-trigger altitude and T_{sub}	no direct mass effect
N_2 inventory ±15%	no direct entry-load effect	at the 56 km target, SP overpressure vanishes at ~246.4 kg; usable loss margin is therefore only ~13.6 kg, not the full −15%	extra gas can be vented after inflation, but stored gas and COPV tankage are paid before entry
Reefing fraction ±20%	opening load shifts over ~20–30 kN	no direct float-altitude effect	minor through canopy / riser sizing
TPS allocation	protects heat-flux and soak-back margin	no direct float-altitude effect	largest EDDI mass recovery lever

8.7. Verification, Compliance and Risk

Verification and Validation

Verification Matrix

The deployment VCD extract translates the Phase 0 deployment requirements into the system verification format. For each requirement, Table 8.9 lists the verification method, the analysis or test basis, and the programme stage at which closure is claimed. Phase 0 closures are analysis-based; test and demonstration items are carried forward to Phase A and remain open in the system VCD.

Phase 0 Verification Status

At Phase 0, every closed requirement is closed by Analysis: heritage-anchored C_d databases, the Monte-Carlo trajectory, and closed-form load and stability cases. No deployment requirement is yet verified by test. Test and Demonstration are deferred to Phase A (mortar ground fire, the inflation rig, and hardware-in-the-loop trigger validation).

Table 8.9: Deployment verification matrix (extract).

Requirement	Method	Model / basis	Status
Peak-g $\leq 200\,g_0$	Analysis	dispersed entry trajectory model	Closed, Phase 0
Deploy in q window	Analysis + HIL	Mach/q trigger logic	Analysis closed; HIL open
Opening shock ≤ cap	Analysis	reefed parachute opening-load case	Closed, Phase 0
TPS flux margin >0	Analysis	peak-flux and ablation sizing model	Closed, Phase 0
Deployment mass ≤ 400 kg	Analysis	bottom-up mass ledger	Closed, Phase 0
Mortar deployment	Test	breadboard fire; flight-like qualification fire	Open, Phase A/D
Inflation full < window	Demo/Test	inflation rig; integrated deployment test	Open, Phase A/C
N_2 blow-down thermal drop	Analysis + Test	thermo-fluid model; cold-flow test	Open, Phase A/B
COPV / pyro safety	Review + Test	safe-arm, no-fire, proof/burst basis	Open, Phase B/D

8.7.1. Risk Update

Relative to the system risk assessment in chapter 11, two deployment risks move to post-mitigation closed at Phase 0: the parachute opening-shock case (load path closed in section 8.3, Figure 8.6) and the TPS thermal case (peak-flux, ablation, and soak-back closed in section 8.4). Both rest on analysis only; their VCD status is in Table 8.9.

Risk 2 is the headline residual: the composite face, core, and TPS bondline carry Earth-return heritage only (TRL 8) and are unqualified for the Venus entry pulse. Three further items stay open:

- **Safety chain.** COPV and pyrotechnic safe-arm, no-fire, proof/burst, and jettison sequencing close in later V&V (Table 8.9).
- **Provisional sequence parameters.** Entry spin rate, riser length L, and P7 jettison altitude are set but not yet verified.
- **Fidelity gaps.** No 6-DOF dynamic-stability simulation has been run yet, and the quasi-terminal subsonic descent-time estimate still ignores parachute-opening transients. These are modelling-depth gaps, not separate failure modes.

The full forward-work set (mortar and inflation ground tests, HIL trigger validation, 6-DOF dynamic-stability simulation, COPV/pyro safety verification, TPS mass-ledger reconciliation, and the saddle FEM) is carried as the Phase A/B open rows of Table 8.9 and expanded in Chapter 9. The Phase-0 contribution here is the prioritisation: four items must close by PDR; the re-dispersed trajectory at the margined entry mass, the saddle FEM with the deployment-to-structures interface allowables freeze, the trigger sensor accuracy specification, and the N_2 inventory / COPV jettison architecture freeze. TPS coupon qualification is gated pre-CDR per Risk 2.

8.8. Conclusion

The deployment architecture closes the Phase 0 analysis requirements, with test-based verification carried to later phases. Against the 400 kg subsystem cap the architecture holds the margined mass with positive headroom (mass ledger, Table 8.1); the loads sit well inside their caps, peak deceleration 78.6 at p97.5 versus the $200\,g_0$ structural cap (Table 8.4), and peak heat flux $13.7\,\mathrm{MW/m^2}$ to $14.4\,\mathrm{MW/m^2}$ versus the ESA VEP $20\,\mathrm{MW/m^2}$ reference. The gondola reaches free float at $\approx 56\,\mathrm{km}$ with $R_{\mathrm{rank}} \approx 0.839$ (Table 8.7). Three risks remain open: Venus qualification of the composite/TPS bondline, COPV/pyro safety closure, and full system-margin closure, the last tied to TPS mass recovery, N_2 inventory control, and COPV tankage reduction.

9 Future Mission Design

This chapter presents the activities that have to be performed post-DSE to ensure the success of the VISTA mission. As the Design Synthesis Exercise corresponds to a Phase 0 (Mission Definition) in the ESA framework, the next development phases are presented in detail in section 9.1. For this, the key visual tool is the Gantt chart (Appendix A), illustrating the key future project design & development logic steps, and aligned with the flow diagrams (Figure A.2 and Figure A.3). The chapter continues with the detailed production plan (section 9.2) and with the breakdown of the cost budget (section 9.3) to ensure the success of the mission.

9.1. Development Phases

The plan and schedule of development phases for the VISTA mission follows the mission development guidelines established by the ECSS. An outline of the reviews and milestones is shown in Table 9.1. Note that the Design Synthesis Exercise effectively covers what can be considered a Phase 0 study. For detailed descriptions, refer to [14].

Table 9.1: ECSS Mission Development Milestones [14].

Development Phase	Short Description	Relevant Milestones	Milestone Description
Phase 0	Mission definition	MDR	Mission Definition Review (comparable to DSE Final Review)
Phase A	Feasibility	PRR	Preliminary Requirements Review
Phase B	Preliminary definition	SRR PDR	System Requirements Review Preliminary Design Review
Phase C	Detailed definition	CDR	Critical Design Review
Phase D	Qualification & production	QR AR ORR	Qualification Review Acceptance Review Operational Readiness Review
Phase E	Operations	FRR LRR CRR ELR	Flight Readiness Review Launch Readiness Review Commissioning Result Review End-of-life Review
Phase F	Disposal	MCR	Mission Close-out Review

The Gantt chart describing high-level task distribution and scheduling can be found in Figure A.1, while an overview diagram is shown in Figure 9.1. The schedule follows the model philosophy and production plan defined for the mission. The V&V activities are included in the schedule through the integrated simulation and hardware-in-the-loop campaign, the assembly, integration, and test flow, and the final hazardous operations. This approach is required because the Venus float environment cannot be fully reproduced on the ground. The operational phase follows the concept of operations and includes cruise, entry, descent and deployment, commissioning, the five-year nominal science phase, and disposal.

Activity dependencies are not shown with explicit links in the Gantt, for the sake of visual clarity. Instead, they are reflected in the start and end dates of each activity. These dates include the relevant finish-to-start, start-to-start, and finish-to-finish relationships, together with the planned overlaps and lags. Overlapping bars therefore indicate intentional concurrent work.

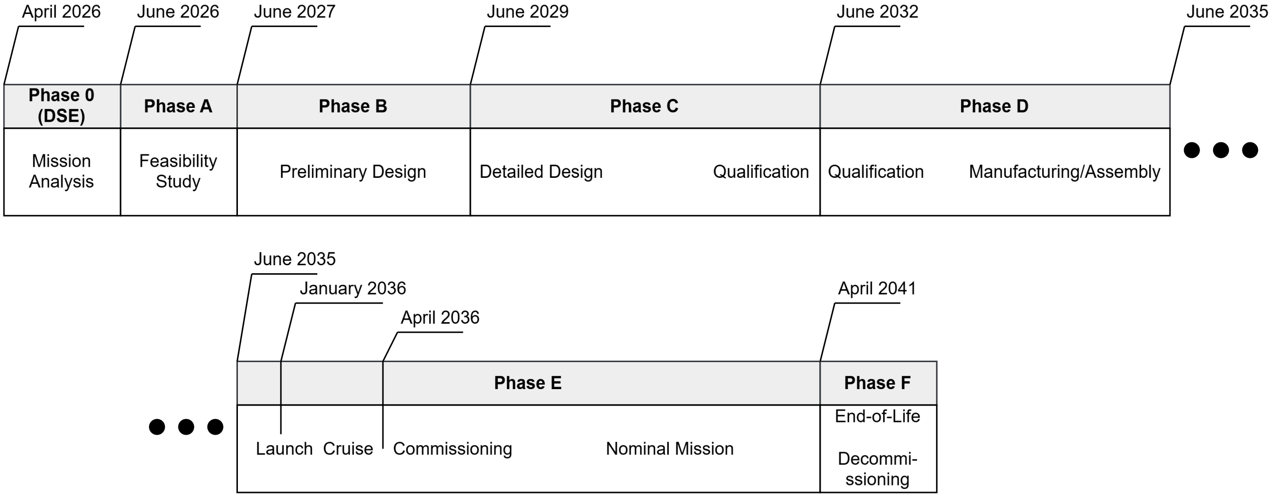

Figure 9.1: Diagram of the Mission Development Phases

9.2. Production Plan

The production plan covers Manufacturing (subsection 9.2.1), Assembly, Integration & Testing (subsection 9.2.2), and the Qualification Program (subsection 9.2.3).

9.2.1. Manufacturing

Approach and Model Philosophy

The guiding principle is heritage-led procurement [65]: buy or adapt flight-qualified hardware wherever a credible Venus or deep-space pedigree exists, and reserve in-house development for elements with no qualified equivalent. This concentrates cost and schedule risk in a small number of items rather than spreading it across the vehicle. The build follows a protoflight (PFM) baseline [142], with dedicated EM/EQM units only for the low-heritage items: the balloon envelope, the ISRU buoyancy system, and any new instruments.

Table 9.2: Make/buy strategy and likely sources.

Element	Strategy	Rationale	Likely source
Aeroshell & TPS	Buy / adapt heritage	Strong pedigree (Pioneer Venus [143], Venera [144], DAVINCI [47]); adapt qualified TPS rather than develop new	Entry-system prime
Parachute & separation	Buy (catalog)	Mature, qualified descent hardware	Descent-system supplier
Balloon envelope	Make (new dev.)	No flight-qualified acid-resistant super-pressure envelope exists for 5-yr Venus life [102], [145]	In-house + balloon specialist
Buoyancy / ISRU (N_2)	Make (new dev.)	Novel subsystem, no heritage	In-house / dev. partner
Gondola structure	Make	Custom; conventional composite/metallic fabrication	Prime / structures sub.
TCS	Make / adapt	Mission-specific Venus float case, built from standard MLI/heater/radiator hardware	Prime
EPS solar array	Buy cells / make array	Triple-junction cells are catalog; layout and Venus-rated coverglass are custom	Cell vendor + integrator
EPS storage / PMAD	Buy cells / make pack	Space-qual cells are catalog (long lead); pack & PMAD built to design	Cell vendor + prime
C&DH, TT&C, mechanisms	Buy (catalog)	Space-qualified OBCs, deep-space transponders, and release devices widely available	Avionics / comms / mech. vendors

Continued on next page

Table 9.2 – continued

Element	Strategy	Rationale	Likely source
Payload	Furnished + selective make	Mass spec. and nephelometer have heritage; pH sensor and sonic anemometer are new dev. for Venus	Instrument institutes / PI teams

Manufacturing and Integration Flow

Element builds proceed in parallel and converge on the gondola. Procured units are incoming-inspected and acceptance-tested; in-house elements are fabricated and checked out. Streams meet at gondola integration — structure, avionics/harness, EPS, TCS, ISRU, payload — after which the integrated aerobot mates to the entry system.

Table 9.3: Long-lead and critical-path items.

Item	Lead driver	Mitigation
Rad-tolerant EEE parts	Procurement + screening (12+ months) [146]	Order at start of Phase C; freeze parts list early
Space-qual battery cells	Vendor lead + lot acceptance	Early procurement of heritage cell type
Deep-space transponder/amp.	Few vendors, long build	Early order of catalog heritage unit
Acid-resistant envelope	New-material qual + 5-yr acid/UV life test (cannot be compressed)	Coupon qual in Phase B; book Venus chamber early [147]
TPS & aeroshell	Arc-jet qual if non-heritage	Down-select to heritage TPS
ISRU N_2 system	Novel development and test	Early breadboard/EM
Novel instruments (pH, sonic anemometer)	New dev. for Venus environment	Early EM + environment testing

The critical path is set by two long poles: rad-tolerant EEE procurement and the envelope acid/UV life test. The latter also drives the qualification program; both must start well before system-level work.

9.2.2. Assembly, Integration & Testing (AIT)

The vehicle is built bottom-up through standard levels (unit → subsystem → element → system) under the protoflight philosophy, with a reduced functional check after each integration step to catch errors at the lowest level.

Mechanical GSE covers integration stands, lifting fixtures, the aeroshell mating jig, transport containers, a CoG/MOI fixture, and laser-tracker metrology; the envelope adds a low-contact folding rig in a large clean volume. Electrical GSE is built around the central checkout system running CST scripts, with break-out boxes, solar-array simulator, RF set, and payload stimulators. Fluid GSE handles N_2 servicing with helium leak detection.

Three constraints dominate the campaign: **contamination control** around payload optics, mass-spectrometer inlets, and acid-sensitive coatings; **envelope handling**, with folding cycles minimised because each fold is a stress event; and **hazardous operations** (pyro install, pressurant servicing) sequenced late under dedicated safety procedures.

The final integrated architecture is shown in the Power-Data-Fluid block diagram (Figure 9.2) and the gondola CAD model (Figure 9.3).

Figure 9.2: Power-Data-Fluid block diagram of the system architecture.

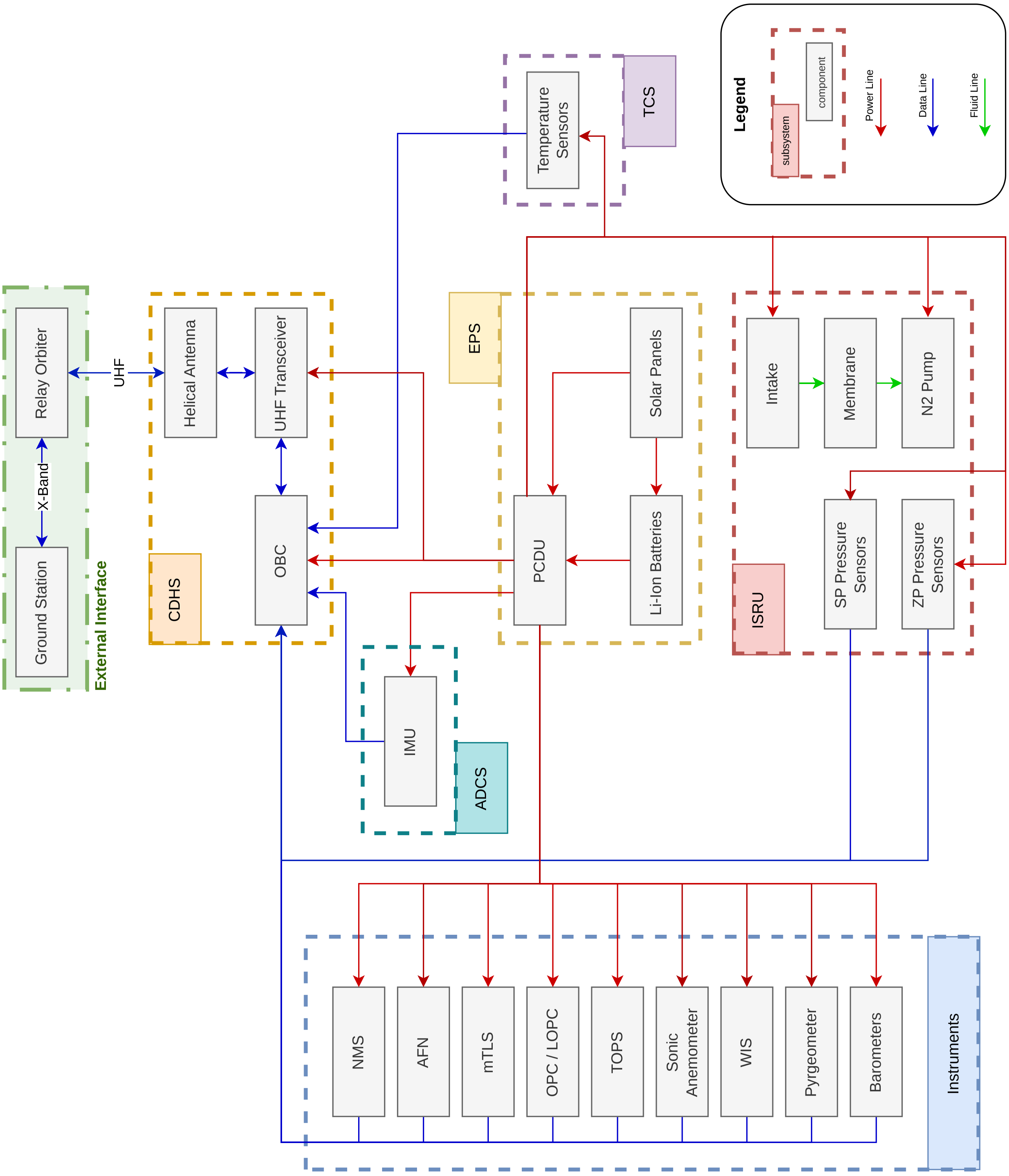

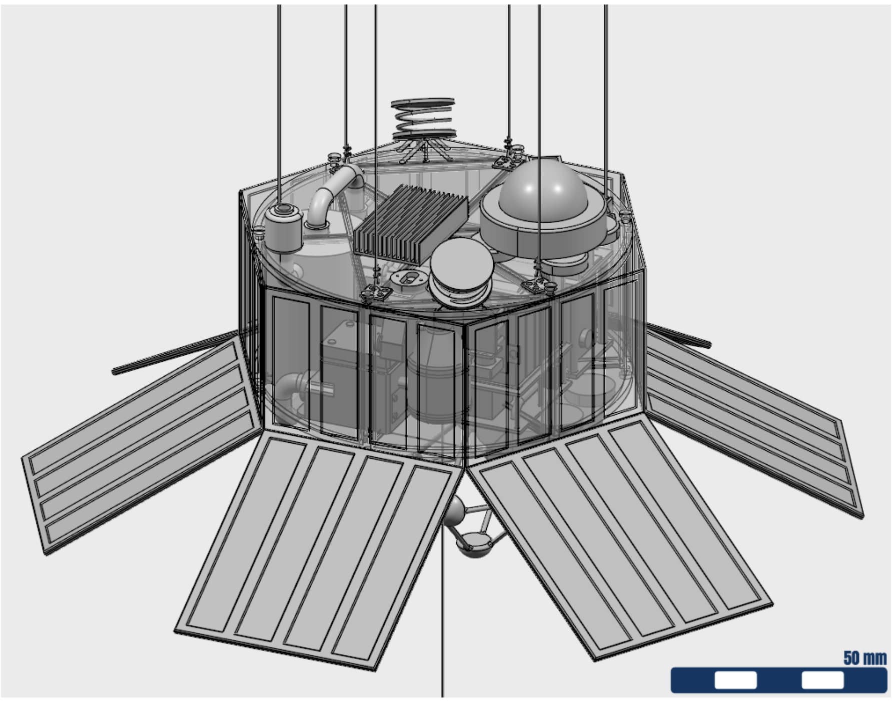

Figure 9.3: 3D model of the gondola.

9.2.3. Qualification Program

The qualification program verifies that VISTA functions in its prescribed environments. The design follows the SMAD methodology [65].

Step 1 – Subsystem Functions

Table 9.4: Spacecraft and payload functions.

Element	Function(s)
Aeroshell / TPS	Protect through hypersonic entry; survive peak heating and deceleration
Parachute & separation	Decelerate through transonic/subsonic; sequence heatshield jettison and aerobot release
Balloon envelope	Deploy, inflate, retain buoyancy; hold ΔP for 5 yr at float
Buoyancy & ISRU	Extract N_2 in situ; control altitude via valves/compressor over 5 yr
Gondola structure	Protect avionics/payload; provide load path through launch, entry, and float
EPS solar array	Generate power under reduced sub-cloud solar flux
EPS storage & PMAD	Cycle ~1905 Wh; support ~10 W dark load; distribute/condition power
TCS	Maintain internal temperature across −10 to 80 °C plus dissipation
C&DH	Autonomously sequence entry/deployment; manage health, data, and science 5 yr
TT&C / Comms	Relay science/telemetry to orbiter or Earth; receive commands
Mechanisms	Execute jettison, deployment, and inflation-release events
Payload	Mass spec. (gases, isotopes); nephelometer+OPC (aerosols); pH sensor; WIS + T/P; sonic anemometer; pyrgeometer

Step 2 – Environments

Table 9.5: Environments across the mission lifecycle (values representative).

Phase	Environment	Characterisation
Ground	Handling, transport	Vibration/shock; controlled T/RH; cleanliness
Launch	QS, vibration, acoustic, shock	Sine+random vibration, acoustic, QS accel., pyroshock, fairing depress. (per LV user's guide)
Cruise	Vacuum, thermal, radiation, $0g$	Hard vacuum; cold and hot cases; thermal cycling; TID, SPE, GCR
Entry & descent	Decel., aero-heating, shock	Shallow low-β entry: ~50–69 g, peak heat rate ~1500 W/cm^2, total ~18 kJ/cm^2. Steeper rigid entries reach hundreds of g
Venus float	Thermal / pressure	−10 to 80 °C; 24–107 kPa; day/night cycling; 5 yr
Venus float	Chemical / UV	Concentrated H_2SO_4 aerosols + UV on envelope, radiators, antenna, coverglass, sensors. **Dominant 5 yr driver**
Venus float	Aerodynamic	Wind shear, gusts, turbulence → envelope/suspension loads, pendulum dynamics
Cross-phase	EMC/EMI	Self-compatibility; inadvertent pyro actuation; sensor susceptibility
Cross-phase	Planetary protection	COSPAR Cat. II; documentation only, no sterilisation

Step 3 – Correlation of Functions and Environments

Table 9.6: Operational state required for each subsystem/environment.

Subsystem	Transp.	Launch	Cruise	Entry	Float	Acid	Wind	EMC
Aeroshell / TPS	Ex	Ex	Ex	**Op**	–	–	–	–
Parachute & sep.	Ex	Ex	Ex	**Op**	–	Ex	–	Op
Balloon envelope	Ex	Ex	Ex	**Op**	**Op**	**Op**	**Op**	–
Buoyancy / ISRU	Ex	Sb	Sb	Op	**Op**	**Op**	Sb	Op
Gondola structure	Op	**Op**	Ex	**Op**	Op	Op	Op	–
EPS solar array	Ex	Ex	Sb	Ex	**Op**	**Op**	Sb	Op
EPS storage / PMAD	Sb	Sb	Sb	**Op**	**Op**	–	–	Op
TCS	Ex	Sb	**Op**	Op	**Op**	Op	–	Sb
C&DH	Ex	Sb	**Op**	**Op**	**Op**	–	–	Op
TT&C / Comms	Ex	Sb	**Op**	Sb	**Op**	Op	Sb	**Op**
Payload instruments	Ex	Ex	Sb	Sb	**Op**	**Op**	**Op**	**Op**

Op = operating; Sb = standby/survival; Ex = exposure only; – = not exposed. **Bold** = design-driving. Float = thermal/pressure; Acid = acid+UV.

Step 4 – Main Configurations

Table 9.7: Main configurations (mapped to SMAD Fig. 12-5).

#	Config.	Description	Fig. 12-5
1	Launch/stowed	Aerobot packed in aeroshell, balloon folded, mated to cruise stage; all systems off or in survival	Boost
2	Cruise	Entry system dormant; C&DH, comms, TCS, EPS in cruise mode; payload periodic health checks	—
3	Entry/descent	Transient: TPS active, pyro separations, parachute, balloon deploy/inflate, jettison	Deployment
4	Float/operational	Inflated envelope, suspended gondola, solar array exposed, ISRU running, full science	Orbital

Step 5 – Functional Tests

Each function from Step 1 is exercised in its active configuration(s). A Comprehensive System Test (CST) is repeated after every environmental exposure to catch latent damage. Tests are: **Launch/stowed** — separation continuity, no-fire checks, survival power/thermal, structural continuity; **Cruise** — C&DH sequencing, comms uplink/downlink, TCS hot/cold modes, EPS charge, payload calibration, FDIR; **EDI** — autonomous entry sequencer, pyro firing + first-motion, parachute deploy, balloon inflation, inflation-system release; **Float** — full science campaign, ISRU N_2 + altitude control, EPS day/night cycling (~1905 Wh, ~10 W dark), TCS in warm CO_2, comms relay, 5 yr-representative life cycling.

Step 6 – Sequence of Tests and Exposures

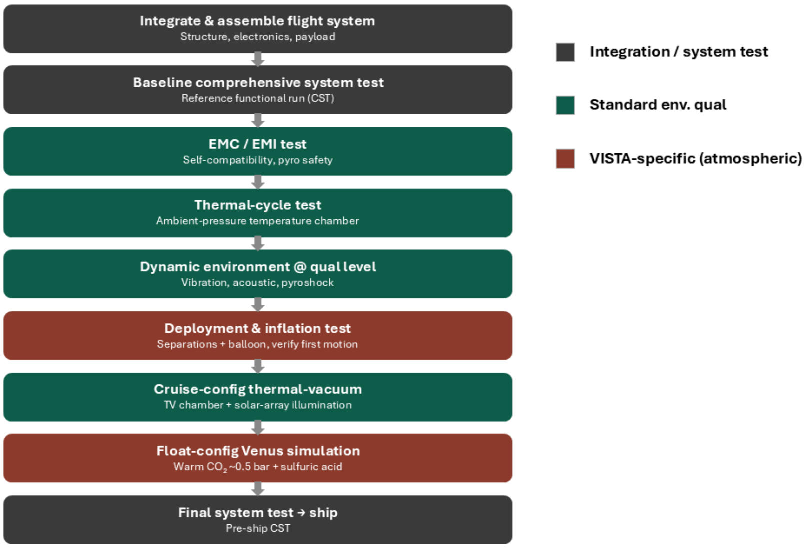

Figure 9.4: Sequence of functional tests and environment exposures.

Step 7 – Span Times and Special Facilities

Table 9.8: Representative span times and facilities.

Activity	Span	Facility
Integration & assembly	4–8 wk	Class-rated cleanroom
EMC/EMI	1–2 wk	Shielded EMC chamber
Thermal cycling	2–3 wk	Ambient-pressure thermal chamber
Vibration + acoustic + pyroshock	2–4 wk	Shaker, acoustic chamber, shock facility
Deployment & inflation	1–3 wk	Large-volume deployment hall
Cruise-config TVAC	2–4 wk	TVAC with solar simulation
Float-config Venus simulation	4–8+ wk	Venus chamber (e.g. GEER; JPL)
Life/endurance (acid + cycling)	Months (long pole)	Venus cloud/acid rig
Final system test	1–2 wk	Cleanroom

9.3. Cost Budget

The cost budget is a parametric Rough-Order-of-Magnitude (ROM) estimate following [148], expressed in FY26 €M. The estimate assumes that VISTA is implemented as a hosted payload or mission-of-opportunity element on a larger Venus-bound spacecraft; launch procurement and interplanetary delivery are therefore excluded from the VISTA Cost at Completion (CaC) and treated as a mission-level accommodation requirement. Subsystem masses from the component database are scaled to Venus and deep-space cost analogues using the PCEC method with a $\beta = 0.5$ mass exponent [149], covering Phases 0–E1, where E1 denotes launch, commissioning, and early operations; Phase F disposal is excluded. The WBS lines include the associated engineering labour, flight software, ground-segment software, AIV effort, and operations labour rather than treating these as separate, standalone cost items. Per-element maturity margins are highest on the low-heritage envelope, ISRU, and payload elements, while programmatics (PM – project management; PA – product assurance; SE – systems engineering) and an 8% ESA overhead bring the launch-excluded base CaC to Table 9.9, assessed against the €400M cap of REQ-COST-01. The €400M cap (REQ-C-COMP-02) is defined exclusive of launch and interplanetary transfer, and the mission is accommodated as a hosted payload (REQ-C-COMP-04), so the CaC and the cap are compared on the same basis. If internalised, launch/transfer would add an order-of-magnitude €150–200M Discovery-class share outside the REQ-C-COMP-02 boundary. All WBS lines are parametric (PCEC, $\beta = 0.5$); no vendor quotes exist at Phase 0, so per-line uncertainty is carried by the maturity margins, not bid data.

Table 9.9: ROM cost build by WBS element, excluding launch procurement (PCEC $\beta = 0.5$ scaling, FY26 €M).

WBS element	Scaled cost (€M)	Margin	Cost w/ margin (€M)
Payload (science instruments)	65.2	20%	78.3
Platform / bus (ADCS+CDHS+TT&C+PWR+STR)	7.6	20%	9.1
ISRU subsystem (N_2 lift gas)	26.0	30%	33.8
TCS (Venus environment)	3.8	25%	4.7
Aeroshell / EDDI	117.8	15%	135.5
AIV (assembly, integration, verification)	26.5	10%	29.1
Ground Segment & Ops (Phase E1)	60.0	10%	66.0
Hardware + AIV + GS&Ops	306.9		356.5
Programmatics (PM/PA/SE)	22.0		43.2
ESA internal overhead (8%)	17.6		57.0
Base Cost at Completion (CaC)	**346.6**		**456.6**

Applying the [148] contingency factors to the launch-excluded base CaC and adding the cost-risk reserve gives the costs at the 50/70/90% confidence levels in Table 9.10. The base CaC remains below the €400M cap before contingency and risk reserve, while higher-confidence cases exceed the cap. Cost is reported at the 70% confidence level per ECSS practice, where the CaC of €433.7M exceeds the cap by €33.7M (8.4%); the cap is met only at 50%.

Table 9.10: Cost at Completion at ECSS confidence levels.

Confidence level	Cont. ×	CaC (€M)	Cap (€M)	Status
CaC @ 50%	1.00	364.4	400	Under cap by €35.6M
CaC @ 70%	1.20	433.7	400	Over cap by €33.7M
CaC @ 90%	1.45	520.4	400	Over cap by €120.4M

The cost-risk reserve follows the final-phase technical risk register in Table 11.3. Each residual (post-mitigation) risk is monetised under ECSS-M-ST-80C [150] from the mid-point of its ECSS likelihood band and a severity-based overrun ladder ($S = 3/4/5 \to$ €17.8M, with launch total-loss exposure to be covered separately by insurance. The largest residual contributions come from the low-heritage ISRU/buoyancy chain (N_2 leakage and separator degradation, TR-ISRU-02/03/04/05), post-deployment gondola instability (TR-D-04) and suspension-cable creep (TR-STR-03).

Cost sensitivity follows the PCEC exponent, $\Delta\mathrm{CaC}/\mathrm{CaC} \approx 0.5\,(\Delta m/m)$. The aeroshell/EDDI line (€135.5M) dominates: a ±10% EDDI dry-mass excursion moves the CaC by ≈ ±€6.8M, against ≈ ±€3.9M for payload (€78.3M). EDDI mass is therefore the primary cost lever.

The estimate is consistent with Venus Discovery/M-class cost references in FY26 €M: it sits below the DAVINCI/VERITAS development awards (≈€500M each) and EnVision's M-class budget (≈€650M), while remaining well below large atmospheric/flagship comparators such as Dragonfly and VFM. The launch-excluded base CaC is €346.6M (CBE), rising to €456.6M with ECSS maturity margins (Table 9.9). After contingency and cost-risk reserve it remains under the €400M cap at the 50% confidence level (€364.4M) but exceeds it at 70% (€433.7M) and 90% (€520.4M) (Table 9.10). Cost closure at higher confidence therefore requires reductions in the dominant WBS lines, aeroshell/EDDI (€135.5M) and payload (€78.3M), alongside early maturation of the ISRU and envelope elements.

10 System Verification & Validation

This chapter presents the System Verification and Validation (V&V) approach adopted for the VISTA mission design. The objective is to demonstrate that the system meets all allocated technical requirements (verification) and that the resulting design is fit for its intended operational purpose in the Venus atmosphere (validation). To increase confidence in proposed design, additional emphasis is placed on mass and power budget closure (section 10.1), including Monte Carlo uncertainty propagation with secondary cascading effects.

The verification strategy (section 10.2) is based on a combination of test, analysis, inspection, and design review, applied across the Engineering Model, Structural-Thermal Model, and Protoflight Model. Validation activities (section 10.3) assess system-level performance against stakeholder objectives and mission-level scenarios. This includes end-to-end mission simulation, operational readiness assessment, stress testing, and robustness evaluation under off-nominal conditions.

10.1. Mass Budget Closure and Sensitivity Analysis

Mass budget closure is verified probabilistically using a Monte Carlo uncertainty propagation ($N = 100{,}000$ iterations) over all components in the Product Breakdown Structure [94], results shown in Figures 10.2-10.3. Each component mass m_i is sampled from a triangular distribution:

$$m_i \sim \text{Triangular}\left(m_i^{\text{nom}},\ m_i^{\text{nom}}\left(1 + \frac{\delta_i}{2}\right),\ m_i^{\text{nom}}(1 + \delta_i)\right) \tag{10.1}$$

where m_i^{nom} is the nominal mass and δ_i is the maturity-based design margin fraction: 5 % for A/B components, 10 % for C, and 20 % for D.

This approach, however, samples each component independently. This captures within-subsystem margin uncertainty but does not capture the *cascading* effect that occurs when one subsystem grows: an increase in gondola-housed hardware mass requires additional gondola structure, which demands more lift gas, which in turn requires a larger balloon envelope. Likewise, any increase in average electrical power demand drives an increase in the electrical power subsystem (EPS) mass, which re-enters the structural chain. A coupled mass-propagation model is therefore implemented on top of the baseline Monte Carlo to quantify this second-order effect.

The chain consists of four sequential linear transfer factors, each derived from the current VISTA subsystem sizing relationships:

$$\Delta m_{\text{EPS}} = k_{P\to\text{EPS}} \cdot \Delta P_{\text{avg}} \tag{10.2}$$

$$\Delta m_{\text{STR}} = k_{\text{gondola}\to\text{STR}} \cdot \left(\Delta m_{\text{gondola,direct}} + \Delta m_{\text{EPS}}\right) \tag{10.3}$$

$$\Delta m_{\text{N}_2} = k_{\text{STR}\to\text{N}_2} \cdot \Delta m_{\text{STR}} \tag{10.4}$$

$$\Delta m_{\text{env}} = k_{\text{N}_2\to\text{env}} \cdot \Delta m_{\text{N}_2} \tag{10.5}$$

where $\Delta(\cdot)$ denotes the stochastic excess mass or power relative to the nominal (point-estimate) value for each Monte Carlo sample. The four transfer factors and their physical basis are summarised in Table 10.1.

Table 10.1: Cross-subsystem mass-propagation transfer factors used in the coupled Monte Carlo model.

Symbol	Value	Units	Physical basis
$k_{P\to\text{EPS}}$	0.84	$\text{kg}\,\text{W}^{-1}$	EPS sizing: solar array area and battery capacity scale approximately linearly with average power demand at the current VISTA operating point.
$k_{\text{gondola}\to\text{STR}}$	0.04	$\text{kg}\,\text{kg}^{-1}$	Gondola shell sizing: an additional 1 kg of gondola-housed hardware requires approximately 40 g of additional Al 6061 shell and inner-structure material to maintain the current safety factor.
$k_{\text{STR}\to\text{N}_2}$	5.5	$\text{kg}\,\text{kg}^{-1}$	Buoyancy sizing: at the 56 km float altitude the static lift equation requires approximately 5.5 kg of additional stored N_2 lift gas per 1 kg increase in suspended gondola mass to maintain the design buoyancy margin.
$k_{\text{N}_2\to\text{env}}$	0.75	$\text{kg}\,\text{kg}^{-1}$	Balloon envelope sizing: scales with lift-gas volume, which scales with lift-gas mass.

The propagation is applied for each of the $N = 100{,}000$ iterations. The stochastic excess power demand ΔP_{avg} and the stochastic excess mass of every gondola-housed component ($\Delta m_{\text{gondola,direct}}$, covering ADCS, CDHS, payload, EPS hardware, and TCS) are first computed relative to their nominal values, then Equations (10.2)-(10.5) are evaluated sequentially. The propagated mass increments are added to the baseline (uncoupled) totals to yield coupled system mass distribution. The propagation chain is illustrated schematically in Figure 10.1.

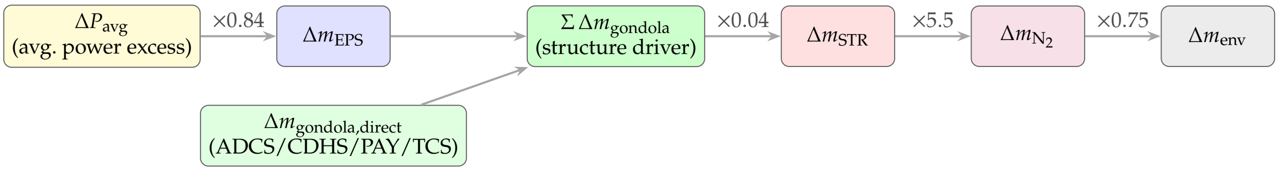

Figure 10.1: Cross-subsystem mass-propagation chain implemented in the coupled Monte Carlo model. Excess average power demand and direct gondola mass growth both enter the chain and cascade sequentially through the EPS, gondola structure, stored N_2, and balloon envelope. Transfer factors are listed in Table 10.1.

10.1.1. Monte Carlo Propagation Results

The total system mass $M = \sum_i m_i$ and the aerobot-only mass $M_{aerobot} = \sum_{i \in gondola} m_i$ are evaluated at each iteration and compared against the applicable requirements caps. Both distributions - the one derived purely from Monte Carlo and the refined coupled approach accounting for cascading effect - are shown.

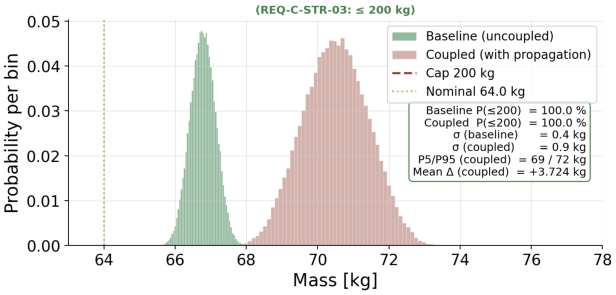

Figure 10.2: Monte Carlo probability distribution of the aerobot gondola mass only ($N = 100{,}000$ iterations), evaluated against the gondola structural cap (REQ-C-STR-03). The dotted gold line marks the nominal gondola mass of 64 kg. The distribution is narrow ($\sigma = 0.4$ kg, $P(5)/P(95)$: 69 kg to 72 kg) because most gondola components are TRL A/B with small 5 % margins, giving $P(M_{aerobot} \leq 200\,\text{kg}) = 100.0\,\%$.

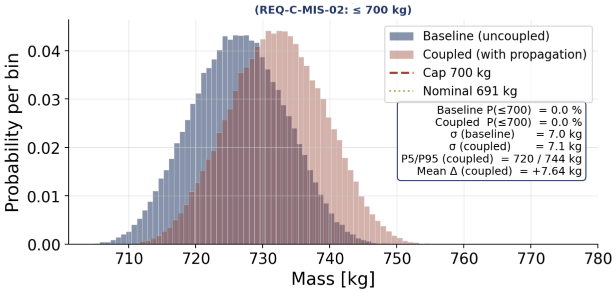

Figure 10.3: Monte Carlo probability distribution of the total VISTA system mass ($N = 100{,}000$ iterations). Each bar height is the fraction of samples falling in that 1 kg-wide bin (probability per bin, summing to unity). The dashed red line marks the 700 kg system cap (REQ-C-MIS-02); the dotted gold line marks the nominal total of 691 kg. The distribution has mean 732 kg, $\sigma = 3.5$ kg, and a $P(5)/P(95)$ interval of 720 kg to 744 kg.

The nominal VISTA system mass of 691 kg sits 9 kg below the 700 kg cap, yet both the uncoupled and coupled Monte Carlo distributions lie above the requirement threshold. The uncertainty-coupling increment of 7.64 kg shifts the mean further from the cap, placing the coupled $P5$ and $P95$ at 720 kg and 744 kg respectively, with $\sigma_{coupled} = 7.1$ kg. REQ-C-MIS-02 (≤ 700 kg) requirement re-negotiation is thus needed to restore conservative compliance.

For the gondola, the picture is markedly more benign. The nominal mass of 64.0 kg lies well within the 200 kg structural cap (REQ-C-STR-03), and both distributions remain entirely below it ($P(M \leq 200\,\text{kg}) = 100.0\,\%$). The coupling adds a mean increment of 3.72 kg, raising the coupled $P95$ to 72 kg and leaving a 128 kg (63 %) residual margin against the cap. The gondola structural cap is hence not a design driver.

Figure 10.4 summarises the mean propagated mass increment at each stage of the chain.

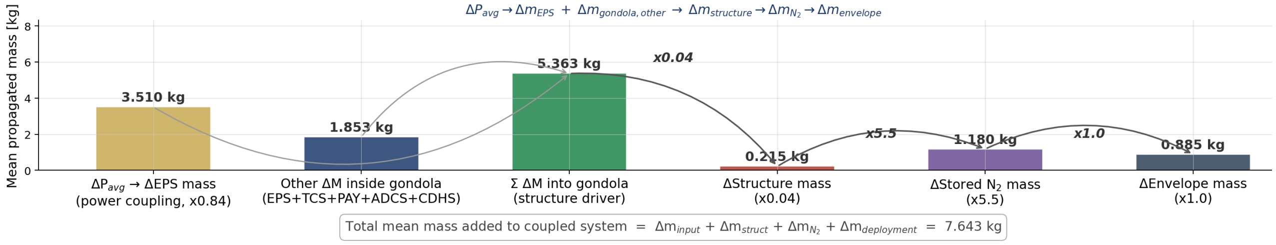

Figure 10.4: Cascading mass growth effect, per stage.

10.1.2. Key Assumptions of Monte Carlo Mass Uncertainty Assessment

The following assumptions bound the validity of these closure results and should be revisited at each subsequent design phase.

- **Triangular margin model.** The triangular distribution of Equation (10.1) assumes the nominal mass is the true minimum (no mass can be below the MEL value) and that the full maturity margin represents a hard upper bound rather than a statistical tail. This is conservative in the sense that real component masses can in principle come in below the MEL estimate, which would shift the distribution left; however, it is non-conservative in that it excludes mass growth beyond the stated margin.
- **Independent sampling.** Component masses within the gondola are sampled independently. In practice, design changes driven by one subsystem (e.g. an increase in shell thickness) are likely to co-vary with related components (TCS layout, choice of ADCS hardware). Positive correlations between related components would increase the system-level standard deviation above the 3.5 kg value reported here.
- The propagation model is a first-order linear chain and relies on the following assumptions, which bound its validity at Phase 0.
    - **Linear transfer factors.** All four factors in Table 10.1 are treated as constants. In reality, buoyancy sizing and balloon envelope scaling are nonlinear functions of altitude, gas density, and superpressure differential. The factor $k_{\mathrm{STR}\to\mathrm{N}_2} = 5.5$ is derived from the static lift equation at the nominal float altitude; at the altitude extremes of the operational band (50 – 60 km) this factor varies by approximately ±10 %, according to ISRU subsystem sizing algorithm.
    - **One-directional chain.** The chain is evaluated once per sample in the forward direction only. Secondary feedback effects - for example, the additional TCS mass itself increasing the EPS mass which re-drives the structural loop - are not iterated.
    - **Independence of propagation sources.** The model treats ΔP_{avg} and $\Delta m_{\mathrm{gondola,direct}}$ as independent inputs. In practice they are correlated: subsystems with larger mass also tend to draw more power (e.g. the NMS contributes both 10.9 kg mass and 14 W average power). Treating them as independent slightly underestimates the joint propagated variance, making the reported coupled distribution marginally optimistic. Incorporating the empirical Pearson correlation between mass and power excess across subsystems is recommended at Phase A.

10.1.3. Mass & Power Budget Uncertainty Drivers

System-level mass closure is confirmed with high confidence at Phase 0.

The relatively small standard deviation ($\sigma = 3.5\,\mathrm{kg}$) is a consequence of the central limit effect: with over 60 independent components, individual margin uncertainties partially cancel, and the aggregate distribution is substantially narrower than any single component's margin band. The dominant contributors to what residual variance exists are identified via the mass tornado diagram.

The tornado diagram quantifies which individual component mass uncertainties contribute most to the variance of the total VISTA system mass. For each component i, the Pearson correlation coefficient r_i is computed between its Monte Carlo sample vector $\mathbf{m}_i \in \mathbb{R}^N$ and the total system mass vector $\mathbf{m}_{\mathrm{total}} \in \mathbb{R}^N$ across all $N = 100{,}000$ simulation trials:

$$r_i = \frac{\sum_{k=1}^{N} \left(m_{i,k} - \bar{m}_i\right)\left(m_{\mathrm{total},k} - \bar{m}_{\mathrm{total}}\right)}{\sqrt{\sum_{k=1}^{N} \left(m_{i,k} - \bar{m}_i\right)^2} \cdot \sqrt{\sum_{k=1}^{N} \left(m_{\mathrm{total},k} - \bar{m}_{\mathrm{total}}\right)^2}} \tag{10.6}$$

where $m_{i,k}$ is the sampled mass of component i in trial k and overbars denote sample means. The coefficient $r_i \in [-1, +1]$ measures the linear association between component i and the system total: $r_i = +1$ indicates that every unit increase in component i produces a proportional increase in the total, while $r_i = 0$ indicates statistical independence. All components in the VISTA mass model are sampled from triangular distributions with $m_{\mathrm{low}} = m_{\mathrm{nom}}$ and $m_{\mathrm{high}} = m_{\mathrm{nom}}(1 + \delta)$, where δ is the assigned design margin, so by construction all correlations are non-negative.

The Pearson coefficient is preferred over a simple margin-rank ordering because it accounts simultaneously for both the *magnitude* of the uncertainty and the *weight* of the component in the total. A component with a large nominal mass and a small relative margin can contribute more variance than a component with a small nominal mass and a large relative margin, even though the latter looks riskier when margins alone are compared. Formally, the variance contribution of component i to the total (under the approximation of linear, uncorrelated uncertainties) is $r_i^2\,\sigma_{\mathrm{total}}^2$, so the tornado chart ranked by $|r_i|$ is equivalent to ranking by explained variance fraction r_i^2. The results are shown in Figure 10.5.

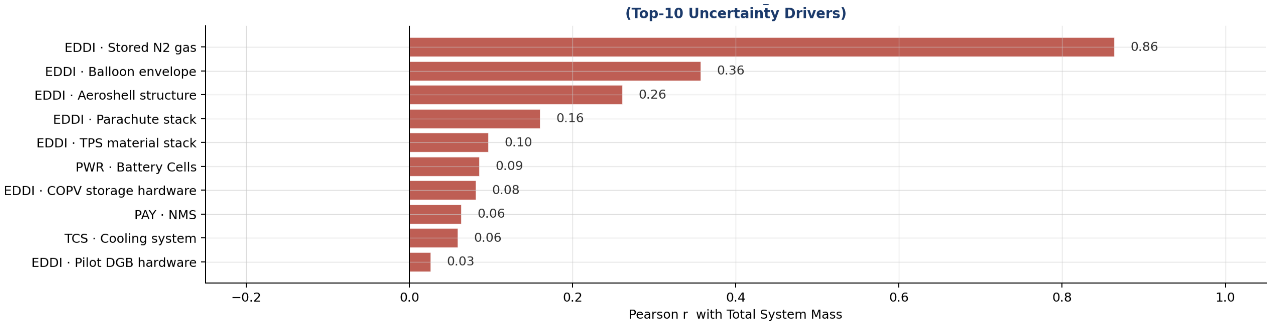

Figure 10.5: Tornado Diagram

The tornado diagram (Figure 10.5) ranks all modelled components by $|r_i|$ and displays the top ten. It reveals that 3 largest uncertainty contributors are all within the EDDI deployment stage rather than the aerobot gondola.

The stored nitrogen is by far the largest single component in the mass budget, at a nominal 260 kg. Although its assigned margin is only 5 %, the absolute uncertainty band $\Delta m = 0.05 \times 260 = 13$ kg is an order of magnitude larger than the absolute uncertainty of any single gondola component. The Pearson coefficient of +0.86 indicates that stored-N_2 mass growth accounts for approximately $0.86^2 = 74\,\%$ of the total system-mass variance on its own. This dominance reflects a fundamental architectural fact rather than a modelling artefact: any uncertainty in the required lift-gas inventory (driven by balloon sizing, altitude target, atmospheric density model uncertainty, and leakage budget) propagates one-for-one into the system entry mass. Reducing this sensitivity requires either tightening the balloon-sizing model inputs or accepting a fixed stored-N_2 allocation that is sized to the worst-case atmospheric density at the chosen float altitude.

Despite the gondola aerobot subsystems carrying higher margins due to lower maturity (several D-rated items at 20 %), their individually small nominal masses keep their correlations low.

The tornado analysis leads to a clear and non-obvious design recommendation: mass-reduction effort guided by requirement REQ-C-MIS-02 ($m_{\text{VISTA}} \leq 700$ kg) should focus on the EDDI lift-gas inventory and COPV hardware rather than on component selection within the aerobot gondola. Specifically:

1. **Tighten the stored-N_2 allocation.** The N_2 inventory is driven by the balloon buoyancy model, the atmospheric density uncertainty at the float altitude, and the leakage budget over the 5-year mission. Reducing the uncertainty on any of these inputs directly reduces r_{N_2} and the probability of exceeding the 700-kg system cap. The coupled Monte Carlo model shows that the current P(system ≤ 700 kg) with propagation is **0.0 %**, confirming that the system-level mass cap is not closed at nominal and that the lift-gas allocation is the primary driver of non-closure.
2. **Mature the COPV structural design.** Advancing the COPV tankage from ROM to PDR-level sizing (reducing the margin from 20 % to 10 %) would halve the absolute uncertainty contribution of this item and reduce system mass variance by approximately 15 % after the N_2 term is addressed.
3. **Gondola bus components are not the priority.** Even if all 20 %-margin gondola components were replaced with zero-margin items (an unrealistic best case), the reduction in system-level mass variance would be smaller than the effect of tightening the N_2 margin by 2 percentage points. This does not mean gondola component margins are unimportant for the gondola-cap requirement REQ-C-STR-03 (≤ 200 kg), where their relative influence is larger, but it confirms they are not the lever to pull for system-level mass closure.

10.2. System Verification

The V&V programme is structured in accordance with the V-model, ECSS-E-ST-10-02C Rev.1 [142] and its companion handbook ECSS-E-HB-10-02A [151]. Verification demonstrates that the delivered system meets its specified requirements; validation confirms that those requirements correctly address the mission's intended use. V&V is conducted at three levels: equipment, subsystem, and system. This section covers system-level V&V only, i.e. the fully integrated gondola platform including the balloon envelope, tethered barometer array, and all deployed interfaces.

Four verification methods are applied to each system requirement. Test (T) is the preferred method and is mandatory for all safety-critical requirements; Analysis (A) is used when full environmental conditions cannot be replicated on the ground or testing is not economically feasible; Review of Design (R) relies on existing records and documentation; and Inspection (I) relies on visual determination of physical characteristics.

A hybrid model philosophy is adopted, comprising three physical models. The Engineering Model (EM) is flight-representative in form and function and is used for functional qualification, interface verification, and software validation. The Structural-Thermal Model (STM) is fully representative of the mechanical and thermal properties of the gondola and is used for structural qualification under launch loads, thermal qualification under Venus float conditions, and correlation of finite element and thermal mathematical models. Lastly, the Protoflight Model (PFM) is the flight end-product, on which a protoflight qualification and acceptance campaign is performed before flight.

Four main system-level campaigns are conducted sequentially:

1. Structural, Mechanical, and Thermal Tests on the STM: qualification of the gondola under launch vibration, acoustic, shock, and thermal-vacuum conditions and correlating the thermal mathematical model against test results;
2. Functional and EMC Tests on the EM: verification of all subsystem interfaces, the dual antenna architecture, leakage-control loop, and the end-to-end communication chain with a simulated relay orbiter;
3. Entry, Descent, and Deployment Tests on the PFM: exercising the complete COPV inflation chain, balloon-envelope deployment, and launch-lock release, which comprises all classified safety-critical since deployment failure forfeits the mission;
4. Earth Stratospheric Analogue Flight at reduced scale: validation of float stability, tether pendulum dynamics, solar-array performance, and GNC position propagation, following JPL Venus aerobot analogue heritage.

Requirements verified by Analysis alone need explicit justification. **REQ-C-MIS-01** and **REQ-C-MIS-03** (5-year lifetime and survival probability) cannot be tested within a feasible schedule; verification combines accelerated envelope leakage testing, membrane endurance modelling, and fault tree analysis, with a mandatory independent cross-check. **REQ-F-ENV-03** and **REQ-F-ENV-04** (atmospheric degradation and radiation tolerance) cannot be fully replicated on the ground; verification relies on Analysis supported by component-level materials data and VEGA heritage. **REQ-C-MIS-06** (altitude adjustment rate) is verified analytically using the validated altitude control model, with the analogue flight providing an empirical data point. The safety-critical requirements REQ-F-LAU-05, REQ-F-LAU-06, REQ-F-DEP-03, REQ-C-DEP-07, REQ-C-ENV-01, and REQ-C-ENV-02 must be verified by Test.

10.3. System Validation

System validation assesses whether the integrated VISTA mission fulfils the original stakeholder objectives listed in Table 10.2, evaluating the complete mission architecture as an operational whole rather than individual requirements. Four validation strategies are applied in order of increasing formality [152].

Table 10.2: Stakeholder Requirements.

ID	Stakeholder Requirement
REQ-STK-1.1	The mission shall be compatible with the Venus mission architecture, including the launcher, carrier spacecraft, S/C contractors, and a data relay through the orbiter.
REQ-STK-1.2	The mission shall achieve all scientific goals.
REQ-STK-1.3	The mission shall be able to transmit all the data back to Earth.
REQ-STK-1.4	The mission shall avoid harmful contamination of the Venus environment in accordance with applicable planetary protection requirements.
REQ-STK-1.5	The spacecraft shall be shown to be reliable.
REQ-STK-1.6	The spacecraft shall reach the Venus atmosphere safely.
REQ-STK-1.7	The mission shall be able to survive the operating environment of Venus.

1. **End-to-end information system validation**: demonstrates that VISTA can generate, store, transmit, and reconstruct mission data into usable science products, directly validating REQ-STK-1.3. Testing is performed on the EM with a simulated orbiter relay and ground-station interface. Validation is successful if received data products match the generated reference data within the required accuracy.
2. **Mission scenario validation**: evaluates combined subsystem behaviour across five representative scenarios through high-fidelity integrated simulations: deployment-to-float (REQ-STK-1.1, 1.4, 1.6); nominal science-operation cycle (REQ-STK-1.2); altitude-control and ISRU replenishment under disturbances (REQ-STK-1.7); safe-mode recovery from communication loss or thermal exceedance (REQ-STK-1.3); and degraded long-duration operation under battery ageing and increased leakage (REQ-STK-1.7).
3. **Operations readiness validation**: demonstrates that VISTA can be operated using realistic procedures, supporting REQ-STK-1.1, 1.3, and 1.5. Mission rehearsals are conducted on the EM with a ground-segment simulator, covering the full nominal operations cycle and degraded cases including missed relay contacts, low battery state of charge, and subsystem safe-mode entry.
4. **Stress testing and robustness validation**: assesses mission feasibility under off-nominal conditions through Monte Carlo simulations, worst-case analyses, and fault-injection, perturbing atmospheric uncertainty,

balloon and ISRU degradation, power and thermal degradation, communication interruptions, dynamic disturbances, and representative fault-injection cases.

Full reproduction of Venus environmental conditions on Earth is not feasible, particularly regarding the coupled thermal, chemical, atmospheric, and dynamic conditions experienced during long-duration operations within the cloud layer; therefore the validation philosophy uses a hybrid approach combining analytical models, subsystem-level testing, and integrated mission simulations, prioritised around mission-critical functions such as deployment, buoyancy control, survivability, communication, and science-data return. V&V activities are estimated at 20-40% of overall mission cost [65]. ESA-ESTEC (European Space Research and Technology Centre) is the primary facility for integrated qualification, supported by existing strong ties with TU Delft and Noordwijk's proximity to Delft, while TU Delft's DASML (Delft Aerospace Structures and Materials Laboratory) and Delft High-Pressure/Temperature Laboratory for Planetary Materials support dynamic and Venus-environment testing respectively. CNES balloon heritage and collaboration with Group 3 (SILICON SHEPHERD) are considered to reduce cost and complexity.

10.4. Compliance Matrix

The compliance matrix serves as the combined verification and validation record for the VISTA mission, consolidating both the requirements compliance status (validation) and the assigned verification methods from the V&V programme described above. For each system-level requirement it documents: the verification method (T/A/R/I), the physical model on which verification is performed, the verification stage, a one-line compliance note cross-referencing the relevant subsystem analysis, and the achieved value for quantitative constraints. Safety-critical requirements are written in red.

Table 10.3: System Requirements Compliance Matrix. Method: T = Test, A = Analysis, R = Review of Design, I = Inspection. Model: STM = Structural-Thermal Model, EM = Engineering Model, PFM = Protoflight Model. Stage: Q = Qualification, A = Acceptance, P = Pre-launch, C = Commissioning. Red = safety-critical.

Req. ID	Type	Requirement	Compliance Note & Ref.	✓	Value	Method	Model	Stage
Mission Requirements								
REQ-C-MIS-01	C	The aerobot operational lifetime shall be at least 5 Earth years.	*[Ref: Tab. 7.10 - lifetime/reliability analysis; accelerated envelope leakage testing + fault tree]*	✓	≥5 yr	A	EM, PFM	Q
REQ-C-MIS-02	C	Total aerobot system mass shall not exceed 700 kg.	*[Ref: Sec. 10.1 - system mass budget]*	✓	691 kg	I	PFM	A
REQ-C-MIS-03	C	Each aerobot shall have a survival probability > 90% over the 5-year mission.	*[Ref: Sec. 11.2 - FMEA/reliability model; independent cross-check required per ECSS]*		2%	A	EM	Q
REQ-F-MIS-04	F	The design shall incorporate the use of atmospheric nitrogen to compensate for helium leakage.	*[Ref: Chap. 7 - ISRU/nitrogen replenishment subsystem design]*	✓	-	R	-	Q
REQ-C-MIS-05	C	All subsystems shall have a minimum TRL of 4.	*[Ref: Sec. 11.2 - TRL table per subsystem]*	✓	≥4	R	-	Q
REQ-C-MIS-06	C	The aerobot shall be able to adjust its operating altitude at a rate of 100 m/h.	*[Ref: Subsec. 6.8.3 - altitude control model; Earth analogue flight provides empirical data point]*	✓	180 m/h	A	EM, PFM	Q
Launch Requirements								
REQ-C-LAU-01	C	The S/C shall be compatible with 9.5g loads involved in launch.	*[Ref: Sec. 10.3 - structural load cases; STM qualification campaign]*	✓	76g	T	STM	Q
REQ-C-LAU-02	C	The S/C shall be compatible with the 2 m^3 volume envelope of the launcher.	*[Sec. 10.3 - stowed configuration; launcher fairing fit check]*	✓	1.7m^3	I	PFM	A
REQ-F-LAU-03	F	The balloon inflation and deployment mechanism shall not be activated before Venus entry.	*[Ref: Sec. 7.4 - deployment sequence; inhibit design and actuation verification]*	✓	-	T, R	PFM	Q, P
REQ-F-LAU-04	F	All launch-locking mechanisms shall be released after arrival at Venus without preventing deployment.	*[Safety-critical. Ref: Sec. 8.1 – mechanism design; functional actuation test at representative Venus-transit thermal conditions]*	✓	-	T	PFM	Q
REQ-F-LAU-05	F	Pre-launch integration tests shall be performed to verify interfacing compatibility of capsule, launcher, S/C, and aerobot.	*[Safety-critical. Ref: Sec. 10.3 – V&V/integration test plan; full system-level test on PFM at launch site before encapsulation]*	✓	-	T	PFM	P

Continued on next page

Req. ID	Type	Requirement	Compliance Note & Ref.	✓	Value	Method	Model	Stage
Balloon Entry and Deployment Requirements								
REQ-F-DEP-01	F	The aerobot(s) shall be compatible with deployment from a Venus orbiter with a 24-hour elliptical orbit.	*[Ref: Sec. 2.1.4 for the 24-hr elliptical orbit interface; Sec. 5.4 for the link analysis]*	✓	-	R	-	Q
REQ-C-DEP-02	C	The aerobot(s) shall be deployable to an operational altitude of 56 km.	*[Ref: Sec. 8.2 - entry/deployment trajectory analysis; 56 km float-capture ceiling]*	✓	56 km	I	PFM	Q
REQ-F-DEP-03	F	The balloon envelope shall deploy without tearing, snagging, or entanglement.	*[Safety-critical. Ref: Sec. 8.1 – full deployment sequence test on PFM; COPV inflation cascade and αRX-Mt3 redundancy chain exercised]*	✓	-	T	PFM	Q
REQ-F-DEP-04	F	The aerobot(s) shall support post-deployment status assessment.	*[Ref: Sec. 8.5 - C&DH/FDIR interfaces; end-to-end telemetry verification]*	✓	-	T	PFM	Q, C
REQ-C-DEP-06	C	The aerobot shall not vent ≥5% of stored gas before reaching 68 km.	*[Ref: Sec. 8.1 - inflation system sizing; COPV sealed until P8 (actual vent 0%)]*	✓	≤5%, 68 km	A	PFM	Q
REQ-C-DEP-07	C	The system shall sustain the entry load spectrum: 78.6 g_0 axial p97.5, 7.87 g_0 lateral, and 206 kPa peak dynamic pressure.	*[Safety-critical. Ref: Table 8.4 – structural load testing on STM to qualification margins over the re-entry load spectrum]*	✓	78.6 g_0 / 206 kPa	T	STM	Q
REQ-F-DEP-08	F	The system shall ensure dynamic stability during re-entry and deployment.	*[Ref: Sec. 8.3 - aerodynamic/dynamics analysis; re-entry stability demonstrated on PFM (6-DOF sim pending)]*	✓	-	T	PFM	Q
REQ-F-DEP-09	F	The aerobot and all supporting systems shall be compatible with the entry capsule dimensional constraints.	*[Ref: Sec. 8.1 - stowed configuration; structures chapter]*	✓	-	I	PFM	A
REQ-F-DEP-10	F	The parachutes shall be deployed per the deployment sequence to slow the S/C to a terminal descent of 17 m/s (subsonic, $M \leq 0.8$, before disreef).	*[Ref: Sec. 8.2 / Table 8.2 - entry/descent sequence; parachute deployment logic]*	✓	17 m/s	T	PFM	Q
REQ-F-DEP-11	F	The heat shield shall be deployed with the correct orientation relative to the orbit-insertion trajectory.	*[Ref: Sec. 8.3 - ADCS/entry guidance; orientation verification]*	✓	-	A	-	Q
REQ-F-DEP-12	F	The gondola shall be deployed after balloon inflation without any tearing.	*[Ref: Sec. 8.1 - deployment sequence; covered by REQ-F-DEP-03 deployment test]*	✓	-	T	PFM	Q
REQ-F-DEP-13	F	The heat shield shall be discarded without generating damage to the rest of the spacecraft.	*[Ref: Sec. 8.3 - separation mechanism; β-divergence jettison analysis]*	✓	-	A	-	Q
REQ-F-DEP-14	F	The heat shield shall survive the 206 kPa peak dynamic pressure / 78.6 g_0 entry loads (743.6 kN ultimate ring reaction).	*[Ref: Table 8.4 - structural analysis of heat shield]*	✓	206 kPa	T	STM	Q
REQ-F-DEP-15	F	The heat shield shall survive the ≈3000 K char-surface temperatures (14.9 MW/m^2 peak heat flux at p97.5) during entry.	*[Ref: Sec. 8.4 - thermal protection system analysis]*	✓	3000 K	T	STM	Q
REQ-C-DEP-16	C	The deployment subsystem shall prevent inadvertent pyrotechnic initiation and uncontrolled COPV energy release during ground handling, launch, cruise, entry, descent, and deployment through inhibited firing circuits, isolated redundant channels, staged pressurisation, and verified safe-arm procedures.	*[Safety-critical. Ref: Sec. 7.5 – ESI-class no-fire basis, A/B firing isolation, COPV 700 bar MEOP, staged pressurisation, and late pyrotechnic-device installation.]*	Open	–	T/R	EM, PFM	Q, A
Sub-system Budget Requirements								
REQ-C-STR-07 / REQ-C-SUB-01	C	Gondola mass shall not exceed 200 kg.	*[Ref: Sec.6.7.5 - Gondola mass budget]*	✓	74.2 kg	I	PFM	A
REQ-C-SUB-02	C	Balloon envelope mass shall not exceed 100 kg.	*[Ref: Table 7.7, Balloon and ISRU Sizing]*	✓	45.5 kg	I	PFM	A
REQ-C-SUB-03	C	Inflation system mass shall not exceed 150 kg.	*[Ref: Sec. 8.1 - inflation system mass budget]*		153.7 kg	I	PFM	A

Continued on next page

Req. ID	Type	Requirement	Compliance Note & Ref.	✓	Value	Method	Model	Stage
REQ-C-SUB-04	C	Aeroshell and parachute mass shall not exceed 250 kg.	*[Ref: Sec. 8.1 - aeroshell/parachute mass budget]*	✓	167.3 kg	I	PFM	A
REQ-C-SUB-05	C	Data transmission rate shall not exceed 1500 bps.	*[Ref: Sec. 6.4 - link budget; end-to-end comms test with simulated relay orbiter]*	✓	1500 bps	T	EM	Q
REQ-C-SUB-06	C	The balloon leakage shall be no more than 1.88 kg/day.	*[Ref: Table 7.6, Balloon and ISRU sizing. Here, "day" refers to the 144-hour cycle]*	✓	1.87 kg/day	T	PFM	Q
Scientific Goals								
REQ-F-SCI-01	F	The system shall perform aerosol sampling and detailed chemical analysis at least once per month.	*[Ref: Sec.5.1 - Scientific goals for VISTA; instruments duty cycle in 3.2.2]*	✓	-	R	-	Q
REQ-F-SCI-02	F	The sampling system shall not affect the chemical composition of the sample.	*[Ref: Sec.5.2 for selected instruments; inlet design in Sec.6.2.4]*	✓	-	T	EM	Q
REQ-C-SCI-03	C	The maximum altitude separation between samples shall be 20 km.	*[Ref: Sec.5.2 - selected instruments; instruments duty cycle in 3.2.2]*	✓	-	R	-	Q
REQ-C-SCI-04	C	The altitude accuracy of sampling shall be 50 km.	*[Ref: Sec.5.2 - selected; instruments duty cycle in 3.2.2]*		-	T	EM, PFM	Q
REQ-C-SCI-05	C	The S/C shall be able to measure vertical wind speed at ≤ 1 hour intervals.	*[Ref: Sec.5.2 - Sonic Anemometer; instruments duty cycle in 3.2.2]*	✓	-	R	-	Q
REQ-F-SCI-06	F	The S/C shall include ≥ 1 measurement systems to detect seismic activity.	*[Ref: Sec.5.3 - seismic detection system; 5 barometers used]*	✓	5	R	-	Q
REQ-F-SCI-07	F	The S/C shall be able to measure cloud dynamics at ≤1 day intervals.	*[Ref: Sec.5.2 - Sonic Anemometer; instruments duty cycle in Sec.3.2.2]*	✓	-	R	-	Q
REQ-F-SCI-08	F	The S/C shall be able to measure horizontal wind speed at ≤ 1 day intervals.	*[Ref: Sec.6.8 - navigation tracking]*	✓	-	R	-	Q
REQ-F-SCI-09	F	The mission shall address the VEXAG roadmap goals.	*[Ref: Sec.5.1 - Science Goals]*	✓	-	R	-	Q
REQ-F-SCI-10	F	The S/C shall be able to measure the temperature of the Venusian atmosphere.	*[Ref: Sec.5.2 - Temperature sensors]*	✓	-	R	-	Q, C
REQ-F-SCI-11	F	The S/C shall be able to measure the pressure of the Venusian atmosphere.	*[Ref: Sec.5.2 - selected pressure sensors]*	✓	-	R	-	Q, C
Survive Operating Environment								
REQ-C-ENV-01	C	The aerobot shall tolerate the atmospheric temperature range of 263–303 K.	*[Ref: Sec. 6.1 – Thermal Control Subsystem]*	✓	263–303 K	T	STM, PFM	Q
Payload Requirements								
REQ-C-PAY-01	C	Each instrument suite shall achieve a successful analysis probability > 80%.	*[Ref: Sec. 5.2 – selected instruments; Sec. 11.2 – instruments subsystem TRL of 8]*	✓	98%	T	EM, PFM	Q, C
REQ-C-PAY-02	C	The total mass of the payload shall stay below 20 kg.	*[Ref: Sec.5.2 - selected instruments total mass]*	✓	18.9 kg	I	PFM	A
REQ-F-PAY-03	F	Scientific components shall fit within the allocated volume.	*[Ref: Sec.6.7 - gondola layout]*	✓	-	I	PFM	A
REQ-F-PAY-04	F	The generated payload data to be stored shall be no more than 32 MB.	*[Ref: Sec.6.3.1 - C&DH data budget; verified on EM]*	✓	-	T	EM	Q
Structures and Mechanisms								
REQ-OP-STR-01	OP	The gondola primary load path shall withstand a peak uniform axial compressive deceleration of 78.62 g during entry.	*[Ref: Sec.6.7.2 – Concentric load path through longitudinal stringers; verified static qualification testing.]*	✓	78.62 g	T	STM	Q
REQ-OP-STR-02	OP	The structure shall simultaneously sustain a 10% lateral load margin (7.87 g) to account for a maximum entry misalignment angle of 6°.	*[Ref: Sec.6.7.2 – Combined multi-axial stress state handling coupled out-of-plane stringer bending.]*	✓	7.87 g	T	STM	Q
REQ-C-STR-03	C	All combined normal and local cross-sectional shear stresses shall be evaluated using the Von Mises distortion energy criterion.	*[Ref: Sec. 6.7.4 – multi-axial stress verification with a minimum material yield safety factor of 2.5]*	✓	-	A	EM	Q
REQ-C-STR-04	C	The thin-walled outer skin and internal framing shall maintain geometric stability against local and global collapse under peak entry pressure profiles.	*[Ref: Sec.6.7.4 – Instability checks per NASA SP-8007: skin wrinkling, global shell buckling, and Euler column snapping.]*	✓	-	A	EM	Q

Continued on next page

Req. ID	Type	Requirement	Compliance Note & Ref.	✓	Value	Method	Model	Stage
REQ-C-STR-05	C	The internal circular frames shall resist cross-sectional distortion and ovalization under localized radial entry loads.	*[Ref: Sec.6.7.4 – Roark's Formulas for Circular Rings mapping combined hoop thrust and bending.]*	✓	-	A	EM	Q
REQ-C-STR-06	C	The flat end lids of the pressure vessel shall withstand inertial self-weight bending stresses and out-of-plane deflections under peak deceleration.	*[Ref: Sec.6.7.4 – Clamped circular plate boundary condition analysis; out-of-plane deflections restricted to ≤ 5.0 mm.]*	✓	1.12 mm	A	EM	Q
REQ-C-STR-07	C	The primary structural assembly shall comply with the mass allocation budgets.	*[Ref: Sec.6.7.5 – Gondola mass package, including subsystems ≤ 200 kg.]*	✓	74.2 kg	I	PFM	A
REQ-F-STR-08	F	The structure shall supply an attachment point to connect the tether instrumentation to the gondola.	*[Ref: 6.7.1 - tether instrument mechanism design]*	✓	-	I	PFM	A
REQ-F-STR-09	F	The structure shall supply an attachment point to connect the deployment structure to the gondola.	*[Ref: 6.7.1 - deployment attachment point interface design]*	✓	-	I	PFM	A
REQ-F-STR-10	F	The structure shall supply an attachment points to connect the balloon structure to the gondola.	*[Ref: 6.7.1 - balloon attachment point interface design]*	✓	-	I	PFM	A
REQ-F-STR-10	F	The structure shall supply two attachment points to connect the two communication antenna's to the gondola. These will be pointing outwards under 30° w.r.t. the vertical axis, and placed at least 10cm above the gondola shell to avoid interference.	*[Ref: 6.7.1 - antenna attachment point interface design]*	✓	-	I	PFM	A
ADCS								
REQ-F-ADC-01	F	The ADCS shall determine and monitor the local dynamic state of the gondola.	*Ref: subsection 6.6.3 dynamic modelling*	✓	-	T	EM, PFM	Q, C
REQ-F-ADC-02	F	The ADCS shall provide stability and health flags when excessive motion is detected.	*Ref: subsection 6.6.3 - dynamic modelling, subsection 6.6.4 - final configuration*	✓	-	T	EM	Q
REQ-C-ADC-03	C	Swing and yaw amplitudes shall remain 8.7° for analysed disturbance cases.	*Ref: subsection 6.6.3 - dynamic modelling*	✓	< 10°	A	EM, PFM	Q
REQ-C-ADC-04	C	The suspension configuration shall maintain positive cable tension during analysed dynamic cases.	*Ref: subsection 6.6.3 - dynamic modelling*	✓	-	A	-	Q
REQ-C-ADC-05	C	The gondola dynamic response shall remain observable.	*Ref: subsection 6.6.2 - IMU selection*	✓	-	A	-	Q
REQ-F-ADC-06	F	The ADCS shall provide dynamic loads and motion envelopes to Structures.	*Ref: subsection 6.6.3 - dynamic modelling*	✓	-	R	-	Q
REQ-C-ADC-07	C	The suspension configuration shall provide each communications antenna with an unobstructed angular visibility of at least 80° past the balloon limb.	*Ref: subsection 6.6.1 - constraints*	✓	≥ 93°	A	PFM	Q
REQ-C-ADC-08	C	The fundamental structural mode of the suspension and tether assembly shall remain at or above 0.06 Hz, i.e. above the seismic measurement band of 0.02–0.05 Hz, for all analysed configurations.	*Ref: subsection 6.6.1 - constraints, section 5.3*	✓	≥ 0.064 Hz	A	EM	Q
REQ-F-ADC-09	F	The ADCS shall determine the absolute yaw of the gondola at least once per orbiter contact, using the differential carrier phase of the communications link.	*Ref: subsubsection 6.6.2*	✓	1-	A, T	EM	Q
ISRU / Envelope Material								
REQ-C-ISR-01	C	Outer surface shall show no loss of mechanical integrity after 5-year continuous H_2SO_4 exposure at 56 km.	*[Ref: Sec. 7.1.3 - envelope material selection; corrosion test data.]*	✓	-	A, T	EM	Q
REQ-F-ISR-02	F	Total envelope N_2 permeance shall allow steady-state leakage to be replaced by the ISRU system within the power budget.	*[Ref: Sec. 7.3.3 - ISRU power budget]*	✓	0.21 Barrer	A	EM	Q

Continued on next page

Req. ID	Type	Requirement	Compliance Note & Ref.	✓	Value	Method	Model	Stage
REQ-C-ISR-03	C	Envelope tensile load capacity shall provide a safety factor ≥ 3 against worst-case superpressure ($\Delta p \approx 21{,}364\,\mathrm{Pa}$).	*[Ref: Sec. 7.1.3 - balloon structural analysis; material test data]*	✓	SF ≥3	A, T	EM	Q
REQ-C-ISR-04	C	Envelope areal density shall not exceed $150\,\mathrm{g/m^2}$.	*[Ref: Table 7.2, envelope material selection; areal density measurement]*	✓	$117\,\mathrm{g/m^2}$	I	PFM	A
REQ-C-ISR-05	C	Material shall survive stowed/packaged configuration; ≥ 2% elongation at break, ≥ 1000 flex fatigue cycles without gas-barrier loss.	*[Ref: Sec. 7.1.3 - material qualification]*	✓	-	T	EM	Q
REQ-C-ISR-06	C	Material shall retain ≥ 80% initial tensile strength after 1825 thermal cycles (±30°C).	*[Ref: Sec. 7.1.3 - material heritage]*	✓	≥ 80%	T	EM	Q
REQ-C-ISR-07	C	All constituent materials shall have a TRL of at least 4 in relevant environments.	*[Ref: Sec. 7.1.3 - material heritage review]*	✓	-	R	-	Q
REQ-C-ISR-08	C	Material shall retain ≥ 95% initial tensile strength after 5-year UV exposure.	*[Ref: Sec. 7.1.3 - material heritage]*	✓	≥ 95%	A	EM	Q
Communications								
REQ-C-COM-01	C	The bit error rate received on Earth shall not exceed 1×10^{-6}.	*[Ref: Sec. 6.4.4–6.4.6 - end-to-end BER allocation; coded link-budget analysis; representative BER test]*	✓	$\leq 1{\times}10^{-6}$	A, T	EM	Q
REQ-C-COM-02	C	The aerobot-to-orbiter link shall support a useful data rate of at most 1500 bit/s.	*[Ref: Sec. 6.4.4–6.4.5 - UHF relay design; Table 5.10 link budget; end-to-end test]*	✓	1500 bps	A, T	EM	Q
REQ-C-COM-03	C	The orbiter-to-Earth link shall be compatible with the ESTRACK ground-station network.	*[Ref: Sec. 6.4.1 and Sec. 6.4.5 - ESTRACK-compatible X-band selection; Earth–orbiter link budget]*	✓	X-band, 7.175/8.425,GHz	R	-	Q
REQ-C-COM-04	C	Each communication link shall close with a positive link margin under worst-case geometry.	*[Ref: Sec. 6.4.3–6.4.5 - propagation losses and worst-case link budgets for all links]*	✓	min = 3.01,dB	A	-	Q
REQ-OP-COM-05	OP	The antenna shall maintain a link with the orbiter for >90% of time when orbiter is above local horizon.	*[Ref: Sec. 6.4.2 and Sec. 6.4.6 - two-antenna UHF pattern; orbiter-pass coverage verification]*	✓	>90%	A, T	EM	Q
C&DH / OBC								
REQ-F-CDH-01	F	The C&DH system shall acquire, time-tag, validate, buffer and route all scheduled science, housekeeping and subsystem-status data streams during nominal mission operations.	*[Ref: Sec. 6.3 - C&DH data-flow and payload-interface analysis]*	✓	-	A, T	EM	Q
REQ-F-CDH-02	F	The C&DH system shall provide sufficient non-volatile storage to retain all science, housekeeping, diagnostic and command data generated between communication opportunities, including at least one missed contact window and a minimum 25% storage margin.	*[Ref: Sec. 6.3 - storage sizing and missed-contact data-buffer analysis]*	✓	128MB NAND+512kB MRAM	A	EM	Q
REQ-F-CDH-03	F	The C&DH system shall maintain temporary buffers for time-critical or event-triggered data until the data has either been processed, downlinked, or intentionally deleted according to the mission data-management policy.	*[Ref: Sec. 6.3 - event-buffer and diagnostic-data management analysis]*	✓	-	A, T	EM	Q
REQ-F-CDH-04	F	The C&DH system shall retain the latest validated command set until a newly received command set has been completely received, checked and accepted.	*[Ref: Sec. 6.3 - telecommand validation and storage logic]*	✓	-	T	EM	Q
REQ-C-CDH-05	C	The C&DH system shall provide sufficient program memory and volatile memory to execute all required flight-software functions with a minimum 25% memory margin after software-size and buffer sizing analysis.	*[Ref: Sec. 6.3 - flight-software size, RAM and buffer sizing analysis]*	✓	≥ 25% margin	A	EM	Q

Continued on next page

Req. ID	Type	Requirement	Compliance Note & Ref.	✓	Value	Method	Model	Stage
REQ-C-CDH-06	C	The C&DH system shall execute all scheduled processing, storage-management, command-handling and downlink-queue functions while meeting their timing deadlines with a minimum 30% processor-utilisation margin under worst-case operational loading.	*[Ref: Sec. 6.3 - processing-utilisation and timing-margin analysis]*	✓	≥ 30% margin	A, T	EM	Q
REQ-F-CDH-07	F	The C&DH system shall provide electrical interfaces compatible with all connected payload, communication, power, thermal, navigation and ISRU subsystem data streams, with sufficient bandwidth, signal integrity and command/status capability for all defined operational modes.	*[Ref: Sec. 6.3 - electrical-interface and subsystem-connection analysis]*	✓	-	R, T	EM	Q
REQ-F-CDH-08	F	The C&DH system shall preserve critical mission state information through reset or temporary power interruption, including fault state, last valid operating mode and data-queue status.	*[Ref: Sec. 6.3 - persistent-state and reset-recovery design]*	✓	-	T	EM, PFM	Q, A
REQ-F-CDH-09	F	The C&DH system shall detect software hangs, invalid execution states and critical data-handling faults, and shall initiate a controlled recovery action without requiring ground intervention.	*[Ref: Sec. 6.3 - watchdog, FDIR and autonomous recovery design]*	✓	-	T	EM, PFM	Q, A
Thermal & Environment								
REQ-F-TCS-01	F	The TCS shall maintain all critical components within survival temperature limits after deployment.	*[Ref: Subsec. 5.1.4 - Takeaways from simulations]*	✓	-	A	STM	Q
REQ-F-TCS-02	F	The TCS shall maintain batteries, avionics, payload, and sampling hardware within operational limits.	*[Ref: Subsec. 5.1.4 - Takeaways from simulations]*	✓	-	A, T	STM, PFM	Q
REQ-C-TCS-03	C	The TCS exposed to sulfuric-acid aerosol shall retain required function after exposure.	*[Ref: Sec. 5.2 - Environmental Protection]*	✓	-	T	EM	Q
REQ-F-TCS-04	F	The TCS shall provide thermal monitoring for batteries, avionics, and payload.	*[Ref: Subsec. 5.1.2. Thermal-Control Architecture]*	✓	-	T	EM, PFM	Q, C
REQ-C-TCS-05	C	Exposed external surfaces shall be compatible with sulfuric-acid aerosol for the full mission.	*[Ref: Sec. 5.2 - Environmental Protection]*	✓	-	A, T	EM	Q
REQ-C-TCS-06	C	Sensitive electronics and payload shall be isolated from direct Venus atmospheric exposure.	*[Ref: Sec. 5.2 - Environmental Protection]*	✓	-	I	PFM	A
REQ-C-TCS-07	C	Environmental protection materials shall be compatible with the expected thermal range.	*[Ref: Sec. 5.2 - External Coatings and Materials]*	✓	-	A	-	Q
Power								
REQ-F-EPS-01	F	The EPS shall deliver a peak power of at least 301.2 W during Nominal Day mode.	*[Ref: Sec. 6.5.2 - power budget (PEL); peak Nominal Day load incl. margin, supplied via the PCDU from array and battery]*	✓	301.2 W	A, T	EM, PFM	Q
REQ-F-EPS-02	F	The EPS shall deliver an orbit-average power of at least 240.8 W over the 96 h day arc.	*[Ref: Sec. 6.5.3 - solar array sizing; daylight-average energy balance closes at 2.17 m^2 vs 2.2 m^2 available]*	✓	240.8 W	A	-	Q
REQ-F-EPS-03	F	The EPS shall provide at least 1 200.5 Wh of usable energy over the 96 h night arc.	*[Ref: Sec. 6.5.4 - night-arc energy balance; 3000 Wh battery at 48% DoD]*	✓	1200.5 Wh	T	EM, PFM	Q, A
REQ-C-EPS-04	C	The battery depth of discharge shall not exceed 48% during a nominal night arc.	*[Ref: Sec. 6.5.4 - battery sizing; DoD = 48.0% (1200.5/2500 Wh), at the limit]*	✓	40%	A	-	Q
REQ-F-EPS-05	F	The EPS shall sustain Survival mode (0.5 W) from stored energy with no solar input.	*[Ref: Sec. 6.5.4 - battery architecture; two-unit split, Survival sustainable on a single unit]*	✓	0.5 W	T, A	EM, PFM	Q

Continued on next page

Req. ID	Type	Requirement	Compliance Note & Ref.	✓	Value	Method	Model	Stage
REQ-C-EPS-06	C	The EPS shall meet its performance requirements at end of life, after five years at the 56 km float altitude.	*[Ref: Sec. 6.5.3 - array sized at EOL (L_d = 0.86, 3%/yr) incl. coating loss]*	✓	5 yr	A	-	Q
REQ-C-EPS-07	C	The EPS external surfaces shall withstand mission-life sulfuric-acid aerosol exposure with transmission loss ≤5%.	*[Ref: Sec. 6.5.3 - Parylene coating; 96 h 96% H_2SO_4 demo (TRL 5); full-life exposure by test]*	✓	-	T	EM	Q
REQ-C-EPS-08	C	The battery shall operate within $[-20, 40]$ °C.	*[Ref: Sec. 6.5.3 - cell allowable range; maintained by TCS; verified in thermal-vacuum]*	✓	-	T	EM, PFM	Q
REQ-C-EPS-09	C	The PCDU shall operate within $[-30, 60]$ °C.	*[Ref: Sec. 6.5.5 - PCDU allowable range; maintained by TCS; verified in thermal-vacuum]*	✓	-	T	EM, PFM	Q
REQ-C-EPS-10	C	The fuses shall operate within $[-55, 125]$ °C.	*[Ref: Sec. 6.5.5 - protection-device allowable range; verified in thermal-vacuum]*	✓	-	T	EM, PFM	Q
REQ-C-EPS-11	C	The solar array shall operate within $[-150, 100]$ °C.	*[Ref: Sec. 6.5.3 - cell–coverglass allowable range; verified in thermal-vacuum]*	✓	-	T	STM, PFM	Q
External Compliance								
REQ-OP-COMP-01	OP	The mission shall comply with COSPAR planetary protection guidelines.	*[Ref: Sec. 11.3 - planetary protection plan; compliance review against COSPAR policy]*	✓	-	R	-	Q
REQ-C-COMP-02	C	The VISTA project Cost at Completion shall not exceed 400 M€ (FY2026), excluding launch procurement and interplanetary delivery but including hosted-payload accommodation, AIV, ground segment, and Phase E1 operations.	*[Ref: Sec. 9.3 – hosted-payload cost assumption; launch-excluded cost estimate; budget breakdown]*	✓	400 M€	R	-	Q
REQ-C-COMP-03	C	The S/C shall fit inside the launch window of late 2035-2037.	*[Ref: Sec. 9.1 - mission development timeline]*	✓	January 2036	R	-	Q
REQ-C-COMP-04	C	The mission shall be accommodated as a hosted payload or mission-of-opportunity element on a larger Venus-bound spacecraft.	*[Ref: Sec. 9.3 – launch procurement excluded from VISTA CaC; host-mission accommodation required for cost closure]*	✓	-	R	-	Q
REQ-OP-COMP-04	OP	The mission shall comply with the Outer Space Treaty regarding harmful contamination.	*[Ref: Sec. 11.3 - planetary protection/legal compliance review]*	✓	-	R	-	Q
REQ-OP-COMP-05	OP	The mission shall define an end-of-life procedure to avoid harmful contamination of Venus.	*[Ref: Sec. 3.2.3 - end-of-life/disposal strategy]*	✓	-	R	-	Q
REQ-OP-COMP-06	OP	The mission shall not mimic previous Venus aerobot concepts during the last 60 years.	*[Ref: Chap. 2 - concept comparison with prior art]*	✓	-	R	-	Q
REQ-OP-COMP-07	OP	All components shall be compatible with what the available contractors can deliver.	*[Ref: Subsec. 11.1.2 - procurement/risk mitigation plan]*	✓	-	R	-	Q
REQ-F-COMP-05	F	The project shall identify a qualified backup manufacturer for all mission-critical components before final production.	*[Ref: Subsec. 11.1.2 - procurement/risk mitigation plan]*	✓	-	R	-	Q

From the compliance matrix, the vast majority of system requirements are verified and compliant. Two requirements remain non-compliant or open: REQ-C-MIS-03, which specifies a survival probability greater than 90% over the five-year mission but currently yields a value of 2%, and REQ-C-SUB-03, where the inflation system mass of 153.7 kg marginally exceeds the 150 kg allocation. Additionally, REQ-C-DEP-16 remains open, as the safety-critical inhibit design for inadvertent pyrotechnic initiation and uncontrolled COPV energy release has not yet been fully verified. REQ-C-SCI-04 is likewise left open pending altitude accuracy testing on the engineering and protoflight models. The concerns, underlying assumptions, and justifications associated with these non-compliances and open items are discussed in detail throughout the relevant sections of this report.

10.5. Verification and Validation of Numerical Models

All numerical models and simulation tools developed for the VISTA mission were subjected to a two-tier V&V procedure prior to use in design decisions: verification of correct physical behaviour through limit-case testing, and validation against published reference data from Venus exploration heritage.

10.5.1. Limit-Case Verification

Each model was tested at certain boundary conditions for which the correct output is known analytically, independently of any external reference. This approach detects implementation errors in governing equations, unit conversions, and sign conventions without requiring external data.

For the buoyancy model, the force-balance residual was verified to approach zero at the converged equilibrium solution, consistent with the neutral-buoyancy condition. For the thermal model, internal component temperatures were verified to converge asymptotically to the prescribed sink temperature when all internal heat dissipation was set to zero, confirming correct implementation of the radiative exchange terms. For the link budget model, the received power was verified to increase monotonically as the aerobot-to-orbiter range was reduced, and to reproduce the free-space path loss formula exactly at a set of manually computed reference distances. For the structural and mass budget models, total system mass was verified to be strictly additive across subsystem contributions, with no allocation producing a negative margin when individual components were set to their maximum budgeted values. For the power budget model, the energy balance was verified to close at zero net surplus when generation and consumption were set to equal values, and battery state of charge was confirmed to deplete monotonically under a constant load with no regeneration.

10.5.2. Validation Against Reference Data

Each critical model was additionally validated by comparing its output against at least one published reference value from Venus atmospheric science or prior balloon mission heritage, with values within 15% accepted as the validation criterion, given the inherent uncertainty in Venus atmospheric properties.

The buoyancy model was validated against the float altitude and lift performance of the VEGA 1 and VEGA 2 balloon platforms [153], which achieved stable float at approximately 54 km altitude with a balloon diameter of 3.4 m and a total suspended mass of approximately 25 kg. The VISTA model reproduces the VEGA float conditions within 8% when run at the corresponding atmospheric density and temperature profiles from the Venus International Reference Atmosphere (VIRA) [33]. This deviation is attributed primarily to uncertainties in the VEGA balloon film mass and gas purity; incorporating more precise values from the original mission documentation would be the most direct path to reducing this error. The thermal model was validated against the Venus cloud-layer temperature profile from VIRA, confirming that the predicted equilibrium gondola external temperature at 56 km is consistent with the ambient atmospheric temperature of approximately 27 °C within the cloud layer to within 15%. The atmospheric density and pressure profiles used across all models were validated directly against VIRA tabulated values at the operational altitude range of 52-62 km, with deviations below 5% across the full range. Same was done for the remaining models used in this feasibility study.

11 Risk, RAMS and Sustainability

11.1. Technical Risk Assessment

The same procedure for the technical risk assessment was used as in the baseline report [154]. The risks identified previously were kept, while additional ones were added based on the new subsystem design choices made during the final design phase. Each risk is assessed using likelihood and severity, both before and after contingency measures, in order to show how the proposed mitigation procedures reduce overall technical risk.

11.1.1. Likelihood & Severity

Two metrics used to assess risk will be derived from likelihood of the risk occurring and severity of its occurrence. This is in line with standard aerospace practice and will use a **1-5** denotation for both likelihood and severity. The likelihood table presents the probability of occurrence on a five-level scale. It follows the ECSS risk-management approach, but the probability ranges are tailored to the given mission [150].

Score	Label	Prob.	Definition
1	Minimum	$< 1\%$	Only under exceptional coincidence of failures.
2	Low	1–20%	Possible, but requires a specific combination of factors.
3	Medium	20–50%	Could occur; similar projects have faced this issue.
4	High	50–80%	More likely than not; risk drivers are partly present.
5	Maximum	$> 80\%$	Expected to occur if no mitigation is applied.

Table 11.1: Probability scale for organisational risk assessment

Score	Label	Technical impact / scope
1	Negligible	Minor issue with no performance impact.
2	Moderate	Small performance loss; minor design adjustment needed.
3	Significant	Clear performance degradation; partial redesign needed.
4	Critical	Major performance loss; key components need redesign.
5	Catastrophic	Subsystem fails its main function, threatening feasibility.

Table 11.2: Severity scale for technical risk assessment

11.1.2. Risks Table

The scale ranges from negligible, where the impact is absorbed within the same day, to catastrophic, where the impact threatens the project deadline or final review. This follows the ECSS risk-management approach of treating severity separately from likelihood, while adapting the consequence definitions to the 10-week DSE context [150]. This table lists all the risks that have been identified so far and their respective contingency measures. They have been categorised into seven subgroups, which can be identified by the middle letters in the risk ID. Also, as explained previously, pre- and post-mitigation probability and severity have been assigned to each risk, and are denoted by P_b, S_b, P_a, S_a, respectively. Finally, a person who is responsible for that specific risk mitigation has been identified. This results in Table 11.3.

Risk identification is carried out by constructing a risk matrix that compares the likelihood and severity of different risk scenarios. This provides a clear overview of the overall importance of each scenario.

The coloured regions indicate the priority of preventive action: green risks are acceptable and require only monitoring, yellow risks call for active mitigation, and red risks are unacceptable and require immediate response. For example, a moderate severity event of rare likelihood may fall within the green region, whereas a major severity event with a likely chance is classified as red. The Pre-mitigation risk map in Table 11.4 shows risk distribution before any preventive measures are applied.

Table 11.3: Technical Risk Assessment and Mitigation Overview, where $R_b = P_bS_b$ and $R_a = P_aS_a$

Risk ID	Risk	Contingency or Prevention	P_b	S_b	R_b	P_a	S_a	R_a	Responsible Person
Manufacturing									
TR-MA-01	Delays in the manufacturing process	Have a backup manufacturer ready, or account for potential delays in Gantt chart.	4	3	**12**	2	2	**4**	Structures Engineer
TR-MA-02	Damage during the folding and packaging of the balloon	Use controlled handling procedures, secure packaging, and careful assessment before final assembly.	1	5	**5**	1	4	**4**	Structures Engineer / Systems Engineer
TR-MA-03	Late identification of defects may delay the launch	Schedule testing procedures while accounting for possible repair procedures, and keep spare components for critical subsystems.	2	3	**6**	1	2	**2**	Structures Engineer / Systems Engineer
TR-MA-04	Integration mismatch between balloon, gondola, inflation system, and parachute may cause deployment issues	Conduct full-scale checks to ensure all systems function well together. Rehearse the deployment before final assembly if possible.	1	4	**4**	1	3	**3**	Systems Engineer
TR-MA-05	Immature or unreliable manufacturing methods may prevent the required techno- logy from achieving required TRL before launch	Ensure a backup is available, such as older technology that is still reliable, in case qualification tests fail.	2	3	**6**	2	2	**4**	Systems Engineer
TR-MA-06	Mass growth during manufacturing may exceed the allocated mass budget	Keep track of mass continuously and include a mass margin for late manufacturing changes.	3	3	**9**	2	2	**4**	Cost & Budget Controller
Launch									
TR-LAU-01	Launch delay	Plan according to weather expectations during certain seasons, keep the S/C in a safe storage location, keep the trajectory for the next launch window updated, and prepare backup launch data.	4	1	**4**	3	1	**3**	Systems Engineer
TR-LAU-02	S/C incapable of handling launch loads	Verify structural margins before launch through analysis and load testing. In case of failure during launch, place the spacecraft in a safe configuration to prevent further damage while diagnosing which systems should not be turned on.	2	5	**10**	1	4	**4**	Structures Engineer
TR-LAU-03	S/C incapable of handling launch vibrations	Verify structural margins before launch through analysis and vibration testing. In case of failure during launch, place the spacecraft in a safe configuration to prevent further damage while diagnosing which systems should not be turned on.	2	5	**10**	1	4	**4**	Structures Engineer
TR-LAU-04	S/C damaged by pyroshock during separation	Use shock qualification testing and shock isolators. After separation, perform health checks, switch to backup units if needed, and place the spacecraft in a safe configuration while diagnosing damage.	1	5	**5**	1	4	**4**	Structures Engineer
TR-LAU-05	S/C damaged by pressure or thermal changes during ascent	Design the spacecraft for the expected ascent environment, use thermal protection and venting paths, check pressure-sensitive components and electronics after launch, and switch to redundant systems if degradation is detected.	1	5	**5**	1	5	**5**	Structures Engineer
TR-LAU-06	Launcher explodes or fails during ascent	Use mission insurance and replacement spacecraft planning to rebuild the spacecraft.	1	5	**5**	1	4	**4**	Systems Engineer
TR-LAU-07	Stage separation failure	Use redundant separation mechanisms, backup separation commands, and technical verification before launch.	2	5	**10**	1	4	**4**	Systems Engineer
TR-LAU-08	Damage from debris in Earth orbit	Track debris before and after launch, adjust parking orbit or timing if needed, and use shielding for critical components.	1	4	**4**	1	3	**3**	Structures Engineer
TR-LAU-09	Launcher fails to insert S/C into Earth orbit	Use onboard propulsion to correct the orbit if the error is small, keep propellant margin for emergency correction, and prepare a backup mission profile if the nominal Venus transfer is no longer possible.	2	5	**10**	1	4	**4**	Systems Engineer
TR-LAU-10	Launcher puts S/C in wrong transfer orbit	Recalculate the orbit manoeuvre required for Venus orbit immediately, or prepare probable failure trajectories beforehand. Use onboard propulsion and backup fuel to correct the orbit.	2	5	**10**	2	4	**8**	Systems Engineer
TR-LAU-11	Venus orbit insertion fails	Attempt a backup burn using the main engine or smaller thrusters.	2	5	**10**	1	4	**4**	Systems Engineer
TR-LAU-12	Fairing separation failure	Use redundant fairing separation systems and attempt backup separation commands if the first command fails.	1	5	**5**	1	5	**5**	Mechanisms Engineer
TR-LAU-13	Spacecraft separation failure	Attempt redundant separation commands, backup pyrotechnic devices, or spring-release systems.	2	5	**10**	2	5	**10**	Mechanisms Engineer
Deployment									
TR-D-01	Parachute failure during deployment	Conduct deployment testing before launch, use a reliable parachute design, and ensure that there is a backup parachute.	2	5	**10**	1	2	**2**	Deployment Engineer
TR-D-02	Balloon inflation failure	Ensure alternative inflation paths and pressure monitoring. Include enough inflation margin to complete deployment.	1	5	**5**	1	3	**3**	Deployment Engineer
TR-D-03	Incorrect deployment sequence or timing	Test the deployment sequence in advance with correct deployment logic and sufficient timing margins.	2	5	**10**	1	5	**5**	Deployment Engineer
TR-D-04	Gondola instability after deployment	Simulate the descent a sufficient number of times, including damping, proper mass distribution, and stability.	3	5	**15**	2	4	**8**	Deployment Engineer
TR-D-05	Loss of control during Re-entry	Design for stability and resistance to tumbling, verify stability through CFD and re-entry simulations, include attitude-control/passive-stability margins	1	5	**5**	1	5	**5**	Deployment Engineer
TR-D-06	Mach/q trigger or event-validation failure causes premature or delayed parachute extraction	Validate Mach/q trigger logic using trajectory simulations, include sensor cross-checks and timing margins, and verify that parachute extraction occurs only inside the allowable dynamic-pressure window.	2	5	**10**	1	4	**4**	Deployment Engineer / CDHS Engineer
TR-D-07	Aeroshell separation, restraint release, or EDDI jettison failure causes recontact, line snagging, or incomplete balloon release	Use separation switches, redundant release paths, multibody separation simulations, line-snag analysis, and ground deployment tests. Confirm separation and release state before inflation and before hand-over to free-float operation.	2	5	**10**	1	4	**4**	Deployment Engineer / Structures Engineer

Continued on next page

Risk ID	Risk	Contingency or Prevention	P_b	S_b	R_b	P_a	S_a	R_a	Responsible Person
Payload									
TR-PL-01	Aerosampling system fails	Use redundant sampling paths, add particle filters or mesh screens to prevent clogging by cloud aerosols, and include a self-cleaning cycle.	2	4	**8**	1	3	**3**	Payload Engineer
TR-PL-02	Certain or all measurement devices cannot handle the Venus environment	Select sensors with proper thermal, pressure, and chemical compatibility. Place sensitive components in a sealed and thermally controlled gondola compartment, use external sensors only where needed, and add sensor redundancy.	1	4	**4**	1	4	**4**	Payload Engineer
TR-PL-03	Chemical analysis measurement device fails or produces faulty data	Include redundant critical components, use a simplified robust chemical-analysis system, add internal reference gases so the system can check itself, and design to avoid cross-contamination between samples.	2	3	**6**	1	3	**3**	Payload Engineer
TR-PL-04	Seismic/infrared payload device cannot detect Venus-quakes clearly	Use multiple detection methods, switch to safe diagnostic mode, and attempt recovery using backup sensors, recalibration, or updated ground-based data-processing filters. If recovery is not possible, continue with reduced science operations using atmospheric data.	3	4	**12**	2	3	**6**	Payload Engineer
Power									
TR-POW-01	The energy storage needed exceeds 500 Wh	Negotiate the constraint, coordinate with all subsystem departments to reduce energy storage needs, and re-evaluate the mission schedule to separate high-energy tasks.	3	2	**6**	1	2	**2**	EPS Engineer
TR-POW-02	Battery capacity degradation or cell failure reduces available energy below mission needs	Use qualified cells with sufficient margin, battery health monitoring, cell balancing, and redundant battery strings where possible. In flight, reduce non-essential loads and switch to a lower-power operating mode.	2	5	**10**	1	4	**4**	EPS Engineer
TR-POW-03	Power distribution or voltage regulation failure interrupts power to critical units	Use current limiting, fuses, redundant converters or regulators for critical loads, isolated power lines, and autonomous power-bus reset logic. Prioritise essential command, communication, and thermal loads during recovery.	2	5	**10**	1	4	**4**	EPS Engineer
TR-POW-04	Solar array degradation, contamination, or insufficient illumination reduces daytime power generation	Include solar-array sizing margin, account for Venus illumination variability, use degradation factors in the power budget, verify MPPT performance, and prioritise battery charging during favourable daylight periods. In flight, reduce non-essential loads if generated power is lower than expected.	3	4	**12**	2	3	**6**	EPS Engineer
TR-POW-05	Incorrect load shedding or latching-current-limiter behaviour disconnects critical subsystem loads	Define load-priority logic before launch, verify PCDU and LCL behaviour through fault-injection testing, separate critical and non-critical loads, and include autonomous reset or recovery procedures for essential subsystems.	2	4	**8**	1	3	**3**	EPS Engineer
C&DH									
TR-CDH-01	On-board computer failure	Include fault detection and timed automatic reboot.	1	5	**5**	1	3	**3**	Comms & Data Engineer
TR-CDH-02	Data handling memory failure may result in loss of scientific data	Ensure there is a backup so that important data is duplicated and safely stored.	2	4	**8**	2	2	**4**	Comms & Data Engineer
TR-CDH-03	Subsystem interface bus failure prevents command or telemetry exchange with one or more units	Use interface timeout detection, isolate the failed bus or node, route around failed devices where possible, and place affected subsystems in a predefined safe configuration.	2	4	**8**	1	3	**3**	Comms & Data Engineer
TR-CDH-04	On-board data storage fills during extended no-contact periods with the orbiter	Use conservative storage margins, prioritise high-value science and housekeeping data, apply onboard compression, and delete or overwrite low-priority data only after safe downlink confirmation.	2	4	**8**	1	3	**3**	Comms & Data Engineer
TR-CDH-05	Command-routing or time-tagging error causes incorrect subsystem operation or missed science activities	Verify command-routing logic with end-to-end tests, use command validation checks, include time-synchronisation monitoring, and require safe-mode rejection of invalid or out-of-sequence commands.	2	4	**8**	1	3	**3**	Comms & Data Engineer
Communication									
TR-COM-01	The data rate constraint of 1500 bit/s is exceeded	Compress data onboard, reduce sampling frequency during quiet periods, prioritise high-value science and health data, store excess data locally, and coordinate with payload and data-handling teams to reduce generated data.	3	1	**3**	1	1	**1**	Comms & Data Engineer
TR-COM-02	Communication subsystem degradation prevents regular data downlink	Include low-rate emergency telemetry, redundant communication paths where possible, onboard data buffering, and prioritisation of critical housekeeping data until contact is restored.	2	5	**10**	1	4	**4**	Comms & Data Engineer
TR-COM-03	Antenna, RF cable, or connector degradation reduces link margin	Use environmental qualification, RF continuity checks, conservative link margin, robust cable routing, and two-antenna placement to reduce blockage and single-point RF failures.	2	4	**8**	1	3	**3**	Comms & Data Engineer
TR-COM-04	Aerobot-orbiter contact duration or visibility is lower than expected, reducing available downlink time	Include contact-duration margin in the operations plan, store data onboard during missed passes, prioritise critical telemetry during short contacts, and update relay scheduling based on observed orbiter geometry.	3	4	**12**	2	3	**6**	Comms & Data Engineer
Thermal									
TR-TH-01	Gondola internal temperature exceeds allowable limits for critical electronics	Use insulation, coatings, thermal margins, temperature monitoring, and Venus-environment testing before launch. In flight, switch off non-essential payloads, reduce internal heat dissipation, and change altitude to a more favourable temperature region if possible.	2	4	**8**	1	3	**3**	Thermal Engineer
TR-TH-02	Critical components experience excessive thermal gradients or local hot spots	Use thermal interface materials, conductive paths, component spacing, thermal sensors near critical units, and thermal-balance testing. In flight, redistribute duty cycles and reduce operation of affected components.	2	3	**6**	1	2	**2**	Thermal Engineer
TR-TH-03	Heater or cooler control malfunction causes unstable thermal conditions or excessive power use	Use redundant temperature sensors, independent thermostat limits, software fault detection, and safe thermal-control set points. If malfunction is detected, isolate the faulty control loop and operate in a predefined reduced-power thermal mode.	2	4	**8**	1	3	**3**	Thermal Engineer

Continued on next page

Risk ID	**Risk**	**Contingency or Prevention**	P_b	S_b	R_b	P_a	S_a	R_a	**Responsible Person**
Structural									
TR-STR-01	Fatigue structural failure due to long mission time	Perform testing beforehand and analyse known fatigue data of the involved elements. In case of in-flight structural failure, change altitude to reduce loads on the aerobot.	3	4	**12**	2	2	**4**	Structures Engineer
TR-STR-02	Gondola shell, frames, or reinforced hard points fail under entry, deployment, or operational loads	Verify the alloy shell, internal ring frames, trays, and hard points using FEM, quasi-static load analysis, and representative load testing. Include structural margins	2	5	**10**	1	4	**4**	Structures Engineer
TR-STR-03	Suspension cable creep, coating degradation, or abrasion reduces tether load capacity	Use Vectran/LCP cables with PTFE/FEP protective coating, perform long-duration creep, tensile, abrasion, acid-exposure, UV, and thermal-cycle testing, and include load-sharing between the four suspension cables. Monitor gondola motion and cable-load indicators where possible.	3	5	**15**	2	4	**8**	Structures Engineer
TR-STR-04	Mounting interface failure or misalignment affects antennas, pyrgeometers, payload, IMU, or other subsystem units	Use interface-control drawings, alignment checks, reinforced mounting provisions, fit-checks with subsystem mock-ups, and vibration testing of mounted components. Keep mounting margins for critical externally mounted instruments and antennas.	2	4	**8**	1	3	**3**	Structures Engineer
TR-STR-05	Gondola packaging or dimensional mismatch prevents proper accommodation inside the entry capsule	Maintain CAD-based packaging control, include clearance margins, perform physical fit checks during integration, and retain the cuboid gondola as a backup configuration if the cylindrical layout causes packaging conflicts.	2	4	**8**	1	2	**2**	Structures Engineer
TR-STR-06	Gondola mass distribution or structural asymmetry increases pendulum motion, torsional oscillation, or ADCS coupling	Track component placement, centre of gravity, and MMOI throughout the design process. Preserve structural symmetry where possible, coordinate layout changes with ADCS, and verify the final mass distribution through integrated dynamic simulations.	2	3	**6**	1	2	**2**	Structures Engineer / ADCS Engineer
ISRU									
TR-ISRU-01	ISRU/buoyancy-control valve or pump failure prevents altitude regulation	Use pressure monitoring, redundant or fail-safe valves, conservative buoyancy margins, and autonomous fallback modes that minimise power use while maintaining science or survival operation.	2	5	**10**	1	4	**4**	ISRU / Buoyancy Engineer
TR-ISRU-02	N2 separator or intake clogging reduces nitrogen extraction capability	Use intake filters, clogging-resistant flow paths, pressure-drop monitoring, periodic purge cycles, and qualification testing with representative Venus cloud aerosols. In flight, reduce replenishment demand where possible and operate the ISRU system in a lower-throughput recovery mode.	3	4	**12**	2	3	**6**	ISRU / Buoyancy Engineer
TR-ISRU-03	Nitrogen leakage rate exceeds the ISRU replenishment capacity	Include leakage margin in the balloon sizing, verify envelope and seam permeability, monitor balloon pressure continuously, and prioritise N2 replenishment during high-leakage periods. If leakage remains excessive, adjust altitude or reduce mission operations to preserve float capability.	3	5	**15**	2	4	**8**	ISRU / Buoyancy Engineer
TR-ISRU-04	ISRU power consumption exceeds the allocated power budget	Verify the compressor and separator power model against representative hardware tests, include operational duty-cycle margins, coordinate ISRU operation with EPS power modes, and delay non-critical ISRU operation during low-energy periods.	3	4	**12**	2	3	**6**	ISRU / Buoyancy Engineer
TR-ISRU-05	Separator mambrane performance degrades in the Venus atmosphere, reducing N2 separation efficiency	Perform Venus-cloud exposure testing on the selected adsorbent material, verify separation efficiency after thermal cycling and acid exposure, include separator performance margin, and monitor outlet gas composition where possible. If degradation is detected in flight, reduce throughput demand and prioritise ISRU operation for essential buoyancy maintenance.	3	4	**12**	2	3	**6**	ISRU / Buoyancy Engineer
ADCS									
TR-ADCS-01	IMU or navigation-sensor failure degrades motion correction and altitude-state estimation	Cross-check IMU data with barometers and housekeeping sensors, flag affected science data, switch to pressure-based altitude estimation, and continue reduced-accuracy science operations.	2	3	**6**	1	2	**2**	Comms & Data Engineer / Payload Engineer
TR-ADCS-02	Passive damping is insufficient to reduce gondola pendulum or torsional motion to the desired level	Verify the passive damping model using dynamic simulations and representative suspension tests. If motion amplitudes remain above acceptable limits, adjust suspension geometry, or account for increased motion in payload data processing and operations.	2	3	**6**	1	2	**2**	ADCS Engineer
Budget									
TR-B-01	Total expected mission budget exceeds €400 million	Descope the mission by reducing non-essential payload functions, simplifying the aerobot design, using fewer redundant components where acceptable, and focusing on core-science objectives.	3	4	**12**	2	3	**6**	Cost & Budget Controller
TR-B-02	Mission must survive 5 years, so operations cost could grow too high due to certain events	Use less frequent ground contact, more autonomous onboard operations, and incorporate expected higher operations cost in the budget.	3	3	**9**	2	2	**4**	Cost & Budget Controller
Environment									
TR-ENV-01	The aerobot ends up above the habitable zone	Make sure the altitude control devices work as intended, such that when the balloon rises above the intended altitude, it is returned quickly	1	3	**3**	1	1	**1**	Deployment
TR-ENV-02	The aerobot ends up in the pole vortices	In case this happens, turn off non-critical systems to save power and obtain valuable in situ data from poles till the end-of-lifetime	1	5	**5**	1	4	**4**	Deployment
TR-ENV-03	Aerobot surface degrades due to prolonged exposure to Venus' sulfuric-acid cloud droplets	Use acid-resistant fluoropolymer/metalised barrier coatings and sacrificial outer layers	4	3	**12**	3	2	**6**	Materials
TR-ENV-04	The aerobot ends up below the habitable zone	Use altitude monitoring and autonomous buoyancy-control commands to return the aerobot to the nominal cloud-layer altitude. If recovery is not immediately possible, switch to a safe reduced-power mode, protect temperature-sensitive components	2	4	**8**	1	3	**3**	Deployment / ISRU / Buoyancy Engineer
TR-ENV-05	Unexpected Venus atmospheric storms or severe turbulence disturb aerobot stability and altitude control	Use conservative stability margins, monitor pressure, wind, and gondola-motion data for storm-like disturbances. If severe conditions are encountered, reduce non-critical science operations and allow the aerobot to passively ride out the disturbance while maintaining altitude and power safety.	2	4	**8**	1	3	**3**	Deployment / ADCS / ISRU Engineer

Table 11.4: Pre-mitigation risk map

Likelihood ↓ / Severity →	1	2	3	4	5
	Negligible	**Moderate**	**Significant**	**Critical**	**Catastrophic**
A — Minimum			TR-ENV-01	TR-MA-04 TR-LAU-08 TR-PL-02	TR-MA-02 TR-LAU-04 TR-LAU-05 TR-LAU-06 TR-LAU-12 TR-D-02 TR-D-05 TR-CDH-01 TR-ENV-02
B — Low			TR-MA-03 TR-MA-05 TR-PL-03 TR-TH-02 TR-STR-06 TR-ADCS-01 TR-ADCS-02	TR-PL-01 TR-POW-05 TR-CDH-02 TR-CDH-03 TR-CDH-04 TR-CDH-05 TR-COM-03 TR-TH-01 TR-TH-03 TR-STR-04 TR-STR-05 TR-ENV-04 TR-ENV-05	TR-LAU-02 TR-LAU-03 TR-LAU-07 TR-LAU-09 TR-LAU-10 TR-LAU-11 TR-LAU-13 TR-D-01 TR-D-03 TR-D-06 TR-D-07 TR-POW-02 TR-POW-03 TR-COM-02 TR-STR-02 TR-ISRU-01
C — Medium	TR-COM-01	TR-POW-01	TR-MA-06 TR-B-02	TR-PL-04 TR-POW-04 TR-COM-04 TR-STR-01 TR-ISRU-02 TR-ISRU-04 TR-ISRU-05 TR-B-01	TR-D-04 TR-STR-03 TR-ISRU-03
D — High	TR-LAU-01		TR-MA-01 TR-ENV-03		
E — Maximum					

After implementing the measures listed in the previous risk table, both the likelihood and severity of several risks are reduced. The resulting post-mitigation risk map is shown in Table 11.5.

Table 11.5: Post-mitigation risk map

Likelihood ↓ / Severity →	1	2	3	4	5
	Negligible	**Moderate**	**Significant**	**Critical**	**Catastrophic**
A — Minimum	TR-COM-01 TR-ENV-01	TR-MA-03 TR-D-01 TR-POW-01 TR-TH-02 TR-STR-05 TR-STR-06 TR-ADCS-01 TR-ADCS-02	TR-MA-04 TR-LAU-08 TR-D-02 TR-PL-01 TR-PL-03 TR-POW-05 TR-CDH-01 TR-CDH-03 TR-CDH-04 TR-CDH-05 TR-COM-03 TR-TH-01 TR-TH-03 TR-STR-04 TR-ENV-04 TR-ENV-05	TR-MA-02 TR-LAU-02 TR-LAU-03 TR-LAU-04 TR-LAU-06 TR-LAU-07 TR-LAU-09 TR-LAU-11 TR-D-06 TR-D-07 TR-PL-02 TR-POW-02 TR-POW-03 TR-COM-02 TR-STR-02 TR-ISRU-01 TR-ENV-02	TR-LAU-05 TR-LAU-12 TR-D-03 TR-D-05
B — Low		TR-MA-01 TR-MA-05 TR-MA-06 TR-CDH-02 TR-STR-01 TR-B-02	TR-PL-04 TR-POW-04 TR-COM-04 TR-ISRU-02 TR-ISRU-04 TR-ISRU-05 TR-B-01	TR-LAU-10 TR-D-04 TR-STR-03 TR-ISRU-03	TR-LAU-13
C — Medium	TR-LAU-01	TR-ENV-03			
D — High					
E — Maximum					

11.2. Reliability, Availability, Maintainability, and Safety (RAMS)

Reliability, Availability, Maintainability, and Safety (RAMS) form a standard framework for assessing a system's dependability throughout its lifecycle. For the VISTA mission, this analysis is particularly important given the autonomous nature of the balloon aerobot system. Once deployed in the Venusian atmosphere, the system must operate for up to five years in a corrosive, thermally extreme environment without any possibility of maintenance or human intervention. The following subsections address reliability, availability, maintainability, and safety for the mission.

Reliability

Reliability is defined as the probability that a given item performs its intended function without failure, under specified mission conditions, for the required mission duration. Given the nature of this mission, achieving a high level of system reliability is critical, as the spacecraft and its subsystems must operate autonomously, without the possibility of periodic maintenance.

As per **REQ-C-MIS-03**, the aerobot shall have a survival probability of over 90%. At this stage of the design process, estimating reliability at the component level is not feasible due to the limited maturity of the design. Reliability is therefore estimated at the system level, with each system assigned a Technology Readiness Level (TRL) corresponding to the maturity it is expected to reach by the pre-launch phase, based on the current state of technology. Each TRL level definition is shown in Table 11.6. The aerobot system is divided into three component branches: balloon, gondola, and ISRU. These TRL-based estimates could be improved through the development of mission-specific hardware and the completion of additional testing and validation campaigns.

Table 11.6: Technology Readiness Level (TRL) definitions and estimated reliability values [155].

TRL	Definition	Est. Reliability
1	Basic principles observed	0.50
2	Technology concept formulated	0.55
3	Experimental proof-of-concept	0.65
4	Component validated in laboratory	0.75
5	Component validated in relevant environment	0.85
6	System/subsystem model demonstrated in relevant environment	0.93
7	System prototype demonstrated in operational environment	0.96
8	System flight-qualified through test and demonstration	0.98
9	Actual system flight-proven through mission operations	0.99

Apart from TRL definition, a correction is also applied to the systems that have redundancy components. Equation 11.1 [65] assumes a series and parallel reliability model, which is equivalent to partial redundancy of the system. That is, some components within each system are redundant but not the entire system. In this equation, r is the reliability of a single component and n is the number of components in parallel (redundant to each other). In the aerobot system, the balloon has six attachment cables, however only three are needed to prevent mission failure. For the gondola, an extra antenna is present for communication. Although having only one antenna reduces mission capability substantially, it will not cause total mission failure. Finally, five barometer are used. For seismic detection, only one barometer is sufficient, however the radial localization function is lost, but this is not considered mission ending. After applying the reliability corrections, the final estimated reliability is presented in Table 11.7.

$$R_s = R \cdot [1 - (1 - r)^n] \tag{11.1}$$

Table 11.7: Estimated reliability of major mission subsystems by TRL.

System	Component	TRL	Redundancy	Est. Reliability
Orbiter	-	9	None	0.99
Deployment	-	8	None	0.98
Aerobot	Balloon	6	Six cables connecting balloon envelope to gondola.	0.93
	Gondola	6	Two antennas for communication.	0.91
Instruments	-	8	Five barometers for seismic detection.	0.98
Total				0.81

When ISRU and the risk of becoming trapped in a polar vortex are excluded from the analysis, the mission's probability of survival is approximately 81%. However, once these factors are incorporated, the overall mission reliability drops to around 2%, as they only have a reliability of 3% and 80% for a five year duration mission, respectively. The decrease in mission reliability based on mission duration is plotted in Figure 11.1. The sharp decline is primarily attributable to the pump's characteristic life, which falls short of the required mission duration. Therefore, the ISRU subsystem must be redesigned to be mission-specific, with particular emphasis on extending the pump's characteristic life to withstand these extended-duration conditions, with reliability margins tailored to it. That would drastically impact the overall mission reliability. Regarding the chances of becoming trapped in a polar vortex, maintaining a lower altitude would also significantly improve the chances of such event to occur.

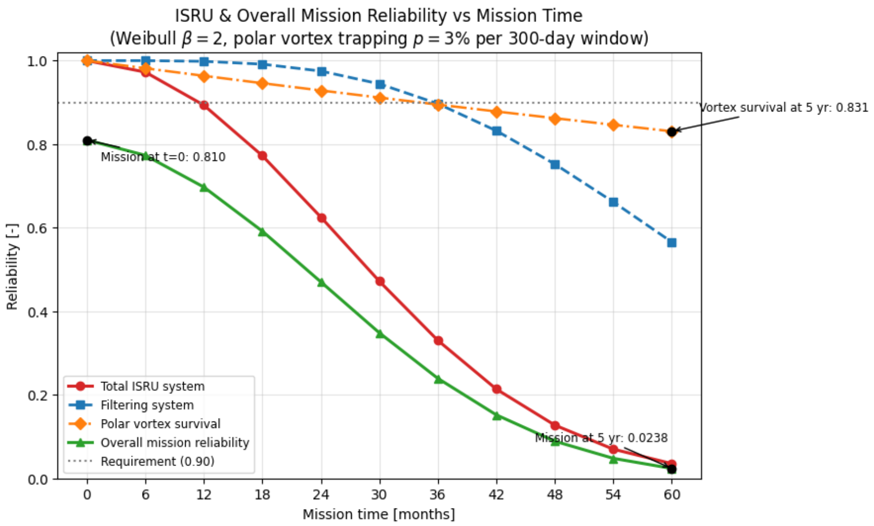

Figure 11.1: Mission reliability over time.

In conclusion, the baseline reliability of 81% already falls short of the 90% required by REQ-C-MIS-03, and the inclusion of ISRU and polar vortex risks drives this down further, since reliability decreases with mission duration and the ISRU pump's characteristic life cannot sustain the extended timeline these risks impose. Closing this gap requires a mission-specific redesign of the ISRU subsystem to extend the pump's characteristic life, further maturation of the balloon and gondola subsystems, and careful assessment of the operational altitude profile to mitigate polar vortex entrapment risk.

Availability

Availability is defined as the probability that a system is in a state to perform its required function at a given instant in time, accounting for both the occurrence of failures and the time required to restore the system to operation following a failure. It is typically expressed as $A = \frac{MTBF}{MTBF+MTTR}$ [156], where MTBF is the mean time between failures and MTTR is the mean time to repair. Availability therefore reflects not only how reliable a system is, but also how quickly it can recover from a failure.

For VISTA, however, no maintenance or repair capability exists once the system is launched: any failure that occurs during the mission is permanent, with no possibility of restoring the affected subsystem to operation. As a result, the concept of availability falls to that of reliability, since the probability that the system is operational at any given time t is simply the probability that it has not yet failed, that is, A(t)=R(t). Consequently, availability is not treated as a separate metric in this analysis, and the reliability estimates presented in Table 11.7 are taken to represent the system's availability throughout the mission duration.

Maintainability

Maintainability describes the ease with which a system can be diagnosed, accessed, and repaired in order to restore its intended function following a failure. For a mission to Venus, however, the conventional concept of maintainability does not apply. Once the aerobot is deployed, no physical access, inspection, or repair is possible for the remainder of the mission. Maintainability must therefore be reiterated not as the ability to fix a failure, but as the system's ability to detect, isolate, and respond to failures autonomously, without external intervention.

Therefore, the design must put emphasis on fault tolerance, functional redundancy, and autonomous fault management, such as onboard anomaly detection and safe-mode entry in response to detected issues. These mechanisms are intended to prevent single-point failures or dangerous conditions from escalating and eventually leaving to total mission failure, effectively substituting the physical maintenance that would normally restore a failed system. As a direct consequence, maintainability and reliability become closely linked as well. As no failure can be corrected post-launch, mission success relies almost entirely onto the reliability of the system, reinforcing the need for the redundancy and design margins discussed in the reliability analysis above. At the current design stage, the autonomous fault-management capabilities required to support this approach have not yet been fully developed, and further design, testing, and validation will be needed to demonstrate that the system can reliably detect and respond to failures without human intervention.

Safety

Finally, safety refers to the system's freedom from conditions that could result in harm to staff, damage to ground equipment, or catastrophic loss of the mission. For the VISTA aerobot, safety considerations span two distinct domains: ground safety during manufacturing, integration, and testing; and flight safety during the operational mission at Venus.

On the ground, the AIT campaign involves several hazardous operations that must be carefully controlled. Pyrotechnic device installation and pressurant servicing of the N_2 buoyancy/ISRU system are sequenced as the final steps before shipment and are carried out under dedicated safety procedures to minimise the time personnel are exposed to armed or pressurised hardware. Fluid GSE incorporates helium leak detection to verify the integrity of pressurised lines before operation, while contamination control measures around acid-sensitive coatings and payload optics reduce the risk of chemical exposure to personnel as well as damage to flight hardware during handling. Special care should be taken during testing and qualification campaigns in emulated Venus conditions, as they necessitate creating hot, high pressure atmosphere filled with sulphuric acid.

During the operational mission, safety is closely linked to the autonomous fault management capabilities discussed in the maintainability section. Since no human intervention is possible once the aerobot is deployed, the system must be capable of autonomously detecting anomalous or hazardous conditions and entering a safe mode to prevent escalation into mission-ending failures. Redundancy in critical subsystems, such as the suspension cables, communication antennas, and barometers discussed in the reliability analysis, further reduces the likelihood that a single failure could create a hazardous condition for the rest of the system. Finally, planetary protection requirements (COSPAR Category II) ensure that the mission does not pose a contamination risk to the Venusian environment, though given the harsh surface and atmospheric conditions of Venus, such requirements do not pose limitations to the design.

11.3. Sustainability

The sustainability assessment of VISTA is used as a design-guidance tool rather than as a full quantitative life-cycle assessment (LCA). Its purpose is to identify the mission phases and design choices that are most likely to drive environmental impact: specialised material production, hazardous-material handling, qualification testing, launch mass, and end-of-life behaviour. The functional unit is one complete VISTA Venus aerobot mission, including material acquisition, component manufacturing, assembly, testing, launch preparation, Venus operations, and end-of-life. Since detailed supplier process data are not available at this design stage, the assessment uses screening-level indicators rather than full CED, GWP, water-use, or toxicity values.

11.3.1. Goals and Scope: Environmental Impact and Planetary Protection

VISTA shall comply with the COSPAR planetary-protection requirement, REQ-OP-COMP-01, and with the mission requirement to avoid harmful contamination of Venus, REQ-OP-COMP-04. Venus missions are treated as Category II missions, meaning that full spacecraft sterilisation is not required, but planetary-protection documentation and contamination control are still necessary. VISTA shall also be consistent with the Outer Space Treaty obligation to avoid harmful contamination of celestial bodies. For VISTA, this means minimising avoidable biological, particulate, and chemical contamination of the Venus cloud layer, where the aerobot operates for most of the mission.

The sustainability assessment is therefore linked to both Earth-side environmental impact and Venus contamination risk. The main screening indicators used in the current design are the total launch mass, the mass of specialised fluoropolymer-containing materials, the battery mass and chemistry, the quantity of pressurised-gas hardware, the number of full-scale test articles, and the end-of-life probability of leaving an active platform in the cloud layer. The nominal VISTA system mass is 691 kg, while the coupled mass-uncertainty analysis gives a mean of 732 kg and a 5–95% interval of 720-744 kg. Launch mass is therefore retained as the dominant quantitative sustainability driver at this design stage, because any mass growth increases launcher demand and propagates into larger structure, lift gas, envelope, and deployment hardware.

11.3.2. Earth-side Development

Manufacturing Manufacturing sustainability is mainly driven by the specialised hardware required for long-duration operation in the Venus cloud environment. Where reliability allows, commercial or heritage-based components are preferred over fully custom parts, since this reduces dedicated tooling, qualification effort, material waste, and manufacturing energy. However, mission-specific components remain unavoidable for the balloon envelope, acid-resistant coatings, sampling inlets, seals, filters, pressure hardware, batteries, and nitrogen-handling components.

Material selection shall therefore consider both performance in the Venus atmosphere and Earth-side environmental burden. This includes extraction impact, processing energy, toxicity, waste generation, supplier controls, and disposal route. Fluoropolymer materials such as PTFE, PCTFE, and related coatings are especially important. They provide strong chemical resistance against sulphuric-acid exposure, but their production and disposal can be environmentally sensitive because fluoropolymer supply chains may involve hazardous fluorinated feedstocks, and PFAS-related processing aids. Consequently, fluoropolymers are not treated as default materials, but as justified functional materials: they are used only where their acid resistance, low reactivity, and low shedding are required for mission success and planetary-protection compatibility. The selected design shall minimise exposed fluoropolymer mass, require suppliers to document PFAS-related production controls where available, avoid unnecessary fluoropolymer coatings, and compare alternatives such as non-fluorinated liners where these can meet the environmental and mechanical requirements.

Battery and gas-handling hardware are treated as additional sustainability-sensitive items. The battery system shall minimise scarce or highly polluting materials where alternatives can still meet the energy-density, thermal, and reliability requirements. The nitrogen itself is not a major toxicity concern, but the associated pressure vessels, valves, compressors, tubing, filters, and adsorbents increase manufacturing burden and should therefore be included in the material inventory.

Testing Testing is necessary to verify launch survival, deployment, and long-duration operation in the Venus cloud layer, but the campaign should avoid unnecessary environmental impact. Early verification should rely on simulations, analytical models, material coupons, and hardware-in-the-loop tests before full-scale articles are built. Physical testing should progress from coupons and subassemblies to larger articles, especially for the balloon envelope, fluoropolymer coatings, seals, sampling inlets, and nitrogen-handling hardware. Sulphuric-acid exposure tests shall include safe handling and waste-disposal procedures, because the test chemicals and degraded coating residues may be hazardous. Where possible, vibration, thermal cycling, pressure testing, deployment trials, EMC testing, and acid-exposure tests shall be combined to reduce repeated facility use, energy demand, and duplicate test hardware.

Launch The launch phase is expected to be one of the dominant life-cycle contributors because launch vehicle production and propellant use are energy intensive. Since the launcher is outside the VISTA design scope, the main mitigation available to the project is strict mass control. Lower system mass reduces launch-performance demand and may improve compatibility with more efficient launch or rideshare options. Therefore, mass growth is treated not only as a technical and cost risk, but also as a sustainability risk. In the current design, the strongest mass-related sustainability drivers are the stored nitrogen inventory, deployment hardware, pressure vessels, balloon envelope, and battery system.

11.3.3. Operations and End-of-life

During nominal operations, the main planetary-protection concern is to avoid unnecessary release of material into the Venus cloud layer. The aerobot therefore interacts with the atmosphere only through intended interfaces, such as sampling inlets, aerosol collection systems, and buoyancy-control hardware. Venting shall be limited to what is required for altitude or pressure management and should preferably involve only nitrogen or other mission-compatible gases. Exposed materials, coatings, and seals are selected to remain chemically stable, low-shedding, and low-outgassing in sulphuric acid, reducing the risk of particulate or chemical contamination.

The end-of-life approach is a best-effort passivation and cloud-layer removal strategy rather than a fully controlled disposal manoeuvre. If the aerobot remains functional near the end of the mission, the preferred sequence is to downlink remaining science data, housekeeping data, fault logs, and final navigation estimates; shut down non-essential payloads; close sampling inlets where possible; isolate or deplete stored electrical energy; stop nitrogen replenishment; and, if buoyancy control remains available, reduce lift through controlled venting so that the aerobot descends out of the scientifically relevant cloud layer. This reduces the probability of leaving an active, long-lived, uncontrolled platform in the region of highest scientific interest.

An uncontrolled end-of-life remains credible because the aerobot has no lateral propulsion and depends on continued power, communication, avionics, envelope integrity, and gas-handling functionality. In such a case, the vehicle may descend passively due to leakage, battery failure, thermal failure, communication loss, or gas-system faults. This case is considered acceptable only because Venus is a Category II planetary-protection target, the final vehicle is passive rather than biologically active, and descent removes the vehicle from the cloud layer into hotter and higher-pressure regions. The limitation is explicitly recognised: the final descent location and timing cannot be guaranteed, so later design phases should refine the passivation logic, material-inventory documentation, and contamination-risk assessment.

11.3.4. Economic and Social Sustainability

Economic sustainability is assessed through efficient use of mass, cost, and qualification resources rather than only compliance with the 400 million euro cost cap. The long operational lifetime is the main value driver: five years of in-situ atmospheric and seismic measurements provide more science return per launched kilogram and per euro than short-duration probes. This is supported by using heritage components and shared subsystem functions where reliability permits.

Socially, VISTA contributes a long-duration Venus cloud-layer dataset that cannot be provided by orbiters or short-lived probes alone. Measurements of atmospheric composition, cloud chemistry, dynamics, and seismic infrasound improve understanding of Venus as an extreme greenhouse planet and provide scientific context for terrestrial climate modelling. These benefits are sustainable only if the mission avoids unnecessary terrestrial environmental burden and complies with planetary-protection obligations, especially through controlled material selection, contamination monitoring, safe hazardous-material handling, and responsible end-of-life planning.

12 Conclusion

The central thesis of VISTA is that in situ nitrogen extraction from the Venusian atmosphere can overcome the lifting-gas leakage problem that has limited all previous Venus balloon missions to lifetimes of days.

12.1. Summary of Findings

The study has shown that this thesis is physically consistent: the Venusian atmosphere at 56 km altitude contains 3.5% N_2 by mole fraction, the leakage rate of the designed balloon envelope (0.62 kg/day at beginning of life, rising to 1.87 kg/day at end of life) can be replenished in real time by an ISRU system operating during the 3.3-day dayside half-cycle, and the power required to do so (147 W peak, 74 W average) is compatible with the solar array sized for the 56 km float altitude. In this sense, the mission concept closes thermodynamically and mechanically.

All subsystems are sized to Phase 0 resolution. The 9-instrument payload and 5-barometer tether seismic array address VEXAG roadmap goals: atmospheric characterisation and interior geophysics, totalling 18.9 kg and 91.1 W peak within gondola limits. The 75 m tether seismic system enables epicentral distance estimation for venusquakes down to $M_s = 4$ at 571 km range and global coverage for $M_s \geq 7$, constituting the first sustained seismic monitoring beyond Earth and Mars.

The gondola structure (14.4 kg, Al 6061-T6) meets all load cases including 78.6 g axial entry. The 2 500 Wh battery sustains the 12.5 W night load over 2.7 days at 48% depth of discharge. The UHF/X-band communications chain achieves 1 500 bit/s downlink with margins exceeding 3 dB, and the passive thermal architecture is viable as proven by CFD simulations. The ADCS dynamic configuration meets the subsystem constraints, including communication visibility and seismic dynamic frequency-filtering. The 6 DOF IMU requires 3 kg and 3.5 W, and is shared with the navigation subsystem, which achieves ~5 km horizontal accuracy via Doppler ranging supplemented by inertial back-propagation.

Pre-filled envelope with ISRU top-up minimises early-mission catastrophic risk occurrence and decreases operational complexity. The 56 km float altitude is a trade-off between insufficient solar flux in lower altitudes and high vortex entrapment risk on upper altitudes, confirmed by Monte Carlo trajectory simulations and power-computing numerical algorithms.

Overall, the Master Equipment List closes at 757 kg (point estimate) against a 700 kg cap; Monte Carlo analysis places the P5/P95 interval at 720–744 kg, with 74% of variance driven by N_2 inventory uncertainty. Cost is €364 M at 50% confidence (cap: €400 M), rising to €434 M at 70%.

12.2. Recommendations

At the current Phase 0 maturity level, the mission is not yet feasible as specified, for multiple reasons:

1. **ISRU technology readiness.** The nitrogen separation and altitude-control compressor system has no flight heritage for Venus-duration operation. The estimated total ISRU reliability of 3.5% over five years is unacceptable. Extensive ground testing, qualification of Venus-representative components, and likely redesign of the pump and separator module are necessary to mature this technology. This is the mission's critical development path.
2. **Balloon envelope qualification.** No acid-resistant superpressure balloon envelope with demonstrated five-year Venus cloud-layer lifetime exists. Long-duration sulphuric acid exposure testing must begin in Phase B to support a 2035 launch readiness date. In fact, no balloon ever has flown for more than 1 Earth year anywhere. At such long timespans, performance is no longer limited by leakage, but by envelope degradation. As such, demonstrating a 5 year duration flight in the easier Earth condition is crucial for certification.
3. **Reconsider the mission duration, reliability, and cost requirements.** The design team recommends reassessing the (5)-year lifetime requirement (REQ-C-MIS-01), the (>90%) reliability requirement (REQ-C-MIS-03), and the cost requirement (REQ-C-COMP-02) together. These requirements compete directly: increasing reliability for a novel architecture with limited flight heritage requires additional validation and TRL maturation, which increases cost. To maintain mission feasibility, the lifetime, reliability, and cost targets should therefore be reviewed as a coupled trade-off.

Subject to resolution of these issues, and with refinement of the mass budget to close the 700 kg system cap, VISTA is assessed as a viable mission concept that would deliver transformative science return for Venus and for planetary science more broadly.

12.3. Final Remarks

The concept of extracting nitrogen from the Venusian atmosphere to sustain a multi-year balloon flight is physically sound. This study has shown that a self-consistent system architecture can be built around it. All subsystems have been designed, sized, and checked at interface level. The mass, power, data, and cost budgets are internally consistent, and the science payload addresses the main gaps in current Venus knowledge.

The main paths to feasibility depend on two technology-development efforts: a mission-specific ISRU compressor qualified for Venus-duration operation, and a balloon envelope demonstrated to survive five years of concentrated sulphuric acid exposure.

The five-year lifetime is the main constraint on the design, and at the same time the largest source of uncertainty in it. Envelope leakage starts near the permeation floor and grows as mechanical damage accumulates: pinholes, microcracks, and seam fatigue, until the envelope eventually tears [157]. This damage-driven life, not the permeation budget, is what sets the achievable mission duration, and there is almost no flight heritage to anchor it: no balloon has ever flown for more than about one Earth year anywhere, the record being 336 days (Aerostar Thunderhead, 2025 [158]), and VEGA lasted only 46 hr at Venus [159]. Designing to five years therefore means qualifying for a regime no balloon has reached, which is where most of the cost and reliability risk sits. To arrive at a more concrete design this uncertainty has to be narrowed, and that requires demonstrating longer-duration balloons on Earth: a long-duration, acid-exposure envelope test campaign must be carried out to establish the life that can actually be achieved, since the current five-year figure is assumed rather than demonstrated.

Nitrogen itself remains clearly viable for long-duration missions; it directly counters the helium leakage that ended every previous Venus balloon, and the ISRU concept closes thermodynamically and mechanically as shown above. Its mass penalty is also not fixed. A large part of the nitrogen inventory follows from the 56 km float altitude, and a lower float altitude reduces the required nitrogen, at the cost of a warmer thermal environment and weaker solar flux. Float altitude is therefore a second lever that should be traded together with lifetime in future work. Notably, this better aligns with airship design: one could imagine a long-endurance rigid airship built for higher temperatures and flown deeper in the atmosphere, where the denser CO_2 sharply increases nitrogen's effective buoyancy, a promising direction for a future study.

If these enabling technologies are matured successfully, VISTA would provide a major advance in Venus exploration. Five years of continuous in-situ measurements of atmospheric chemistry, dynamics, cloud physics, radiative balance, and interior seismicity would return a dataset that cannot be matched by an orbiter, short-duration probe, or lander. It would also establish long-duration Venus balloon missions as a mature platform for future exploration of Venus and other cloud-bearing planetary atmospheres.

12.4. Acknowledgements

The authors would like to thank our tutor, Edgar Steenstra, and our coaches, Alex Luijten and Ernst Schrama for committing to the numerous hours required to listen, give feedback and grade our work. We greatly appreciate your support. Thank you to David Jameux, who despite having no formal responsibility, consistently attended our meetings, listened, explained, and showed us how to conduct proper systems engineering. Thank you to Colin Wilson, for introducing us into the science of Venus, and for providing precious professional feedback during the review sessions. We hope our work helps your future research. Thank you to Iaroslav Iakubivskyi and Sébastien Lebonnois for responding to our questions and sharing their professional insights into our mission.

References

[1] S. S. Limaye and J. B. Garvin. “Exploring Venus: Next Generation Missions Beyond Those Currently Planned”. In: *Frontiers in Astronomy and Space Sciences* 10 (2023), p. 1188096. DOI: `10.3389/fspas.2023.1188096`.

[2] Indian Space Research Organisation. *Mission to the Venus, and to the Moon: Configuration and Scientific Objectives*. Accessed: 2026-04-24. 2024. URL: `https://www.isro.gov.in/UnionCabinetApprovesIndiasMission.html`.

[3] J. A. Cutts et al. *Aerial Platforms for the Scientific Exploration of Venus*. Tech. rep. D-102569. JPL/Keck Institute for Space Studies, 2018. URL: `https://science.nasa.gov/resource/aerial-platforms-for-the-scientific-exploration-of-venus/`.

[4] P. Beauchamp et al. “Venus Flagship Mission Concept: A Decadal Survey Study”. In: *The Planetary Science Journal* 2.5 (2021), p. 175. DOI: `10.3847/PSJ/abf145`.

[5] Richard French et al. “Rocket Lab Mission to Venus”. In: *Aerospace* 9.8 (2022), p. 445. DOI: `10.3390/aerospace9080445`.

[6] Venus Exploration Analysis Group (VEXAG). *Goals, Objectives, and Investigations for Venus Exploration*. Tech. rep. Venus Exploration Analysis Group (VEXAG), 2019. URL: `https://discovery.larc.nasa.gov/PDF_FILES/01a_GOI_Draft_2019March10.pdf`.

[7] Casey Dreier. *The Planetary Exploration Budget Dataset*. The Planetary Society. Compiled from NASA Congressional Budget Justifications and CADRe-derived data; inflation adjustment via NASA New Start Inflation Index (NNSI). Accessed 2026. URL: `https://www.planetary.org/space-policy/planetary-exploration-budget-dataset`.

[8] European Space Agency. *Venus Express Frequently Asked Questions (FAQs)*. Accessed: 2026-05-01. URL: `https://www.esa.int/Science_Exploration/Space_Science/Venus_Express/Venus_Express_Frequently_Asked_Questions_FAQs` (visited on 05/01/2026).

[9] Peter B. de Selding. “Japan Lofts Probe to Study Venus’ Climate”. In: *SpaceNews* (May 2010). Quoting JAXA spokesman A. Hashimoto: ¥14.6 B build + ¥9.8 B launch (≈$280 M, 2010). URL: `https://spacenews.com/japan-lofts-probe-study-venus-climate/`.

[10] UK Government and UK Space Agency. *UK scientists on a mission to Venus*. Accessed: 2026-05-01. June 2021. URL: `https://www.gov.uk/government/news/uk-scientists-on-a-mission-to-venus`.

[11] Jonathan O’Callaghan. “The first private mission to Venus will have just five minutes to hunt for life”. In: *MIT Technology Review* (Aug. 2022). Accessed: 2026-04-24. URL: `https://www.technologyreview.com/2022/08/29/1058724/the-first-private-mission-to-venus-will-have-just-five-minutes-to-hunt-for-life/`.

[12] E. S. Steenstra. *Design of a Long-Duration Balloon-Based Aerobot(s) Mission for Venus Exploration*. Project Description AE3-200. Delft University of Technology, Jan. 2025.

[13] William Frazier, Timothy McElrath, and Charles Lee. “Navigation and Communication through the Venusian Clouds”. In: *Proceedings of the 44th Annual American Astronautical Society Guidance, Navigation, and Control Conference*. 2022.

[14] European Cooperation for Space Standardization. *ECSS-M-ST-10C Rev. 1 — Space project management: Project planning and implementation*. Tech. rep. ECSS-M-ST-10C Rev. 1. Noordwijk, The Netherlands: ESA Requirements and Standards Division, Mar. 2009. URL: `https://ecss.nl/standard/ecss-m-st-10c-rev-1-project-planning-and-implementation/` (visited on 04/30/2026).

[15] European Space Agency. *Building and Testing Spacecraft*. `https://www.esa.int/Science_Exploration/Space_Science/Building_and_testing_spacecraft`. Accessed: 2026-06-16.

[16] European Cooperation for Space Standardization. *ECSS-U-ST-20C: Space Sustainability – Planetary Protection*. ECSS Standard ECSS-U-ST-20C. Noordwijk, The Netherlands: ECSS Secretariat, ESA-ESTEC, Requirements & Standards Division, Aug. 2019. URL: `https://ecss.nl/wp-content/uploads/2019/07/ECSS-U-ST-20C(1August2019).pdf` (visited on 05/21/2026).

[17] Juliusz Ameljan-Kowalski et al. *Venus In-situ Scientific and Technical Aerobot (VISTA) Mission Midterm Report*. AE3200 Design Synthesis Exercise Midterm Report. Group 02, Academic Year 2025–2026, Quarter 4. Faculty of Aerospace Engineering, Delft University of Technology, June 2, 2026.

[18] NASA. *Neutral Mass Spectrometer for Pioneer Venus Large Probe*. `https://pds.mcp.nasa.gov/portal/instruments/urn--nasa--pds--context--instrument--pvmp---lp---lnms/overview`. Accessed May 2026.

[19] J. H. Hoffman, R. R. Hodges Jr., and K. D. Duerksen. “Pioneer Venus Large Probe Neutral Mass Spectrometer”. In: *Journal of Vacuum Science and Technology* 16.2 (Mar. 1979), pp. 692–694. DOI: `10.1116/1.570059`.

[20] Sara Seager et al. *Venus Life Finder Mission Study*. Tech. rep. MIT-led worldwide consortium study partially funded by Breakthrough Initiatives. Breakthrough Initiatives, Dec. 2021. URL: `https://arxiv.org/abs/2112.05153`.

[21] Darrel Baumgardner et al. "Deducing the Composition of Venus Cloud Particles with the Autofluorescence Nephelometer (AFN)". In: *Aerospace* 9.9 (2022), p. 492. DOI: `10.3390/aerospace9090492`.

[22] Tim J. Cheng et al. "Test Flight of a Stratospheric Sonic Anemometer Prototype". In: *Journal of Atmospheric and Oceanic Technology* 41.12 (2024). Manuscript received 29 January 2024, accepted 1 October 2024, pp. 1139–1149. DOI: `10.1175/JTECH-D-24-0010.1`.

[23] *Digiquartz® Pressure Instrumentation*. accessed in May 2026. URL: `https://psl.noaa.gov/data/obs/instruments/Microbarograph.pdf`.

[24] Hukseflux Thermal Sensors. *User Manual: Industrial Series Class A and Class B Pyranometers*. Hukseflux Thermal Sensors.

[25] Lars E. Kalnajs and Terry Deshler. "A New Instrument for Balloon-Borne In Situ Aerosol SizeDistribution Measurements, the Continuation of a 50 YearRecord of Stratospheric Aerosols Measurements". In: *Journal of Geophysical Research:Atmospheres, 127* (2022).

[26] Raphael F. Garcia et al. "Seismic Wave Detectability on Venus Using Ground Deformation Sensors, Infrasound Sensors on Balloons and Airglow Imagers". In: *Earth and Space Science* 11.11 (2024), e2024EA003670. DOI: `10.1029/2024EA003670`.

[27] Iris van Zelst. "Estimates on the Possible Annual Seismicity of Venus". In: *Journal of Geophysical Research: Planets* 129.8 (2024), e2023JE008048. DOI: `10.1029/2023JE008048`.

[28] Raphael F. Garcia et al. "Infrasound From Large Earthquakes Recorded on a Network of Balloons in the Stratosphere". In: *Geophysical Research Letters* 49.15 (2022), e2022GL098844. DOI: `10.1029/2022GL098844`.

[29] R. F. Garcia et al. "An Active Source Seismo-Acoustic Experiment Using Tethered Balloons to Validate Instrument Concepts and Modelling Tools for Atmospheric Seismology". In: *Geophysical Journal International* 225.1 (2021), pp. 186–199. DOI: `10.1093/gji/ggaa589`.

[30] James N. Brune. "Tectonic Stress and the Spectra of Seismic Shear Waves from Earthquakes". In: *Journal of Geophysical Research* 75.26 (1970), pp. 4997–5009. DOI: `10.1029/JB075i026p04997`.

[31] Giulia Sarego et al. "Deployment requirements for deorbiting electrodynamic tether technology". In: *CEAS Space Journal* 13 (2021), pp. 567–581. DOI: `10.1007/s12567-021-00359-2`.

[32] Hebei Huatong Wires & Cables Group. *Subsea Umbilical Cables: Design, Installation, and Critical Offshore Roles*. Hebei Huatong Wires & Cables Group. 2025. URL: `https://www.hebei-huatong.com/blog/subsea-umbilical-cables-design-installation-and-critical-offshore-roles.html` (visited on 06/15/2026).

[33] Sébastien Lebonnois. *The Venus Climate Database Project*. Landing webpage of the Venus Climate Database. URL: `http://www-venus.lmd.jussieu.fr/`.

[34] EaglePicher Technologies. *LP33037 60 Ah Space Cell Datasheet*. 2022. URL: `https://www.eaglepicher.com/sites/default/files/LP33037%2060Ah%20Space%20Cell%20%201222.pdf` (visited on 06/12/2026).

[35] Spectrolab, Inc. *30.7% XTJ Prime Space Qualified Triple Junction Solar Cell, Data Sheet*. Sylmar, CA. Includes maximum-power-point temperature coefficients. 2016. URL: `https://www.spectrolab.com/photovoltaics/XTJ-Prime_Data_Sheet.pdf`.

[36] AAC Clyde Space. *SmallSat PCDU – STARBUCK-MINI*. `https://www.aac-clyde.space/what-we-do/space-products-components/pcdu/smallsat-pcdu-starbuck-mini`. Accessed: 22 June 2026. 2026.

[37] Honeywell Aerospace. *Q-Flex QA-3000 Single Axis Quartz Accelerometer*. `https://aerospace.honeywell.com/us/en/products-and-services/products/navigation-and-sensors/accelerometers-and-gyroscopes/q-flex-qa-3000-single-axis-quartz-accelerometer`. Accessed: 2026-05-21. 2024.

[38] Safran Sensing Technologies. *STIM300 3-Axis Tactical Grade MEMS Inertial Measurement Unit*. `https://www.safran-group.com/products-services/stim300-3-axis-tactical-grade-mems-inertial-measurement-unit-imu`. Accessed: 2026-05-21. 2024.

[39] Microchip Technology Inc. *ATmegaS64M1 Datasheet: Rad-Tol 8-bit AVR Microcontroller, 3.3V, 8 MHz with 64 KB Flash, 2 KB EEPROM, 4 KB SRAM*. DS60001506B. Accessed: 2026-06-09. Microchip Technology Inc. 2018. URL: `https://ww1.microchip.com/downloads/en/DeviceDoc/ATmegaS64M1_datasheet_ds60001506b.pdf`.

[40] Alén Space. *DARA OBC: On-Board Computer Datasheet*. Issue 1.0. Accessed: 2026-06-09. Alén Space. Nov. 2024. URL: `https://satsearch.s3.eu-central-1.amazonaws.com/datasheets/datasheet-aln-space-dara-obc-on-board-computer-tcmiz8.pdf`.

[41] FRANK P. INCROPERA. "Fundamentals of Heat and Mass Transfer Frank P Incropera". In: *Fundamentals of Heat and Mass Transfer* (2005).

[42] John H. Henninger. "SOLAR ABSORPTANCE AND THERMAL EMITTANCE OF SOME COMMON SPACECRAFT THERMAL-CONTROL COATINGS." In: *NASA Reference Publication* (1984). ISSN: 01488589.

[43] R. G. Knollenberg and D. M. Hunten. "The Microphysics of the Clouds of Venus: Results of the Pioneer Venus Particle Size Spectrometer Experiment". In: *Journal of Geophysical Research: Space Physics* 85.A13 (1980), pp. 8039–8058. DOI: `10.1029/JA085iA13p08039`.

[44] Longkang Dai et al. "A Simple Condensation Model for the H_2SO_4–H_2O Gas–Cloud System on Venus". In: *Journal of Geophysical Research: Planets* 127.3 (2022), e2021JE007060. DOI: `10.1029/2021JE007060`.

[45] Andre Yavrouian et al. "Evaluation of Materials for Venus Aerobot Applications". In: *AIAA Balloon Technology Conference*. Discusses fluoropolymer materials and preliminary PTFE exposure testing for Venus aerobot applications. 1999. DOI: `10.2514/6.1999-3859`.

[46] California Pacific Lab. *Teflon PTFE Chemical Compatibility Reference Chart*. Accessed: 2026-06-17. URL: `https://www.calpaclab.com/teflon-ptfe-compatibility/`.

[47] James B. Garvin et al. "Revealing the Mysteries of Venus: The DAVINCI Mission". In: *The Planetary Science Journal* 3.5 (2022), p. 117. DOI: `10.3847/PSJ/ac63c2`.

[48] M. G. Trainer et al. "The DAVINCI Venus Mass Spectrometer Investigation". In: *55th Lunar and Planetary Science Conference*. Houston, TX: USRA, 2024, p. 2436. URL: `https://www.hou.usra.edu/meetings/lpsc2024/pdf/2436.pdf`.

[49] Lorraine E. Prokop. "A requirements-based, bottom-up SLOC estimate and analysis of NASA's Orion crew exploration vehicle spacecraft flight software". In: *Innovations in Systems and Software Engineering* 10.2 (2014), pp. 93–101. DOI: `10.1007/s11334-012-0181-8`.

[50] *COCOMO II Model Definition Manual*. Version 2.1. USC COCOMO II.2000. Center for Software Engineering, University of Southern California. Los Angeles, CA, 2000. URL: `https://www.rose-hulman.edu/class/cs/csse372/201310/Homework/CII_modelman2000.pdf` (visited on 06/04/2026).

[51] Paul A. Judas and Lorraine E. Prokop. "A historical compilation of software metrics with applicability to NASA's Orion spacecraft flight software sizing". In: *Innovations in Systems and Software Engineering* (2012). DOI: `10.1007/s11334-011-0142-7`.

[52] Les Hatton. *Estimating Source Lines of Code from Object Code: Windows and Embedded Control Systems*. Tech. rep. CISM, University of Kingston, Aug. 2005.

[53] John L. Hennessy and David A. Patterson. *Computer Architecture: A Quantitative Approach*. 6th ed. Morgan Kaufmann, 2019.

[54] Arm Limited. *Cortex-M7: High-Performance DSP for Automotive and IoT*. Accessed 2026-06-17. Arm Limited, 2026. URL: `https://www.arm.com/products/silicon-ip-cpu/cortex-m/cortex-m7`.

[55] STMicroelectronics. *Arm Cortex-M7 Microcontrollers*. States Cortex-M7 benchmark performance of 2.14 DMIPS/MHz and 5.29 CoreMark/MHz; accessed 2026-06-17. STMicroelectronics, 2026. URL: `https://www.st.com/content/st_com/en/arm-32-bit-microcontrollers/arm-cortex-m7.html`.

[56] Texas Instruments. *RS-422 and RS-485 Standards Overview and System Configurations*. Tech. rep. SLLA070D. Originally published June 2002; revised May 2010. Accessed: 2026-06-09. Texas Instruments, May 2010. URL: `https://www.ti.com/lit/pdf/slla070`.

[57] NXP Semiconductors. *UM10204 I2C-bus specification and user manual*. Rev. 7.0. Accessed: 2026-06-09. NXP Semiconductors. Oct. 2021. URL: `https://www.nxp.com/docs/en/user-guide/UM10204.pdf`.

[58] Robert Bosch GmbH. *CAN Specification Version 2.0, Part A*. Accessed: 2026-06-09. Robert Bosch GmbH. 1991. URL: `https://www.port.de/fileadmin/user_upload/Dateien_IST_fuer_Migration/CAN20A.pdf`.

[59] Jacob Beningo. *UART: A Hardware Communication Protocol Understanding Universal Asynchronous Receiver/Transmitter*. Accessed: 2026-06-09. Analog Devices. 2020. URL: `https://www.analog.com/en/resources/analog-dialogue/articles/uart-a-hardware-communication-protocol.html`.

[60] Christophe Morlaas, Bernard Souny, and Alexandre Chabory. "Helical-Ring Antenna for Hemispherical Radiation in Circular Polarization". In: *IEEE Transactions on Antennas and Propagation* 63.11 (Nov. 2015), pp. 4693–4701. DOI: `10.1109/TAP.2015.2479640`.

[61] B. Häusler et al. "Venus Atmospheric, Ionospheric, Surface and Interplanetary Radio-Wave Propagation Studies with the VeRA Radio-Science Experiment". In: *ESA Special Publication* SP-1295 (2007), pp. 1–30. URL: `https://sci.esa.int/web/venus-express/-/41535-vera-radio-science-experiment`.

[62] Anne Angsmann. "Magnetic States of the Ionosphere of Venus Observed by Venus Express". Doctoral dissertation. Braunschweig, Germany: Technische Universität Carolo-Wilhelmina zu Braunschweig, 2011. ISBN: 978-3-942171-49-6.

[63] Warren L. Flock. *Telecommunications in Cometary Environments*. Tech. rep. JPL Publication 81-84. Prepared for the National Aeronautics and Space Administration. Pasadena, California: Jet Propulsion Laboratory, California Institute of Technology, July 1981.

[64] Edoardo Gramigna et al. “Analysis of NASA’s DSN Venus Express radio occultation data for year 2014”. In: *Advances in Space Research* 71 (2023), pp. 1198–1215. doi: `10.1016/j.asr.2022.10.070`.

[65] James R. Wertz and Wiley J. Larson, eds. *Space Mission Analysis and Design*. 3rd ed. Space Technology Library. Torrance, CA and Dordrecht: Microcosm Press and Kluwer Academic Publishers, 1999. isbn: 978-0-7923-5901-2.

[66] Simone Brizzolari. “Analysis of the Effect of the Struts on the ESA DSA-4 Antenna Noise Temperature”. Department of Electrical, Computer and Biomedical Engineering, Master’s Degree in Electronic Engineering, A.Y. 2023/2024. Master’s thesis. Pavia, Italy: University of Pavia, 2024.

[67] David D. Morabito et al. *Venus Surface AM Radio Link Analysis: Preliminary Study*. IPN Progress Report 42-236. February 15, 2024. Jet Propulsion Laboratory, California Institute of Technology, Feb. 2024.

[68] Leon W. Couch. *Digital and Analog Communication Systems*. 8th ed. Pearson Education, 2013. isbn: 9780132915380.

[69] Consultative Committee for Space Data Systems. *TM Synchronization and Channel Coding—Summary of Concept and Rationale*. Green Book CCSDS 130.1-G-3. Report Concerning Space Data System Standards; Informational Report, Issue 3. Washington, DC, USA: Consultative Committee for Space Data Systems, June 2020. url: `https://public.ccsds.org/Pubs/130x1g3e1.pdf`.

[70] Chien-Chung Chen. “Link and System Design”. In: *Deep Space Optical Communications*. Ed. by Hamid Hemmati. Vol. 7. JPL DESCANSO Book Series. Hoboken, NJ: John Wiley & Sons, 2006. Chap. 2, pp. 83–119. url: `https://descanso.jpl.nasa.gov/monograph/series7/Descanso%207_chap02.pdf`.

[71] Axon’ Cable. *AXOSAT*^{TM} *Microwave Coaxial Assemblies*. Released November 2021. Axon’ Cable. Nov. 2021. url: `https://www.axon-cable.com`.

[72] Radiall. *Space Coaxial Switches*. Space section, Section 6; product catalogue/datasheet. Radiall. url: `https://www.radiall.com`.

[73] Filippos Atlasis. *Power Equipment List*. Google Sheets dataset. Accessed: 2026-06-17. 2026. url: `https://docs.google.com/spreadsheets/d/1NQVmwhZQQNC725xTPFfnJI5kNyAAYhC1i_9yOXpuFuk`.

[74] Geoffrey A. Landis and Emily Haag. “Analysis of Solar Cell Efficiency for Venus Atmosphere and Surface Missions”. In: *11th International Energy Conversion Engineering Conference*. NASA/TM-2015-216298. American Institute of Aeronautics and Astronautics, 2015. url: `https://ntrs.nasa.gov/citations/20150016298`.

[75] Jonathan Grandidier et al. *Solar Array Technology for Venus Cloud Environments*. JPL Research Poster R22021, Jet Propulsion Laboratory, California Institute of Technology. 2022. url: `https://www.jpl.nasa.gov/site/research/media/posters/2022/R22021p.pdf`.

[76] Specialty Coating Systems. *Solvent Resistance of Parylene*. Parylene chemical-resistance data: non-oxidising sulfuric acid causes <1% reversible swelling at room temperature. 2024. url: `https://scscoatings.com/newsroom/blog/solvent-resistance-of-parylene/` (visited on 06/17/2026).

[77] Clark E. Cohen. “Attitude Determination Using GPS”. PhD dissertation. Department of Aeronautics and Astronautics, Stanford University, Dec. 1992. url: `https://web.stanford.edu/group/scpnt/gpslab/pubs/theses/ClarkCohenThesis92.pdf`.

[78] European Space Agency. *Attitude Determination*. Navipedia, GNSS knowledge base. Accessed: 2026-06-17. 2026. url: `https://gssc.esa.int/navipedia/index.php/Attitude_Determination`.

[79] R. A. Preston et al. “Determination of Venus Winds by Ground-Based Radio Tracking of the VEGA Balloons”. In: *Science* 231.4744 (1986), pp. 1414–1416. doi: `10.1126/science.231.4744.1414`.

[80] Twan Burger Traian Bistriceanu. *Venus-Balloon-project*. `https://github.com/Taran212121/Venus-Balloon-project`. GitHub repository, accessed: 2026-05-21. 2026.

[81] E. Kassarian et al. “Modeling and stability of balloon-borne gondolas with coupled pendulum-torsion dynamics”. In: *Aerospace Science and Technology* 112 (May 2021), p. 106607. issn: 1270-9638. doi: `10.1016/j.ast.2021.106607`.

[82] François Aubin et al. “Torsional balloon flight line oscillations: Comparison of modelling to flight data”. In: *Advances in Space Research* 60.3 (2017), pp. 702–708. issn: 0273-1177. doi: `10.1016/j.asr.2017.05.003`.

[83] NASA. *Lesson 19101*. `https://llis.nasa.gov/lesson/19101`. Accessed: 2026-05-21. 2017.

[84] Enidine. *Wire Rope Isolators*. `https://www.enidine.com/en-us/products/wire-rope-isolators`. Accessed: 2026-05-21. 2024.

[85] Klaus Hofer. “Wire Rope Isolators for Space Applications”. In: *Proceedings of the 10th European Space Mechanisms and Tribology Symposium (ESMATS)*. Vienna, Austria: European Space Agency (ESA), 2009. url: `https://www.esmats.eu/esmatspapers/pastpapers/pdfs/2009/hofer.pdf`.

[86] Raymond J. Roark et al. *Roark’s Formulas for Stress and Strain*. 9th. Accessed: 2026-06-12. McGraw-Hill Education, 2020. url: `http://nguyen.hong.hai.free.fr/EBOOKS/SCIENCE%20AND%20ENGINEERING/MECANIQUE/THEORIE%20DE%20BASE/Roark%27s%20Formulas%20For%20Stress%20And%20Strain.pdf`.

[87] V. I. Weingarten, P. Seide, and J. P. Peterson. *Buckling of Thin-Walled Circular Cylinders*. Tech. rep. NASA SP-8007. Washington, D.C.: NASA, 1968.

[88] Kudzanai Sekerere and Tawanda Mushiri. "Finite Element Analysis of a Cubesat". In: *Proceedings of the 2017 International Conference on Industrial Engineering and Operations Management (IEOM)*. Bristol, UK, July 2017.

[89] ScienceDirect Topics. *Aerospace Material*. Accessed: 2026-06-10. URL: `https://www.sciencedirect.com/topics/materials-science/aerospace-material`.

[90] Aisha H. Al-Moubaraki and Hind H. Al-Rushud. "The Red Sea as a Corrosive Environment: Corrosion Rates and Corrosion Mechanism of Aluminum Alloys 7075, 2024, and 6061". In: *International Journal of Corrosion* 2018 (2018). URL: `https://onlinelibrary.wiley.com/doi/abs/10.1155/2018/2381287`.

[91] S. Venkataraman et al. "Prototype design and testing of a Venus long-duration, high-altitude balloon". In: *Advances in Space Research* 42.10 (2008). Accessed: 2026-06-15, pp. 1648–1658. DOI: `10.1016/j.asr.2007.12.032`. URL: `https://www.sciencedirect.com/science/article/pii/S0273117707002360`.

[92] LIROS GmbH. *LIROS Rope Catalogue 2026/2027*. Accessed: 2026-06-15. 2026. URL: `https://www.liros.com/userdata/files/LIROS_rope_catalogue_2026_2027_eng___low_res.pdf`.

[93] European Space Agency. *Margin Philosophy for Science Assessment Studies*. Tech. rep. SCI-PA/2007/029/. Version 1.3. European Space Agency, June 2012. URL: `https://sci.esa.int/documents/34375/36249/1567260131067-Margin_philosophy_for_science_assessment_studies_1.3.pdf`.

[94] VISTA Group 02. *VISTA Aerobot Master Equipment List*. `https://drive.google.com/drive/folders/1_wbSaaPchTwculYuhVyHdTL1PH5knaFZ?usp=drive_link`. Accessed: 2026-06-16. 2025.

[95] Patricia Apostol et al. "Planning and optimal control of a Venus variable altitude aerobot". In: *Acta Astronautica* 223 (2025). DOI: `https://doi.org/10.1016/j.actaastro.2025.03.008`.

[96] Sébastien Lebonnois et al. "Superrotation of Venus' atmosphere analyzed with a full general circulation model". In: *Journal of Geophysical Research* 115 (2010). DOI: `10.1029/2009JE003458`.

[97] Sébastien Lebonnois, Norihiko Sugimoto, and Gabriella Gilli. "Wave analysis in the atmosphere of Venus below 100-km altitude, simulated by the LMD Venus GCM". In: *Icarus* 278 (2016). DOI: `10.1016/j.icarus.2016.06.004`.

[98] Antoine Martinez et al. "Exploring the variability of the venusian thermosphere with the IPSL Venus GCM". In: *Icarus* 389 (2023). DOI: `10.1016/j.icarus.2022.115272`.

[99] Sébastien Lebonnois et al. *VENUS CLIMATE DATABASE v2.3 DETAILED DESIGN DOCUMENT*. Tech. rep. ESA, 2023.

[100] Masahiro Takagi et al. "A GCM Study on the 4-Day and 5-Day Waves in the Venus Atmosphere". In: *Journal of Geophysical Research: Planets* 127.4 (2022). DOI: `https://doi.org/10.1029/2021JE007164`.

[101] Dexin Lai, Sebastien Lebonnois, and Tao Li. "Contribution of Thermal Tides to Venus Upper Cloud-Layer Superrotation". In: *AGU Advances* 6 (2024). DOI: `https://doi.org/10.1029/2025AV001880`.

[102] J. L. Hall et al. "Technology development for a long duration, mid-cloud level Venus balloon". In: *Advances in Space Research* 48.7 (2011), pp. 1238–1247. DOI: `10.1016/j.asr.2011.06.010`.

[103] Jeffery L. Hall et al. "Prototype Development of a Variable Altitude Venus Aerobot". In: *AIAA AVIATION 2021 FORUM*. 2021. DOI: `10.2514/6.2021-2696`.

[104] Honeywell International Inc. *Aclar® barrier films product information*. `https://advancedmaterials.honeywell.com/us/en/brands/aclar-barrier-films`. Accessed May 2026. 2024.

[105] Benchchem. *A comparative guide to the gas permeability of PCTFE films and other fluoropolymers*. `https://pdf.benchchem.com/104/A_Comparative_Guide_to_the_Gas_Permeability_of_PCTFE_Films_and_Other_Fluoropolymers.pdf`. Data sourced from Adtech Polymer Engineering Ltd. 2024.

[106] J. L. Hall et al. "Prototype design and testing of a Venus long duration, high altitude balloon". In: *Advances in Space Research* 42.10 (2008), pp. 1648–1655. DOI: `10.1016/j.asr.2007.04.027`.

[107] Q. Meng and J. Hu. "Article review on Vectran: super fiber from thermotropic crystals of rigid-rod polymer". In: *Journal of Industrial Textiles* 51.2 (2021). Available via ResearchGate publication 351356966, pp. 1–24. DOI: `10.1177/1528083721994941`.

[108] Ehsan Kianfar and Viet Cao. "Polymeric membranes on base of PolyMethyl methacrylate for air separation: a review". In: *Journal of Materials Research and Technology* 10 (2021), pp. 1437–1461. DOI: `10.1016/j.jmrt.2020.12.061`.

[109] Mohammad Ali Semsarzadeh, Morteza Sadeghi, and Mehdi Barikani. "Effect of Chain Extender Length on Gas Permeation Properties of Polyurethane Membranes". In: *Iranian Polymer Journal* 17.6 (2008), pp. 431–440.

[110] Allison Vercasson et al. "Applicability of the series resistance model in predicting the permeability of coated papers to oxygen and water vapor: importance of data quality and associated metadata". In: *Polymer Testing* 150 (2025), p. 108907. DOI: `10.1016/j.polymertesting.2025.108907`.

[111] Howard B. Stanford. *The Measured Permeability to Nitrogen Tetroxide of Some Potential Bladder Materials*. Technical Memorandum 33-123. NASA Contract NAS 7-100. Jet Propulsion Laboratory, California Institute of Technology, Mar. 1963. URL: `https://ntrs.nasa.gov/citations/19660014189`.

[112] Sunil Jha, Ronald S. Sekellick, and Kenneth L. Rubow. “Sintered Metal Hot Gas Filters”. In: *Proceedings of the 4th International Symposium on Gas Cleaning at High Temperatures*. Karlsruhe, Germany, Sept. 1999. URL: `https://mottcorp.com/wp-content/uploads/2020/05/Sintered-Metal-Hot-Gas-Filters.pdf`.

[113] Victor A. DesCamp et al. *Regenerative Particulate Filter Development*. Tech. rep. NASA-CR-115505. Martin Marietta Corporation, 1972.

[114] V. I. Bondar, B. D. Freeman, and I. Pinnau. “Gas transport properties of poly(ether-b-amide) segmented block copolymers”. In: *Journal of Polymer Science Part B: Polymer Physics* 38 (2000), pp. 2051–2062.

[115] Roman Selyanchyn, Miho Ariyoshi, and Shigenori Fujikawa. “Thickness Effect on CO2/N2 Separation in Double Layer Pebax-1657®/PDMS Membranes”. In: *Membranes* 8.4 (2018), p. 121. DOI: `10.3390/membranes8040121`.

[116] Hossein Hassanzadeh, Reza Abedini, and Mohsen Ghorbani. “Dual synergistic modification of Pebax 2533 membranes with sorbitol and silver nanoparticles for enhanced CO2 separation efficiency”. In: *Scientific Reports* 15 (2025), p. 31233. DOI: `10.1038/s41598-025-14227-1`.

[117] J. G. Wijmans and R. W. Baker. “The solution-diffusion model: a review”. In: *Journal of Membrane Science* 107 (1995), pp. 1–21.

[118] NETZSCH Analyzing & Testing. *PSU: Polysulfone*. `https://analyzing-testing.netzsch.com/en/polymers-netzsch-com/high-temperature-resistant-thermoplastics/psu-polysulfone`. Accessed: 2026-06-11.

[119] Xometry Europe. *Standard PEEK Material Properties*. `https://xometry.pro/en-eu/materials/standard-peek/`. Accessed: 2026-06-11.

[120] ReliaSoft. *Another Look at the Shape Parameter of the Weibull Distribution*. `https://help.reliasoft.com/articles/content/hotwire/issue110/hottopics110.htm`. Accessed: 2026-06-12.

[121] Minitab. *Weibull distribution in reliability analysis*. `https://support.minitab.com/en-us/minitab/help-and-how-to/statistical-modeling/reliability/supporting-topics/distribution-models/weibull-distribution/`. Accessed: 2026-06-12.

[122] The Lee Company. *LHD Series 2-Way Control Solenoid Valve*. `https://www.theleeco.com/product/lhd-series-2-way-control-solenoid-valve/`. Accessed: 2026-06-12.

[123] Honeywell Advanced Sensing Technologies. *Using DPR Series and ABP2 Series Board Mount Pressure Sensors to Help Determine Optimal HVAC Air Filter Replacement*. Tech. rep. 008351-1-EN. Honeywell International Inc., Apr. 2021. URL: `https://prod-edam.honeywell.com/content/dam/honeywell-edam/sps/siot/ja/products/sensors/pressure-sensors/board-mount-pressure-sensors/basic-abp2-series/documents/sps-siot-using-dpr-abp2-series-air-filter-replace-application-note-008351-en.pdf`.

[124] C. W. Hunt et al. “SIPCO2: A simple, inexpensive surface water pCO2 sensor”. In: *Limnology and Oceanography: Methods* 15 (2017), pp. 291–301. DOI: `10.1002/lom3.10157`.

[125] Nitto Kohki Co., Ltd. *Nitto Kohki’s Air Compressors & Vacuum Pumps: Liquid Pumps*. `https://www.nitto-kohki.eu/images/stories/products/pdf_catalogs/New_Linear_Catalog.pdf`. Cat. No. Lk001a. Accessed: 2026-06-12.

[126] Parker Hannifin Corporation. *Membrane Modules for Nitrogen and Oxygen Generator Systems – Technology Overview*. Catalog K3.1.333a_NA, `https://www.parker.com/content/dam/Parker-com/Literature/IGFG/PDF-Files/K3.1.333-Technology-overview-membrane-modules-for-nitrogen-and-oxygen-systems_NA.pdf`. Accessed June 2026. 2016.

[127] NASA Technology Transfer Program. *Venus Global Reference Atmospheric Model (Venus-GRAM) 2005, Version 1.0*. `https://software.nasa.gov/software/MFS-32314-1`. NASA Software Catalog, reference number MFS-32314-1. Accessed 16 June 2026. 2005.

[128] NASA. *Pioneer Venus 2*. Accessed 2026-06-16. 2024. URL: `https://science.nasa.gov/mission/pioneer-venus-2/`.

[129] Hughes Aircraft Company. *System Design of the Pioneer Venus Spacecraft, Volume 5: Probe Vehicle Studies*. Tech. rep. NASA-CR-132416. Accessed 2026-06-16. NASA, 1974. URL: `https://ntrs.nasa.gov/citations/19740019262`.

[130] M. L. van den Berg et al. “ESA Venus Entry Probe Study”. In: *55th International Astronautical Congress*. Accessed 2026-06-16. 2004. URL: `https://core.ac.uk/download/pdf/42754792.pdf`.

[131] Ethiraj Venkatapathy et al. *Next Generation Thermal Protection Systems for Outer Planet Missions*. NASA Ames Research Center / OPAG presentation. Accessed 2026-06-16. 2021. URL: `https://www.hou.usra.edu/meetings/OPAG2021Aug/eposter/6008.pdf`.

[132] Dinesh K. Prabhu. *45 Degree Sphere-Cone Rigid Aeroshells and Ballistic Entries*. Tech. rep. Accessed 2026-06-16. NASA Ames Research Center, 2013. URL: `https://ntrs.nasa.gov/api/citations/20130010987/downloads/20130010987.pdf`.

[133] Juan R. Cruz. *Parachutes for Planetary Entry Systems*. Accessed 2026-06-16. NASA Langley Research Center. URL: https://mae-nas.eng.usu.edu/MAE_6530_Web/New_Course/launch_design/Parachute.pdf.

[134] Juan R. Cruz et al. “Reconstruction of the Mars Science Laboratory Parachute Performance and Comparison to the Descent Simulation”. In: *AIAA Aerodynamic Decelerator Systems Technology Conference*. Accessed 2026-06-16. 2013. URL: https://ntrs.nasa.gov/api/citations/20130012763/downloads/20130012763.pdf.

[135] Anita Sengupta et al. “Findings from the Supersonic Qualification Program of the Mars Science Laboratory Parachute System”. In: *20th AIAA Aerodynamic Decelerator Systems Technology Conference and Seminar*. Accessed 2026-06-16. 2009. URL: https://ntrs.nasa.gov/citations/20150011941.

[136] Mahendra Pratap et al. “Forebody Wake Effects on Parachute Performance for Re-entry Space Application”. In: *Defence Science Journal* 70.3 (2020). Accessed 2026-06-16, pp. 223–230. URL: https://core.ac.uk/download/pdf/333723105.pdf.

[137] Theo W. Knacke. *Parachute Recovery Systems Design Manual*. NWC TP 6575. Santa Barbara, CA: Para Publishing, 1992.

[138] David Novotney et al. “Qualification of a Networked Pyrotechnic Initiation System for the CST-100 Starliner Spacecraft”. In: *Proceedings of the 44th Aerospace Mechanisms Symposium*. 2018, pp. 263–267. URL: https://esmats.eu/amspapers/pastpapers/pdfs/2018/novotney.pdf.

[139] European Cooperation for Space Standardization. *ECSS-E-ST-20-21C: Space Engineering – Electrical Design and Interface Requirements for Actuators*. Tech. rep. ECSS-E-ST-20-21C. European Cooperation for Space Standardization, May 2019. URL: https://ecss.nl/standard/ecss-e-st-20-21c-electrical-design-and-interface-requirements-for-actuators-15-may-2019/.

[140] *Space Engineering: Explosive Systems and Devices*. ECSS-E-33-11A. European Cooperation for Space Standardization, Apr. 17, 2008.

[141] Marotta Controls. *MV602 Solenoid Valve Datasheet*. Marotta Controls. URL: https://marotta.com/wp-content/uploads/2020/09/MV602.pdf.

[142] European Cooperation for Space Standardization. *ECSS-E-ST-10-02C Rev.1: Space Engineering – Verification*. ECSS Standard ECSS-E-ST-10-02C Rev.1. Noordwijk, The Netherlands: ECSS Secretariat, ESA-ESTEC, Feb. 2018. URL: https://ecss.nl/standard/ecss-e-st-10-02c-rev-1-verification-1-february-2018/.

[143] L. Colin. “The Pioneer Venus Program”. In: *Journal of Geophysical Research: Space Physics* 85.A13 (1980), pp. 7575–7598. DOI: 10.1029/JA085iA13p07575.

[144] M. Ya. Marov and D. H. Grinspoon. *The Planet Venus*. New Haven, CT: Yale University Press, 1998.

[145] M. Pauken, V. Kerzhanovich, J. Hall, et al. “Acid Testing of Materials for Venus Aerobot Missions”. In: *AIAA Balloon Systems Conference*. 2006. DOI: 10.2514/6.2006-6228.

[146] ECSS. *Space Product Assurance — Electrical, Electronic and Electromechanical (EEE) Components (ECSS-Q-ST-60C Rev. 2)*. Tech. rep. Noordwijk, The Netherlands: European Cooperation for Space Standardization, 2013.

[147] T. Kremic, G. Hunter, R. Trejo, et al. “Long-Duration Venus Surface and Atmosphere Measurements Enabled by the Glenn Extreme Environments Rig (GEER)”. In: *Acta Astronautica* (2020).

[148] European Cooperation for Space Standardization. *ECSS-M-ST-60C: Space Project Management – Cost and Schedule Management*. Tech. rep. Noordwijk, The Netherlands: ECSS Secretariat, July 2008. URL: https://ecss.nl/standard/ecss-m-st-60c-cost-and-schedule-management/.

[149] Michel van Pelt. “Phase 0 Space Mission Estimates”. In: *Proceedings of the 2019 ICEAA Professional Development and Training Workshop*. Tampa, FL, USA, May 2019. URL: https://www.iceaaonline.com/wp-content/uploads/2019/06/SM04-Paper-Phase-0-Space-Mission-Estimates-van-Pelt.pdf.

[150] European Cooperation for Space Standardization. *ECSS-M-ST-80C: Space Project Management – Risk Management*. Tech. rep. Noordwijk, The Netherlands: ECSS Secretariat, July 2008. URL: https://ecss.nl/standard/ecss-m-st-80c-risk-management/.

[151] European Cooperation for Space Standardization. *ECSS-E-HB-10-02A: Space Engineering – Verification Guidelines*. ECSS Handbook ECSS-E-HB-10-02A. Noordwijk, The Netherlands: ECSS Secretariat, ESA-ESTEC, Dec. 2010. URL: https://ecss.nl/hbstms/ecss-e-10-02a-verification-guidelines/.

[152] Jian Guo. *Verification and Validation for the Attitude and Orbit Control System*. AE3211-I Systems Engineering Methods lecture slides, Delft University of Technology. Version 2.0, February 26, 2026. 2026.

[153] R. Z. Sagdeev et al. “The VEGA Venus balloon experiment”. In: *Science* 231.4744 (Mar. 1986), pp. 1407–1408. DOI: 10.1126/science.231.4744.1407. URL: https://www.science.org/doi/10.1126/science.231.4744.1407.

[154] Juliusz Ameljan-Kowalski et al. *Venus In-situ Scientific and Technical Aerobot (VISTA) Mission Baseline Report*. Tech. rep. Group 02. Design Synthesis Exercise (DSE), Course AE3200, Academic Year 2025-2026, Quarter Q4. Delft, Netherlands: Delft University of Technology, Faculty of Aerospace Engineering, May 2026.

[155] NASA Earth Science Technology Office (ESTO). *Technology Readiness Levels (TRLs)*. 2026. URL: `https://esto.nasa.gov/trl/` (visited on 06/15/2026).

[156] Alex Vedan. *RAM Analysis: The Complete Guide*. TRACTIAN. 2026. URL: `https://tractian.com/en/glossary/ram-analysis` (visited on 06/15/2026).

[157] Jeffery L. Hall and Andre Yavrouian. “Pinhole Effects on Venus Superpressure Balloon Lifetime”. In: *AIAA Balloon Systems (BAL) Conference*. AIAA 2013-1292. Session: Materials and Small Balloons. Daytona Beach, Florida: American Institute of Aeronautics and Astronautics, Mar. 2013. DOI: `10.2514/6.2013-1292`. URL: `https://doi.org/10.2514/6.2013-1292`.

[158] Aerostar International, LLC. *Aerostar Thunderhead Balloon System Breaks World Record for Stratospheric Flight Duration*. `https://aerostar.com/news/aerostar-thunderhead-balloon-system-breaks-world-record-for-stratospheric-flight-duration`. Accessed: 2026-06-23. Mar. 2025.

[159] R S Kremnev et al. “Design and technical characteristics of the VEGA balloon system”. In: *Soviet Astronomy Letters* 12.1 (1986), pp. 7–10.

A Diagrams

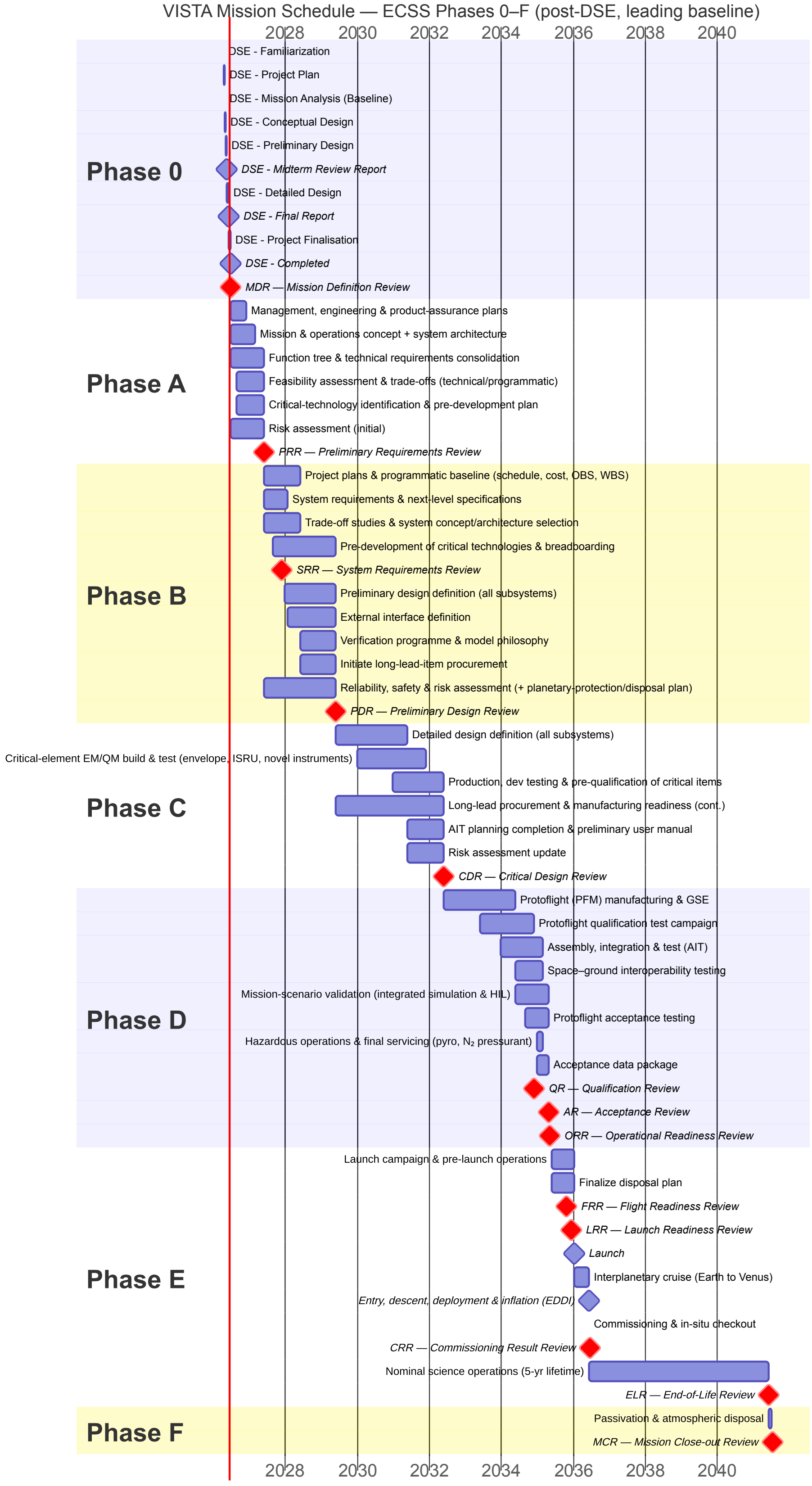

Figure A.1: VISTA Mission Schedule Gantt Chart following ESA mission phases[15]

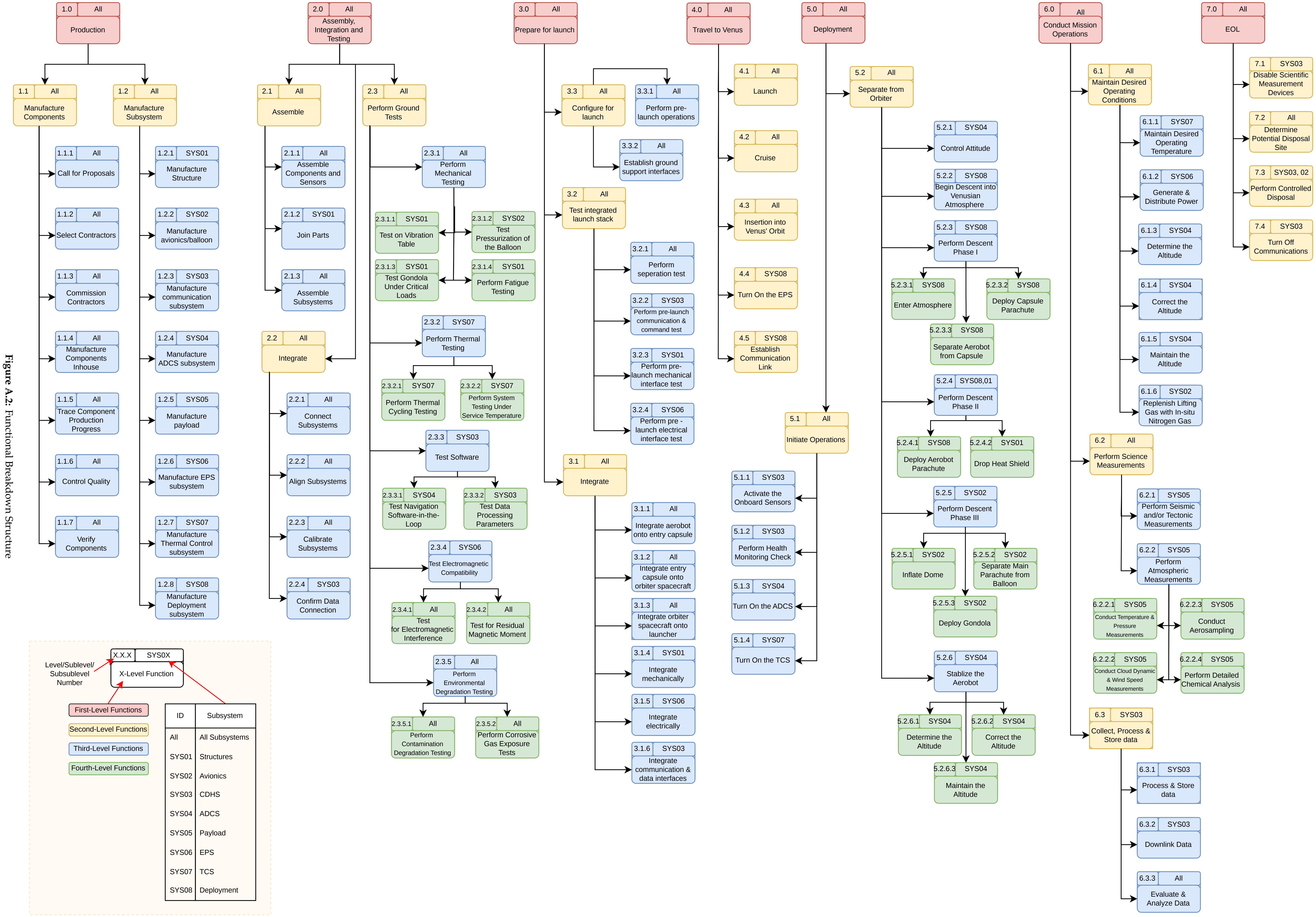

ID	Subsystem
All	All Subsystems
SYS01	Structures
SYS02	Avionics
SYS03	CDHS
SYS04	ADCS
SYS05	Payload
SYS06	EPS
SYS07	TCS
SYS08	Deployment

Figure A.2: Functional Breakdown Structure

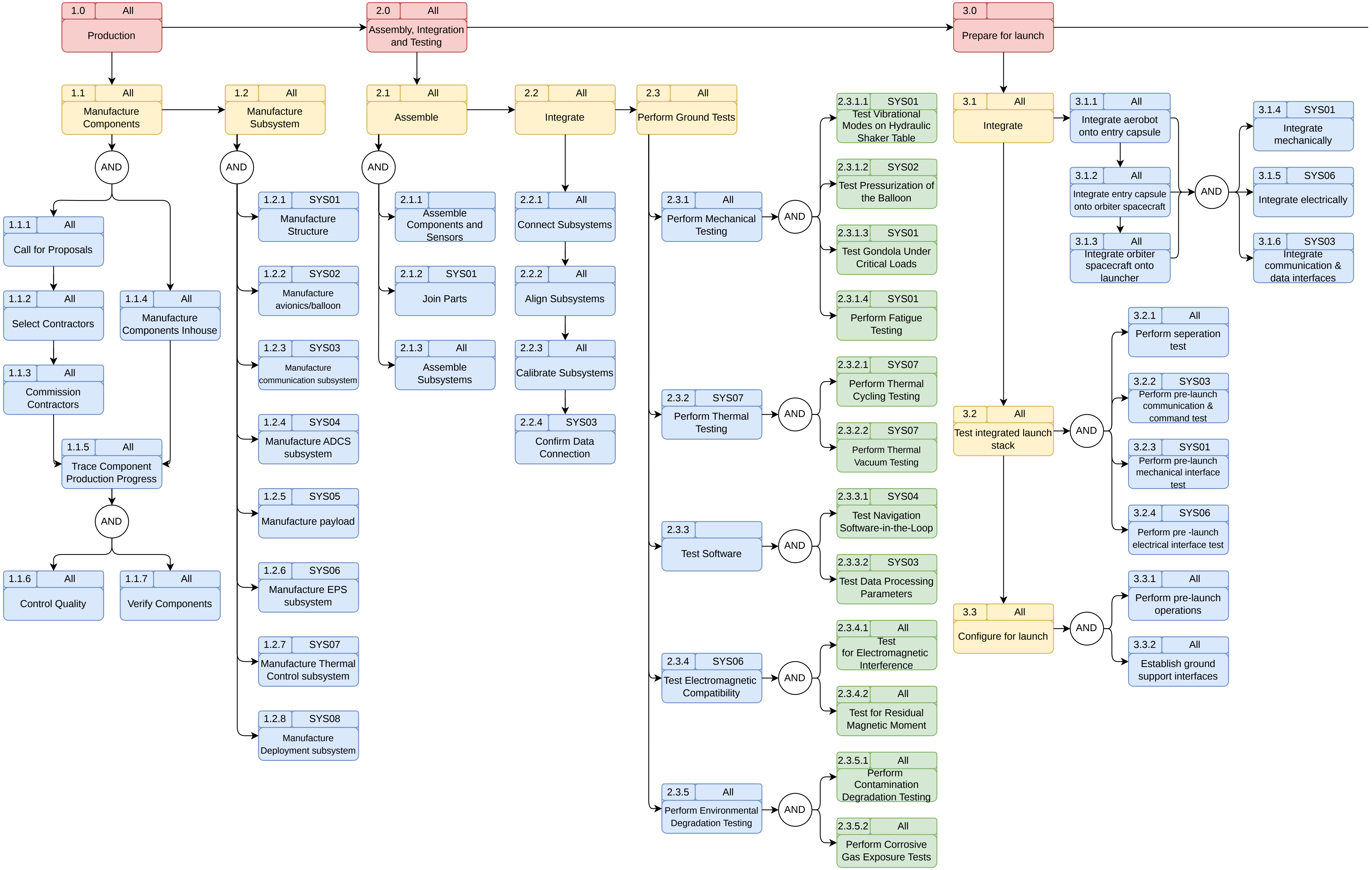
1.0 All Production
2.0 All Assembly, Integration and Testing
3.0 Prepare for launch
1.1 All Manufacture Components
AND
1.1.1 All Call for Proposals
1.1.2 All Select Contractors
1.1.3 All Commission Contractors
1.1.4 All Manufacture Components Inhouse
1.1.5 All Trace Component Production Progress
AND
1.1.6 All Control Quality
1.1.7 All Verify Components
1.2 All Manufacture Subsystem
AND
1.2.1 SYS01 Manufacture Structure
1.2.2 SYS02 Manufacture avionics/balloon
1.2.3 SYS03 Manufacture communication subsystem
1.2.4 SYS04 Manufacture ADCS subsystem
1.2.5 SYS05 Manufacture payload
1.2.6 SYS06 Manufacture EPS subsystem
1.2.7 SYS07 Manufacture Thermal Control subsystem
1.2.8 SYS08 Manufacture Deployment subsystem
2.1 All Assemble
AND
2.1.1 Assemble Components and Sensors
2.1.2 SYS01 Join Parts
2.1.3 All Assemble Subsystems
2.2 All Integrate
2.2.1 All Connect Subsystems
2.2.2 All Align Subsystems
2.2.3 All Calibrate Subsystems
2.2.4 SYS03 Confirm Data Connection
2.3 All Perform Ground Tests
2.3.1 All Perform Mechanical Testing
AND
2.3.1.1 SYS01 Test Vibrational Modes on Hydraulic Shaker Table
2.3.1.2 SYS02 Test Pressurization of the Balloon
2.3.1.3 SYS01 Test Gondola Under Critical Loads
2.3.1.4 SYS01 Perform Fatigue Testing
2.3.2 SYS07 Perform Thermal Testing
AND
2.3.2.1 SYS07 Perform Thermal Cycling Testing
2.3.2.2 SYS07 Perform Thermal Vacuum Testing
2.3.3 Test Software
AND
2.3.3.1 SYS04 Test Navigation Software-in-the-Loop
2.3.3.2 SYS03 Test Data Processing Parameters
2.3.4 SYS06 Test Electromagnetic Compatibility
AND
2.3.4.1 All Test for Electromagnetic Interference
2.3.4.2 All Test for Residual Magnetic Moment
2.3.5 All Perform Environmental Degradation Testing
AND
2.3.5.1 All Perform Contamination Degradation Testing
2.3.5.2 All Perform Corrosive Gas Exposure Tests
3.1 All Integrate
3.1.1 All Integrate aerobot onto entry capsule
3.1.2 All Integrate entry capsule onto orbiter spacecraft
3.1.3 All Integrate orbiter spacecraft onto launcher
AND
3.1.4 SYS01 Integrate mechanically
3.1.5 SYS06 Integrate electrically
3.1.6 SYS03 Integrate communication & data interfaces
3.2 All Test integrated launch stack
AND
3.2.1 All Perform seperation test
3.2.2 SYS03 Perform pre-launch communication & command test
3.2.3 SYS01 Perform pre-launch mechanical interface test
3.2.4 SYS06 Perform pre -launch electrical interface test
3.3 All Configure for launch
AND
3.3.1 All Perform pre-launch operations
3.3.2 All Establish ground support interfaces

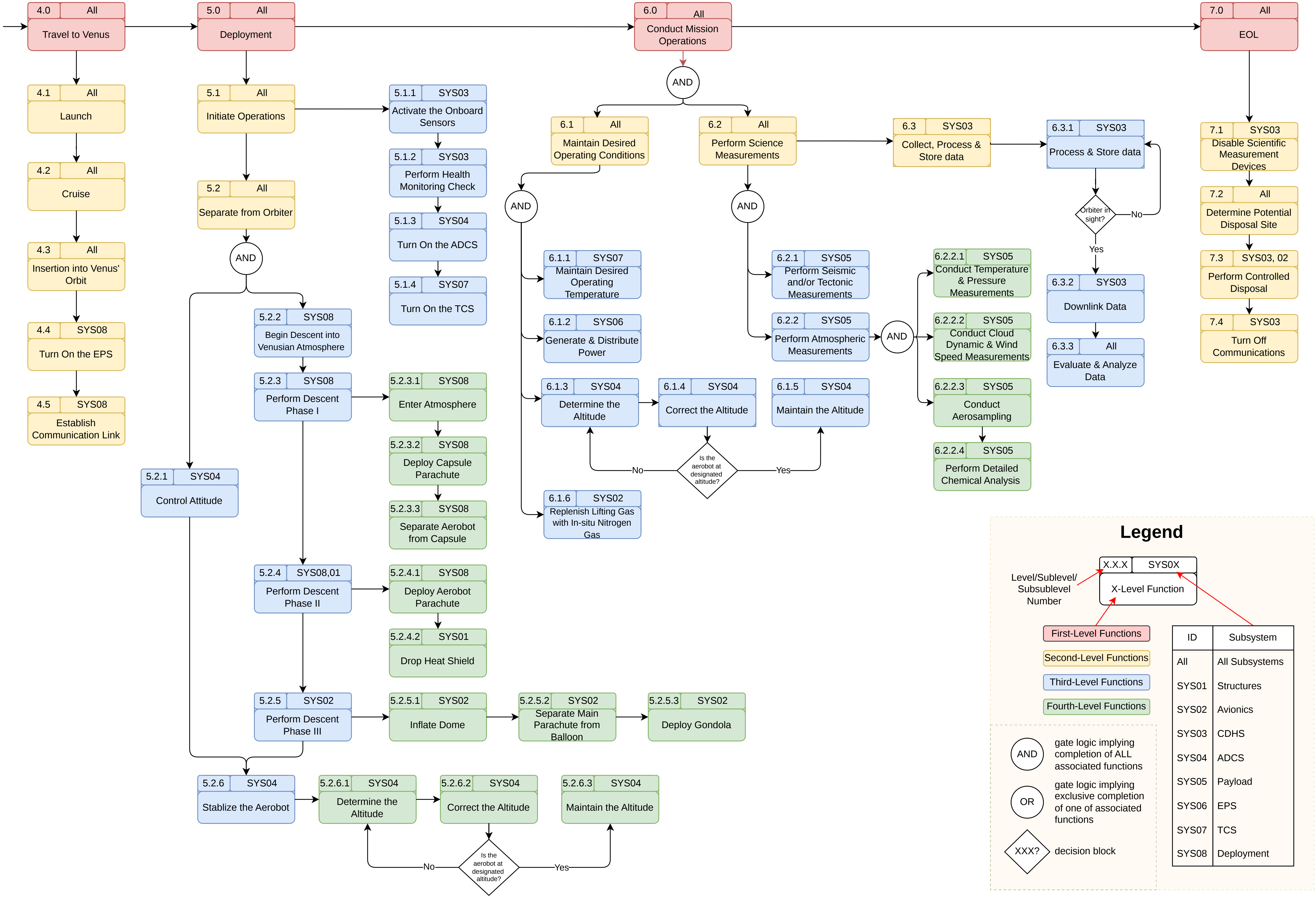

Figure A.3: Function Flow Diagram